VOLUME 30 SEPTEMBER 1952 NUMBER 5

# Canadian Journal of Physics

*Editor:* G. M. VOLKOFF

*Published by* THE NATIONAL RESEARCH COUNCIL
OTTAWA CANADA

# CANADIAN JOURNAL OF PHYSICS

(*Formerly Section A, Canadian Journal of Research*)

The CANADIAN JOURNAL OF PHYSICS is published bimonthly by the National Research Council of Canada under the authority of the Chairman of the Committee of the Privy Council on Scientific and Industrial Research. Matters of general policy are the responsibility of a joint Editorial Board consisting of members of the National Research Council of Canada and the Royal Society of Canada.

The National Research Council of Canada publishes also: *Canadian Journal of Botany, Canadian Journal of Chemistry, Canadian Journal of Medical Sciences, Canadian Journal of Technology, Canadian Journal of Zoology.*


---


## EDITORIAL BOARD

*Representing*
NATIONAL RESEARCH COUNCIL

DR. J. H. L. JOHNSTONE (*Chairman*),
Professor of Physics,
Dalhousie University,
Halifax, N.S.

DR. OTTO MAASS,
Macdonald Professor of
Physical Chemistry,
McGill University,
Montreal, P.Q.

DR. CHARLES W. ARGUE,
Dean of Science,
University of New Brunswick,
Fredericton, N.B.

DR. A. G. MCCALLA,
Dean, Faculty of Agriculture,
University of Alberta,
Edmonton, Alta.

*Representing*
ROYAL SOCIETY OF CANADA

DR. G. M. VOLKOFF,
Professor of Physics,
University of British Columbia
Vancouver, B.C.

Dr. T. Thorvaldson,
Dean Emeritus of Graduate
Studies,
University of Saskatchewan,
Saskatoon, Sask.

} Section III

Dr. D. L. Bailey,
Department of Botany,
University of Toronto,
Toronto, Ont.

DR. E. HORNE CRAIGIE,
Department of Zoology,
University of Toronto,
Toronto, Ont.

} Section V

*Ex officio*

DR. LÉO MARION, *Editor-in-Chief*,
Director, Division of Pure Chemistry,
National Research Laboratories,
Ottawa.

DR. H. H. SAUNDERSON,
Director, Division of Information Services,
National Research Council,
Ottawa.

*Representing*
THE CHEMICAL INSTITUTE OF CANADA

DR. H. G. THODE,
Department of Chemistry,
McMaster University,
Hamilton, Ont.



**Manuscripts** should be addressed to:

DR. LÉO MARION,
Editor-in-Chief,
Canadian Journal of Physics,
National Research Council,
Ottawa, Canada.

Each manuscript should be typewritten, double-spaced, and the original and one extra copy submitted (see **Notice to Contributors,** inside of back cover).

**Subscription, renewals, and orders for back numbers** should be addressed to:

Administrative Services,
National Research Council,
Ottawa, Canada.

---

Subscription rate: $3.00 a year; single numbers: 50 cents. Special rates can be obtained for subscriptions to more than one of the Journals published by the National Research Council.

Canadian Journal of Physics

*Issued by* THE NATIONAL RESEARCH COUNCIL OF CANADA

VOLUME 30 SEPTEMBER, 1952 NUMBER 5

# ALPHA PARTICLES FROM THE PHOTODISINTEGRATION OF SILVER AND BROMINE[1]

BY R. N. H. HASLAM, A. G. W. CAMERON, J. A. COOKE,[2] AND E. H. CROSBY

ABSTRACT

Ilford E1 nuclear emulsions were exposed behind 4 cm. of lucite to the X-ray beam of the University of Saskatchewan betatron operating at energies from 12 Mev. to 26.6 Mev. They were developed by a "grain-gradation" process in order to suppress proton tracks and $\gamma$-ray fog. The variation in yield with energy of the double-peaked single $\alpha$-particle energy spectrum resulting from the photodisintegration of silver and bromine was studied. Preliminary results are given concerning the cross-section curves corresponding to various portions of this $\alpha$-particle spectrum. The energy distributions and cross-section curves have been interpreted in terms of the statistical theory of nuclear reactions.

## I. INTRODUCTION

Single $\alpha$-particles have been reported by Millar and Cameron (20, 21, 22) to result from the photodisintegration of silver and bromine in nuclear emulsions. The energy distribution of these particles exhibits a characteristic double peak. A typical spectrum, plotted in Fig. 1, shows similar results obtained in the present experiment. The lower and higher energy peaks were attributed, respectively, to $(\gamma, n\alpha)$ and $(\gamma, \alpha)$ reactions in silver and bromine (22).

For a few photonuclear reactions, such as $C^{12}(\gamma, \alpha)Be^{8*}$ and $O^{16}(\gamma, 4\alpha)$ (22), the energies of all the disintegration products may be determined separately for each event. An irradiation at a single bremsstrahlung energy is in these cases sufficient to determine reaction cross sections as functions of photon energy. This procedure cannot be used in connection with the $\alpha$-particles reported here, since these particles are expected to have evaporated from excited silver and bromine nuclei; they may be accompanied by the emission of protons, neutrons, or $\gamma$-rays, which would not have been recorded in this experiment. However, if the yield of such $\alpha$-particles could be obtained as a function of bremsstrahlung energy, it would be possible to solve for the photo-alpha cross-section curves by the "photon difference" method (15).

An experiment of this type has been carried out. The results presented here are of a preliminary nature, but they suffice to determine the broad features of the cross-section curves for some rare types of photonuclear reactions. Several hundred thousand $\alpha$-particle tracks should be observed before their yield curves can be considered adequately determined; a program of this magnitude is not

[1] *Manuscript received January 21, 1952.*
*Contribution from the Department of Physics, University of Saskatchewan, Saskatoon, Sask.*
[2] *Now with Canadian Westinghouse Corporation, Hamilton, Ont.*

likely to be completed for several years. The general features of the cross-section curves have been interpreted in terms of the statistical theory of nuclear reactions. Owing to the crudeness of both the experimental results and the development of the statistical theory, much of this discussion is of necessity highly speculative.

## II. THEORY

### (*a*) *Statistical Theory of Photonuclear Reactions*

It is possible in general for an excited compound nucleus to decay initially by the emission of photons or of several types of particle. Such modes of decay will be said to be in "parallel" competition with one another. The residual nucleus is usually left excited. There follows a "cascade" competition between emission of photons or of further particles from this nucleus. In the special case where the residual nucleus is left sufficiently excited to emit charged particles but not neutrons, the emission of such charged particles will be termed in "threshold-favored cascade" competition with the emission of $\gamma$-rays. The latter type of reaction has been discussed by le Couteur (17).

There exists some question as to the manner in which a compound nucleus may be formed by photonuclear excitation. According to the theories of Goldhaber and Teller (10) and of Levinger and Bethe (18) such excitation takes place usually by means of an electric dipole interaction between photons and nuclei. Some experimental evidence (8, 14, 16) suggests that the interaction may result principally in the direct excitation of a nuclear proton. If the proton fails to escape before the excitation energy is spread among the nucleons (thus bringing about "thermal equilibrium") a compound nucleus is thereby formed. The effect of the potential barrier insures the formation of a true compound nucleus in the majority of photonuclear excitations of medium-heavy and heavy nuclei, including silver and bromine.

According to statistical theory (3, 24, 26), the energy distribution of a particle $b$ emitted from a compound nucleus is

$$I(E_b)\,dE_b = \text{const.}\; E_b\,\sigma_b(E_b)\,\omega_R(\epsilon)\,dE_b\,, \tag{1}$$

where $E_b$ is the energy of particle $b$, $\sigma_b(E_b)$ is the cross section of the residual nucleus for capture of a particle $b$ with energy $E_b$, and $\omega_R(\epsilon)$ is the level density of the residual nucleus at an energy $\epsilon$. If the compound nucleus was excited by a photon of energy $h\nu$, then

$$\epsilon = h\nu - E_b - Q_b\,, \tag{2}$$

where $Q_b$ is the binding energy of the particle $b$ in the original nucleus. In Equation (1) it is assumed that the nuclear "sticking function" for a particle $b$ is unity.

Very little is known about nuclear level densities except near the ground level and at excitations in the vicinity of the neutron binding energy. Attempts have been made (3, 24) to fit the existing information by an equation of the form

$$\omega_R(\epsilon) = C \exp 2(a\epsilon)^{\frac{1}{2}} \tag{3}$$

Approximate values of the constants "$C$" and "$a$" for representative nuclei of odd mass number are given by Blatt and Weisskopf (3). Nuclei of even mass number are expected to have smaller level densities, requiring smaller values of "$C$".

For neutron emission the capture cross section $\sigma_n(E_n)$ should be fairly constant, and Equation (1) can be rewritten in the approximate form

$$I(E_n)\,dE_n = \text{const.}\; E_n \exp(-E_n/T)\,dE_n\,, \tag{4}$$

where $T$ is a "nuclear temperature" defined by

$$T = ((h\nu - Q_n)/a)^{\frac{1}{2}}. \tag{5}$$

Equation (4) represents a Maxwellian distribution of the energies of the emitted neutrons.

An "$f$-function", proportional to the integral of Equation (1), may be defined by the relation

$$f_b(h\nu - Q_b) = 2\int_0^{h\nu - Q_b} \frac{m_b E_b}{h^2}\,\sigma_b(E_b)\,\omega_R(\epsilon)\,dE_b, \tag{6}$$

where $m_b$ is the mass of the particle $b$. This is related to the probability of emission of the particle $b$ by the equation

$$\eta_b = f_b \Big/ \sum_c f_c\,, \tag{7}$$

where $\eta_b$ is the fraction of the compound nuclei which decay by emission of the particle $b$, and the summation is taken over all such particles (including photons) which can be emitted. Equation (7) therefore governs the probability for emission of particles in parallel competition with one another. The particle emission width is given by

$$\Gamma_b = f_b/\omega_c(h\nu), \tag{8}$$

where $\omega_c(h\nu)$ is the level density of the compound nucleus.

In parallel competition the emission of neutrons is greatly favored over that of charged particles. The precise computation of relative emission probabilities from Equation (7) is limited by lack of accurate information concerning nuclear level densities; one can hope only to predict the correct order of magnitude for such ratios. If the level density formula of Equation (3) can be trusted, then values of $\eta_b$ become subject to errors in "$C$" and "$a$". However, the relative energy distribution of any particle is subject only to errors in "$a$" (on which it depends in a fairly insensitive manner), and such computations should be somewhat more reliable.

The emission of photons from the compound nucleus is also possible. It has long been known that radiation widths for $\gamma$-ray emission following neutron capture are of the order of magnitude expected for electric quadrupole and magnetic dipole transitions; they are much less than might be expected for electric dipole transitions, since nuclear electric dipole moments are very small. The decay of a compound nucleus at higher excitations by the emission of

likely to be completed for several years. The general features of the cross-section curves have been interpreted in terms of the statistical theory of nuclear reactions. Owing to the crudeness of both the experimental results and the development of the statistical theory, much of this discussion is of necessity highly speculative.

## II. THEORY

### (*a*) *Statistical Theory of Photonuclear Reactions*

It is possible in general for an excited compound nucleus to decay initially by the emission of photons or of several types of particle. Such modes of decay will be said to be in "parallel" competition with one another. The residual nucleus is usually left excited. There follows a "cascade" competition between emission of photons or of further particles from this nucleus. In the special case where the residual nucleus is left sufficiently excited to emit charged particles but not neutrons, the emission of such charged particles will be termed in "threshold-favored cascade" competition with the emission of $\gamma$-rays. The latter type of reaction has been discussed by le Couteur (17).

There exists some question as to the manner in which a compound nucleus may be formed by photonuclear excitation. According to the theories of Goldhaber and Teller (10) and of Levinger and Bethe (18) such excitation takes place usually by means of an electric dipole interaction between photons and nuclei. Some experimental evidence (8, 14, 16) suggests that the interaction may result principally in the direct excitation of a nuclear proton. If the proton fails to escape before the excitation energy is spread among the nucleons (thus bringing about "thermal equilibrium") a compound nucleus is thereby formed. The effect of the potential barrier insures the formation of a true compound nucleus in the majority of photonuclear excitations of medium-heavy and heavy nuclei, including silver and bromine.

According to statistical theory (3, 24, 26), the energy distribution of a particle $b$ emitted from a compound nucleus is

$$I(E_b)\, dE_b = \text{const.}\, E_b\, \sigma_b(E_b)\, \omega_R(\epsilon)\, dE_b\,, \tag{1}$$

where $E_b$ is the energy of particle $b$, $\sigma_b(E_b)$ is the cross section of the residual nucleus for capture of a particle $b$ with energy $E_b$, and $\omega_R(\epsilon)$ is the level density of the residual nucleus at an energy $\epsilon$. If the compound nucleus was excited by a photon of energy $h\nu$, then

$$\epsilon = h\nu - E_b - Q_b\,, \tag{2}$$

where $Q_b$ is the binding energy of the particle $b$ in the original nucleus. In Equation (1) it is assumed that the nuclear "sticking function" for a particle $b$ is unity.

Very little is known about nuclear level densities except near the ground level and at excitations in the vicinity of the neutron binding energy. Attempts have been made (3, 24) to fit the existing information by an equation of the form

$$\omega_R(\epsilon) = C \exp 2(a\epsilon)^{\frac{1}{2}} \tag{3}$$

Approximate values of the constants "$C$" and "$a$" for representative nuclei of odd mass number are given by Blatt and Weisskopf (3). Nuclei of even mass number are expected to have smaller level densities, requiring smaller values of "$C$".

For neutron emission the capture cross section $\sigma_n(E_n)$ should be fairly constant, and Equation (1) can be rewritten in the approximate form

$$I(E_n)\,dE_n = \text{const.}\; E_n \exp(-E_n/T)\,dE_n\,, \tag{4}$$

where $T$ is a "nuclear temperature" defined by

$$T = ((h\nu - Q_n)/a)^{\frac{1}{2}}. \tag{5}$$

Equation (4) represents a Maxwellian distribution of the energies of the emitted neutrons.

An "$f$-function", proportional to the integral of Equation (1), may be defined by the relation

$$f_b(h\nu - Q_b) = 2\int_0^{h\nu - Q_b} \frac{m_b E_b}{h^2}\,\sigma_b(E_b)\,\omega_R(\epsilon)\,dE_b, \tag{6}$$

where $m_b$ is the mass of the particle $b$. This is related to the probability of emission of the particle $b$ by the equation

$$\eta_b = f_b \Big/ \sum_c f_c\,, \tag{7}$$

where $\eta_b$ is the fraction of the compound nuclei which decay by emission of the particle $b$, and the summation is taken over all such particles (including photons) which can be emitted. Equation (7) therefore governs the probability for emission of particles in parallel competition with one another. The particle emission width is given by

$$\Gamma_b = f_b/\omega_c(h\nu), \tag{8}$$

where $\omega_c(h\nu)$ is the level density of the compound nucleus.

In parallel competition the emission of neutrons is greatly favored over that of charged particles. The precise computation of relative emission probabilities from Equation (7) is limited by lack of accurate information concerning nuclear level densities; one can hope only to predict the correct order of magnitude for such ratios. If the level density formula of Equation (3) can be trusted, then values of $\eta_b$ become subject to errors in "$C$" and "$a$". However, the relative energy distribution of any particle is subject only to errors in "$a$" (on which it depends in a fairly insensitive manner), and such computations should be somewhat more reliable.

The emission of photons from the compound nucleus is also possible. It has long been known that radiation widths for $\gamma$-ray emission following neutron capture are of the order of magnitude expected for electric quadrupole and magnetic dipole transitions; they are much less than might be expected for electric dipole transitions, since nuclear electric dipole moments are very small. The decay of a compound nucleus at higher excitations by the emission of

electric quadrupole and magnetic dipole photons is predicted to be much less probable than decay by neutron emission (4, 25). However, a large radiation width, probably corresponding to electric dipole emission, has recently been observed (6) in the photonuclear excitation of gold at photon energies near 15 Mev. This implies that the decay of a highly-excited compound nucleus by $\gamma$-ray emission may be comparable in probability with that by neutron emission. Such initially-emitted photons may be expected to be of relatively low energy (6). Hence in this region of excitation, initial $\gamma$-ray emission will usually be followed by particle emission in cascade reactions of the types $(\gamma, \gamma' n)$, $(\gamma, \gamma' p)$, and $(\gamma, \gamma' \alpha)$. (In this paper reaction products are written in the assumed order of emission.)

(*b*) *Parallel and Cascade Photo-alpha Reactions*

It is expected that the energy distribution of $\alpha$-particles emitted initially from a compound nucleus will be given by Equation (1). Such distributions are strongly dependent on the capture cross section, $\sigma_\alpha(E_\alpha)$, which is proportional to the barrier penetrability of the $\alpha$-particles summed over the relative angular momenta with which they may be emitted. If a nucleus is presumed to have a rapidly increasing level density as a function of excitation energy, then calculations show that the most probable evaporation energy of the $\alpha$-particles is of the order of half the height of the potential barrier. Millar and Cameron (22) attributed their higher energy $\alpha$-particle peak to such $(\gamma, \alpha)$ reactions in silver and bromine. By analogue with the measured cross sections for $(\gamma, \alpha)$ reactions in $Rb^{87}$(12) and in $Cu^{65}$(13), it may be expected that the main contribution to this peak results from photonuclear excitation by photons with energies between 20 and 25 Mev.

Cascade reactions of the type $(\gamma, \gamma' \alpha)$ may possibly also provide a source of higher energy $\alpha$-particles. In such reactions initial photon absorption is followed by the electric dipole radiation of a low energy $\gamma$-ray. The relative emission probabilities of neutrons, protons, and $\alpha$-particles from the residual compound nucleus are in this case only slightly changed from those in the original compound nucleus.

Hence, following absorption of photons of energy $h\nu$ by the nucleus, $\alpha$-particles should be emitted partly with an energy distribution as computed from Equation (1), and partly with energy distributions which would be computed from Equation (1) for excitations less than $h\nu$. A quantitative computation of this character is impossible at present, owing to the crudeness of the knowledge concerning electric dipole radiation widths. However, since the $\alpha$-particle energy distributions are primarily governed by $\sigma_\alpha(E_\alpha)$, the composite distribution should differ only slightly from that computed directly from Equation (1) for excitations of $h\nu$.

Following $\alpha$-particle emission from a highly excited compound nucleus, the residual nucleus will generally be left sufficiently excited to emit further particles in cascade reactions of the types $(\gamma, \alpha n)$, $(\gamma, \alpha p)$, and $(\gamma, \alpha\alpha)$. The secondary emission of neutrons will be greatly preferred when that is energetically possible,

since the emission of charged particles is impeded by the presence of the potential barrier. When neutron emission is not energetically possible, secondary charged particle emission is classified as threshold-favored and will be discussed in the next subsection.

If the initial $\alpha$-particle energy distribution is known for some excitation energy, then it is possible to find what percentage of the $\alpha$-particle emissions can be followed by neutron emission. This provides a rough basis for an estimate of the yield of $(\gamma, \alpha n)$ reactions. Such an estimate is very crude, owing to the uncertain effects of cascade reactions of the types $(\gamma, \gamma' \alpha)$ and $(\gamma, \alpha \gamma')$. A similar computation has previously been used to separate $(\gamma, p)$ and $(\gamma, pn)$ cross sections in lead (7).

(*c*) *Threshold-favored Emission of Alpha Particles*

The heavier nuclei possess regions of excitation from which the emission of protons and $\alpha$-particles, but not of neutrons, is energetically possible. Alpha particles have a typical binding energy of about 3 Mev. in nuclei in the neighborhood of silver. The binding energies of protons and neutrons are about 7 and 9 Mev. respectively. Charged particle emission from this threshold-favored region must compete with $\gamma$-ray decay, but the latter will have a radiation width characteristic of electric quadrupole and magnetic dipole radiation. It has been estimated by le Couteur (17) that in residual nuclei somewhat lighter than silver and bromine protons of energy less than 0.5 Mev. and $\alpha$-particles of energy less than 4 Mev. have much longer emission lifetimes than photons and hence should not be observed. The actual observation of very low energy $\alpha$-particles by Millar and Cameron (22) indicates that such a condition is too restrictive.

Cross sections for the nuclear absorption of photons of energy less than 10 Mev. are very small, so that the threshold-favored emission of $\alpha$-particles by direct excitation is not expected to be important. However, the initial de-excitation of compound nuclei which have absorbed higher energy photons may very often leave a residual nucleus excited in this energy region. Hence low energy $\alpha$-particles may be expected to be emitted mainly in threshold-favored cascade reactions of the types $(\gamma, \gamma' \alpha)$, $(\gamma, n\alpha)$, $(\gamma, p\alpha)$, and $(\gamma, \alpha\alpha)$.

It is evident that the differences between the binding energies of $\alpha$-particles and neutrons and of $\alpha$-particles and protons are principal factors governing the ease with which threshold-favored $\alpha$-particles may be emitted from possible intermediate nuclei. Such differences and also the thresholds for parallel and cascade photo-alpha reactions have been calculated from the semiempirical masses of Metropolis (19). The results, subject to errors of the order of 1 Mev., are given in Table I. It may be seen that $\alpha$-particles have larger energy advantages for threshold-favored cascade reactions originating in silver than in bromine. The greater part of the low energy peak of Fig. 1 is therefore presumed to have arisen from such reactions in silver.

Consider a typical intermediate residual nucleus. At low excitation energies only $\alpha$-particles and $\gamma$-rays can be emitted; as the excitation energy is raised $\alpha$-particle emission becomes relatively more probable. At higher excitation

TABLE I

THRESHOLDS AND THRESHOLD DIFFERENCES FOR PHOTONUCLEAR REACTIONS IN WHICH α-PARTICLES CAN BE EMITTED FROM THE INDICATED PARENT SILVER AND BROMINE ISOTOPES

| Reactions | Thresholds (Mev.) | | | |
|---|---|---|---|---|
| | $Br^{79}$ | $Br^{81}$ | $Ag^{107}$ | $Ag^{109}$ |
| $(\gamma, \alpha)$, $(\gamma, \gamma' \alpha)$ | 4.9 | 5.4 | 2.3 | 2.7 |
| $(\gamma, n \alpha)$, $(\gamma, \alpha n)$ | 14.7 | 14.5 | 11.9 | 11.8 |
| $(\gamma, p \alpha)$, $(\gamma, \alpha p)$ | 12.4 | 14.0 | 8.5 | 9.8 |
| $(\gamma, \alpha \alpha)$ | 10.3 | 11.5 | 5.1 | 6.0 |
| **Reactions** | **Difference in thresholds (Mev.)** | | | |
| $(\gamma, n n) - (\gamma, n \alpha)$ | 3.2 | 1.9 | 6.0 | 5.0 |
| $(\gamma, n p) - (\gamma, n \alpha)$ | 1.8 | 2.3 | 3.3 | 3.6 |
| $(\gamma, \gamma' n) - (\gamma, \gamma' \alpha)$ | 5.2 | 3.8 | 7.6 | 6.6 |
| $(\gamma, \gamma' p) - (\gamma, \gamma' \alpha)$ | 3.1 | 3.6 | 4.5 | 4.8 |
| $(\gamma, p n) - (\gamma, p \alpha)$ | 4.1 | 2.7 | 6.7 | 5.6 |
| $(\gamma, p p) - (\gamma, p \alpha)$ | 4.9 | 5.3 | 5.7 | 5.9 |
| $(\gamma, \alpha n) - (\gamma, \alpha \alpha)$ | 4.4 | 3.0 | 6.8 | 5.8 |
| $(\gamma, \alpha p) - (\gamma, \alpha \alpha)$ | 2.1 | 2.5 | 3.4 | 3.8 |

energies, protons can also be emitted and the α-particle yield will be relatively reduced. When neutron emission becomes possible, that of charged particles becomes very improbable. At still higher energies, electric dipole radiation may lower the intermediate nuclear energy to the threshold-favored region. This may produce tertiary reactions of such types as $(\gamma, n \gamma' \alpha)$, $(\gamma, p \gamma' \alpha)$, etc.

The energy distribution of any primary photodisintegration particle, given by Equations (1) and (4), is quite strongly peaked. The peak energy is a slowly-varying function of the nuclear excitation energy. A residual nucleus of given excitation is consequently most probably formed by the emission of some particle when the original excitation is equal to the sum of the residual excitation, plus the binding energy of the particle, plus the most probable kinetic energy of the particle. This provides a criterion from which the energies of the cross-section peaks for threshold-favored cascade reactions may be predicted. It may be expected that threshold-favored α-particle emission will be most probable when a nucleus is not quite sufficiently excited to emit a neutron, or not quite sufficiently excited to emit a proton with an energy of the order of 0.5 Mev., whichever energy is the lower. Thus the peak cross section for such reactions should occur at an energy equal to the sum of the binding energies of the emitted particles plus their most probable kinetic energies. Various possible reactions will be considered individually.

(*i*) $(\gamma, n \alpha)$ *reactions.*—The primary neutrons have Maxwellian energy distributions given by Equation (4), with most probable energies of the order of 1 Mev. The dotted line in Fig. 4 is a quantitative prediction of the shape to be expected for $(\gamma, n \alpha)$ reactions in silver and bromine. It was assumed that the principal contribution to the curve comes from silver due to larger threshold energy differences than occur in bromine. The peak cross-section energy was

predicted by the method of the preceding paragraph. The half-width of the curve was assumed to be the square root of the sum of the squares of the width of the low energy α-particle peak observed by Millar and Cameron (22) and of the width of the Maxwellian neutron energy distribution.

(*ii*) ($\gamma, \gamma' \alpha$) *reactions.*—Owing to the complicated manner in which the excitation of the compound nucleus can be lowered to the threshold-favored region by photon cascades, the previous criterion for the energy of the peak cross section cannot be applied in this case. It is probable, however, that this energy is equal to or lower than the energy of the maximum photonuclear absorption cross section. In silver the latter energy is about 16 Mev. (5, 9).

(*iii*) ($\gamma, p \alpha$) *reactions.*—The primary protons may be considered to fall into two classes: those emitted from compound nuclei and those emitted in direct photonuclear ejection processes. The distribution of protons between these classes is highly uncertain, but it is evident that the second class will become relatively more favored as the energy of the bombarding photons is increased. The protons of the first class will have an energy distribution given by Equation (1); those of the second class will be emitted with somewhat higher energies. The energy distribution of photoprotons from silver has been measured by Diven and Almy (9) for photon energies up to 21 Mev. The use of their most probable proton energy leads to a prediction of 20 Mev. for the peak energy of the ($\gamma, p \alpha$) cross section in silver. But both classes of protons emitted from excited nuclei of such an excitation energy may have most probable kinetic energies larger than that in the distribution of Diven and Almy. The above value must accordingly be considered a lower limit of the expected peak energy.

(*iv*) ($\gamma, \alpha \alpha$) *reactions.*—The initial α-particle is expected to have an energy distribution similar in shape to the higher energy peak of Fig. 1. These events should be manifest as two-pronged α-particle stars. Such stars have been observed by Millar and Cameron (22). The most probable cross-section peak position is approximately the sum of the binding energies of two α-particles plus the energies of the α-particle peaks in Fig. 1.

Estimates for the peak energies expected for these four types of reactions are given in Table II. No account has been taken of contributions by tertiary reactions such as ($\gamma, n \gamma' \alpha$).

TABLE II

EXPECTED ENERGIES (MEV.) FOR THE MAXIMUM CROSS SECTIONS OF VARIOUS THRESHOLD-FAVORED CASCADE REACTIONS

| Reaction | Parent isotope | | | |
|---|---|---|---|---|
| | $Br^{79}$ | $Br^{81}$ | $Ag^{107}$ | $Ag^{109}$ |
| ($\gamma, n \alpha$) | 18.6 | 18.0 | 16.9 | 17.1 |
| ($\gamma, \gamma' \alpha$) | $\sim 17$ | $\sim 17$ | $\sim 16$ | $\sim 16$ |
| ($\gamma, p \alpha$) | $> 22$ | $> 22$ | $> 20$ | $> 20$ |
| ($\gamma, \alpha \alpha$) | 22 | 23 | 18 | 19 |

The energy distribution of the α-particles emitted by the threshold-favored mechanism may also be predicted by Equation (1). However, the penetrability of the potential barrier exerts a major restraint on such distributions, and in general the α-particles should be emitted with nearly their maximum possible energy.

## III. EXPERIMENTAL PROCEDURE

In the determination of a photonuclear cross-section curve by the activation method at this laboratory, samples are irradiated in the X-ray beam behind 4 cm. of lucite. The dose delivered to the sample is monitored by a Victoreen ionization chamber in the same position. A curve of saturated specific activity per unit dose is obtained as a function of the betatron operating energy; this is the "activation", or "yield" curve. It can be solved for the photonuclear cross-section curve by the "photon difference" method (15). In this experiment a yield curve of this type was obtained for the single α-particles resulting from the photodisintegration of silver and bromine.

Eight 100 micron Ilford E1 nuclear research emulsions were exposed to approximately 200 roentgens of X-radiation at various betatron energies under the above conditions. Dosages were measured at the center of the plate. The measured area of the plate subtended an angle of 2.7° at the target of the betatron. Curves supplied by the betatron manufacturer (Allis-Chalmers) were used to find the average dose delivered to this area of each plate at the various energies.

The plates were developed with a modification of Van der Grinten's "grain-gradation" developer (27, p. 62) as used by Millar and Cameron (22). This procedure suppresses γ-ray fog and proton tracks. Occasionally a thin line of grains can be seen denoting the end of a proton or deuteron track, but these cannot be mistaken for α-particles, which leave much heavier tracks.

The plates were searched under a Cooke, Troughton, and Simms binocular microscope with a nominal magnification of 1000 diameters. The energies of all single α-particle tracks found on equivalent areas of 1.3 cm.$^2$ on each plate were measured. Each observer measured a given equivalent fractional part of the area on each plate, and the plates of various energies were measured in random order. This procedure minimized as much as possible the effects of personal equations on the resulting yield curves.

Each α-particle track was examined carefully to make sure it did not represent one of the reactions $C^{13}(\gamma, \alpha)Be^9$, $N^{14}(\gamma, \alpha)B^{10}$, or $O^{16}(\gamma, \alpha)C^{12}$. Such reactions occur in the light elements of the emulsion (20, 22), and are recognizable by virtue of the fact that the light recoiling nucleus leaves a short, heavy stub at the origin of the α-particle track. In cases of doubt (which are few) the event was not accepted for measurement.

A background plate which had not been exposed was developed at the same time. Unexposed emulsions contain a few α-particle tracks due to natural contamination by uranium and thorium ions, which give a background energy peak lying between 4 and 5 Mev. (a modification of this spectrum is shown in (23)).

The plates used in this experiment were exposed and developed shortly after receipt from the manufacturer, and were from a freshly-made batch of emulsion, so that background contamination was small. The observed numbers of α-particle tracks were much larger than background in all except the lowest energy plate.

The numbers of α-particle tracks measured in the various plates are shown in Table III. The α-particle energy spectrum (corrected for background) ob-

TABLE III

NUMBERS OF α-PARTICLES FOUND IN 1.3 cm.² OF THE PLATES EXPOSED AT VARIOUS BETATRON ENERGIES

| Betatron energy (Mev.) | α-Particles/1.3 cm.² |
|---|---|
| 12.0 | 13 |
| 14.0 | 67 |
| 16.0 | 135 |
| 18.0 | 231 |
| 20.0 | 375 |
| 22.0 | 433 |
| 24.0 | 590 |
| 26.6 | 781 |
| Unexposed | 20 |
| Total | 2645 |

tained for the plate irradiated at 24 Mev. is plotted in Fig. 1; it exhibits the characteristic double peak discussed in Section II. The spectrum resulting from each plate was plotted in a similar manner and corrected for escape of tracks

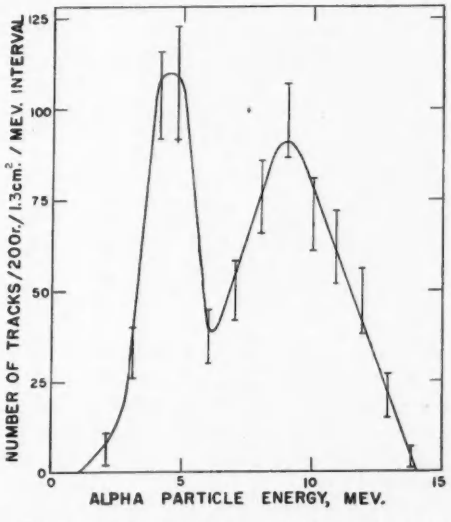


FIG. 1. Energy spectrum of the α-particles resulting from the photodisintegration of silver and bromine in an irradiation with 24 Mev. X rays. The spectrum has been corrected for background and for the escape of α-particles from the emulsion.

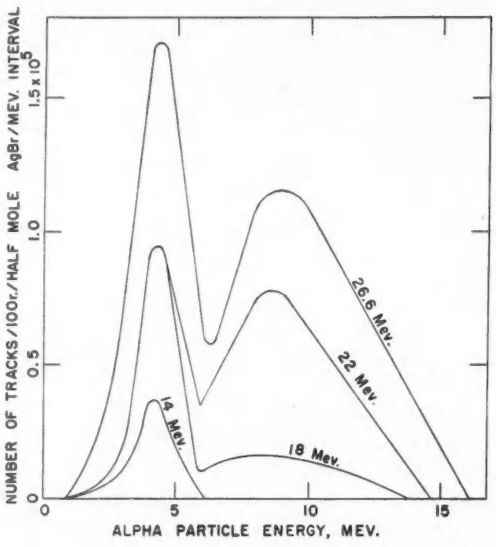


FIG. 2. Energy spectral shapes for α-particles resulting from the photodisintegration of silver and bromine in irradiations at various X-ray energies. The spectra have been corrected for background and for the escape of α-particles from the emulsion. They have been normalized to equal total dosages.

from the emulsion (22). The spectra were then normalized to correspond to irradiation dosages of 100 roentgens. The general way in which the yield of the two peaks varies as a function of betatron energy may be seen in Fig. 2, in which four of the spectral shapes are plotted together.

## IV. EXPERIMENTAL RESULTS

### (a) *Low Energy Alpha Particles*

It was indicated in Section II that the lower energy α-particle peak was expected to arise from threshold-favored cascade reactions. It was postulated that the higher energy peak represented parallel and cascade reactions of the types $(\gamma, \alpha)$, $(\gamma, \alpha\ n)$, etc. The yields of α-particles in each peak have therefore been treated separately.

The yield of the lower energy α-particles as a function of betatron energy is shown in Fig. 3. It is apparent that the yield curve for these α-particles contains at least two points of inflection, so that the corresponding cross-section curve contains at least two major peaks. The yield points have been fitted by a composite of two yield curves each having smooth first and second derivatives. Experience with the photon difference method (15) has indicated that such criteria regarding the derivatives of a yield curve seem to give the broad general features of a photonuclear cross-section curve, and to locate the peak position fairly accurately.

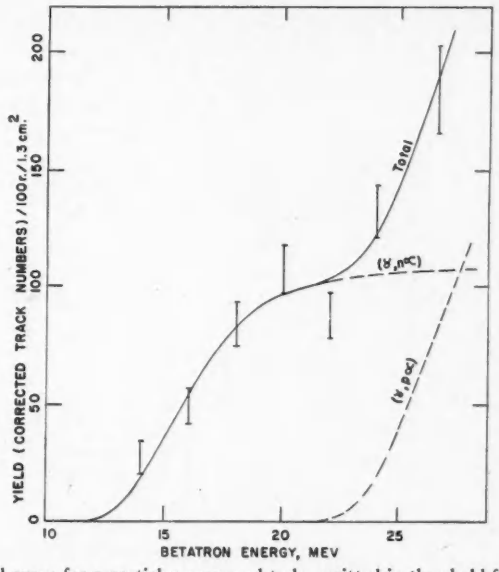


FIG. 3. Yield curve for $\alpha$-particles presumed to be emitted in threshold-favored reactions in silver and bromine. The curve is thought to consist mainly of a composite yield curve for $(\gamma, n\,\alpha)$ and $(\gamma, p\,\alpha)$ reactions.

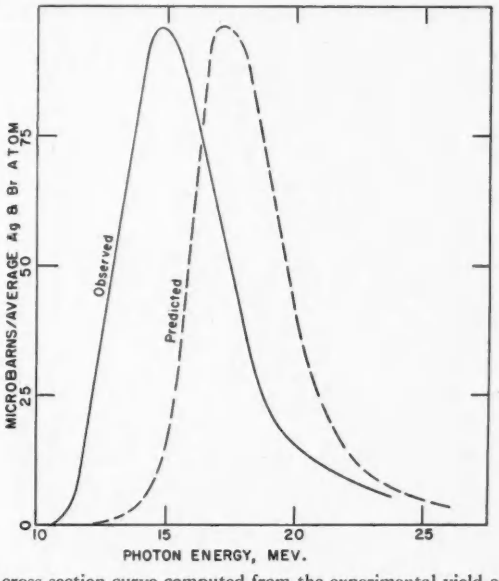


FIG. 4. The cross-section curve computed from the experimental yield curve for $(\gamma, n\,\alpha)$ and $(\gamma, \gamma'\alpha)$ reactions is shown as the solid line. The dotted line is the shape of the cross-section curve predicted by theory for $(\gamma, n\,\alpha)$ reactions mainly in silver.

The cross-section curve resulting from an analysis of the first of these yield curves is plotted as the solid line in Fig. 4. The dotted line in the figure is the cross-section shape predicted in Section II (*c*) (i) for $(\gamma, n\,\alpha)$ reactions mainly in silver. The cross section has been averaged over the silver and bromine atoms, but as pointed out above it is expected that silver gives the principal contribution to this curve. The peak energy of the observed cross-section curve is subject to an error of the order of 1 Mev., but the width of the curve is subject to a much larger error.

It may be seen from Table II that threshold-favored $(\gamma, n\,\alpha)$ and $(\gamma, \gamma'\,\alpha)$ reactions have cross-section peaks predicted in this region of the bombarding photon energy. If the threshold differences favoring $\alpha$-particle emission were equal for each type of reaction, one would expect that the yield of $(\gamma, \gamma'\,\alpha)$ and $(\gamma, n\,\alpha)$ reactions would be approximately in the ratio of the yield of $(\gamma, \gamma')$ and $(\gamma, n)$ reactions. By analogue with the $(\gamma, \gamma')$ reaction in gold (6), this ratio can be estimated as of the order of magnitude 0.1. This estimate is extremely crude. The actual ratio is quite sensitive to the threshold energy differences, and the possibility cannot be excluded that $(\gamma, \gamma'\,\alpha)$ reactions give the major contribution to the observed cross-section curve of Fig. 4.

It is assumed, however, that the greater part of this cross-section curve may be attributed to $(\gamma, n\,\alpha)$ reactions. It will be noted that the peak of this curve is about 2 Mev. lower than predicted. The expected peak position was equal to the sum of the neutron and $\alpha$-particle binding energies in silver plus the most probable kinetic energies of the particles. The authors doubt that the kinetic energies were appreciably overestimated. The binding energies were computed from semiempirical masses (19); an error of 2 Mev. in their sum is not inconsistent with the uncertainties inherent in the use of such mass values.

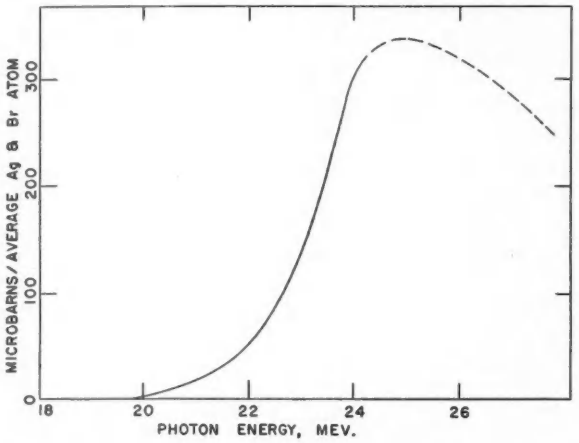


FIG. 5. The cross-section curve computed for $(\gamma, p\,\alpha)$ threshold-favored reactions.

The peak $(\gamma, n\,\alpha)$ cross section is about 100 microbarns. In silver the peak $(\gamma, n)$ cross section is about 300 millibarns (9). Hence threshold-favored $\alpha$-particle emission from the $(\gamma, n)$ residual nucleus is at best about three orders of magnitude less probable than photon emission.

The cross-section curve resulting from an analysis of the second yield curve of Fig. 3 is plotted in Fig. 5. From Table II it may be seen that $(\gamma, p\,\alpha)$ reactions are expected to become most probable in this region of the bombarding photon energy. The proton tracks would not have been observed in this experiment. The shape of the cross-section curve is not established by the experimental data; it is merely consistent with the sudden increase in yield of the low energy $\alpha$-particles at the highest betatron energies. The maximum cross section is most probably at an energy higher than 23 Mev., and the curve should give the correct order of magnitude for the cross section in the neighborhood of 26 Mev.

It may be expected from the trend of Halpern and Mann's proton yields (11) that silver and bromine have $(\gamma, p)$ cross sections of the order of 20 mbarns in the neighborhood of 25 Mev. The $(\gamma, p\,\alpha)$ peak cross section is about 300 $\mu$barns. Hence threshold-favored $\alpha$-particle emission from the $(\gamma, p)$ residual nucleus is about two orders of magnitude less probable than photon emission. This emission probability is much greater than in the case of $(\gamma, n\,\alpha)$ reactions; the implication is that for $(\gamma, p\,\alpha)$ reactions $\alpha$-particle emission is favored by larger threshold difference energies.

In further work at this laboratory with an Ilford C2 emulsion irradiated at 24 Mev., a few of the low energy $\alpha$-particles were seen to be associated with a long proton track. It may be seen from the yield curves of Fig. 3 that such two-pronged events can be expected for only a small percentage of the low energy $\alpha$-particles emitted at that bremsstrahlung energy. This lends qualitative support to the above identification of the $(\gamma, p\,\alpha)$ cross-section curve.

During the course of this experiment a few examples were observed of double $\alpha$-particle emission of the type reported by Millar and Cameron (22). Such events may in part be attributed to threshold-favored $(\gamma, \alpha\,\alpha)$ reactions whose peak cross-section energies are predicted in Table II. No cross-section shapes can be inferred from the few examples seen, but it appears that $(\gamma, \alpha\,\alpha)$ reactions are between two and three orders of magnitude less probable than $(\gamma, \alpha)$ reactions. This is consistent with the yields of $(\gamma, n\,\alpha)$ and $(\gamma, p\,\alpha)$ reactions as discussed above.

From the theory of alpha-radioactivity (1) it may be calculated that medium-heavy nuclei will have lifetimes comparable to geologic epochs for the emission of $\alpha$-particles with energies of about 2 Mev. Yet in this experiment the emission of $\alpha$-particles with even smaller energies has been consistently observed. Moreover, these $\alpha$-particles were emitted in competition with $\gamma$-rays, so that their lifetimes should not be longer than about $10^{-8}$ sec. It therefore seems necessary to conclude that when nuclei have small excitations, low energy $\alpha$-particles may penetrate the potential barrier much more easily than predicted by theory. Similar phenomena have been observed in cosmic-ray stars (17).

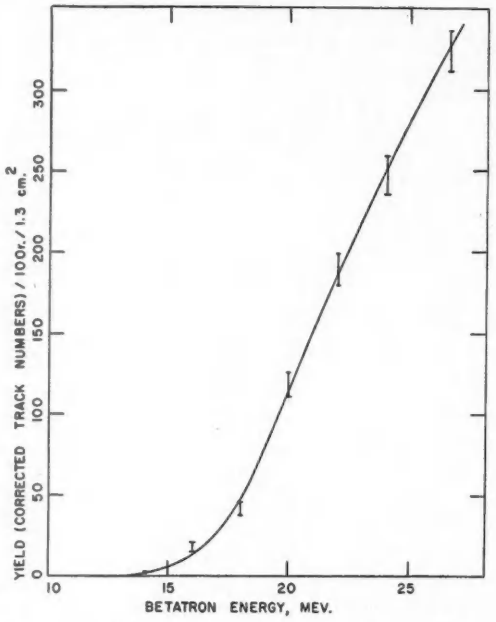


FIG. 6. Yield curve for the higher-energy α-particles resulting from the photodisintegration of silver and bromine.

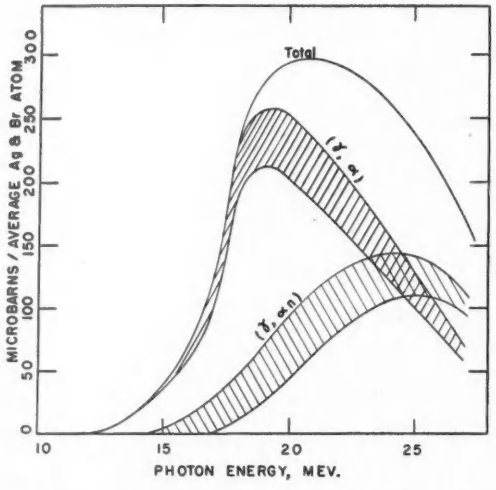


FIG. 7. The upper curve is the cross-section curve computed for higher energy α-particles resulting from the photodisintegration of silver and bromine. This has been broken up into contributions from $(\gamma, \alpha)$ and $(\gamma, \alpha\ n)$ reactions. The higher $(\gamma, \alpha)$ and lower $(\gamma, \alpha\ n)$ curves are computed with semiempirical masses; the other curves are based on revised $(\gamma, \alpha\ n)$ thresholds in silver as discussed in the text.

(*b*) *High Energy Alpha Particles*

The yield curve for the α-particles in the higher energy peak is plotted in Fig. 6. A curve having smooth first and second derivatives has been drawn through the points. The corresponding cross-section curve is shown as the upper curve in Fig. 7. The manner in which this has been broken up into ($\gamma$, $\alpha$) and ($\gamma$, $\alpha$ $n$) contributions will be discussed later.

Similar yield curves were drawn for α-particles of given energies from 7 to 15 Mev. Curves having smooth first and second derivatives were drawn through the points, thus effecting a cross-plot of the α-particle spectral shapes. These curves were solved for the partial cross sections for the emission of α-particles of the given energies. The partial cross sections were then cross-plotted to obtain the α-particle energy distributions corresponding to photonuclear excitation by monochromatic photons of various energies.

Such distributions corresponding to excitation by 15, 20, and 25 Mev. photons are plotted as the solid lines in Figs. 8, 9, and 10. These have been compared in

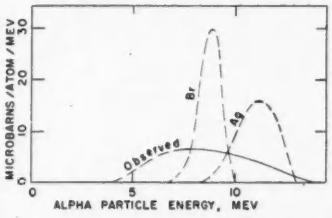


FIG. 8. The solid line is the observed α-particle energy distribution resulting from the photodisintegration of silver and bromine by 15 Mev. photons. The dotted lines are theoretical distributions computed from Equations (1) and (3).

each case with the expected energy distributions for the photodisintegration of silver and bromine, which were computed from Equations (1) and (3) using values for "$a$" and $\sigma_\alpha(E_\alpha)$ interpolated in tables given by Blatt and Weisskopf (3). The theoretical distributions are plotted as dotted lines in the figures; each is normalized to contain the same area as the observed distribution.

In each case the observed energy distribution peaks at a lower energy than both of the calculated ones. The disagreement is largest at the lowest photon energies. Although the effects of ($\gamma$, $\gamma'$ $\alpha$) reactions have been neglected, it is not expected that their inclusion would materially reduce the disagreement.

Blatt (2) has suggested to us that, owing to the effects of nuclear shell structure, nuclear level densities may be approximately constant for a few Mev. above the ground state, and they may then start rising rapidly. We have therefore assumed a constant level density of 0.5 Mev.$^{-1}$ for the first 4 Mev. above ground level; above that energy we have assumed a level density formula

$$\omega_R(\epsilon) = 0.5 \exp 2[b(\epsilon - 4)]^{\frac{1}{2}} \tag{8}$$

in which the constant "$b$" was evaluated by letting the right-hand sides of Equations (3) and (8) be equal at 8 Mev.* Theoretical energy distributions

**Evidence that this type of level density formula may be preferred is contained in the final report of the fast neutron data project, by Feld et al. NYO—636. Government Printing Office, Washington, D.C. 1951.*

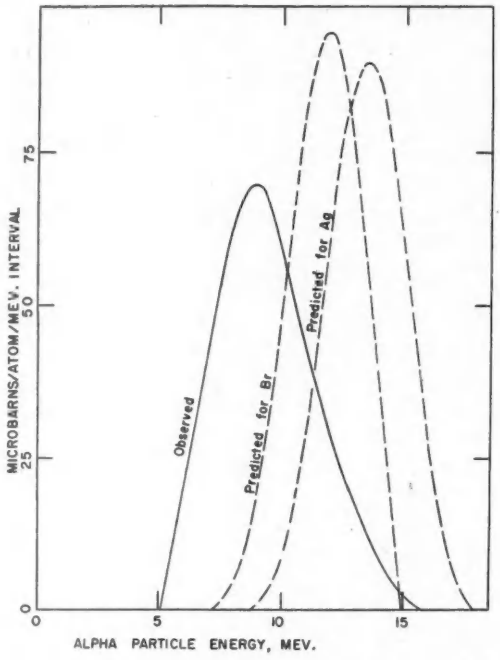


FIG. 9. The solid line is the observed α-particle energy distribution resulting from the photodisintegration of silver and bromine by 20 Mev. photons. The dotted lines are theoretical distributions computed from Equations (1) and (3).

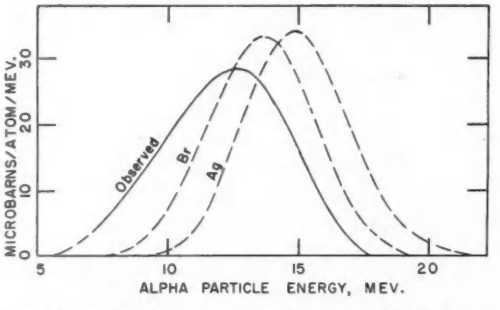


FIG. 10. The solid line is the observed α-particle energy distribution resulting from the photodisintegration of silver and bromine by 25 Mev. photons. The dotted lines are theoretical distributions computed from Equations (1) and (3).

have been computed with these alternative level densities. The results are plotted in Figs. 11, 12, and 13, which correspond respectively to Figs. 8, 9, and

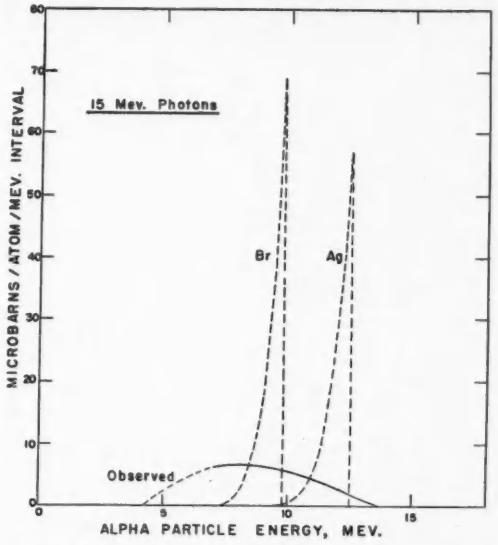


FIG. 11. The solid line is the observed α-particle energy distribution resulting from the photodisintegration of silver and bromine by 15 Mev. photons. The dotted lines are theoretical distributions computed from Equations (1) and (8).

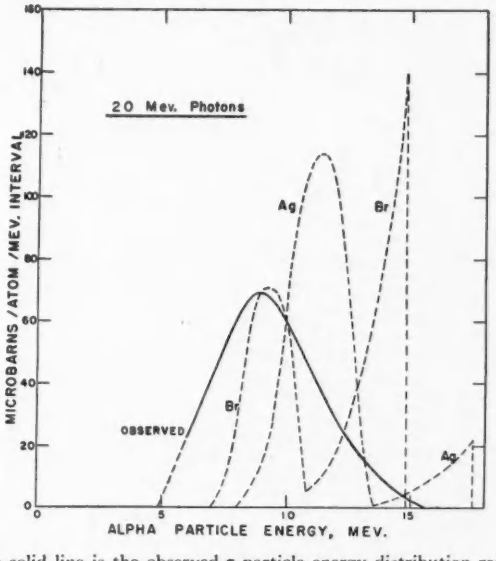


FIG. 12. The solid line is the observed α-particle energy distribution resulting from the photodisintegration of silver and bromine by 20 Mev. photons. The dotted lines are theoretical distributions computed from Equations (1) and (8).

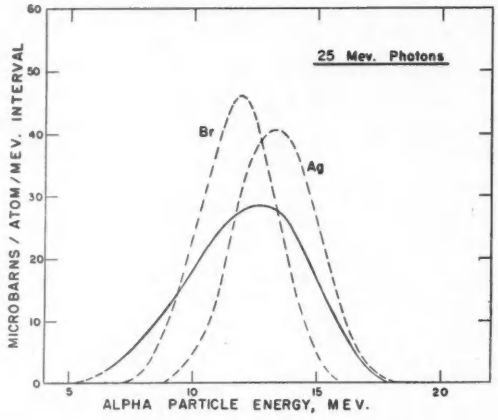


FIG. 13. The solid line is the observed $\alpha$-particle energy distribution resulting from the photodisintegration of silver and bromine by 25 Mev. photons. The dotted lines are theoretical distributions computed from Equations (1) and (8).

10. The sharp high energy peaks in Figs. 11 and 12 arise from the effects of the region of constant level density; they appear to be without counterparts in the experimental distributions. These tails are negligible in Fig. 13, where the experimental and theoretical distributions are in good agreement.

The distributions corresponding to excitation by lower energy photons are strong functions of $\sigma_\alpha(E_\alpha)$, while the distribution for 25 Mev. photons is more dependent on $\omega_R(\epsilon)$. When the faster-rising level densities of Equation (8) were assumed, it was possible to obtain agreement with experiment for the latter (25 Mev.) distribution. In order to obtain agreement with the lower energy distributions, it appears necessary to assume, in addition, that, for low $\alpha$-particle energies, $\sigma_\alpha(E_\alpha)$ (and hence the barrier penetrability for $\alpha$-particles) is larger than predicted from theory. This is consistent with the conclusion of the previous subsection.

With the experimental energy distributions thus obtained it was possible to make a rough estimate of the $(\gamma, \alpha\, n)$ cross-section curve by the method outlined in Section II (*b*). The effects of primary photon emission were neglected, and it was assumed that, when the emission of a primary $\alpha$-particle leaves a residual nucleus sufficiently excited to emit a neutron, such neutron emission usually takes place. The contributions of ordinary cascade reactions of the types $(\gamma, \alpha\, p)$ and $(\gamma, \alpha\, \alpha)$ were neglected.

The value of the neutron binding energy exerts a strong influence on this type of calculation. $(\gamma, \alpha\, n)$ reactions have the same thresholds as $(\gamma, n\, \alpha)$ reactions, and it was shown previously that the calculated values for the latter thresholds in silver may be 2 Mev. in error.

The percentage of the observed $\alpha$-particle energy distribution which will leave a residual nucleus sufficiently excited to emit a neutron is plotted in Fig. 14

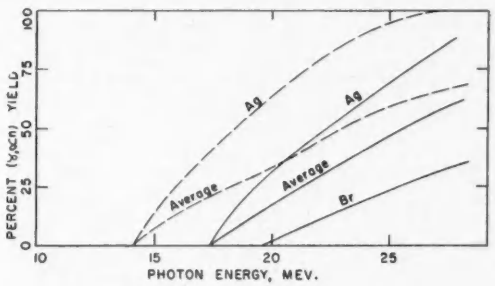


FIG. 14. The percentage of $\alpha$-particle emissions which can be followed by neutron emission in $(\gamma, \alpha\ n)$ reactions. This has been computed separately for silver and bromine and has been averaged. The lower percentages in the average and silver curves result from computations with semiempirical thresholds; the larger percentages are based on revised $(\gamma, \alpha\ n)$ thresholds in silver as discussed in the text.

as a function of the original energy of excitation. In these computations it was assumed that an observed energy distribution might be attributed half to silver and half to bromine. The percentage of the distribution which could be followed by neutron emission was computed separately for each element; in the case of silver two computations were carried out, one with the semiempirical $(\gamma, \alpha\ n)$ threshold and one with a threshold 2 Mev. lower in energy. The individual percentages for silver and bromine were then averaged, two curves being obtained corresponding to the alternative computations made for silver. This averaging procedure partially eliminated errors introduced in the arbitrary splitting of the observed $\alpha$-particle distributions between silver and bromine.

The primary $\alpha$-particle cross-section curve in Fig. 7 was multiplied by these average percentages to obtain rough $(\gamma, \alpha\ n)$ cross-section curves. The remainder of the $\alpha$-particle cross-section curve was attributed principally to $(\gamma, \alpha)$ reactions. The corrected silver threshold leads to the larger $(\gamma, \alpha\ n)$ cross sections in Fig. 7, but the effect of primary or intermediate electric dipole radiation would be to reduce this cross section. The curve computed with semiempirical thresholds may therefore more nearly represent the truth. The shaded areas in Fig. 7 give an indication of the uncertainties involved in the computation.

The emission of $He^3$, $He^5$, or $He^6$ in photonuclear reactions would also leave "alpha"-particle tracks in the emulsion. However, these have binding energies in medium-heavy nuclei much larger than $\alpha$-particles. Consequently they cannot be emitted in threshold-favored reactions, and computations on the basis of Equation (7) indicate that they have statistically a much smaller probability of emission than $\alpha$-particles. The contributions of such particles have therefore been neglected in the above considerations. Similar considerations show that the emission of lithium and heavier ions may likewise be neglected.

Quantitative data concerning characteristic features of the cross-section curves presented in this paper are given in Table IV.

TABLE IV

CHARACTERISTIC FEATURES OF THE AVERAGE CROSS-SECTION CURVES FOR PHOTONUCLEAR REACTIONS IN SILVER AND BROMINE INVOLVING THE EMISSION OF $\alpha$-PARTICLES. THE CROSS-SECTION CURVES HAVE BEEN INTEGRATED TO AN ENERGY OF 27 MEV.

| Reaction | Energy of max. cross section (Mev.) | Half-width of cross section (Mev.) | Maximum cross section ($\mu$ barns) | Integrated cross section (mbarns Mev.) |
|---|---|---|---|---|
| $(\gamma, n\,\alpha) + (\gamma, \gamma'\,\alpha)$ | 15 | $\sim 5$ | 100 | 0.5 |
| $(\gamma, p\,\alpha)$ | $> 23$ | ? | $\sim 300$ | $\sim 1.4$ |
| $(\gamma, \alpha)$ | 19 | $\sim 8$ | $\sim 230$ | $\sim 2.1$ |
| $(\gamma, \alpha\, n)$ | $\sim 24$ | ? | $\sim 130$ | $\sim 0.7$ |

## V. CONCLUSIONS

The double-peaked $\alpha$-particle energy distribution resulting from the photodisintegration of silver and bromine has been studied as a function of bremsstrahlung energy. Rough cross-section curves were obtained for the peaks as a whole, and the upper peak was analyzed to yield partial cross sections corresponding to photons of definite energy. These have been interpreted in terms of the statistical theory of nuclear reactions.

The lower energy peak has been considered to arise from threshold-favored $\alpha$-particle emission in reactions of the types $(\gamma, n\,\alpha)$, $(\gamma, \gamma'\,\alpha)$, and $(\gamma, p\,\alpha)$. The higher energy peak has been considered to arise from parallel and cascade reactions principally of the types $(\gamma, \alpha)$ and $(\gamma, \alpha\, n)$.

The experimental cross-section curves were found to be in semiquantitative agreement with the above predictions. The characteristics of these curves are listed in Table IV.

Evidence was obtained from the analysis of each of the peaks that low energy $\alpha$-particles can penetrate nuclear potential barriers more easily than predicted from theory.

## VI. ACKNOWLEDGMENTS

We should like to thank Dr. L. Katz for valuable discussions. The research has received financial assistance from the National Research Council of Canada.

## REFERENCES

1. BETHE, H. A. Revs. Modern Phys. 9: 161. 1937.
2. BLATT, J. M. Private communication.
3. BLATT, J. M. and WEISSKOPF, V. F. The theory of nuclear reactions. Tech. Report No. 42, Laboratory for Nuclear Science and Engineering, M.I.T. 1950.
4. BLATT, J. M. and WEISSKOPF, V. F. Privately circulated notes to appear as Chapter XII in their book, Theoretical nuclear physics.
5. CAMERON, A. G. W. Phys. Rev. 82: 272. 1951.
6. CAMERON, A. G. W. and KATZ, L. Phys. Rev. 84: 608. 1951.
7. CAMERON, A. G. W., HARMS, W., and KATZ, L. Phys. Rev. 83: 1264. 1951.
8. COURANT, E. D. Phys. Rev. 82: 703. 1951.
9. DIVEN, B. C. and ALMY, G. M. Phys. Rev. 80: 407. 1950.
10. GOLDHABER, M. and TELLER, E. Phys. Rev. 74: 1046. 1948.
11. HALPERN, J. and MANN, A. K. Phys. Rev. 83: 370. 1951.
12. HASLAM, R. N. H. and SKARSGARD, H. M. Phys. Rev. 81: 479. 1951.
13. HASLAM, R. N. H., SMITH, L. A., and TAYLOR, J. G. V. Phys. Rev. 84: 840. 1951.
14. HIRZEL, O. and WÄFFLER, H. Helv. Phys. Acta, 20: 373. 1947.

15. KATZ, L. and CAMERON, A. G. W. Can. J. Phys. 29: 518. 1951.
16. KATZ, L. and CAMERON, A. G. W. Phys. Rev. 84: 1115. 1951.
17. LE COUTEUR, K. J. Proc. Phys. Soc. (London), A, 63: 259. 1950.
18. LEVINGER, J. S. and BETHE, H. A. Phys. Rev. 78: 115. 1950.
19. METROPOLIS, N. and REITWEISER, G. U.S.A. E.C. document NP—1950. 1950.
20. MILLAR, C. H. and CAMERON, A. G. W. Phys. Rev. 78: 78. 1950.
21. MILLAR, C. H. and CAMERON, A. G. W. Bull. Roy. Soc. Can. June, 1950.
22. MILLAR, C. H. and CAMERON, A. G. W. To be published.
23. MILLAR, C. H., CAMERON, A. G. W., and GLICKSMAN, M. Can. J. Research, A, 28: 475. 1950.
24. WEISSKOPF, V. F. *In* Lecture series in nuclear physics. MDDC 1175. U.S. Government Printing Office. 1948.
25. WEISSKOPF, V. F. Phys. Rev. 83: 1073. 1951.
26. WEISSKOPF, V. F. and EWING, D. H. Phys. Rev. 57: 472. 1940.
27. YAGODA, H. Radioactive measurements with nuclear emulsions. John Wiley and Sons, Inc., New York. 1949.

# ELECTRON MICROSCOPE STUDIES OF EVAPORATED CADMIUM AND ZINC[1]

By R. S. SENNETT,[2] T. A. MCLAUCHLAN,[3] and G. D. SCOTT

ABSTRACT

Employing a technique, previously described, whereby evaporations are carried out within the specimen chamber of an electron microscope, continuous observations have been made on the formation of evaporated deposits of cadmium and zinc. The particles first seen appear suddenly, have a regular crystalline shape, and are often relatively large (200 Å). At first they remain regular while increasing in size, but later develop irregular spurs, secondary crystallites, or link together with their neighbors. This behavior is quite different from that of silver and gold in which the aggregates appear irregular at all stages.

## INTRODUCTION

In a previous paper from this laboratory (6), a technique was described whereby continuous observations can be made with the electron microscope on the formation of evaporated metal films. Results were given for silver, gold, and tin, which showed the manner in which the aggregates initially formed increase in size and link together to form the final continuous film. These three metals fall into a group for which no "critical density" has been observed. The basic result in regard to the phenomenon of critical density is that in the evaporation of some metals the intensity of the incident beam must reach a definite minimum value, which is dependent on substrate temperature, before a permanent deposit is obtained. The theory of this effect was given by Frenkel (5) in 1924. For beam intensities below the minimum it is assumed that all the atoms are reflected or re-evaporated from the substrate (4). Cadmium and zinc exhibit the effect of a critical density on substrates at room temperature (1, 3), and hence it would be expected that evaporated deposits of these metals would show considerable differences in structure as compared to deposits of metals such as silver, gold, and tin.

## EXPERIMENTAL RESULTS

A series of electron micrographs of successive stages in the formation of a deposit of cadmium is reproduced in Fig. 1. The substrate is a formvar film which in this case happened to contain several small holes; the holes serve as reference points in the field. It can be noted that the initial particles have a regular shape which is often maintained during growth unless two or more particles coalesce. A second series of cadmium is given in Fig. 2. Several polystyrene latex spheres can be seen on the mount. In this series the growth has been carried further and the particles are beginning to develop irregular spurs and secondary crystallites.

A typical series for zinc is illustrated in Fig. 3; the particles are likewise of regular shape in the initial stages and then as they grow become irregular. A

[1] *Manuscript received January 28, 1952.*
*Contribution from the Department of Physics, University of Toronto, Toronto, Ont.*
*Part of the work described in this paper was presented at the annual meeting of the Electron Microscope Society of America, Washington, October, 1949.*

[2] *Now with Canadian Radio Mfg. Corp. Ltd., Toronto, Ont.*
[3] *Now with U.S. Steel Co., Pittsburgh, Pa.*

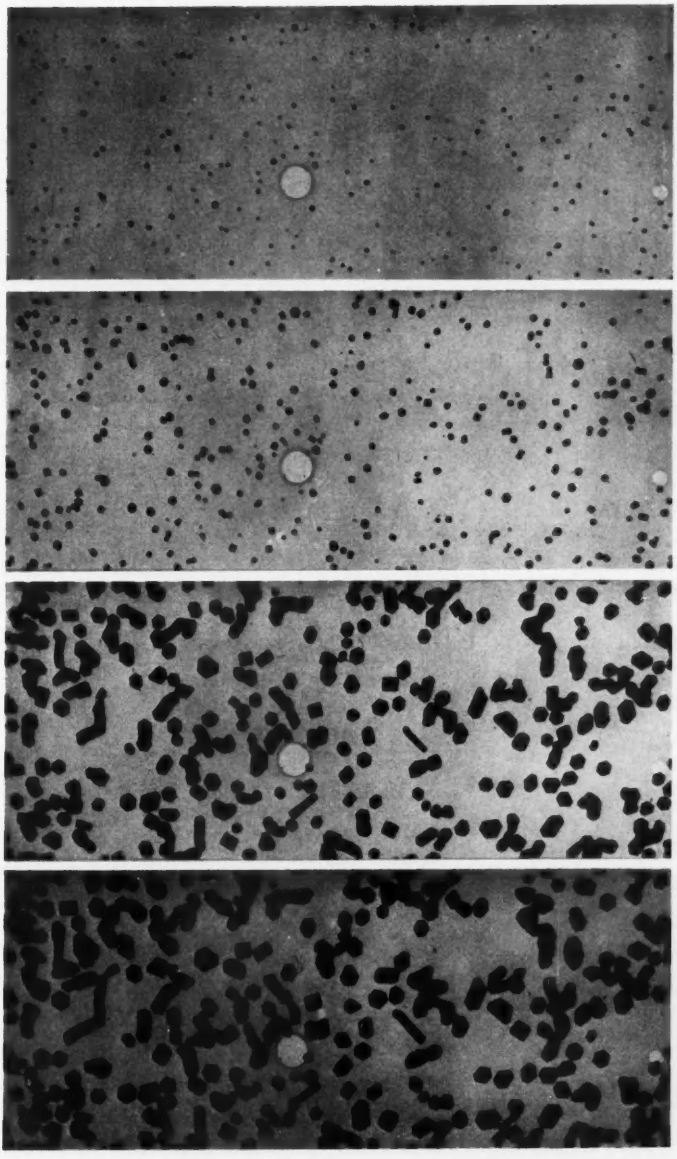

FIG. 1. Electron micrographs of successive stages in the formation of a vacuum evaporated deposit of cadmium on a formvar substrate. (× 30,000).

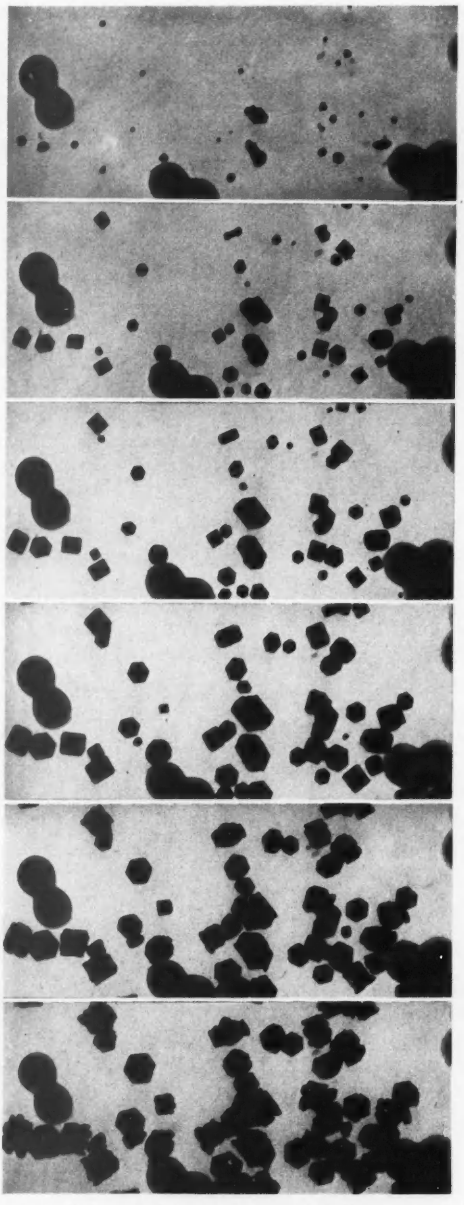

FIG. 2. Cadmium series illustrating the manner in which the larger particles develop. The polystyrene latex spheres serve as reference points in the field. (× 22,500).

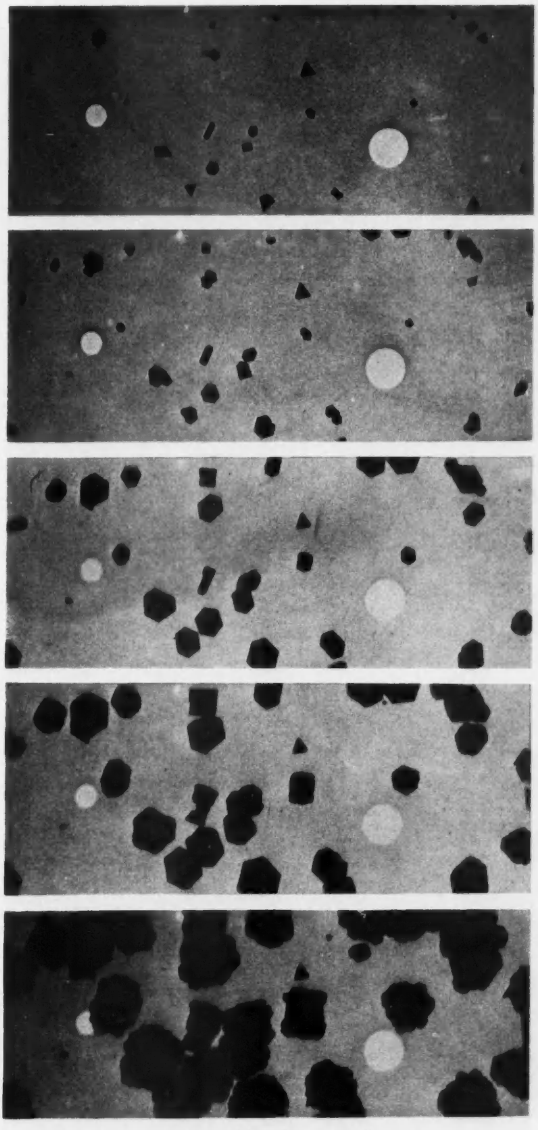

FIG. 3. The growth of evaporated particles of zinc on formvar. (×30,000).

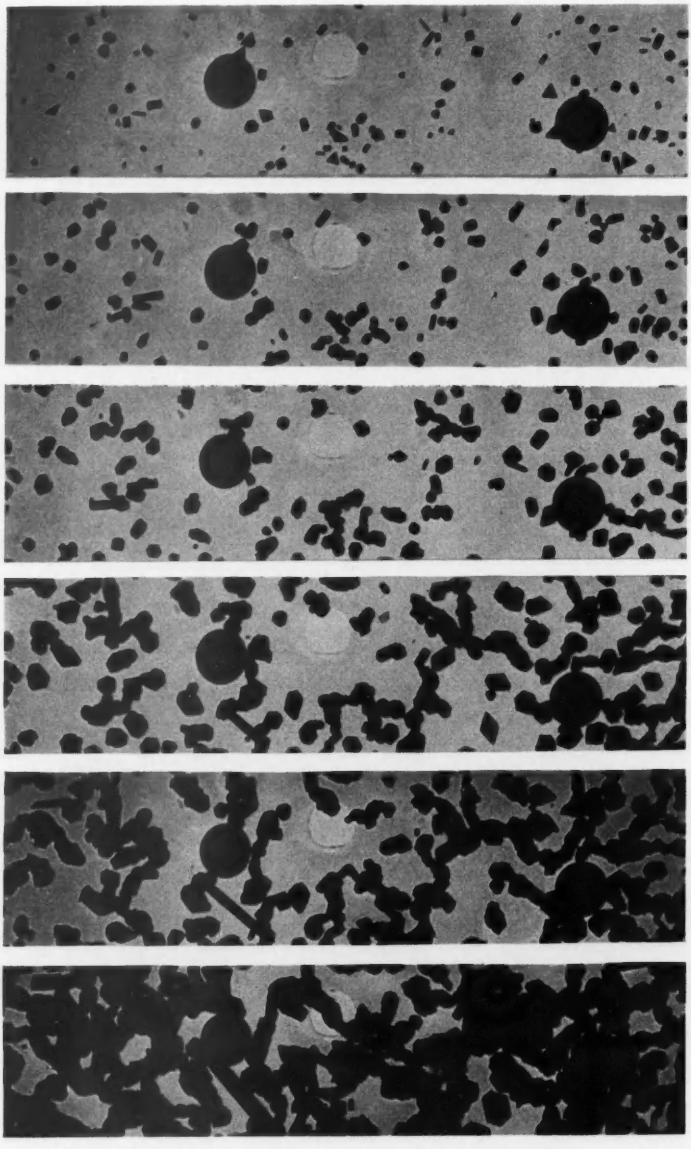

FIG. 4. Zinc series indicating the way in which particles link together. (× 30,000).

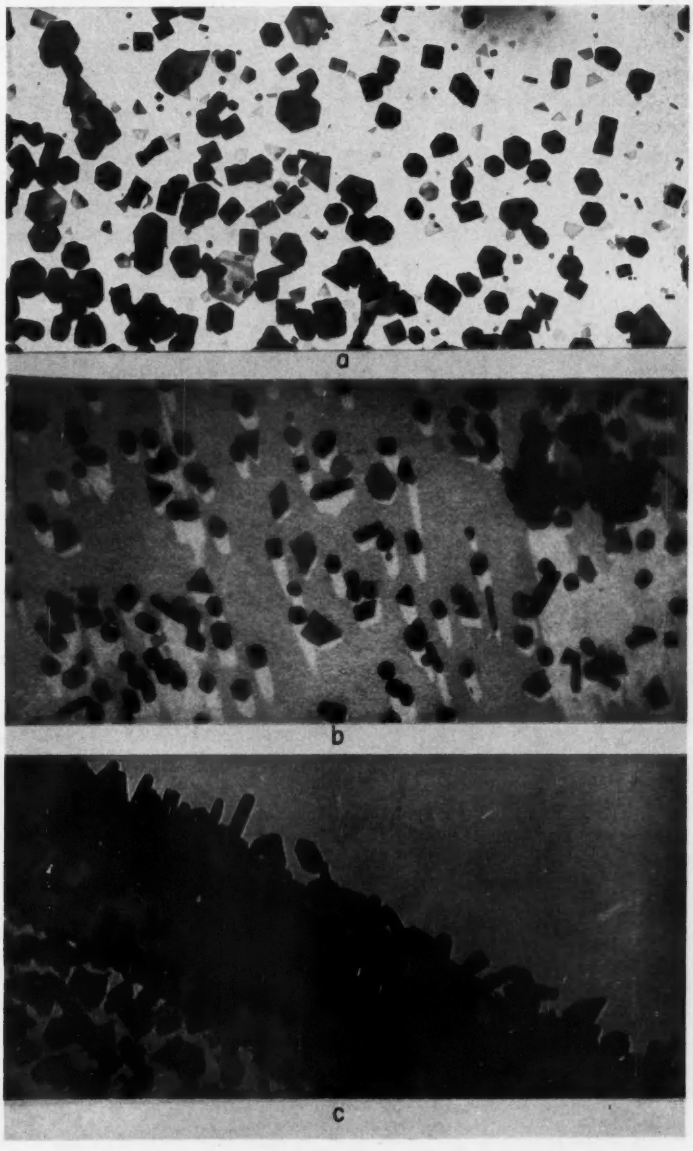


FIG. 5. Zinc particles.

(*a*) Semitransparent platelets with secondary crystallites. (× 45,000).
(*b*) Chromium shadow-cast particles indicating heights and shapes. (× 22,500).
(*c*) Profile of particles along the edge of a curl in the formvar film. (× 60,000).

triangular particle in the center of the field did not change in size during the evaporation for some unknown reason. A second series for zinc is given in Fig. 4. Two polystyrene latex spheres are present in the field to serve as reference points. In the final stages shown in this series the particles are linking together to form irregular chains. In general very few new particles appeared during the development of the deposit but one example can be noted in the clear area on the right-hand side of the field. It was found that if at any stage the deposit was exposed to the air new nuclei were formed quite readily. This may be on account of the formation of an oxide on the original particles which inhibited further growth.

It can be observed particularly in the pictures of the zinc deposits that some of the particles are transparent to the electron beam. This effect is strikingly illustrated in Fig. 5(*a*) which shows zinc particles of a considerable range of thicknesses as judged by their opacity to the beam. There are numerous instances where nucleation of secondary crystallites has occurred on the original platelets. At the top center of the field is a hexagon with three squares attached. This is suggestive of the development of the larger particles which no longer maintain their original shape.

To determine the shape of the particles in a direction perpendicular to the substrate a number of mounts of zinc were shadow-cast with chromium. A typical field is illustrated in Fig. 5(*b*). Since it was necessary to remove the mounts from the microscope to the evaporating unit for shadow-casting, the mounts were in contact with the air for a few minutes. The layer to be noted around each particle was found on all mounts. It may be an oxide film formed by the exposure to air or perhaps a contamination layer produced by the electron bombardment. An examination of the shadows which are cast by the individual particles reveals that the transparent crystals must indeed be in the form of flat platelets. The transparent particles have short shadows, the denser ones longer shadows. The small 45° triangular particles of which there are a number in Fig. 5(*a*) can be interpreted as an equilateral triangle standing on one edge making an angle of about 60° with the substrate. Such a particle and the shadow it gives is found in Fig. 5(*b*) in the upper part of the field just to the right of the center.

Further evidence of the manner in which the particles grow into the space above the substrate is given in Fig. 5(*c*). This micrograph shows a curl which occurred at a chance break in the film so that the profile of the particles can be seen. It is clear how some of them project clear above the substrate.

## DISCUSSION

One of the most interesting features of all the evaporations of cadmium and zinc as contrasted to those of silver, gold, and tin was the way in which the initial particles often as large as 200 Å appear on the substrate instantaneously. The sudden formation of these regular crystals was somewhat like the rapid crystallization which may occur from a supersaturated solution. This observation is in keeping with the known critical density phenomenon for these metals.

A certain minimum intensity of the atoms incident on the substrate is necessary before nuclei can be formed and then rapid condensation on these nuclei gives rise to the sudden appearance of the particles.

The fact that the particles grow in a regular fashion during the initial stages and very few new nuclei are formed would indicate that the atoms which strike the substrate are generally re-evaporated or migrate over the substrate and that those which strike the particles directly or by migration are captured. There is little evidence from the micrographs of the precise mechanism by which the atoms are added to the particles. It is to be expected that the development of screw dislocations as observed for example by Dawson and Vand (2) in a *n*-paraffin crystal would in the case of these metals be beyond the resolution of the electron microscope.

## REFERENCES

1. COCKCROFT, J. Proc. Roy. Soc. (London), A, 119: 293. 1924.
2. DAWSON, I. M. and VAND, V. Nature, 167: 476. 1951.
3. DITCHBURN, R. W. Proc. Roy. Soc. (London), A, 141: 169. 1933.
4. ESTERMANN, I. Revs. Modern Phys. 18: 300. 1946.
5. FRENKEL, J. Z. Physik, 26: 117. 1924.
6. MCLAUCHLAN, T. A., SENNETT, R. S., and SCOTT, G. D. Can. J. Research, A, 28: 530. 1950.

# THE LOW ENERGY SPECTRUM OF COSMIC-RAY MESONS AT SEA LEVEL AT HIGH GEOMAGNETIC LATITUDES[1]

By D. C. Rose and A. G. Voisin

ABSTRACT

The differential range spectrum of cosmic-ray mesons has been measured by three different methods the first of which was used at two northern geomagnetic latitudes 56.8 (Ottawa) and 83.0 (Resolute in the Canadian Arctic). In the first method the integral spectrum was measured by absorption, and after various corrections the differential spectrum was derived. In the second method the number of particles stopped in a block of lead was measured by a coincidence–anticoincidence arrangement of counters. In the third method the delayed coincidence method was used, the meson being identified by its decay electron. Over the range studied (ranges in lead up to 700 gm. per cm.$^2$) the results of the three methods are in general agreement and agree with others in that the smoothed data show only a small variation in intensity over the range studied. Some of the results suggest that a more detailed study of the spectrum might show some irregularities in the intensity variation with range. As would be expected no significant difference was found in the shape of the curves at the two stations.

## I. INTRODUCTION

During the summer of 1950 an accurate comparison (11) was made between the intensities of the vertical hard component of cosmic rays at Resolute (geomagnetic latitude 83.0°N.) in the Canadian Arctic and Ottawa (geomagnetic latitude 56.8°N.). The results showed the intensity to be higher at Resolute than at Ottawa even when corrected for atmospheric differences, but the residual difference was consistent with geomagnetic effects. During the following winter further experiments (to be described herewith) were carried out at the two stations to compare the energy distributions of the $\mu$-mesons with ranges in lead below 700 gm. per cm.$^2$ (energies below about 820 Mev.) in vertical cosmic rays at sea level. Since the primary objective was a comparison at the two stations a simple absorption method was used.

Besides these measurements two additional direct measurements were made at Ottawa on the differential range spectrum of mesons. A detailed knowledge of the sea level spectrum of mesons is important, if such calculations as those made by Sands (14) and Rose (10) on the production spectrum of mesons in the upper atmosphere are to be of value. Rossi (12) in 1948 reviewed the measurements then available on the meson spectrum at sea level and presented what was considered to be the most probable spectrum. Direct measurements such as those of Wilson (17) using magnetic methods probably give the best values at high energy, say above 1 Bev., but at lower energies difficulties due to geometry and scattering become prominent. At such energies Rossi places considerable reliance on measurements taken by the delayed coincidence technique, particularly those of Sands (14) wherein uncertainties due to geometry and scattering are a minimum. Such measurements show relatively a much greater intensity at low energies than those of Wilson.

[1] *Manuscript received April 3, 1952.*
*Contribution from the Division of Physics, National Research Laboratories, Ottawa, Canada. Issued as N.R.C. No. 2787.*

Earlier experiments at Ottawa and Resolute on the barometer effect (10), interpreted in relation to calculations of the barometer coefficients for particles of different momenta, suggested (without high statistical significance) that a spectrum in accordance with Wilson's measurements was more likely to be right. Other measurements by Kraushaar (5) on the absolute intensity, and an analysis using magnetic methods by Caro, Parry, and Rathgeber (2) add greatly to the weight of evidence in favor of the spectrum selected by Rossi. One of the experiments to be described here (Experiment III) is also in general agreement with Rossi's spectrum. The other two (Experiments I and II) suggest a lower intensity at the lowest energies studied but the difference is hardly enough greater than the errors involved to be significant.

## II. APPARATUS AND MEASUREMENTS

Three different sets of apparatus were used which will be described separately. The first, that designed for comparison at the two stations, was similar to that used by Sarabhai (15) and by Hall (3). It measures the integral spectrum by absorption, and after corrections the differential spectrum can be derived. In the second method the number of mesons stopped in a block of lead is measured by a coincidence and anticoincidence arrangement of counters. The differential spectrum therefore is measured directly. In the third case the mesons are identified by their decay electrons using the well-known delayed coincidence technique.

### Experiment I—The Sarabhai and Hall Method

Fig. 1 is a sketch, drawn to scale, showing the arrangement of counters and absorbers. It applies to the experiment at Resolute and the first experiment at Ottawa. Counter trays 1, 2, and 3 each contained two counters in parallel. The counters were brass tubes having effective length of 16 in. and were 1 in. in diameter. The manufacturers specify a wall thickness of 0.020 in.

The block of lead $A$ (2.5 cm. thick and 3 in. wide) and the counter trays 4 and 5 were arranged so that they would separate electrons from mesons by taking advantage of the high probability that the former will produce showers in $A$. These showers were detected by double coincidences (4,5). Trays 4 and 5 were placed one above the other instead of following the more usual practice of using a row of counters side by side, alternative counters being connected in parallel. The reason for this arrangement was because the circuit used with this apparatus required that the cathode of the counter be insulated; therefore tubes in immediate contact could not be connected to separate preamplifiers. The trays were aligned very carefully so that the efficiency in indicating showers starting in the block of lead $A$ would be the same as if the counters had been in one row. Coincidences between trays (1,2,3) and (1,2,3,4,5) and anticoincidences (1,2,3) − (4,5) were recorded automatically and a constant check was maintained on each individual tray of counters.

To obtain the absorption spectrum of mesons various thicknesses of lead were placed over the bottom tray (No. 3). This tray was surrounded on the sides,

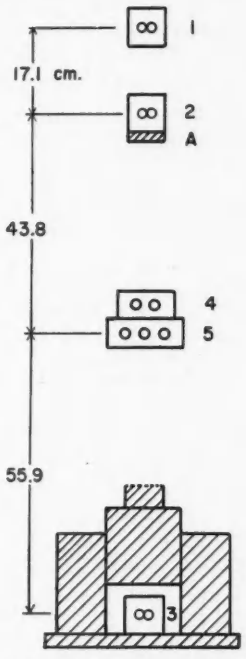


FIG. 1. Arrangement of counters and absorbers for Experiment I at north geomagnetic latitudes 56.8 (Ottawa) and 83.0 (Resolute).

bottom, and ends with 4 in. of lead. The lead on top was added in $\frac{1}{2}$-in. slabs 6 in. wide fitting into the side shielding except that for thicknesses over 6 in. 3-in. wide slabs were used as shown.

The roof over the apparatus in Ottawa was uniform in thickness consisting of 2 in. of wood, some glass wool insulation, and a galvanized sheet iron cover. At Resolute the roof was of plywood and rock wool insulation with an aluminum cover. The total amount of such material including the sheet aluminum of which the trays were made and the brass walls of the counters was effectively the same in both cases and is equivalent to approximately 19 gm. per cm.$^2$ of lead in stopping power of $\mu$-mesons.

The results are shown in Fig. 2. The abscissa represents the total thickness of absorber through which the particles have passed in gm. per cm.$^2$ of lead. The thickness was corrected for small angle scattering in the absorber by adding 10% to the actual thickness in accordance with calculations made by Koenig (4). The errors shown are standard deviations based on the number of particles counted. No barometer corrections were made because the procedure in taking the measurements was planned so that meteorological corrections would be averaged out. Each point represents five or six days of counting with one thick-

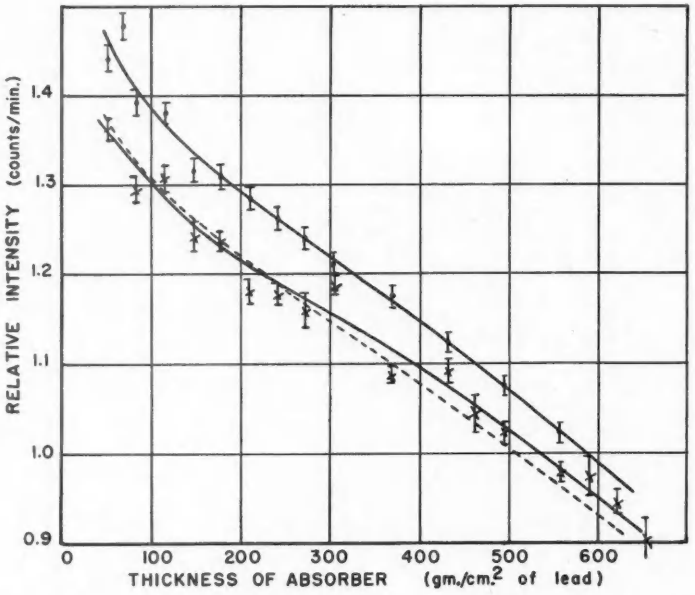


FIG. 2. Uncorrected results of Experiment I, upper curve Resolute, lower curve Ottawa.

ness of absorber, but these five or six days of observations were not taken consecutively. The thickness of lead over tray No. 3 was changed every day at Resolute and every two days at Ottawa, the changes being made in a random way spread over the four months of observations (September to December 1950 at Resolute and December 1950 to March 1951 at Ottawa). It seemed highly probable that in this way meteorological fluctuations would be averaged out. The points for Ottawa are noticeably more irregular than those for Resolute. This suggests irregularities in the Ottawa spectrum, but it may be partly due to the fact that during the winter months temperature and barometer changes at Ottawa are usually greater than those at Resolute, and the random distribution in changing absorber thickness was not as carefully carried out at Ottawa. Actually barometer corrections were worked out for the Ottawa results from coefficients previously measured (10) but the corrections made a negligible difference in the data; therefore they were not used in preparing the curves shown.

The two smooth curves in Fig. 2 were drawn to make a good fit with the data assuming that the actual integral spectrum has no irregularities. The broken curve represents the Resolute curve normalized at 200 gm. per cm.$^2$ to fit the Ottawa results. It is apparent that there are no significant differences in the shape of spectra at the two stations.

The absolute differences in the counting rate are consistent with previous measurements wherein the relative intensities at the two stations were compared accurately (11). The two sets of apparatus in this case were as nearly as possible identical but no comparison calibration was made.

To reduce the results to curves comparable with those obtained from Experiments II and III, and for comparisons with the results of other observers the following corrections are necessary.

(*a*) Mesons excluded because they are accompanied by a knock-on electron in such a way that both trays 4 and 5 are discharged

The number of such occasions can be obtained from the fivefold coincidence rate for thick layers of absorber. The fivefold coincidence rate is shown in the upper curves in Fig. 3 for Ottawa and Resolute. These curves include both knock-ons and true showers. The number of showers decreases rapidly as the absorber thickness over tray 3 is increased. Since a knock-on electron would have to be quite energetic to penetrate the trays and counter walls the knock-on occasions must all be produced by the higher energy part of the meson spectrum; therefore over the range of energies studied, the number of knock-on occasions would be expected to be constant. The flattening out of the curves in Fig. 3 show this to be the case; therefore a constant correction was added, 0.033 counts per minute for the Ottawa curve and 0.037 for the Resolute curve. These values are consistent with the numbers of knock-on electrons found by other observers under similar experimental conditions.

(*b*) Inefficiency of shower detection

With the arrangement of counters in trays 4 and 5 the detection of showers of two or more particles is not completely efficient. A two particle shower has the same chance of tripping only one tray of 4 and 5 as it has of tripping both. A three particle shower would have a 25% chance of being missed and larger showers would be detected correspondingly more efficiently. This is based on the assumption that the angular spread is large enough to produce a random distribution of particles but not large enough so that showers of only a few particles are likely to spread sufficiently to miss the trays entirely. Using the calculations of Arley (6) for the relative number of showers of various sizes the total efficiency of shower detection was calculated to be 84%. A correction for inefficiency of shower detection was made accordingly.

(*c*) The number of electrons that are counted as mesons

Some electrons will not create a shower in $A$, or if they do will result in only one particle leaving $A$. This correction is small and falls off rapidly with increasing absorber thickness. It can be estimated approximately as follows. The number of two or more particle showers can be obtained from the measurements mentioned above. From this and Arley's shower calculations the number of shower producing incident particles can be estimated. The number obtained is 0.3 per min. or 22% of the hard component, that is the intensity under 10 cm. of lead. This should represent a large portion of the soft component of the local

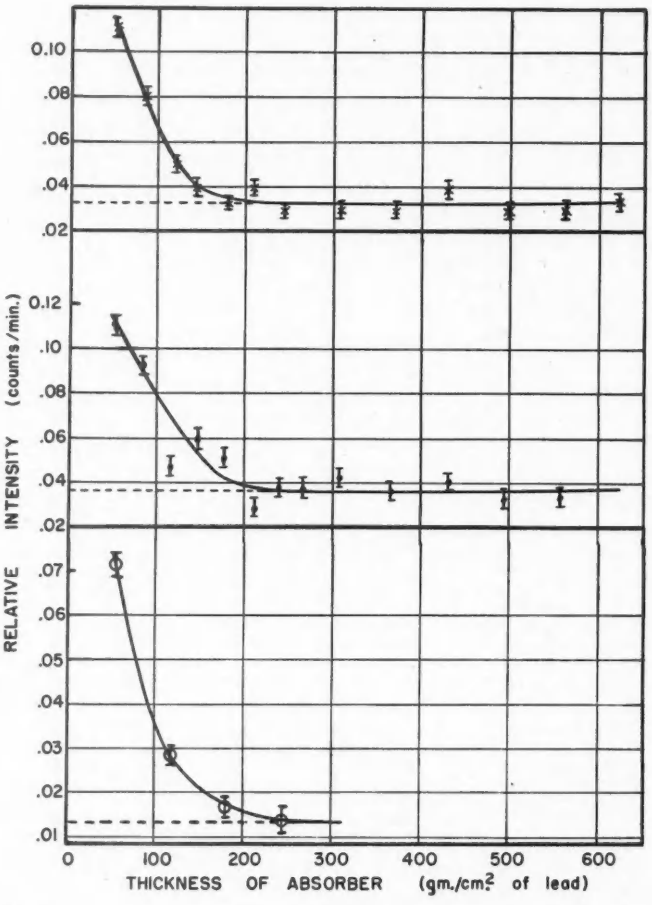


FIG. 3. Two upper curves—showers and knock-on occasions for Experiment I, upper curve Ottawa, center curve Resolute. Lower curve—side showers for both stations.

cosmic rays. In measurements of this type the soft component is usually found to be one-quarter to one-third of the hard component. In another experiment at Ottawa where a counter telescope was used with and without lead the soft component appeared to be more like 50% of that under 10 cm. of lead. The figure 0.3 is therefore probably low but since this correction is not very accurate and since increasing it would have little effect on the conclusion, this value was used. The number of single particle showers that would be detected as mesons can then be calculated from Arley's tables for the first two points observed. Beyond about 100 gm. per cm.$^2$ the correction is too small to be significant.

(*d*) Side showers

Side showers were observed by displacing counter tray No. 2 a distance of 3 in. to one side of its in-line position. Records were taken for different thicknesses of absorber over tray No. 3. The results from the two stations are averaged together and shown in Fig. 3. The horizontal broken line represents knock-on occasions as in the case of (*a*) above. The correction is represented by the difference between the solid and the broken line.

(*e*) Particles other than mesons

It is known (8) that about 1% of the ionizing particles at sea level are protons. The present apparatus would not separate these. However, it would be expected that they would be reasonably well spread over the range of absorber studied and this experimental method would not tend to exaggerate their effect in any part of the curves. They would therefore have a negligibly small effect on these results.

(*f*) Loss of particles due to scattering out of the beam

No way of making a quantitative estimate of the effect of particles being scattered out of the beam is available. At the lowest energies there would be considerable scattering by the block *A*. Further, the first few centimeters of lead over tray No. 3 will change the effective solid angle of the telescope by local scattering and the inclusion of knock-on electrons. After a few centimeters of lead have been placed over tray No. 3 the loss due to scattering will depend on the relative magnitudes of the half angle of the telescope formed by counter 1 and 2, and the root-mean-square angle of scattering at *A* for the lowest energy particle accepted. If the latter is much smaller than the former there will be compensation between particles scattered out of the beam and those scattered in, which otherwise would miss tray No. 3. The r.m.s. scattering angle can be calculated from formulae given by Rossi and Greisen (13). The half angle of the (1-2) telescope in a plane at right angles to the axis of the counters is 14°. Calculations indicate that at the lowest points on the curve the r.m.s. scattering angle at *A* for the lowest energy particles accepted is of about the same magnitude but it decreases rapidly with increasing minimum energy. When the total absorber thickness is 200 gm. per cm.$^2$ it is about 6°. The lowest points on the curves representing these results therefore are considerably in error owing to scattering at *A*.

With very thick layers of absorber there might also be some loss due to scattering in the upper layers of the absorber since the width of the lead sheet was only an inch wider than the beam. The energy here would be high so that this loss, though it would compensate at high energies for the low energy scattering at *A*, would be expected to be small.

Since quantitative corrections for scattering seemed impossible, the curves in Fig. 2 were corrected for all the other faults and are shown in Fig. 4 (lower curves). To compare these with Experiments II and III the differential range spectrum was required. The curves in Fig. 4 show that the change in slope of the

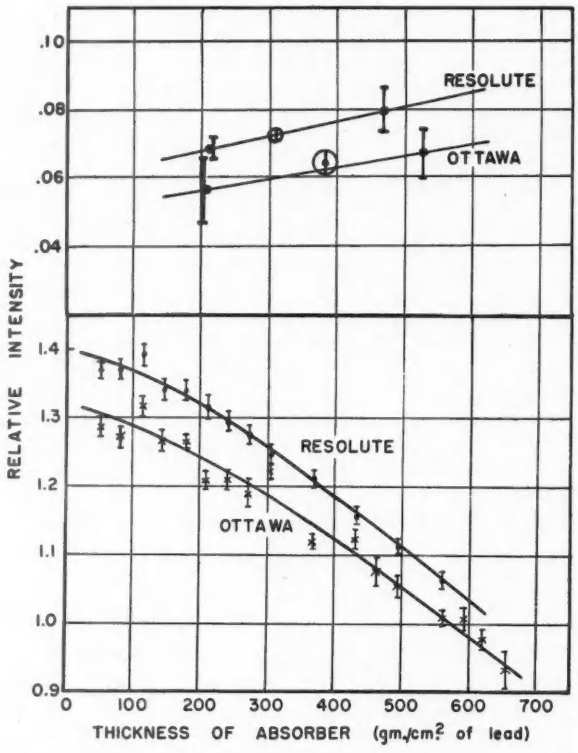


FIG. 4. Lower part of figure—the integral meson range spectra for Resolute and Ottawa. Upper part of figure—the differential meson spectra derived from the lower curves.

integral spectrum over the range studied is small so the differential spectrum is reasonably flat. Owing to the uncertainty due to scattering, the two points at lowest absorber thickness were discarded and linear regression coefficients were calculated for the remainder of the data in the following way. By dividing the data in two about the center of the range of the absorber thickness used, a best mean slope for the integral curves in Fig. 4 could be calculated for each half of each curve. This gives two points for the differential spectrum at each station. These two points are plotted in the upper part of Fig. 4 and a straight line joining them shows the best representation of the differential spectrum that can be obtained from these data. A linear regression coefficient was also calculated using all the data at each station (except the first two points as mentioned above). Such a calculation would assume that the differential spectrum was flat having the value represented by the circles on the upper curves of Fig. 4. The errors represent the standard deviations of the regression coefficients.

These straight lines can only be taken as the best representation of the differential spectra at the two stations if it is accepted that the differential spectrum over this range is a smooth curve without irregularities or inflections. There are two interesting features in the integral spectrum curves which probably have no significance but should not be overlooked. Firstly, the points between 75 and 200 gm. per cm.$^2$ deviate from the solid line in the same way at Ottawa and at Resolute. Secondly, a more complicated curve could be drawn through the points for the Ottawa station which would show a region of less slope in the integral spectrum (and hence a minimum in the differential spectrum) at an absorber thickness between 200 and 300 gm. per cm.$^2$ There is other evidence for such a minimum which will be discussed with the results of Experiment II. It does not appear, however, in the Resolute results, and in consideration of these irregularities the possibility of accidental meteorological variations cannot be eliminated.

## Experiment II

In this experiment the differential range spectrum was measured directly at four points by a coincidence–anticoincidence arrangement of counters. The apparatus is shown in Fig. 5. Counter trays $A$, $B$, and $C$ define a beam of cosmic-ray particles. Trays $D$ and $E$ include the solid angle of the $ABC$ telescope but

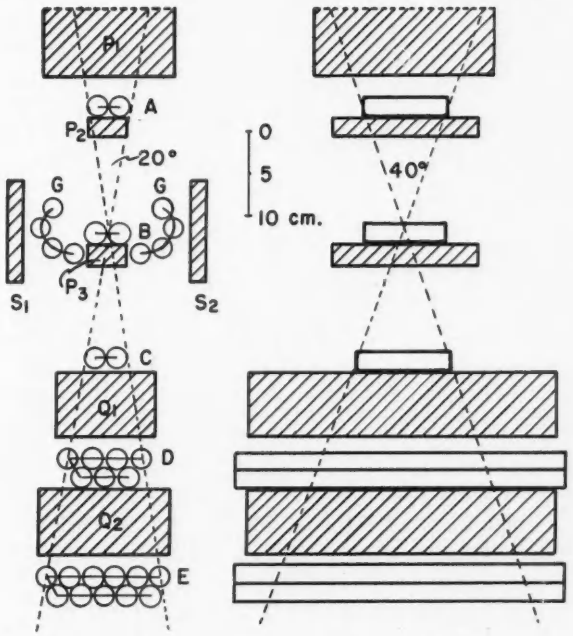


Fig. 5. The arrangement of counters and absorbers in Experiment II.

are connected so that particles which penetrate as far as $C$ but not to $D$ can be counted. Also particles that reach $D$ but not $E$ are recorded. This allows two bands in the differential spectrum to be measured simultaneously, the widths of the bands being defined by the thickness of the absorbers $Q_1$ and $Q_2$. The counters $G$ were included to eliminate side showers. This is the same apparatus that was used in another experiment on the zenithal distribution of cosmic-ray particles (16) and it is described in more detail in the published report on that experiment.

Actually the following coincidences were recorded $(A,B,C)$, $(A,B,C,D)$, $(A,B,C,D,E)$, and $(A,B,C,G)$ from which may be deduced $(a)$ the number of particles which reach $C$ but which are stopped between $C$ and $D$ and are not accompanied by showers, that is, $(A,B,C,) - \{(A,B,C,G) + (A,B,C,D)\}$; $(b)$ the numbers of particles which reach $D$ but not $E$ and are not accompanied by a shower, that is, $(A,B,C,D) - \{(A,B,C,G) + (A,B,C,D,E,)\}$. The background of the apparatus was observed by removing the absorbers $Q_1$ and $Q_2$. The rate with these removed was subtracted from that with the absorbers present. The effect of particles being scattered out of the bottom absorber could be shown by making two independent measures of the intensity in one band. By adding 7.5 cm. (an amount equal to $Q_2$) of lead at $P_1$ the group of particles previously stopped in $Q_2$ would be stopped in $Q_1$ and the number should be the same if there was no loss by scattering. It was found that only 5% of the particles were lost in $Q_2$ by scattering. The geometry was such that the loss in $Q_1$ would be expected to be much smaller so corrections for scattering were limited to 5% in $Q_2$.

The arrangement of the shower counters $G$ beneath the absorber $P_2$ was such that the protection against electrons which produce showers in $P_1$ and in $P_2$ was reasonably efficient. Very few electrons not so eliminated would penetrate to $C$ through $P_1 + P_2 + P_3$ for the minimum thickness of absorber used, namely 87 gm. per cm.$^2$ of lead including the lead equivalent of the roof. The loss of particles in the telescope by scattering in the roof and absorber $P_1$ need not be considered since there is about an equal probability of particles being scattered into the beam as well as out of it, and in the present case no attempt was made to estimate an absolute intensity. There should be no effect due to $P_3$ as a scatterer since the particles actually being observed would have the same momentum distribution at this point no matter what band of the spectrum was being measured.

On the other hand this method does not make any distinction between mesons and other particles which would stop between trays $C$ and $D$ or $D$ and $E$. The results at four thicknesses of lead absorber are shown in the lower curve of Fig. 6. As was done in Experiment I the absorber thickness indicated is the actual thickness of lead plus the lead equivalent of the roof tray walls and counter walls, the total being increased by 10% to give a rough correction for small angle multiple scattering. The abscissa value for each point is midway between the thickness which represents the top and bottom of the absorber $Q_1$ or $Q_2$. The ordinate represents actual counting rate in counts per hour.

The high value at the lowest absorber thickness is difficult to explain. Very few electrons would be expected to penetrate this thickness of absorber. The

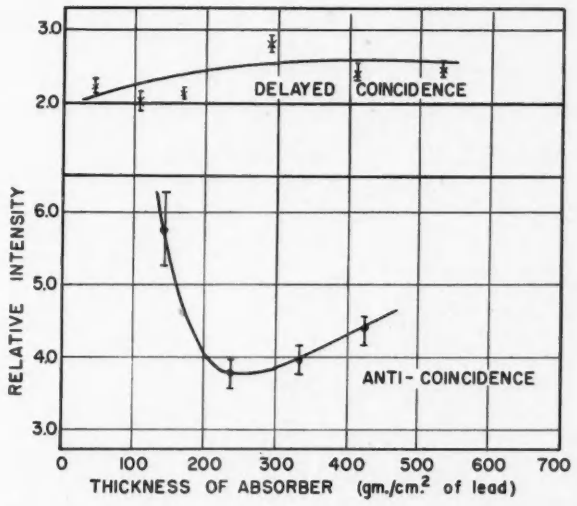


FIG. 6. Lower curve—the differential meson range spectrum measured by coincidence–anticoincidence methods in Experiment II. Upper curve—the differential meson range spectrum measured by the delayed coincidence technique used in Experiment III.

apparatus would be particularly sensitive to those that do, and would include a wider energy band of protons than of mesons; hence some error at low absorber thickness should be expected but the observed value seems too high to be explained in this way. A similar experiment by Rogozinski and Lesage (9) gave a similar curve. The results of Experiment I also suggest that the differential spectrum is not necessarily simple but the accuracy is hardly great enough to justify definite conclusions.

## EXPERIMENT III—THE DELAYED COINCIDENCE METHOD

Since the delayed coincidence technique is often considered to be the best way of identifying mesons, a third apparatus was built to measure the differential range spectrum. The arrangement of counters is shown in Fig. 7. Counter trays $A$ and $B$ define a wide beam of mesons which have passed through the roof of the building and an absorber above the trays $A$ and $B$. Below $B$ there was a block of carbon surrounded by two rows of counters placed as shown. $A$ and $B$ were connected in coincidence. The pulse from the coincidence circuit was fed through a delay line to a coincidence circuit from the rows of counters $C$ and $D$. The carbon block was $45 \times 15 \times 10$ cm. in size and the counters $C$ and $D$ surrounded it closely. To reduce chance delayed coincidences, coincidences between $C$ and $D$ were used. The circuit was so arranged that a coincidence $(A,B)$ without delay and a pulse in any counter in $C$ or $D$ would block the apparatus for about 12 $\mu$sec. The apparatus records only $(A,B)$ coincidences not accompanied by an immediate pulse from $C$ or $D$ but followed by a $(C,D)$ coincidence at any time

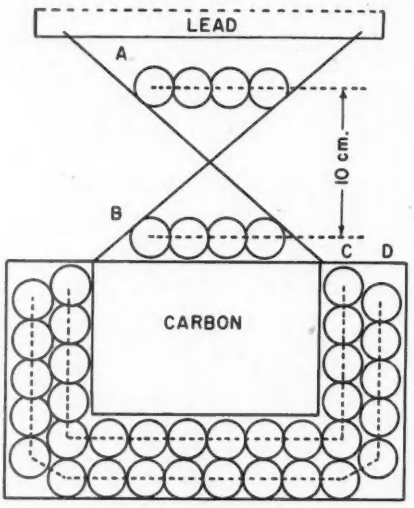


FIG. 7. Arrangement of counters and absorbers in Experiment III. The thickness of absorber on top was varied.

between 1.2 and 7.2 μsec. after $(A,B)$. The counting rates of the $(A,B)$ and $(C,D)$ coincidences were about 230 and 750 per min. respectively but with the above arrangement of connections chance delayed coincidences were negligible. The remaining background, probably mostly due to decaying mesons in the aluminum boxes and counter walls, could be observed by taking counts with the carbon block removed.

The results are shown in the upper curve in Fig. 6, the ordinates being in counts per hour plotted against total thickness of absorber above the carbon block. A correction was made in the absorber thickness for width of the angular beam defined by trays $A$ and $B$. Voisin (16) has shown that the angular distribution of mesons in low energy ranges does not obey the cosine squared law but measured angular distributions fit closer to a relation of the form $I/I_0 = 1 - a \sin^b \theta$. Assuming that on the average the telescope $(AB)$ includes all particles at angles up to 60° with the zenith and the distribution is that found by Voisin, a rough numerical integration shows that the mean particle penetrates about 1.27 times the vertical thickness of absorber. As in the other experiments 10% was added to the absorber thickness to take scattering into consideration. Therefore in plotting the results of this delayed coincidence experiment the absorber thickness was increased by a factor of 1.4 to give a better representation of these results for comparison with others. The results show considerable irregularity over the range of absorber thickness used. If it is assumed that the correct spectrum should be a smooth curve these results show that the differential spectral intensity varies very little over the range studied, a fact that is in agreement with other observers using this method, but it is not in complete agreement with Experiments I and II.

## III. CONCLUSIONS

The results of the measurements on the differential range spectrum by the three methods described here and of some published measurements by others are shown together in Fig. 8. Curve (I) is the mean of the derived differential range

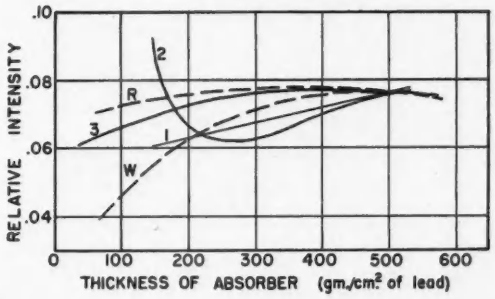


FIG. 8. Different measurements of the differential range spectrum of mesons. Curve(1) is the result of Experiment I; curve (2) of Experiment II; curve (3) of Experiment III. The broken curve *R* represents the spectrum selected by Rossi and *W* the results of Wilson's measurements.

spectra at Ottawa and Resolute as shown in Fig. 4. Since there is no significant difference in shape between the two the results are averaged to obtain this curve. Curve (2) represents the results of the measurements in Experiment II as shown in the lower curve of Fig. 6. Curve (3) is the same as the upper curve in Fig. 6 representing the delayed coincidence measurement in Experiment III. Curves (2) and (3) have been normalized to fit curve (1) at 500 gm. per cm.$^2$ The measured points and standard deviations have been omitted to simplify the figure. Curve *W* was derived from the differential momentum spectrum of Wilson (17). The actual curve was taken from a smooth curve drawn through Wilson's points as presented by Rossi (Fig. 4 of Ref. (12)). The abscissa was converted from momenta to gm. per cm.$^2$ of lead by using the figures given by Montgomery (7). Curve *R* represents the differential range spectrum in air shown by Rossi (Fig. 6 of Ref. (12)). The abscissa is converted from gm. per cm.$^2$ of air to gm. per cm.$^2$ of lead. Since the absolute values are not being compared but only relative values over the range of absorbers used in the present experiments both the *W* and *R* curves were normalized to fit curve (1) at 500 gm. per cm.$^2$ The slope of Rossi's curve over this range was based largely on measurements by Sands using the delayed coincidence technique.

In examining the curves in Fig. 8 it is apparent that there are differences in the results using different methods of measuring the differential range spectrum. The results of Experiment III using the delayed coincidence technique are in fair agreement with Rossi's curve *R*. The results of Experiment I are in agreement with Experiment II except for the rise at the lower end of curve (2). The Wilson curve shows lower intensities at low absorber thickness. The uncertain errors however in curves (1) and (2) are in a direction that would tend to bring them into agreement with curves *R* and (3). In Experiment I no correction was

made for the relative losses due to scattering at different absorber thicknesses. By eliminating some of the data at low absorber thicknesses this effect was presumed to be small, but slightly different results would have been obtained by a different grouping of the data in deriving the differential spectrum. In curve (2) (Fig. 8), if the high point at the lowest absorber thickness is taken as being due to protons and electrons, this curve might be normalized to fit curve (3) within the limits of accuracy. These differences, therefore, have no real significance though the combined results indicate a curve with a slightly greater slope than Rossi's. The possibility of a more complicated form of spectrum is also suggested by the results of Experiments I and II.

The present results therefore, being in reasonable agreement with Rossi's spectrum, support a production spectrum of the shape calculated by Sands. In a previous paper (10) it was shown that the barometer coefficient was very sensitive to the shape of the production spectrum. Two groups of measurements of barometer coefficients with different absorber thicknesses were described. These, when averaged together, were in fair agreement with a production spectrum like that of Sands (14) and Rossi's sea level spectrum. The relative values of the barometer coefficients with different thicknesses of absorber, however, suggested (with low statistical accuracy) a double peaked production spectrum and a sea level spectrum at low energies more in agreement with Wilson's measurements. The weight of evidence from measurements at sea level is now against this and indicates that the relative values of the two groups of barometer coefficients measurements may well have been fortuitous. An exact measurement of the meson spectrum at an altitude of about 40,000 feet, if it were possible, would be very valuable.

## IV. SUMMARY OF CONCLUSIONS

Measurements on the range spectrum of $\mu$-mesons at sea level taken at geomagnetic latitude 83.0° and 56.8° over ranges up to 700 gm. per cm.$^2$ of lead show no significant differences at the two latitudes. Small differences due to different mean atmospheric conditions might be expected but the present results are not sufficiently accurate to show this. The shape of the differential range spectrum derived from absorption methods was found to be in reasonable agreement with more direct methods when careful consideration was given to all errors particularly those due to scattering. The agreement with other observers is good though the combined results suggest a spectrum with a little greater slope over the range studied than that suggested by Rossi in 1948.

## ACKNOWLEDGMENTS

The apparatus at Resolute was housed in the Ionosphere Station of the Radio Division of the Department of Transport of the Government of Canada. The Meteorological Division of the same Department supplied the meteorological data and made available the facilities of the joint Canadian–American weather station at Resolute. The apparatus at Resolute was operated by Mr. W. Heikkila and much of the analysis of data from that station was carried out

by him. Our thanks are also due to Dr. J. Katzman for assisting in the operation of the Ottawa equipment and to Mrs. E. Grummisch for assistance with the analysis of the results.

## REFERENCES

1. BROWN, W. W., MCKAY, A. S., and PALMATIER, E. D. Phys. Rev. 76: 506. 1949.
2. CARO, D. D., PARRY, J. K., and RATHGEBER, H. D. Australian J. Sci. Research, A, 4: 16. 1951.
3. HALL, D. B. Phys. Rev. 66: 321. 1944.
4. KOENIG, H. P. Phys. Rev. 69: 590. 1946.
5. KRAUSHAAR, W. L. Phys. Rev. 76: 1045. 1949.
6. MONTGOMERY, D. J. X. Cosmic ray physics, Princeton University Press. 1949. Appendix C; or ARLEY, N. On the theory of stochastic processes and their application to the theory of cosmic radiation. John Wiley and Sons, New York. 1948.
7. MONTGOMERY, D. J. X. See Ref. 6, Appendix E.
8. MYLROY, M. G. and WILSON, J. G. Proc. Phys. Soc. (London), A, 64: 404. 1951.
9. ROGOZINSKI, A. and LESAGE, M. Compt. rend. 227: 1027. 1948.
10. ROSE, D. C. Can. J. Phys. 29: 97. 1951.
11. ROSE, D. C., HEIKKILA, W., and FORD, E. Phys. Rev. 84: 986. 1951.
12. ROSSI, B. Revs. Modern Phys. 20: 537. 1948.
13. ROSSI, B. and GREISEN, K. Revs. Modern Phys. 13: 240. 1941.
14. SANDS, M. Phys. Rev. 77: 180. 1950.
15. SARABHAI, V. Phys. Rev. 65: 250. 1944.
16. VOISIN, A. G. Can. J. Phys. 29: 505. 1951.
17. WILSON, J. G. Nature, 158: 414. 1946.

# FURTHER OBSERVATIONS ON THE MACROMOSAIC STRUCTURE OF TIN SINGLE CRYSTALS[1]

By E. Teghtsoonian[2] and Bruce Chalmers[3]

ABSTRACT

Further studies are reported on the bands, or striations, into which single crystals of high purity tin, grown by a modified Bridgman method, are partitioned. This striation structure is shown to exist throughout the whole volume of the crystal. The direction in which the boundaries of the striations form relative to the specimen axis is shown to be a compromise between thermal and crystallographic conditions, in which the orientation of the (110) planes is the determining factor. When new striations are formed, they are found to have an incubation period which is longer the slower the rate of growth of the crystal. A qualitative mechanism is developed, based on the formation of dislocations into transition surfaces constituting the striation boundaries, which is consistent with all the experimental observations.

## INTRODUCTION

In a previous paper (3), some observations on a macromosaic structure occurring in single crystals of high purity tin were reported. The crystals were grown by the progressive solidification of a seeded melt, using a method developed by Chalmers (1). The structure is revealed after a short etch in a ferric chloride solution. Further observations are reported in the present paper, and a fuller development of the mechanism of its formation is offered.

## SUMMARY OF PREVIOUS OBSERVATIONS

For a crystal whose axis is parallel to the [110] direction, striations of the order of 1 mm. in width always form parallel to the axis. The widths of the striations have been shown to increase on the average as the rate of growth of the crystal is decreased. From back-reflection X-ray Laue pictures, it is evident that there exists a difference of orientation of the lattice in neighboring striations. This orientation difference, between 1° and 5°, is always a rotation about the specimen axis. The sense of this rotation alternates irregularly for successive striations across the width of the specimen. Thus, the orientation of the lattice in any one striation is within approximately 8° of the orientation of the lattice in any other striation.

Experiments had shown the striated structure to exist throughout the whole volume of the specimen, but the exact cross-sectional character had not been revealed. The structure of the imperfection is very stable, not being affected by prolonged high temperature annealing. In crystals grown with an angle between the [110] direction and the axis of longitudinal heat flow, the striations were found to form parallel to the axis at low rates of growth, and approached paral-

[1] *Manuscript received April 2, 1952.*
*Contribution from the Department of Metallurgical Engineering, University of Toronto, Toronto, Ont.*

[2] *Graduate Student, Department of Metallurgical Engineering, University of Toronto; Present Address: Mines Branch, Division of Mines and Technical Surveys, Ottawa.*
[3] *Professor of Physical Metallurgy, University of Toronto.*

lelism with the [110] direction at high growth rates. Preliminary work had indicated the presence of an incubation period before the formation of new striations.

## RESULTS OF PRESENT INVESTIGATION

### *Average Orientation Difference*

Series of X-ray pictures were taken to determine whether the orientation differences between neighboring striations were affected by the rate of growth. Just as the widths of the striations were found to vary considerably for a given growth rate, so did the orientation difference between neighboring striations. If this variation is due to the variation in striation width, then it would be expected that a similar relationship should exist between the average orientation difference and the rate of growth.

Accordingly, X-ray pictures were taken across the width of crystals grown at rates of from 10 mm. per min. down to less than 1 mm. per min. The specimen was moved a distance equal to the diameter of the X-ray spot at the surface of the crystal (0.7 mm.) between X-ray pictures, resulting in a continuous series of measurements of orientation difference from one striation to the next. The averages were calculated without regard to the sense of the rotation. The results are summarized in Table I which shows that the average orientation

TABLE I

| Rate of growth, mm. per min. | Average orientation difference, degrees |
|---|---|
| 0.85 | 2.8 |
| 1.5 | 2.6 |
| 1.7 | 2.3 |
| 3.0 | 1.8 |
| 6.4 | 1.6 |
| 6.5 | 1.4 |
| 9.6 | 1.2 |

difference also increases as the rate of growth decreases. Thus, it is concluded that the average orientation difference increases as the average width increases.

### *Orientation Effect*

The conditions under which the striations would form at an angle to the specimen axis were investigated. When the crystals were oriented so that the [110] direction was parallel to the specimen axis and the [001] direction was perpendicular to the top surface, the striations always formed parallel to the specimen axis. This will be referred to as Type 1 orientation. When, however, the [110] direction is not parallel to the specimen axis, the striations may also be oblique; the angle between the [110] direction and the specimen axis will be designated by $\phi$.

The four most closely packed sets of planes whose orientations might be most likely to influence the formation of the striations are the (100), (110), ($1\bar{1}0$),

and the (001). For crystals of Type 1 orientation, the relations between the direction of longitudinal heat flow and these planes are shown in Column 2 of Table II.

TABLE II

| Plane | Angle between plane and specimen axis | | |
|---|---|---|---|
| | $\phi = 0, \theta = 0$ | $\phi \neq 0, \theta = 0$ | $\phi \neq 0, \theta = 90$ |
| $(00\bar{1})$ | 0 | 0 | $\phi$ |
| $(1\bar{1}0)$ | 0 | $\phi$ | 0 |
| (110) | 90 | $90 - \phi$ | $90 - \phi$ |
| (100) | 45 | $45 \pm \phi$ | $45 \pm \phi$ |

For crystals in which the angle $\phi$ is not zero, $0° < \phi < 45°$, the angles between the direction of longitudinal heat flow and these four sets of planes are shown in Column 3 of Table II. Thus, if the change in the angle between the striations and the specimen axis by the introduction of the angle $\phi$ may be attributed to a change in the direction of longitudinal heat flow with respect to one of these four sets of planes, the above analysis shows that the (001) planes are inoperative in this process.

To determine which of the remaining sets of planes is the one governing the direction of striation formation, crystals were grown in which the crystal axes were rotated by an angle $\theta$ about the specimen axis as well as the angle $\phi$ about

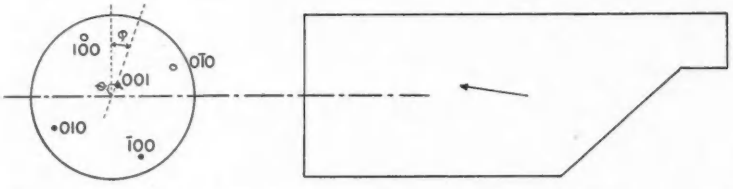


FIG. 1. Schematic diagram showing orientation of crystal by simplified stereographic projection. Arrow indicates direction of striations.

the [001] direction. This is illustrated by Fig. 1. In the extreme case when $\theta = 90°$ and $\phi = 0°$, the angles between the direction of longitudinal heat flow and the four sets of planes under consideration are exactly the same as before, i.e., for $\theta = 0°$ and $\phi = 0°$. Now, however, when the angle $\phi$ is not zero, the angles between the direction of heat flow and these planes are as shown in Column 4 of Table II. Under these conditions, the only planes of the sets not previously eliminated whose orientations relative to the growth direction are changed by virtue of the $\theta$ angle are those (110) planes originally parallel to the direction of longitudinal heat flow.

Crystals were grown with $\theta = 90°$ and $\phi = 4°$, 14°, 24°, and 34°, over all rates of growth previously used, and in all cases, the striations always formed parallel to the specimen axis. Crystals were then grown for $\theta$ values intermediate between 0° and 90° and for $\phi = 14°$, and the angle $\alpha$ between striations and specimen axis

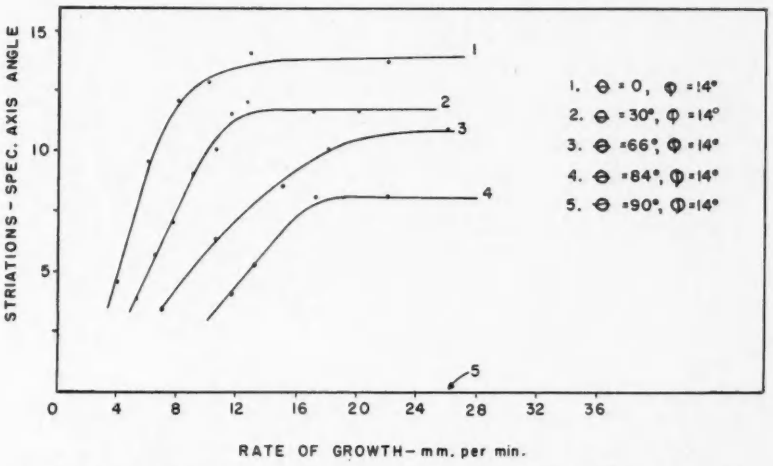


FIG. 2. Curves relating direction of striations and rate of growth for different orientations.

plotted for each orientation as a function of the rate of growth. The results are shown in Fig. 2. As $\theta$ is increased, the angle $\alpha$ for a given growth rate is decreased. The greatest change in the behavior of $\alpha$ for a given growth rate occurs at $\theta$ close to 90°. Also, as $\theta$ is increased, the rate of growth required to produce constant $\alpha$ is increased.

The results of these orientation experiments show conclusively that whatever the mechanism producing the striations, it is very closely connected with the (110) planes which are parallel or nearly parallel to the direction of longitudinal heat flow.

*Cross Section of the Striations*

The cross-sectional character of the striations was examined by means of an improved etching technique. This consisted of masking off part of the crystal with electroplating tape and then etching the exposed region electrolytically in a 10% hydrochloric acid solution. This resulted in the removal of layers of the metal from the unmasked portion of the crystal, revealing the striation patterns on the newly exposed surfaces. These patterns could then be compared with that on the unetched portion of the original surface. The depth of the etched portion was measured using the fine focusing adjustment of a microscope. Using this method, up to more than 1 mm. of metal was removed in approximately 0.1 mm. steps.

The results for a Type 1 orientation crystal are shown in Fig. 3. This shows a series of photographs of the specimen at various stages of the etching process, the depth of the etched region in millimeters being shown under each photograph. It can be seen that the striations extend down into the crystal to a distance approximately equal to their width. When the layer containing these striations

is removed, new striations are revealed which in turn also extend down a distance approximately equal to their width. The widths of the striations below the ones visible on the top surface are, on the average, equal to those on the top surface. The vertical boundaries that separate one striation from its neighbors extend down into the crystal parallel to the specimen axis and perpendicular to the top surface. Thus, these boundaries are very closely defined by (110) planes within the limit of the disorientations of the striations themselves.

The gradual, rather than abrupt, disappearance of a particular striation is probably due to a combination of two factors: (1) the amount of material removed by etching may not be uniform over the entire surface, and (2) the "horizontal" boundaries between the striations in one layer and those in the layer beneath may not be strictly parallel to the original surface. It does appear, however, that these "horizontal" boundaries are closely coincident with the (001) planes. It should also be noted that the vertical boundaries of the striations in one layer are not in alignment with those of the striations in the next layer. Thus, the "single crystal" is made up of a bundle of rectangular striations. This is shown schematically in Fig. 5.

Etching experiments of this type were then done on crystals in which both $\theta$ and $\phi$ differed from zero. In one specimen $\theta = 30°$ and $\phi = 24°$ and a region of the crystal was etched where the striations formed at their maximum angle $\alpha$. After the first etching period of one hour, during which 0.52 mm. of metal was removed, the boundaries of the same striations were still visible. They were still parallel to their original directions, but displaced slightly from their original positions in a direction perpendicular to their lines of formation. Further etching resulted in an increasing displacement of these boundaries. Fig. 4 shows these boundary displacements. Knowing the depth of the etch and the corresponding boundary displacements, the angle made by the bounding plane of the striations with the top surface may be calculated. The results are shown in Table III.

TABLE III

| Depth of etch, mm. | Displacement of boundary, mm. | Angle of bounding plane, degrees |
|---|---|---|
| 0.70 | 0.3 | 67 |
| 1.08 | 0.5 | 65 |

These values may be compared with the value of the angle formed between the (110) planes and the top surface (66°) which may be calculated from the known orientation of the crystal.

These experiments were repeated on a crystal of the same orientation, but in a region where the angle $\alpha$ was much smaller owing to a slower growth rate. Under these conditions, the bounding planes of the striations formed at greater angles with the top surface. These results show that just as the direction of the striations tends to be as close to the [110] direction as possible for a given growth rate, the "vertical" bounding planes of the striations tend to be as close as possible to the (110) planes.

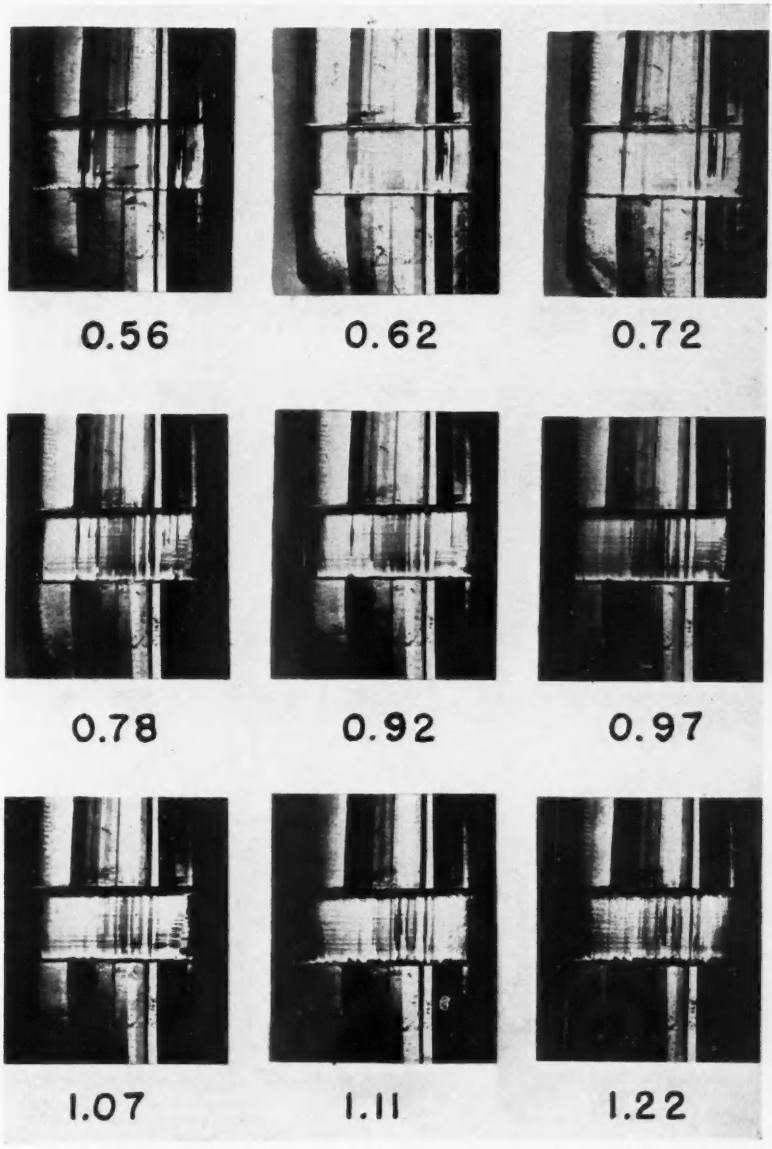


FIG. 3. Etched crystal indicating cross-sectional character of striations. Depth of etched region shown in millimeters.

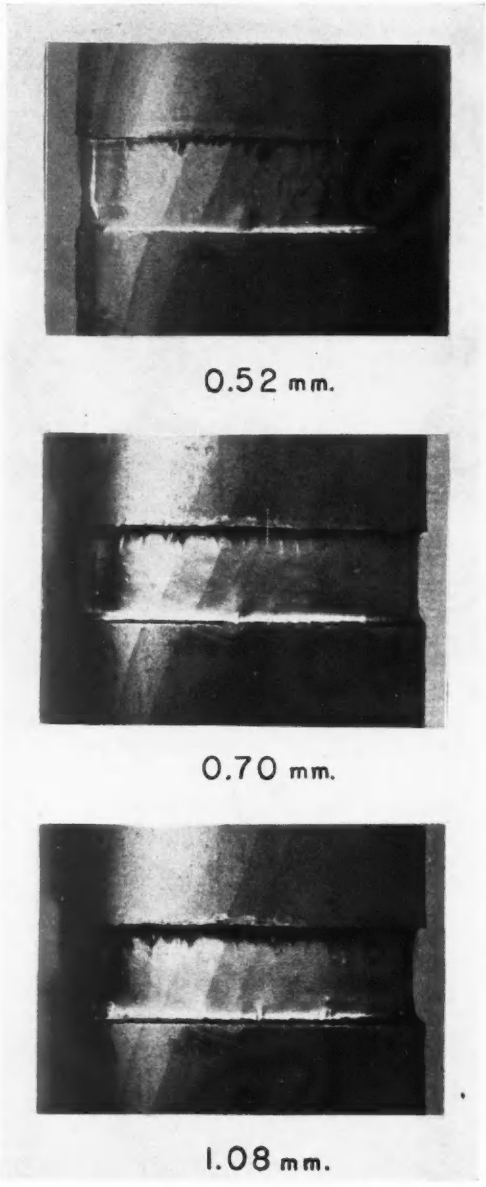


FIG. 4. Etched crystal indicating sloping striation boundaries.

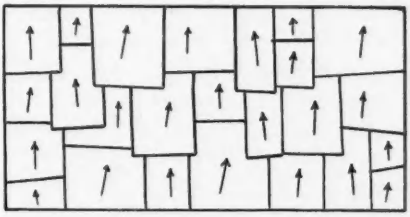

FIG. 5. Schematic representation of striation cross section.

*Formation of New Striations*

As mentioned in the previous paper (3), striations form independently from those present in the seed in that part of the crystal growing in line with the graphite insert. These striations become visible only after some finite interval, and X-ray surveys along pairs of striations in this region had shown that the orientation difference between a pair of striations gradually increased up to some maximum value.

Bicrystal specimens were grown in which each member of the specimen was grown from a seed which was of a Type 1 orientation with an angle $\phi > 0$, in the opposite sense for each seed. The same sort of incubation was found to be present in each member of the bicrystal with the striations forming at an angle to the bicrystal boundary. This showed that the presence of the incubation period is not due to any distortions of the isothermals due to the graphite insert in the growth of the single crystal specimens.

Quantitative measurements of this incubation period were made on single crystals of Type 1 orientation rather than on the bicrystal specimens for two reasons: (1) for this orientation, the growth of the specimen is in the same direction as that for the formation of the striations; (2) for the bicrystals, relatively high rates of growth are necessary to produce striations at a sufficiently

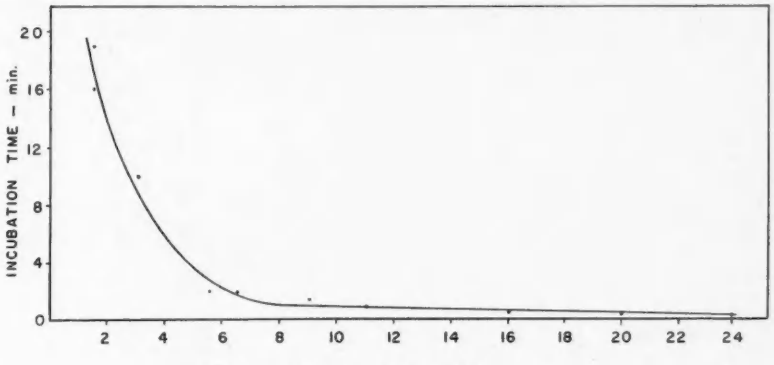


FIG. 6. Curve relating incubation period and growth rate.

large angle to permit of measurements of the incubation period. This would render impossible measurements at low rates of growth.

For crystals grown at rates ranging from 1.5 mm. per min. up to 24 mm. per min., measurements were made of the distance from the edge of the graphite

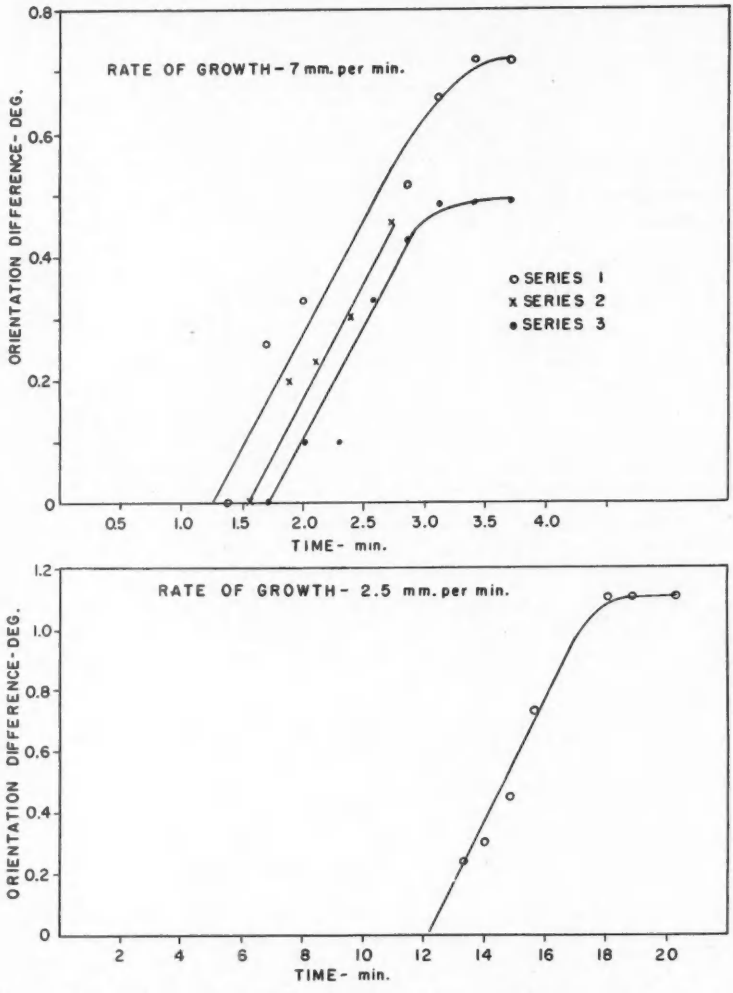
RATE OF GROWTH - 7 mm. per min.
ORIENTATION DIFFERENCE - DEG.
TIME - min.
o SERIES 1
x SERIES 2
• SERIES 3
RATE OF GROWTH - 2.5 mm. per min.
ORIENTATION DIFFERENCE - DEG.
TIME - min.

FIG. 7. Curves showing increase of orientation difference with time across one pair of striations in region of incubation.

insert to the point where the striations first become visible. There may be some subjectivity in this type of measurement, but it is believed that the results of the

X-ray experiments to be described below indicate that these measurements are, in fact, significant.

Anticipating the explanation of the formation of the striations as somewhat analagous to a nucleation and growth process, the incubation period was measured in terms of time rather than distance. The results are shown in Fig. 6. These results show that the incubation time increases as the rate of growth decreases.

Series of X-ray pictures were taken along pairs of striations that had formed in the manner described above independently from those present in the seed, and the general results were the same for all specimens. At regions on the crystal where the striations are prominently visible, there is a fixed difference of orientation between a given pair of striations. As the region where the striations become less distinct is approached, the orientation difference between the striations gradually decreases.

The results for two crystals are shown in Fig. 7. Again, the measured orientation differences are plotted against time rather than distance. Extrapolating the curves back to zero orientation difference, it can be seen that the intercept on the time axis agrees very well with the incubation period as measured from visual observation. This indicated that the striations become visible when the orientation difference between them is still very small, approximately 6′ of arc. The curves also show that the increase of the orientation difference is very closely linear with time. This rate of increase of orientation difference is obtained from the slope of the linear portion of the curves. This is found to be 0.45° per min. for a crystal grown at 7 mm. per min., and 0.23° per min. for a crystal grown at 2.5 mm. per min. Thus, the rate of attainment of maximum orientation difference increases as the rate of growth increases.

## SUMMARY OF OBSERVATIONS

The various aspects of the properties and behavior of striations that should be explained by a satisfactory theory are summarized below:

1. Single crystals of tin are found to be partitioned into striations of rectangular section.

2. There exists a difference of orientation between neighboring striations which is always a rotation of from $\frac{1}{4}°$ up to 5° about an axis parallel to the specimen axis.

3. The direction of formation of the striations and the bounding planes are governed by both the orientation of the crystal relative to the direction of longitudinal heat flow, and the rate of growth. The striations grow at an angle to the specimen axis when the (110) planes, originally parallel to the direction of longitudinal heat flow, are inclined at some angle to this direction.

4. In a given crystal, the sum of all the rotations of the lattice in one sense in going from one striation to the next is very nearly equal to the sum of all the rotations in the opposite sense.

5. The widths of the striations vary for a given rate of growth, but, on the average, the width increases as the rate of growth decreases.

6. In the same way, the average orientation difference between neighboring striations also increases as the rate of growth decreases.

7. The striation boundaries are very stable structures. They are not altered by prolonged annealing at temperatures close to the melting point.

8. When new striations form, they require an incubation period which is greater for slowly grown crystals than for rapidly grown crystals.

9. Lower growth rates result in a more rapid increase of the difference of orientation between a pair of incubated striations than higher growth rates.

## PROPOSED MECHANISM

In the previous paper (3), an outline of a mechanism was proposed to account for the formation of the striations. This mechanism was based on the condensation of vacant lattice sites into disks and the subsequent collapse of these disks to form pairs of edge type dislocations of opposite signs. No further details of this mechanism will be given here, but the dislocations so formed will be examined, and the balance of their potential and kinetic energies will be considered in the formation of striation boundaries.

The energy per unit length of a single dislocation may be divided into two main parts. The first, which may be called a "potential" energy, is due to the deformation of the lattice in the neighborhood of the dislocation. The second may be called its "kinetic" energy due to its motion.

The potential, or static component of its energy, may be subdivided into two parts: (1) the "*core*" energy in a small region around the center line of the dislocation where the lattice strains are so large that a treatment by classical elasticity theory is not possible; (2) the "*elastic*" energy, in a considerably larger region outside the core region, where the lattice distortions are much less, and the theorems of elasticity theory may be legitimately applied. For free dislocations, i.e., dislocations which are not bound in a stable array, or are relatively far away from other dislocations, the total static energy per unit length of dislocation line depends only on the orientation of the dislocation relative to the crystallographic axes.

The kinetic or dynamic component may also be subdivided into two parts: (1) the "*stress*" component due to the application of an external shear stress; this external stress sets the dislocation into accelerated motion. If the velocity of the dislocation reached the velocity of sound, the kinetic energy would become of the same order as the potential energy; (2) the "*thermal*" component. This is probably much smaller than the stress component and virtually negligible in comparison. However, in the absence of an external shear stress, the thermal component gives the dislocation a mobility which cannot be neglected. It will be strongly temperature dependent, decreasing very rapidly with a drop in temperature.

Let us denote the core energy by $E_C$,
the elastic energy by $E_E$,
and the thermal energy by $E_T$.

Since no external stress is being applied, the stress energy may be neglected. Thus, the energy per unit length of the dislocations as they are formed a short distance behind the interface is $E_D = E_C + E_E + E_T$.

Let us now consider the energy of a dislocation in a stable array. Provided the dislocations are not too close together (i.e., for small orientation differences across the transition surface defined by the array of dislocations), the core energy remains unchanged at $E_C$. However, since the region of elastic energy extends over much larger distances, there will be interactions between the lattice strains due to neighboring dislocations. Thus, the elastic energy of a dislocation in the array $E_E'$ will be less than the elastic energy of the dislocation when free. As the temperature drops, the thermal energy too will decrease very rapidly, so that at room temperature (probably even long before room temperature is reached) the thermal energy will be effectively zero. Thus, the energy per unit length of a dislocation in the stable array at room temperature will be $E_D' = E_C + E_E'$. This is less than the energy of the free dislocation by an amount $(E_D - E_D') = (E_E - E_E') + E_T$.

We can now consider the conditions under which a transition surface may be nucleated. Under the action of the thermal energy, the dislocations will migrate through the specimen in a direction perpendicular to the direction of the dislocation line. This migration process will occasionally bring numbers of dislocations of the same sign into line in possible transition surfaces. Since the dislocations still possess their thermal energy at the instant of alignment, the decrease of energy that would be effected by the dislocations being in alignment would be $(E_E - E_E')$. Thus, at the instant of alignment, the dislocations will be under two opposing influences; the decrease of elastic energy due to the alignment tending to anchor the dislocations, and the thermal energy tending to keep the dislocations moving. The stability of the array would then depend on the relative values of $(E_E - E_E')$ and $E_T$. If $(E_E - E_E') > E_T$, the array would be stable, while if $(E_E - E_E') < E_T$, the array would be unstable and would tend to break up.

The probability of the initiation of a stable array of dislocations depends on the probability of the alignment of a number of dislocations of sufficient density so that $(E_E - E_E') > E_T$. As a dislocation is formed immediately behind the interface, its thermal energy will be near its maximum value, since the temperature at this position is almost the melting point. As the interface advances, the temperature at the point where the dislocation was formed decreases owing to the temperature gradient in the solid, and thus the thermal energy of the dislocation also decreases. Thus, the rate of decrease of the thermal energy will be higher at the higher growth rates, resulting in a higher probability, per unit of time, of an array forming so that $(E_E - E_E') > E_T$. This would result in a shorter incubation period for quickly grown crystals than for slowly grown crystals, which is in agreement with observation.

Once the striations have been nucleated in this way, we can examine their subsequent behavior, and the way this behavior depends on the conditions of growth.

The magnitude of $(E_E - E_E')$ will depend on the closeness of the dislocations in the array, being greater for dislocations that are closer together. Thus, once a transition surface is nucleated, $(E_E - E_E')$ will become progressively greater than $E_T$ as more dislocations are trapped in the array. Since the rate of decrease of the thermal energy increases for higher rates of growth, it follows that the rate at which further dislocations join the array will be higher for the higher rates of growth. This will result in a higher rate of increase of orientation difference for higher growth rates as is experimentally observed.

The dislocations in the transition surface would act as good sinks for vacant lattice sites. Thus, more and more vacant lattice sites will be eliminated at the transition surfaces rather than by forming disks. There will then come a time when the number of free dislocations will be decreased to such an extent that their mobilities will be reduced to zero before they can reach the transition surfaces. Thus, an equilibrium number of dislocations will be in the transition surface. This will result in the attainment of a maximum orientation difference across that surface. Since $E_T$ decreases more quickly at the high growth rates, this equilibrium condition will be attained sooner, and the maximum orientation difference will be smaller.

Since the nucleation of a transition surface depends on the chance alignment of a number of dislocations of a critical density to make $(E_E - E_E') > E_T$, it would be expected that this alignment would occur at positions across the width of the crystal separated by distances which are not all equal. This would result in the variation in striation width that is observed for a given rate of growth. However, owing to the more rapid decrease of $E_T$ at high growth rates, a greater number of transition surfaces would be expected to nucleate in a given width of crystal, resulting in striations that are, on the average, narrower for the higher growth rates.

One result of the mechanism described is that the dislocations are produced in pairs of opposite signs. Thus, there will be an equal number of positive and negative dislocations nucleating transition surfaces and migrating to these surfaces. Since the sense of the rotation of the lattice across one of these transition surfaces depends on the sign of the dislocations constituting that surface, one would expect to find an equality in the sums of all the rotations in the two senses which is, in fact, the case.

The persistence of the striation boundaries once they are nucleated and their stability to prolonged annealing follows as a consequence of the increase of $(E_E - E_E')$ with the density of the dislocations in the transition surface. Raising the temperature in annealing, even to just below the melting point, can only raise $E_T$ to the value it had when the dislocations were first formed during the growth process. Now, however, the value of $(E_E - E_E')$ is much higher than is necessary for it to be greater than $E_T$, so that it is impossible to cause the array to break up by annealing.

The behavior of the striations when the orientation of the crystal is other than a Type 1 orientation may follow as a consequence of the assumption that the vacant lattice sites condense into disks which are preferentially in the (110)

planes. An actual proof of the validity of this assumption is not offered in this paper. Such a proof would involve a rather complex analysis of the forces between atoms, for as Frank has indicated (2), the manner in which vacancies condense would depend on two factors. These are: (1) the relief in the broken neighbor–neighbor contacts effected by the agglomeration of the vacancies, and (2) the work done in the collapse of the lattice across the vacancy disks. These considerations would be further complicated by the existence of the temperature gradient in the present work.

However, if the vacancy condensation mechanism, as previously described (3), is essentially correct, then the properties of the striations in crystals of other than Type 1 orientation follow logically. Since the elimination of vacancies is also a strongly temperature dependent phenomenon, the ultimate manner of their condensation will be a compromise between thermal and crystallographic conditions. Assuming that at low growth rates, thermal conditions are dominant, and at high growth rates crystallographic conditions predominate, the following processes could occur. When the (110) planes are not parallel to the direction of the longitudinal temperature gradient, the vacancies will condense in those planes that are parallel to this direction, for low growth rates, producing dislocations perpendicular to the interface. These will ultimately form into transition surfaces parallel to the specimen axis. At higher growth rates, the tendency will be towards closer alignment with the (110) planes. Thus, the dislocations parallel to the specimen axis will be broken periodically, the segments being joined by elements of screw dislocations parallel to the interface. The direction of the boundary will thus approach the direction of the (110) planes. At the same time, the difference of orientation will remain a rotation about the specimen axis.

## APPENDIX

*Some order of magnitude calculations on the number of dislocations involved in the formation of striation boundaries*

Consider for example a crystal grown at a rate of 1.7 mm. per min. For this crystal the average difference of orientation between neighboring striations is 2.3°. The average width of the striations is 0.85 mm.

Consider a section of crystal 1 cm. × 1 cm. For purposes of calculation, we may assume that the vertical and horizontal boundaries go right through the specimen. We will assume that the average width of the striations is equal to the average depth, and further that the difference of orientation between neighboring striations is the same for striations that are above one another as for those which are side by side. Thus, the total length of the vertical boundaries in the 1 cm. square section of crystal is $10 \times 10/0.85 = 118$ mm., and this is also the total length of the horizontal boundaries. On the simple picture of an array of edge type dislocations constituting the boundary, the difference of orientation across the boundary is given by $\theta = \tan^{-1}\frac{\lambda}{h}$ or $h = \frac{\lambda}{\tan\theta}$ where $\lambda$ is the Buergers vector, and $h$ is the separation of the dislocations in the array. For

the Type 1 orientation crystals, for the vertical boundaries, $\lambda = 8.2$ Å, and $\tan\theta = \tan 2.3° = 0.04$. Therefore

$$h = 8.2/.04 = 205 \text{ Å},$$

the density of dislocations per mm. of vertical boundary is

$$10^7/205 = 4.88 \times 10^4,$$

and the number of dislocations in the vertical boundaries is

$$118 \times 4.88 \times 10^4 = 5.75 \times 10^6.$$

For the horizontal boundaries, $\lambda = 3.2$ Å, and $\tan\theta = 0.04$. Therefore

$$h = 3.2/.04 = 80 \text{ Å},$$

the density of dislocations per mm. of horizontal boundary is

$$10^7/80 = 1.25 \times 10^5,$$

and the number of dislocations in the horizontal boundaries is

$$118 \times 1.25 \times 10^5 = 1.47 \times 10^7.$$

Therefore, the total number of dislocations arrayed in the boundaries is

$$2.05 \times 10^7.$$

Similar calculations have been done for crystals grown at various rates and the results are summarized in the table below:

| Rate of growth, mm./min. | Number of dislocations in boundaries |
|---|---|
| 0.85 | $1.79 \times 10^7$ |
| 1.5 | $1.85 \times 10^7$ |
| 1.7 | $2.05 \times 10^7$ |
| 3.0 | $2.66 \times 10^7$ |
| 6.5 | $3.60 \times 10^7$ |
| 9.6 | $3.70 \times 10^7$ |

These figures are all in the range between 0.1 and 0.3 of the number of dislocations that are thought to be present in an annealed specimen which is of the order of $10^8$ per cm.$^2$ This would suggest that between one-tenth and one-third of the total number of dislocations in the specimen are arrayed in the striation boundaries which seems to be reasonable based on the proposed mechanism.

The progressive increase of the number of dislocations in the boundaries with an increase in the growth rate is rather interesting. On the basis of the proposed mechanism, this might be interpreted in the following manner. At higher growth rates, there will be formed a greater number of disks of vacant lattice sites which in turn will be able to grow to a smaller size before collapse of the lattice occurs, than there will be at the lower growth rates. Since each collapsing disk gives rise to a pair of dislocations, the number of vacancies used in producing a pair of dislocations will be smaller for the higher growth rates than for the lower growth

rates. Therefore, the number of dislocations produced by collapsing disks will be greater for the higher growth rates than for the lower growth rates. Thus, the number of dislocations that will eventually migrate into striations boundaries will be greater for the higher growth rates.

Such an argument is consistent with the general theory that the degree of perfection of a crystal will increase as the rate of growth is decreased. However, it should be noted that at the higher growth rates, more vacancies will be "frozen" into the lattice because their rapidly decreasing mobility will prevent them from aggregating into disks. This would mean that fewer vacancies would be operative in the disk formation mechanism, so that in spite of the fact that a smaller number of vacancies in the collapsing disk would give rise to a pair of dislocations, the total number of dislocations so formed may not be any greater at the higher growth rates than at the lower growth rates.

## ACKNOWLEDGMENTS

The authors acknowledge the financial assistance of the Research Council of Ontario for scholarships under which this work was carried out, and the National Research Council of Canada for a summer grant. The tin was bought from funds supplied by the School of Engineering Research, University of Toronto.

## REFERENCES

1. CHALMERS, BRUCE. Proc. Roy. Soc. (London), A, 175: 100. 1940.
2. FRANK, F. C. Symposium on plastic deformation. Mellon Institute, Pittsburgh, Pa., May, 1950.
3. TEGHTSOONIAN, E. and CHALMERS, BRUCE. Can. J. Phys. 29: 370. 1951.

# EFFICIENCY OF THE LONG BORON COUNTER FOR FAST NEUTRONS[1]

By S. A. KUSHNERIUK

ABSTRACT

The efficiency of the long boron counter is calculated as a function of the incident neutron energy using the two-group model of neutron diffusion in conjunction with the age and exponential approximations for the slowing down of neutrons. The neutron energies considered are $\leqslant$ 10 Mev. Results are summarized graphically for several counter geometries.

## 1. INTRODUCTION

For certain types of measurements it is advantageous to use detectors whose "efficiency" for neutrons of widely different energies is relatively uniform. One such instrument devised and extensively used is the "long counter" (4, 1, 6).

The essential components of the usual long counter are a cylindrical block of paraffin and a boron trifluoride filled chamber which lies along the axis of the cylinder. The cylindrical block, except for one face, is covered by a thin sheath of cadmium and, in some instances, the complete mechanism is fitted into another paraffin bath (see Fig. 1).

In the application of such a counter a neutron beam is incident on the cadmium-free face of the counter and some of the neutrons are slowed down to "thermal" energies and detected on absorption in the $BF_3$ chamber. The strength of the entrant beam may be obtained from the calibrated efficiency rating. The layer of cadmium and the outer paraffin bath are used in order to minimize the background count, though, in addition, the paraffin bath acts as a "reflector" for the "fast" neutrons originally part of the beam.

It has been felt that a theoretical investigation of the dependence of the efficiency (by our definition, the ratio of the number of neutrons counted per second to the number incident upon the counter per second) of this counter upon the neutron characteristics of the paraffin, upon the geometric factors, as well as upon the absorption potentialities of the chamber medium would serve a useful purpose by providing some basis for monitoring of neutron sources as well as for the design of new counters. Such an investigation is described below.

Our model of the phenomenon is as follows. Since "thermal" neutrons are those primarily absorbed in the $BF_3$ chamber, we classify the neutrons into two groups, the "fast" and "thermal". We then determine the distribution of the fast neutron group using for the source the incident neutron beam. To derive this distribution we neglect the effect of the presence of the $BF_3$ chamber, this effect being small since the volume of the chamber is much less than the total volume of the counter and the chamber is nearly transparent to fast neutrons. The thermal neutron distribution is derived next in the presence

[1] *Manuscript received March 5, 1952.*
*Contribution from the Atomic Energy Project, National Research Council of Canada, Chalk River, Ont. Issued as N.R.C. No. 2789.*
*A preliminary report is contained in Proc. Roy. Soc. Canada (Ser. 3), 45: 197. 1951.*

(the perturbed density) and absence (the unperturbed density) of the $BF_3$ chamber using the fast neutron distribution as the thermal neutron source distribution. The number of thermal neutrons absorbed in the $BF_3$ chamber per unit time may be deduced by evaluating the flow of thermal neutrons into the chamber using the perturbed distribution. Simpler approximations are derived for weakly absorbing chambers by utilizing the unperturbed distributions.

The thermal and fast neutron distributions were both derived in the diffusion approximation only. This approximation is good as far as thermal neutrons are concerned since the geometric dimensions of the counter are large in comparison with the mean free path for neutrons of this energy while for fast neutrons, although this is approximately true for neutrons of the energies considered ($\leqslant$ 10 Mev.), the choice of this approximation is believed to yield the best estimate obtainable in tractable form. Another plausible approach is to use the "age" theory of neutron slowing down (5) to define the thermal source distribution assuming that the primary fast neutrons are a plane $\delta$ source. The age theory approximation has certain limitations, the most serious of which from our point of view are that the resultant Gaussian spatial distribution is valid only up to distances of the order of a slowing down length from the source and that the approximation is worst when the average logarithmic energy loss per collision is greatest, i.e. for hydrogeneous media. The age and exponential theories of neutron slowing down (5) are, however, utilized for estimating the various characteristic lengths involved.

In the instance in which the perturbed neutron distributions are evaluated in detail, our system is idealized to that of a semi-infinite cylindrical block with a semi-infinite $BF_3$ chamber immersed at a depth $d$ from the outer face of the cylinder. This system is representative of most neutron counters that do not contain an outer paraffin bath, in that in most counters the $BF_3$ chambers are so long that a large fraction of the counter is relatively inactive, the depth of penetration of neutrons into the counter being limited by both scattering of neutrons out of the counter and absorption in the $BF_3$ chamber and paraffin.

The relevant approximations to the efficiency are discussed in Section 2, the characteristic lengths involved in Section 3, while in Section 4 the results obtained are summarized.

## 2. THE EFFICIENCY

In the diffusion approximation, the steady state neutron density distribution $\rho(\mathbf{r})$ is a solution of the conservation equation (in the absence of multiplication)

$$\operatorname{div} \mathbf{j}(\mathbf{r}) + \frac{1}{\tau}\rho(\mathbf{r}) = q(\mathbf{r}) \tag{2.1}$$

where $\mathbf{j}(\mathbf{r})$ is the neutron current density, $\tau$ is the mean life of the neutron, $q(\mathbf{r})$ represents the distributed source strength. It is assumed further that

$$\mathbf{j}(\mathbf{r}) = -D\,\mathbf{grad}\,\rho(\mathbf{r}) \tag{2.2}$$

in which $D$, the diffusion coefficient, is related to the second spatial moment of the

neutron distribution in an infinite medium due to a plane source of neutrons, viz.

$$L^2 = D\tau = \frac{Z^2_{\text{av}}}{2} \approx \frac{l_{\text{tr}} v \tau}{3}. \tag{2.3}$$

In the above $l_{\text{tr}}$ is the transport mean free path, $v$ is the neutron velocity.

The solutions of (2.1) are also subject to a set of boundary conditions. These are of the usual form. We assume that the densities and currents are continuous across the interface of two scattering media and that the densities vanish at a "free" surface. ( A free surface is one at which no neutrons return once they have left the system. Actually, from transport theory considerations, it is known that the correct condition to apply on the diffusion approximation to the density is the vanishing of the density at a distance of the order of a transport mean free path beyond the free surface.)

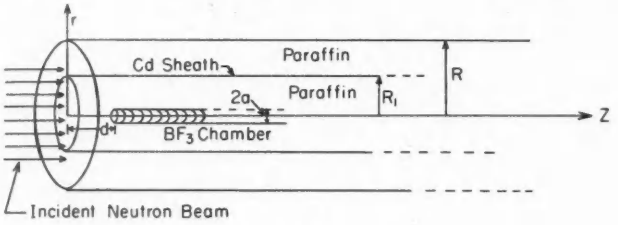


FIG. 1. The long counter.

We derive now the fast neutron distribution. Let $p$ be the current density of neutrons of energy $E$ incident at the face $z = 0$. Then the distributed fast neutron source density is

$$q(r, z) = \frac{p}{l} e^{-z/l} = y\, e^{-z/l} \tag{2.4}$$

where $l$ is the mean free path for neutrons of energy $E$ in the paraffin. The fast neutron density satisfying the correct boundary conditions (if the effects of the $BF_3$ chamber are ignored) may be expressed as

$$\rho_f(r, z) = \sum_{m=1}^{\infty} \chi_m \rho_m(z) J_0\left(\frac{j_{0m}}{R} r\right) \tag{2.5}$$

where $j_{0m}$ are the roots of the equation $J_0(x) = 0$,

$$\chi_m = 2y\tau_f / j_{0m} J_1(j_{0m}) [\beta_m{}^2 - 1/l^2] L_s{}^2, \tag{2.6}$$

$$\rho_m(z) = e^{-\beta_m z} - e^{-z/l}, \tag{2.7}$$

and

$$\beta_m{}^2 = j_{0m}{}^2/R^2 + 1/L_s{}^2. \tag{2.8}$$

The thermal neutron distribution is then a solution of the equation

$$\left(\nabla^2 - \frac{1}{L^2}\right)\rho_t(r, z) = -\frac{\tau}{L^2\tau_f}\rho_f(r, z). \tag{2.9}$$

Since cadmium is black to thermal neutrons, we now assume that the density vanishes at $r = R_1$. The unperturbed neutron distribution (i.e. the density in the absence of the $BF_3$ chamber) is given by

$$\rho_t(r, z) = \sum_{m,s=1}^{\infty} \chi_m' \pi_{sm} J_0\left(\frac{j_{0s}}{R_1} r\right) \rho_{ms}(z) \tag{2.10}$$

in which

$$\chi_m' = \chi_m / L^2\tau_f, \tag{2.11}$$

$$\pi_{sm} = 2j_{0s} J_0\left(\frac{j_{0m}}{R} R_1\right) \Big/ \left(j_{0s}^2 - j_{0m}^2 \frac{R_1^2}{R^2}\right) J_1(j_{0s}), \tag{2.12}$$

$$\rho_{ms}(z) = \frac{e^{-\mu_s z} - e^{-\beta_m z}}{\mu_s^2 - \beta_m^2} - \frac{e^{-\mu_s z} - e^{-z/l}}{\mu_s^2 - 1/l^2}, \tag{2.13}$$

and

$$\mu_s^2 = j_{0s}^2/R_1^2 + 1/L^2. \tag{2.14}$$

In the absence of the outer paraffin bath, i.e. $R_1 = R$, (2.10) reduces to

$$\rho_t(r, z) = \sum_{m=1}^{\infty} \chi_m' J_0\left(\frac{j_{0m}}{R} r\right) \rho_{mm}(z). \tag{2.15}$$

The perturbed thermal distribution (i.e. the density in the presence of the $BF_3$ chamber) has been estimated only in the absence of the outer paraffin bath, i.e. $R_1 = R$. We shall not give the explicit forms of the solutions but quote directly the formulae for the efficiency as computed according to this model. The efficiency, which by definition is

$$\text{Eff} = \frac{\int_d^\infty 2\pi a \times (\text{current density into the } BF_3 \text{ chamber})\, dz}{\pi R^2 l y}$$

$$= \frac{2aD_t}{R^2 l y} \sum_{s=1}^{\infty} (\psi_s'(a)/\alpha_s) \sum_{m=1}^{\infty} p_{sm} \tag{2.16}$$

where

$$p_{sm} = \mu_m \theta_{sm} \chi_m' \left\{ \frac{1/l^2 - \beta_m^2}{(\mu_m^2 - \beta_m^2)(1/l^2 - \mu_m^2)} + \right.$$

$$+ \cosh \mu_m d \left[ \frac{l(\mu_m^2 + \alpha_s/l)e^{-d/l}}{(\mu_m^2 - 1/l^2)(\alpha_s + 1/l)} - \frac{(\mu_m^2 + \alpha_s\beta_m)e^{-\beta_m d}}{\beta_m(\mu_m^2 - \beta_m^2)(\beta_m + \alpha_s)} \right] \tag{2.17}$$

$$\left. + \sinh \mu_m d \left[ \frac{l\mu_m e^{-d/l}}{\mu_m^2 - 1/l^2} - \frac{\mu_m e^{-\mu_m d}}{\beta_m(\mu_m^2 - \beta_m^2)} \right] \right\} \{\mu_m \cosh \mu_m d + \alpha_s \sinh \mu_m d\}^{-1},$$

$$\theta_{sm} = \int_a^R r\psi_s(r)\, J_0\left(\frac{j_{0m}}{R} r\right) dr \Big/ \int_a^R r\psi_s^2(r)\, dr, \tag{2.18}$$

and $\psi_s(r)$ are a set of functions, orthogonal in the range $a$ to $R$,

$$\psi_s(r) = J_0(\nu_s r) - \frac{J_0(\nu_s R)}{Y_0(\nu_s R)} Y_0(\nu_s r) \tag{2.19}$$

in which $\nu_s$ are the roots of the equation

$$\lambda\nu = \frac{J_0(\nu R)\,Y_0(\nu a) - J_0(\nu a)\,Y_0(\nu R)}{J_1(\nu a)\,Y_0(\nu R) - J_0(\nu R)\,Y_1(\nu a)}. \tag{2.20}$$

Also in (2.16)

$$\alpha_s^2 = \nu_s^2 + 1/L^2 \tag{2.21}$$

and

$$\psi_s'(a) = \frac{d\psi_s(r)}{dr} \text{ (at } r = a).$$

The parameter $\lambda$ appearing in (2.20) is the inverse logarithmic derivative of the density taken at the $BF_3$ chamber – paraffin interface. The details regarding the estimation of $\lambda$ are given in Section 3. In the limit as $d \to 0$, i.e. the $BF_3$ chamber extends to the face of the paraffin, (2.17) reduces to

$$p_{sm} = \theta_{sm}\chi_m' \left\{ \frac{l}{(\alpha_s + 1/l)} - \frac{1}{\beta_m(\beta_m + \alpha_s)} \right\}. \tag{2.22}$$

If the $BF_3$ chamber is weakly absorbing one would expect that its influence upon the thermal density distribution is small (provided its lateral dimensions are also small). In this case the number of neutrons absorbed in the chamber per unit time may be approximated by calculating the mass absorption on the basis of the unperturbed density and correcting for the depression of this density. The efficiency then becomes (using (2.10))

$$\text{Eff} = \frac{4a}{\lambda l R_1^2 L_s^2} f(a, L, \lambda, R_1) \sum_{m=1}^{\infty} t_m \sum_{s=1}^{\infty} r_{ms} J_0\left(\frac{j_{0s}}{R_1} a\right) \tag{2.23}$$

with

$$t_m = 1/j_{0m}\, J_1(j_{0m}), \tag{2.24}$$

$$r_{ms} = \pi_{sm}[(\mu_s^2 - \beta_m^2)(\mu_s^2 - 1/l^2)]^{-1} \left\{ \frac{e^{-\mu_s d}}{\mu_s} - \frac{(\mu_s^2 - 1/l^2)e^{-\beta_m d}}{\beta_m(\beta_m^2 - 1/l^2)} + \frac{l(\mu_s^2 - \beta_m^2)e^{-d/l}}{\beta_m^2 - 1/l^2} \right\} \tag{2.25}$$

while the depression factor $f(a, L, \lambda, R_1)$ is readily estimated to be

$$f(a, L, \lambda, R_1) \approx \left[ \frac{a}{\lambda} K_0\left(\frac{a}{L}\right) + \frac{a}{L} K_1\left(\frac{a}{L}\right) \right]^{-1}, \qquad R_1 \gg L. \tag{2.26}$$

When $R_1 \equiv R$, these formulae reduce to

$$\text{Eff} = \frac{4aL^2}{\lambda l R^2 (L_s^2 - L^2)} f(a, L, \lambda, R) \sum_{m=1}^{\infty} r_m t_m J_0\left(\frac{j_{0m}}{R} a\right) \tag{2.27}$$

where now

$$r_m = \left\{\frac{1}{\mu_m} e^{-\mu_m d} - \frac{\mu_m^2 - 1/l^2}{\beta_m(\beta_m^2 - 1/l^2)} e^{-\beta_m d} + \frac{l(L_s^2 - L^2)}{L^2 L_s^2(\beta_m^2 - 1/l^2)} e^{-d/l}\right\}(\mu_m^2 - 1/l^2)^{-1}. \tag{2.28}$$

## 3. THE CHARACTERISTIC LENGTHS $L$, $L_s$, $l$, $l_{tr}$; THE EXTRAPOLATION LENGTH $\lambda$; AND THE ROOTS $\nu_s$

It is to be noted that the efficiency, defined in the preceding section, is a function of the geometric constants $a, R, R_1, d$; the neutron characteristics of the paraffin medium $l(E), L, L_s(E), l_{tr}$; and the extrapolation length for the thermal neutron distribution, $\lambda$, at the $BF_3$–paraffin interface.

The diffusion length $L$ and the transport mean free path $l_{tr}$ for thermal neutrons in paraffin have been measured experimentally (7) and are $L = 2.42$ cm., $l_{tr} = 0.39$ cm. There is, however, only limited data for the value of the slowing down length $L_s$ in paraffin as a function of the source neutron energy. These are therefore estimated theoretically using the known scattering cross sections for carbon and hydrogen (3).

Various models that one might adopt for computing $L_s(E)$ and the practical range of validity of each model have been discussed by R. E. Marshak (5). For hydrogeneous materials the exponential theory (in which the mean free path of the neutrons is approximated to by a sum of exponentials) is the most satisfactory. The simplest theory for media which are mixtures of different nuclei is the age theory (in which the fundamental assumption is that the neutrons lose energy continuously in such a manner that to any given age there corresponds a definite value of the energy) but the approximations on the basis of this theory are worst when the average logarithmic energy loss per collision is greatest, i.e. for hydrogen.

We have computed $L_s$ in paraffin using the age theory and correcting for the model by the relationship

$$L_s(\text{P, corrected}) \approx \frac{L_s(\text{P, age})}{L_s(\text{H, age})} L_s(\text{H, Exp.}). \tag{3.1}$$

The basis for the correction lies in the fact that, within the energy range considered, a good first approximation to $L_s(\text{P})$ is

$$L_s(\text{P}) \approx \overline{l_\text{P}/l_\text{H}}\, L_s(\text{H}) \tag{3.2}$$

where in (3.2) $\overline{l_\text{P}/l_\text{H}}$ is the ratio of the mean free path in paraffin to the mean free path in hydrogen averaged over the complete slowing down energy range. Plots of the characteristic lengths $l(E)$ and $L_s(E)$ are given in Figs. 2 and 3.

In the evaluation of $L_s$, inelastic collisions have been neglected. Part of the data for $L_s(\text{H, Exp.})$ were taken over from Table VIII, p. 236 of Marshak's paper (5).

In the application of these results to our problem we must take into consideration a further factor and this is that our fast neutron source consists of

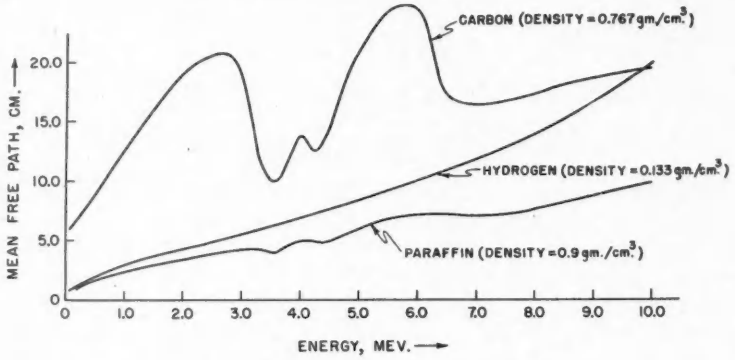


FIG. 2. Mean free paths as a function of the energy.

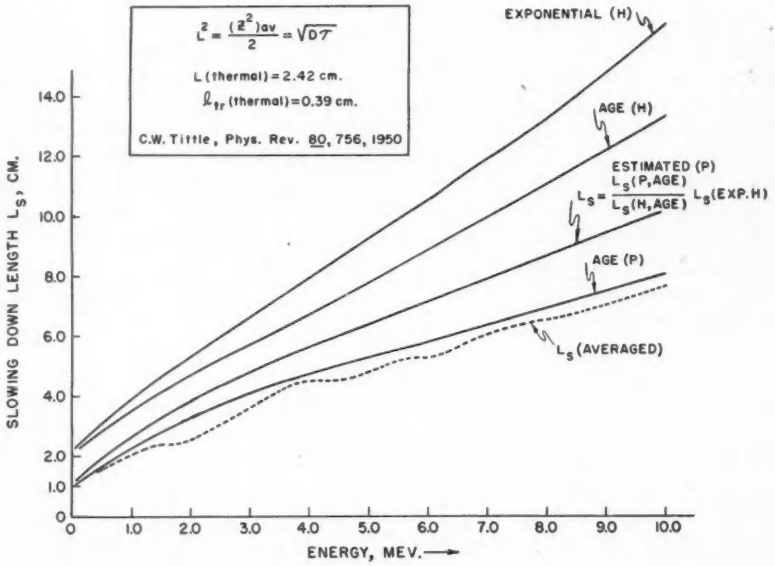


FIG. 3. The slowing down length $L_s$ as a function of the initial neutron energy. The hydrogen and paraffin densities are as indicated in Fig. 2.

those neutrons in the beam that have suffered a single collision with paraffin nuclei. We therefore average $L_s(E)$ over the resultant energy spectrum. The probability that a neutron, initially with energy $E$, lies in the energy interval $E'$ and $E' + dE'$ after its first collision in a mixture is given by

$$p(E')\,dE' = \sum_k c_k(E)\, f_k(E')\,dE' \tag{3.3}$$

where $f_k(E')dE'$ is the probability that a neutron be in this range on collision with a nucleus of type $k$, $c_k$ is the relative probability of such a collision. Assuming isotropic scattering in the center of mass system

$$f_k(E')\,dE' = \frac{1}{E}\frac{(1+M_k)^2}{4M_k}\,dE'$$

in which $M_k$ is the mass of the nucleus of type $k$. In our case then

$$L_s(E) = \int_{E\min}^{E} p(E')\,L_s(E')\,dE' \tag{3.4}$$

$$= c_{\mathrm{H}}(E)\,\frac{1}{E}\int_{E_t}^{E} L_s(E')\,dE' + c_{\mathrm{C}}(E)\,\frac{1}{1-p}\,\frac{1}{E}\int_{pE}^{E} L_s(E')\,dE'. \tag{3.5}$$

The first term in (3.5) is the average over those neutrons that collide with the H nucleus, $p$ is $p = \dfrac{Mc-1}{(1+Mc)^2} \approx 0.72$. The values of $L_s(E)$ computed according to (3.5) are plotted as the dotted curve in Fig. 3.

We turn now to the evaluation of $\lambda$. A typical chamber filling is 60 cm. of $BF_3$, 96% of the boron being $B^{10}$. Using a cross section of 711 barns for natural boron, 18.6% of which is $B^{10}$, we find that the capture mean free path in the chamber gas is $l_c = 13.7$ cm. This value is large compared with the lateral extent of the $BF_3$ chamber ($\approx 1.3$ cm. diameter) and indicates that absorption is relatively weak. For weak absorbers and, particularly, small volumes of absorbing material we can make the assumption that the flow of neutrons into the absorber is equal to the mass absorption with the flux in the absorber approximated to by the flux at the surface of the absorber, i.e. per unit length of the chamber

$$2\pi a\, D_t\, \rho_t'(r)]_{r=a} \approx \pi a^2\, \rho_t(a)\, v_t(N\sigma_c). \tag{3.6}$$

Then

$$\lambda = \frac{\rho_t(a)}{\rho_t'(a)} \approx \frac{2l_{\mathrm{tr}}l_c}{3a}. \tag{3.7}$$

For $a = 0.65$ cm., $l_{\mathrm{tr}} = 0.39$ cm., $l_c = 13.7$ cm., $\lambda = 5.5$ cm.

The capture mean free path is inversely proportional to the gas pressure. Formula (3.7) should be approximately valid for pressures up to the order of two to three standard pressures ($l_c$ varies from 5.4 cm. to 3.6 cm. in this pressure range). For $l_c \backsim 0.5$ cm. and less, approximate values of $\lambda$ may be obtained from a set of transport theory calculations (2). For a chamber black to thermal neutrons and $a = 0.65$ cm., $l_{\mathrm{tr}} = 0.39$ cm., $\lambda = 0.40$ cm.

The roots of equation (2.23) have been evaluated for two values of $\lambda$ with $a = 0.65$ cm., $R_1 = 12$ cm. These are

$\lambda = 0.4$ cm.; $\nu_1 = 0.250$ cm.$^{-1}$, $\nu_2 = 0.520$ cm.$^{-1}$, $\nu_3 = 0.795$ cm.$^{-1}$, $\nu_4 = 1.076$ cm.$^{-1}$;

$\lambda = 5.5$ cm.; $\nu_1 = 0.221$ cm.$^{-1}$, $\nu_2 = 0.476$ cm.$^{-1}$, $\nu_3 = 0.745$ cm.$^{-1}$, $\nu_4 = 1.013$ cm.$^{-1}$

## 4. DISCUSSION OF THE RESULTS

The efficiency ratings as computed on the basis of formulae quoted in Section 3 and the neutron characteristics of the paraffin medium as summarized in Figs. 2 and 3 are plotted in Fig. 4 as functions of the energy of the incident neutrons,

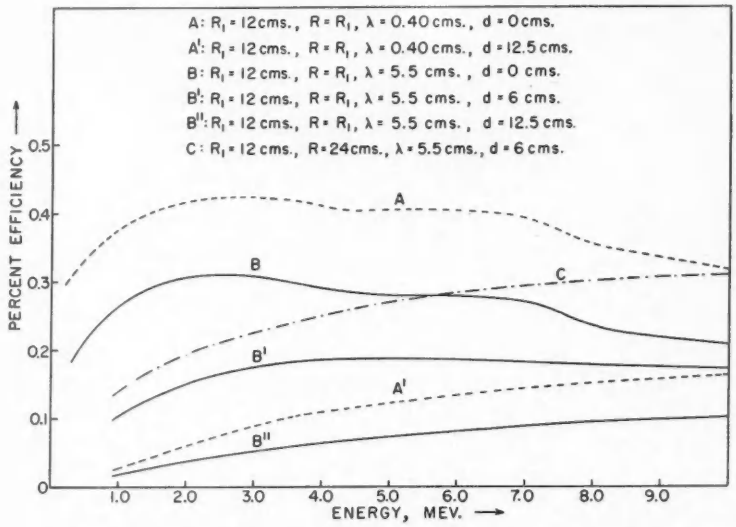
A: $R_1$ = 12 cms., R = $R_1$, λ = 0.40 cms., d = 0 cms.
A': $R_1$ = 12 cms., R = $R_1$, λ = 0.40 cms., d = 12.5 cms.
B: $R_1$ = 12 cms., R = $R_1$, λ = 5.5 cms., d = 0 cms.
B': $R_1$ = 12 cms., R = $R_1$, λ = 5.5 cms., d = 6 cms.
B'': $R_1$ = 12 cms., R = $R_1$, λ = 5.5 cms., d = 12.5 cms.
C: $R_1$ = 12 cms., R = 24 cms., λ = 5.5 cms., d = 6 cms.
PERCENT EFFICIENCY
0
0.1
0.2
0.3
0.4
0.5
A
B
C
B'
A'
B''
1.0
2.0
3.0
4.0
5.0
6.0
7.0
8.0
9.0
ENERGY, MEV.

FIG. 4. Per cent efficiency as a function of the incident neutron energy.

the geometric configurations of the counter, and the absorption capabilities of the $BF_3$ chamber. Three fundamentally different types of systems were considered, type *A* in which the $BF_3$ chamber was assumed black to thermal neutrons (i.e. $\lambda = 0.40$ cm.), type *B* in which the $BF_3$ chamber contains approximately 60 cm. of $BF_3$, 96% of the boron being $B^{10}$, and type *C* which contained a $BF_3$ chamber similar to that of type *B* but in addition was surrounded by an outer paraffin bath 12 cm. in thickness. In each instance the radius of the $BF_3$ chamber was assumed to be 0.65 cm. The label *d* designates the depth of immersion of the $BF_3$ chamber from the face of the counter.

Comparison of the curves *B*, *B'*, and *B''* gives a fair appreciation of the dependence of the efficiency upon the depth of immersion, *d*, of the $BF_3$ chamber from the face of the counter; in particular it is evident that for a properly chosen *d* a fairly constant efficiency may be achieved over a wide range of energies. Comparison of curves *B'* and *C* gives some indication of the effect of the outer paraffin bath upon the efficiency and the variation of this effect with the energy of the incident beam. Similarily comparison of curves *B* and *A*, *B''* and *A'* indicates what effect one might achieve by increasing the absorption potentialities of the $BF_3$ chamber.

The results given in Fig. 4 which refer to weakly absorbing chambers (i.e. curves *B* and *C*) may be extended to chambers whose radii differ and which contain different pressures of $BF_3$. Thus for fixed $R_1$ and $d$ the efficiency of a chamber whose radius is $a$ cm. and which contains $y$ cm. of $BF_3$($z$% $B^{10}$) is approximately

$$\text{Eff} \approx \text{Eff(Fig. 4)} \times \left(\frac{a}{0.65}\right)^2 \times \frac{y}{60} \times \frac{z}{96}.$$

The dependence of the efficiency on $R_1$, the counter radius, is more complex. For incident neutron energies of $\backsim$ 3 Mev. and for small deviations from the 12 cm. radius used in computing the results of Fig. 4 an approximate correction is $(R_1/12)^{\frac{1}{2}}$.

A comparison of the theoretical prediction for the efficiency is made with one of the experimental results quoted in Hanson and McKibben's article (4). They state that the absolute sensitivity of a counter with 25 cm. $BF_3$(80%$B^{10}$) and a chamber radius of 1 in., counter radius of 4 in., is one count for every $10^5$ neutrons emitted by the source. The source was essentially a point source and the counter face was located at a distance of 1 meter from it. The experimental efficiency rating is then $\approx$ 0.4%. The active area of the $BF_3$ chamber extended to the face of the counter and the neutron energy was $\approx$ 2.5 Mev. Using result *B*, Fig. 4, and applying corrections outlined above we arrive at the value

$$\text{Eff} = 0.32 \times \left(\frac{1.27}{0.65}\right)^2 \times \frac{80}{96} \times \frac{25}{60} \times \left(\frac{10}{12}\right)^{\frac{1}{2}} = 0.39\%.$$

## REFERENCES

1. Crews, R. W. Phys. Rev. 82: 100. 1951.
2. Davison, B. Proc. Phys. Soc. (London), A, 64: 881. 1951.
3. Goldsmith, H. H., Ibser, H. W., and Fell, H. T. The science and engineering of nuclear power. Addison-Wesley Press Inc., Cambridge, Mass. 1948.
4. Hanson, A. O. and McKibben, J. L. Phys. Rev. 72: 673. 1947.
5. Marshak, R. E. Revs. Modern Phys. 19: 185. 1947.
6. Russel, B., Sacks, D., and Wattenberg, A. Argonne National Laboratory Report, MDDC-1431.
7. Tittle, C. W. Phys. Rev. 80: 756. 1950.

# SUPERLATTICE STUDIES IN THE SYSTEMS SILVER–MAGNESIUM–TIN AND SILVER–MAGNESIUM–ZINC[1]

By W. G. Henry[2] and G. V. Raynor

ABSTRACT

The 3/2 electron compound in the system silver–magnesium, in which tin and zinc are soluble, has an ordered structure of the cesium chloride type (second zone superlattice). The first additions of tin to this phase do not affect the ordered structure. Above a certain limit, a third zone superlattice is formed, and the tin atoms themselves occupy ordered positions. X-ray examination at high temperatures shows that the third zone superlattice disorders independently of the main, second zone superlattice. The transformation temperature increases with increasing tin content; that of the cesium chloride superlattice, however, decreases with increasing tin content. In the silver–magnesium–zinc system, the introduction of zinc into the binary silver–magnesium 3/2 electron compound causes no development of a third zone superlattice. The temperature at which the second zone superlattice disorders decreases with increasing zinc content.

It is suggested that the reason for the existence of the second superlattice depends upon a combination of the following factors:

(i) The lattice distortion due to the high valency of tin creates a long-range distortion which is more easily distributed, leading to a minimum interaction strain energy, by the formation of a doubly ordered structure.

(ii) The electrochemical effect between magnesium and tin atoms at a distance "*a*" apart (where "*a*" is the lattice spacing of the body-centered cubic cell) contributes to the lowered free energy of a doubly ordered structure.

## INTRODUCTION

The constitutions of the silver-rich silver–magnesium–tin and silver–magnesium–zinc alloys have been described previously (5, 6). In the course of work on these systems, interesting examples of the formation of ordered structures in ternary alloys were encountered.

In the system silver–magnesium, the electron compound ($\beta'$), which has an electron:atom ratio of 3/2, possesses a crystal structure of the ordered body-centered cubic or cesium chloride type. If sufficient tin is added to the $\beta'$ phase, an additional ordering of the atoms occurs. The phase persists to a maximum of 10 atomic per cent of tin; beyond this tin content a two-phase region exists between the doubly-ordered body-centered cubic phase and the hexagonal 3/2 electron compound $Ag_5Sn$, in which some of the tin atoms have been replaced by magnesium atoms.

The addition of zinc to the silver–magnesium $\beta'$ phase causes no additional ordering. It has been observed that, in slowly cooled specimens, the ordered cesium chloride structure of $\beta'$ exists even at very high zinc concentrations.

From an analysis of X-ray powder photographs of quenched alloys (5), it has been shown that the crystal structure of the doubly ordered $\beta'$ phase in the silver–magnesium–tin system is similar to that of $Fe_3Al$. The structure observed may be considered in terms of four interpenetrating face-centered cubic lattices

[1] *Manuscript received April 8, 1952.*
*Contribution from the Department of Metallurgy, University of Birmingham, Birmingham, England.*

[2] *Present address: Division of Applied Chemistry, National Research Council of Canada, Ottawa, Ontario.*

(Fig. 1), with a lattice spacing twice that of the simple body-centered unit cell; the distribution of atoms is indicated in Fig. 2. Silver atoms occupy sites 1 and 2,

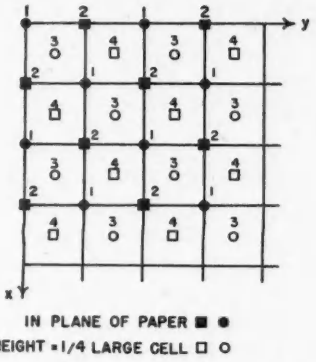


FIG. 1. Four interpenetrating face-centered cubic lattices.

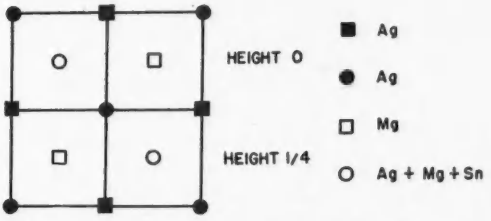


FIG. 2. Unit cell of ternary Ag–Mg–Sn 3/2 electron compound.

while magnesium atoms occupy site 3. All the tin atoms, plus the extra magnesium and silver atoms not accommodated in the sites 1, 2, and 3, are placed in site 4.*

These observations, and comparison with the silver–magnesium–zinc system, stimulated an investigation into the dependence of the stability of the ternary superlattice on composition and temperature. From the results obtained, it has been possible to discuss the effect of metallurgical factors associated with zinc and tin on the internal energies of the ordered ternary phases.

## EXPERIMENTAL METHODS

### (i) *Preparation of Alloys*

The alloys employed were prepared from pure materials, details of which are given in Appendix I; analyzed compositions are summarized in Appendix II. Alloys were made by melting together, under a potassium chloride flux, weighed

**In the previous work (5) intensity calculations were carried out for an alloy of composition 60 at.% silver, 33 at.% magnesium, and 7 at.% tin. Since sites 1 and 2 will together accommodate only 50% of the atoms present, and site 3 only 25%, site 4 must be considered to contain a random mixture of the 10% silver, 8% magnesium, and 7% tin otherwise unaccounted for.*

amounts of the pure components; after stirring with a sintered alumina rod, the melts were cast into chilled copper molds. The resulting ingots were homogenized by annealing at 550°C. for seven days *in vacuo*, and quenched in water.

(ii) *X-ray Technique*

High temperature X-ray diffraction techniques provide a convenient method of investigation of superlattice transformations; they were therefore used in the present work. Since the alloys under consideration oxidize at high temperatures, filings prepared from the alloys and screened to pass 100 mesh were enclosed in evacuated silica tubes of diameter 0.5 mm. and of wall thickness approximately 0.01 mm. Such specimens were satisfactory up to 575°C. but difficulty was experienced above this temperature owing to attack of the silica by magnesium. This difficulty increased with temperature; the results for the high temperature region of the silver–magnesium–zinc system were thus incomplete. The methods adopted for manipulation and temperature calibration of the Unicam high-temperature Debye-Scherrer camera in which specimens were exposed have been previously described (1). In the present experiments, the temperature calibration employed pure silver as a standard substance. The lattice spacings of silver filings, contained in an evacuated silica capillary, were measured for various readings of the e.m.f. of a rigidly fixed platinum/platinum–rhodium thermocouple whose tip projected into the heated zone of the camera. From the lattice spacing/temperature data published by Hume-Rothery and Reynolds (3), the specimen temperature relative to that indicated by the fixed thermocouple was deduced. It is estimated that the specimen temperatures quoted in this paper are correct to within ±2°C. All specimens were annealed at the chosen temperature for one half-hour before exposure; longer annealing periods up to four hours made no apparent difference to the diffraction patterns obtained. Throughout annealing periods and exposures the camera temperature was constant within ±1°C. Copper $K\alpha$ radiation was used, and the wave lengths assumed were: $K\alpha_1 = 1.537395\ kX$, $K\alpha_2 = 1.541232\ kX$. The presence of ordering in the specimens was revealed by the occurrence of characteristic diffraction lines. Lattice spacing measurements were made, and in order to check the constancy of composition of the specimen, room-temperature lattice spacing measurements were carried out in between the high temperature experiments. Occasionally these measurements indicated that small composition changes had occurred. For the lattice spacing measurements an estimated accuracy of ± 0.00015 $kX$ was obtained.

## EXPERIMENTAL RESULTS

The third zone superlattice* in the silver–magnesium–tin system has been described above (Figs. 1 and 2); the corresponding diffraction lines are listed by Raynor and Frost (5). For reference purposes the low angle reflections observed for a doubly ordered alloy are given in Table I. Fig. 3 shows the compositions of the alloys investigated in relation to the boundaries of the $\beta'$ field at 450°C.; the broken line indicates a constant electron:atom ratio of 1.5.

**The nomenclature used is that of Hume-Rothery and Powell (2).*

TABLE I

LOW ANGLE REFLECTIONS FOR THE DOUBLY ORDERED STRUCTURE

| Line $h^2+k^2+l^2$ | Indices $(h,k,l)$ | Intensity | Classification |
|---|---|---|---|
| 3 | (1,1,1) | Very faint | 3rd zone |
| 4 | (2,0,0) | Faint | 2nd zone |
| 8 | (2,2,0) | Very strong | b.c.c. line (1,1,0) |
| 11 | (3,1,1) | Faint | 3rd zone |
| 12 | (2,2,2) | Faint | 2nd zone |
| 16 | (4,0,0) | Medium | b.c.c. line (2,0,0) |

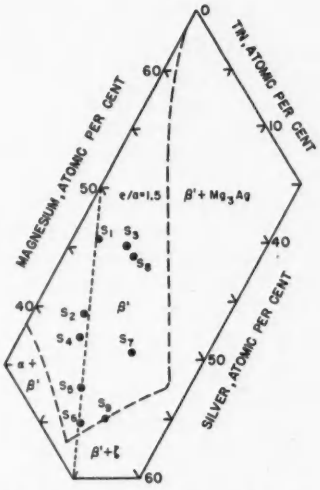


FIG. 3. Compositions of alloys examined—system silver–magnesium–tin.

Visual estimates of the temperature variation of the relative intensities of the first six lines, for the three representative alloys *S*3, *S*5, and *S*7, are summarized in Table II.

The addition of a small amount of tin to the binary $\beta'$ superlattice (alloy *S*3) therefore has little effect on the structure; the second zone superlattice remains stable at least up to 675°C. Further tin additions cause the appearance of the third zone superlattice, which, in the alloy containing 6.8 at.% tin, is stable up to a temperature between 375° and 415°C.; in this temperature range it disorders independently of the second zone superlattice, the diffraction lines of which remain in existence at least up to 450°C. At higher concentrations of tin (9.1 at. %) the third zone superlattice becomes more stable and does not disorder until a temperature of 525° to 550°C. is reached; the second zone superlattice is intact at 550°C. At this high tin content the second zone superlattice breaks

TABLE II

SILVER–MAGNESIUM–TIN SYSTEM

| Indices | Specimen | | | | | | | | | | | | | |
|---|---|---|---|---|---|---|---|---|---|---|---|---|---|---|
| | *S*3 (4.2% Sn) | | *S*5 (6.8% Sn) | | | | | | *S*7 (9.1% Sn) | | | | | |
| | Temperature, °C. | | | | | | | | | | | | | |
| | RT. | 675 | RT. | 325 | 350 | 375 | 415 | 450 | RT. | 475 | 500 | 525 | 550 | 615* |
| (1,1,1) | — | — | VF | VF | VF | VF | — | — | VF | VF | VF | — | — | — |
| (2,0,0) | M | M | M | M | M | M | M | M | M | M | M | M | M | — |
| (2,2,0) | S | S | S | S | S | S | S | S | S | S | S | S | S | S |
| (3,1,1) | — | — | F | F | F | F | — | — | F | F | F | — | — | — |
| (2,2,2) | M | M | F | F | F | F | F | F | F | F | F | F | F | — |
| (4,0,0) | MS | MS | MS | MS | MS | MS | MS | MS | MS | MS | MS | MS | MS | S |

S = strong; M = medium; F = faint; VF = very faint.

**Although this film was excellent, room temperature lattice spacing checks indicated that a small composition change had occurred at the exposure temperature.*

down below the melting point of the ternary $\beta'$ phase, and disorders between 550° and 615°C.

The lattice spacings of these alloys, referred to the side of the small body-centered cubic cell, are plotted against the corresponding temperature in Figs. 4, 5, and 6. The curve for alloy *S*3 is smooth and shows no indication of any discontinuity, in agreement with the fact that the structure remains unaltered over the temperature range investigated. Figs. 5 and 6, however, indicate a

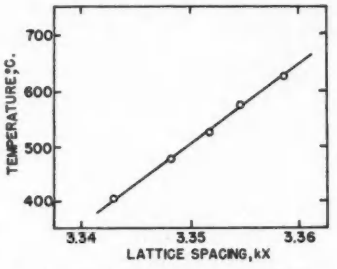


FIG. 4. Lattice spacing/temperature relations, alloy *S*3.

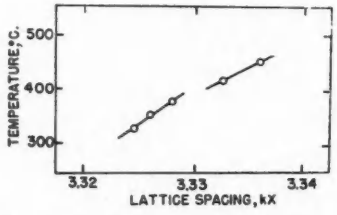


FIG. 5. Lattice spacing/temperature relations, alloy *S*5.

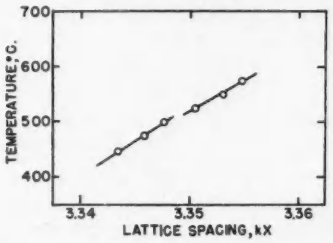


FIG. 6. Lattice spacing/temperature relations, alloy *S7*.

change in the coefficient of thermal expansion in the temperature ranges corresponding to destruction of the third zone superlattice. The existence of these anomalies confirms the results of the visual examination of films.

Owing to the volatility of zinc, high-temperature experiments on the silver–magnesium–zinc alloys were incomplete, but interesting results were obtained. Four alloys were investigated, with silver contents of 50 at. % and zinc contents of 10, 20, 30, and 40 at. %. In no case was the development of a third zone superlattice detected. The results obtained from high-temperature X-ray work are summarized in Fig. 7. The replacement of magnesium in the binary $\beta'$ phase by zinc decreases the stability of the second zone superlattice, as indicated by the transformation temperatures; it was unfortunately impossible to obtain good results above 575°C.

X-ray investigation of the two systems thus shows that the addition of tin to the binary silver–magnesium $\beta'$ phase causes the development of a third zone superlattice which increases in stability with rising tin content and disorders independently of the second zone superlattice already present. Zinc does not cause the development of a third zone superlattice, but merely decreases the temperature at which the second zone superlattice disorders. In this respect its influence is similar to that of tin.

Although it is possible in principle to determine transformation temperatures by repeated high-temperature X-ray experiments, the procedure is tedious. It

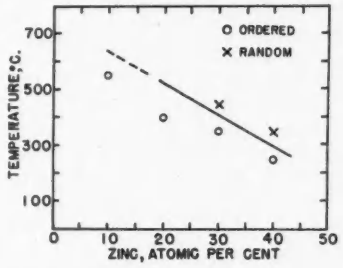


FIG. 7. Variation of the transformation temperature in the silver–magnesium–zinc system, at 50 atomic per cent of silver.

was considered preferable to attempt detailed investigation of transformation temperatures by thermal analysis. An apparatus employing a differential thermocouple was therefore constructed. A copper cradle at the center of a vertical tube furnace supported two identical closed graphite crucibles; one crucible contained the homogenized experimental alloy and the other a copper specimen of the same dimensions. Opposed alumel–chromel thermocouples were spot welded into the bases of small holes in the specimens, any temperature difference between which was indicated by a mirror galvanometer. Alloy specimens were heated above the liquidus to allow the establishment of good thermal contact between specimen and thermocouple and annealed for one hour at a temperature slightly below the solidus. Observations were made while the system was cooled at a uniform rate of 5°C. per minute, and reheated at the same rate. During sensitivity tests of the apparatus, using a specimen of $\beta$-brass, a well marked transformation was observed at 470°C., in good agreement with the value of 467°C. given by Sykes and Wilkinson (7). Experiments with silver–

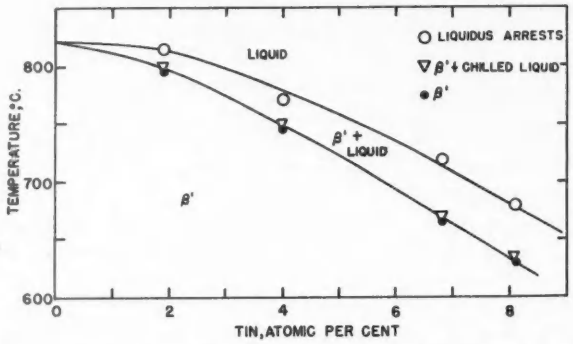


FIG. 8. Liquidus and solidus curves along a line of constant electron:atom ratio 1.5—system silver–magnesium–tin.

magnesium–tin alloys in the temperature ranges critical for the third zone superlattice change, however, indicated no thermal effects. The transformation thus cannot be accompanied by a large heat effect, and the rate of change is probably low. The thermal analysis experiments, however, made it possible to examine the melting and freezing points of the alloys of electron:atom ratio 1.5. Well marked solidus arrests were not obtained because of the existence of the second zone superlattice; except at high tin contents heating curves showed an absorption of heat due to disordering in addition to the latent heat at the solidus temperature, and it was impossible to locate accurately the point at which the solidus occurred. The freezing point results are shown in Fig. 8; the solidus curve also shown was determined metallographically.

## DISCUSSION

The occurrence of a third zone superlattice in the silver–magnesium–tin system, but not in the silver–magnesium–zinc system, probably depends on the following factors:

(i) The lattice distortion due to the high valency of tin may be more easily distributed in an ordered structure.

(ii) The electrochemical interaction between magnesium and tin atoms in sites 3 and 4 (Fig. 2) may contribute to the lowering of the free energy in the ordered state. When a second metal goes into solid solution in a given solvent the resulting mean lattice distortion may be regarded as the resultant of two factors, one due to the difference in atomic size of the components, and the other due to their valency difference (4). Four-valent tin (atomic diameter 2.797 Å) expands the lattice of silver (atomic diameter 2.883 Å) in spite of its smaller atomic size. The silver–magnesium $\beta'$ phase is particularly stable because of the strong electrochemical interaction between silver and magnesium and because of the relatively small lattice distortion due to the unit valency difference between the components. As tin is added, magnesium atoms are replaced by four-valent tin atoms, which form isolated, severely distorted body-centered cells of the cesium chloride type. It is reasonable to expect that at high tin concentrations the severely distorted cells will tend to avoid each other, forming an ordered structure. In this way the strain energy of interaction of neighboring distorted cells is minimized at the lower temperatures. Since the interaction strain energy is associated with regions beyond the nearest neighbors of the solute atom, theories based on nearest neighbor interactions would be inadequate.

The doubly ordered arrangement provides the maximum number of Mg–Sn "bonds" of length "$a$" (the second superlattice zone distance). Although bond energy is usually associated with nearest neighbor distances ($a\sqrt{3}/2$ for a body-centered cubic structure) the Mg–Sn bond energy may be sufficient to give the ordered structure a lower energy. On disordering sites 3 and 4, Mg–Sn bonds are lost, that is, offset by the effect of the entropy of mixing. In this connection it may be noted that the lattice spacings of alloys which do not contain the third zone superlattice are larger than would be expected from a reasonable extrapolation of the lattice spacing/temperature curves for the doubly ordered alloys (Figs. 5 and 6). Thus loss of Mg–Sn bonds of length "$a$" causes a relative expansion of the structure, consistent with the suggestion that electrochemical interactions between magnesium and tin atoms are important in the formation of the third zone superlattice.

The absence of similar effects in silver–magnesium–zinc alloys is explicable according to this explanation. Zinc (atomic diameter 2.659 Å) has a smaller atomic size than that of tin, and is divalent. The distortion of the AgMg superlattice cells is thus smaller than for the substitution of tin, and there is less cause for the formation of a third zone superlattice. In addition the heats of formation of magnesium–zinc alloys are smaller than those of magnesium–tin alloys, so that a smaller tendency exists for magnesium and zinc to associate in solid solution in a third metal than in the corresponding tin-bearing alloys.

It is probable that the combined effect of both factors is responsible for the lower free energy of the doubly ordered state in the silver–magnesium–tin alloys at sufficiently high tin contents; as more tin is introduced, the greater is the amount of strain relieved on ordering and the greater is the number of Mg–Sn "bonds" of length "$a$".

The decreasing stability of the second zone superlattice with increase in tin concentration is due to the electrochemical factor operative between nearest neighbors. As tin replaces magnesium the electrochemical interaction energy of the structure, as measured by the number of nearest neighbor Ag–Mg "bonds", decreases. The decreased disordering temperature of the second zone superlattice in the silver–magnesium–zinc alloys is similarly accounted for; the binary silver–zinc 3/2 electron compound, though body-centered cubic above 300°C., does not form an ordered structure, which indicates a relatively weak electrochemical factor.

The experimental work was carried out in the Metallurgy Department of the University of Birmingham, England, where one of us (W.G.H.) held the Raymond Priestley Fellowship, for which acknowledgment is due to the University of Toronto.

## APPENDIX I

### Materials

The alloys used in the present work were prepared from the following materials:

(i) Assay silver, 99.99% pure, supplied by Messrs. Johnson, Matthey and Company, Ltd., England.

(ii) Magnesium, 99.95% pure, supplied by Messrs. F. A. Hughes and Company, Ltd., England.

(iii) Pure zinc, which was kindly presented by the Imperial Smelting Corporation, Ltd., of Avonmouth, England, and in which the only elements detected spectrographically were: lead, 0.0001%; cadmium, 0.0005%; and calcium, 0.0001%.

(iv) Chempur tin, 99.992% pure, obtained from Messrs. Capper, Pass and Son, Ltd., England.

## APPENDIX II

### Analysis of alloys

(i) *Silver–Magnesium–Zinc System*

| Alloy | Composition, atomic per cent | | |
|---|---|---|---|
| | Ag | Mg | Zn |
| *Z*1 | 51.0 | 9.5 | 39.5 |
| *Z*2 | 51.0 | 19.0 | 30.0 |
| *Z*3 | 52.8 | 30.0 | 17.2 |
| *Z*4 | 51.5 | 40.0 | 8.4 |

(ii) *Silver–Magnesium–Tin System*

| Alloy | Composition, atomic per cent | | |
|---|---|---|---|
| | Ag | Mg | Sn |
| *S*1 | 51.5 | 46.6 | 1.9 |
| *S*2 | 56.9 | 39.1 | 4.0 |
| *S*3 | 50.8 | 45.0 | 4.2 |
| *S*4 | 58.1 | 37.5 | 4.4 |
| *S*5 | 60.1 | 33.2 | 6.8 |
| *S*6 | 62.0 | 29.9 | 8.1 |
| *S*7 | 55.2 | 35.6 | 9.1 |
| *S*8 | 51.1 | 43.5 | 5.4 |
| *S*9 | 60.2 | 30.0 | 9.8 |

## REFERENCES

1. BERRY, R. L., HENRY, W. G., and RAYNOR, G. V. J. Inst. Metals, 78:643. 1950-51.
2. HUME-ROTHERY, W. and POWELL, H. M. Z. Krist. 91:23. 1935.
3. HUME-ROTHERY, W. and REYNOLDS, P. W. Proc. Roy. Soc. (London), A, 167:25. 1938.
4. RAYNOR, G. V. Trans. Faraday Soc. 45:698. 1949.
5. RAYNOR, G. V. and FROST, B. R. T. J. Inst. Metals, 75: 777. 1949.
6. RAYNOR, G. V. and SMITH, R. A. J. Inst. Metals, 76:389. 1949.
7. SYKES, C. and WILKINSON, J. J. Inst. Metals, 61: 223. 1937.

# SELF-DIFFUSION AT SILVER SURFACES[1]

By W. C. Winegard and B. Chalmers

ABSTRACT

The surface self-diffusion of silver on specific crystallographic surfaces of silver single crystals and on polycrystalline specimens was investigated. Various methods of surface preparation were used and the general conclusion was reached that surface diffusion is accelerated during changes of surface shape. The theory is advanced that "surface" diffusion takes place by a lattice vacancy mechanism; an abnormally high concentration of lattice vacancies is believed to be necessary for changes of surface shape to occur. This accounts for the accelerated surface diffusion observed under these conditions.

## INTRODUCTION

The most important part of a metal from the point of view of corrosion, friction, catalysis, and many other phenomena of practical significance is the surface. There can be little doubt that both the physical structure and the chemical composition of the surface may differ materially from the corresponding bulk properties on which measurements are normally made. The structure at the surface of a crystal must be different from that of the interior (11) and the surface has been shown (14) in certain cases to contain a higher proportion of solute atoms than the remainder of the metal. These are apparently equilibrium conditions. Another property of the surface is the free energy associated with it; this has the form of surface tension or surface free energy. As a result, a specimen of a metal will tend to change shape so that the surface energy, including that of the grain boundaries, is decreased; this change of shape has been shown to occur under suitable conditions.

Chalmers, King, and Shuttleworth (4) have established that in polycrystalline silver, grooves are formed at the crystal boundaries after short periods of heating. This groove formation is represented schematically in Fig. 1. Fig. 1(*a*) depicts the surface after electropolishing, and Fig. 1(*b*) represents the surface after annealing.

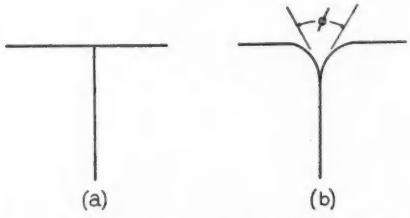


Fig. 1. Specimen surface before and after annealing.

Greenough and King (5) have measured the angle $\phi$ for boundaries between differently oriented crystals. Andrade and Martindale (1) found that a silver

[1] *Manuscript received April 30, 1952.*
*Contributed from Department of Metallurgical Engineering, University of Toronto, Toronto, Ontario.*

film on quartz when heated to 280°C. coalesced to spherulites. This effect has been verified by other investigators using various methods; for example, Sennett and Scott (13) studied the redistribution of atoms in thin films by means of the electron microscope.

The mechanism of this process which may be described as surface diffusion, however, is not known; this is because the process has hitherto not been studied fully enough to indicate how it is affected by various conditions, such as surface shape, surface chemistry, and surface crystallography.

The authors have studied the self-diffusion of silver on specific crystallographic surfaces of silver single crystals; polycrystalline specimens were also examined for comparison. Various methods of surface preparation were used, and it was concluded that the change of surface shape that occurred during the annealing of the specimen at high temperatures had a marked effect on the rate of diffusion. This effect was not observed by Nickerson and Parker (10) whose measurements constitute the only previous quantitative study of surface self-diffusion.

## EXPERIMENTAL

Single crystals and polycrystalline specimens were prepared from spectrographic silver*, metallographically polished and electropolished to remove worked material (16). The single crystals were grown from the melt in a nitrogen atmosphere by the Chalmers' technique (3).

Specimens were used in the polished or the etched condition as shown in Table I.

TABLE I

| Specimen | Surface condition | Surface orientation |
|---|---|---|
| 1 | Electropolished | (111) plane horizontal |
| 2 | Electroetched | (111) plane horizontal |
| 3 | Chemically etched | (111) plane horizontal |
| 4 | Electropolished | (110) plane horizontal |
| 5 | Electroetched | (110) plane horizontal |
| 6* | Electropolished | (100) plane horizontal |
| 7* | Electroetched | (100) plane horizontal |
| 8 | Electropolished | Polycrystalline |
| 9 | Electroetched | Polycrystalline |
| 10 | Chemically etched | Polycrystalline |

The polycrystalline specimens were coarse-grained with an average grain diameter of 3 to 4 mm.

* *These specimens contained striations as described by Teghtsoonian and Chalmers (15).*

A definite region of the surface was electroplated with silver containing the radioactive isotope Ag 110, which emits beta particles and gamma rays. The specimen surface was covered with "electroplating" tape except for a small

* *This material was analyzed as 99.999% silver. Trace amounts of Ca, Si, Fe, Cu, and Na were detected.*

region where the active material was to be deposited. The electroplating bath contained the following materials:

30 gm. per liter potassium cyanide
15 gm. per liter potassium carbonate
4.5 gm. per liter silver
0.5 gm. per liter irradiated silver

The activity of the irradiated silver was 10 millicuries per gram. This corresponds to approximately 500,000 atoms of Ag 109 to each atom of Ag 110. It is evident that the amount of Cd 110 formed by the disintegration of the Ag 110 will not produce significant contamination.

Autoradiographs were obtained by placing the specimen on a photographic plate for 24 hr. so that the active material was in contact with the photographic emulsion. An autoradiograph was taken of the initial distribution and additional autoradiographs gave the distribution after various heat treatments.

In order to use standard methods of computing diffusion constants, it is necessary to define the term concentration as used in this investigation. Con-

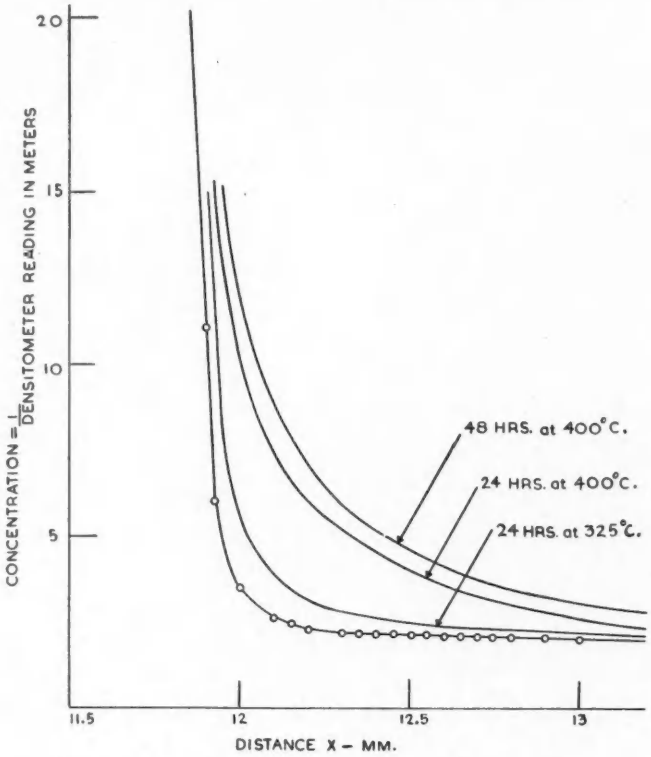


FIG. 2. Concentration–distance curves for a single crystal surface.

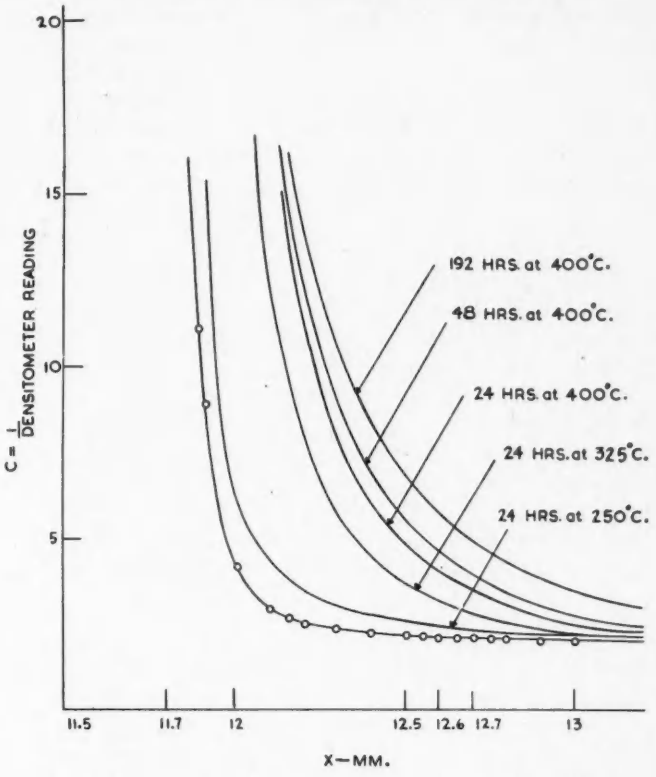


FIG. 3. Concentration–distance curves for a polycrystalline surface.

centration is taken to mean the ratio of Ag 110 to Ag 109 in the layer near the surface from which beta particles can reach the photographic plate. The emulsion will not be greatly affected by the gamma rays because of their high penetrating power. The observed photographic effect is therefore a measure of the concentration. The concentration so determined is the average value over an area defined by the slit of the microphotometer. A Hilger, nonrecording type microphotometer was used with an effective slit 1.5 mm. long and 0.02 mm. wide. The concentration was assumed to be inversely proportional to the microphotometer reading, $R$, or $C=1/R$. This relationship assumes that the curve relating plate blackening (density) to $\log_{10}$ exposure is a straight line of slope $\gamma$ where $\gamma$ is unity. These assumptions undoubtedly affect the numerical values obtained, but it is believed that the results are within an order of magnitude of the true diffusion coefficients. All of the results to be reported below were obtained in the same way; it is, therefore, certain that the relative values are significant although the absolute values may be in error.

The distribution of the active material was followed by plotting the concentration, $C$, at a series of definite distances ($x$) from the center of the electroplated area. Concentration versus distance curves were constructed for each specimen after every heat treatment and a final composite graph was made for each crystal. Typical curves for single crystals and polycrystalline specimens are shown in Figs. 2 and 3 respectively.

## APPARENT DIFFUSION COEFFICIENTS AND EXPERIMENTAL RESULTS

The general equation for diffusion in one direction is $\partial c/\partial t = Dx\ \partial^2 c/\partial x^2$ where $Dx$ is the diffusion coefficient in the $x$ direction, $\partial^2 c/\partial x^2$ is the second partial derivative of concentration with respect to distance, and $\partial c/\partial t$ is the partial derivative of concentration with time. In these experiments $\partial^2 c/\partial x^2$ and $\partial c/\partial t$ were evaluated by the tangent method to find $Dx$. The diffusion coefficients obtained are listed in Table II.

TABLE II

DIFFUSION COEFFICIENTS OBTAINED AFTER VARIOUS HEAT TREATMENTS

| Specimen | $Dx$ cm.$^2$ per sec. after heat treatment as shown | | | | | |
|---|---|---|---|---|---|---|
| | 24 hr. at 250°C. | 24 hr. at 325°C. | 24 hr. at 400°C. | 48 hr. at 400°C. | 192 hr. at 400°C. | 384 hr. at 400°C. |
| Single crystal | No diffusion detected | $2 \times 10^{-9}$ | $6 \times 10^{-9}$ | $2 \times 10^{-9}$ | $2 \times 10^{-9}$ | $2 \times 10^{-9}$ |
| Polycrystalline | $2 \times 10^{-9}$ | $5 \times 10^{-9}$ | $3 \times 10^{-9}$ | $2 \times 10^{-9}$ | $1 \times 10^{-9}$ | $1 \times 10^{-9}$ |

The diffusion coefficient did not change materially when different etching solutions were used and it was not possible to determine the effect of surface crystallography because of the effect of the change of surface shape.

## DISCUSSION

One of the early investigations of surface diffusion was made by Langmuir (9) who studied the diffusion of thorium on the surface, along the grain boundaries, and through the crystals of tungsten. He found that surface diffusion ($Ds$) was faster than boundary diffusion ($Dg$), which was faster than volume diffusion ($Dv$). Hoffman and Turnbull (7) report a volume self-diffusion coefficient for silver of approximately $10^{-15}$ cm.$^2$ per sec. at 400°C. and a grain boundary self-diffusion coefficient of approximately $10^{-8}$ or $10^{-9}$ cm.$^2$ per sec. at 400°C. The self-diffusion coefficient obtained in the present work for surface migration on single crystals of silver at 400°C. is approximately $2 \times 10^{-9}$ cm.$^2$ per sec. which is very close to the grain boundary coefficient obtained by Hoffman and Turnbull (7). This suggests that grain boundary and surface diffusion may be closely associated.

It is clear from Table II that the "surface" diffusion process is accelerated when a change of surface shape occurs, such as thermal etching of the grain boundaries (Fig. 1) or the smoothing out of the surface of single crystals. It is probable that the results of Nickerson and Parker (10) were influenced by

this thermal etching effect. They conducted their experiments on drawn silver wires. These were certainly polycrystalline. The wires would be expected to recrystallize and undergo subsequent grain growth. These processes must affect the shape of the surface and consequently must have had a marked influence on the value that was obtained for the surface self-diffusion coefficient.

The three possible mechanisms of volume diffusion are represented schematically in Fig. 4. The interchange mechanism is shown in Fig. 4 (*a*). The atoms can only interchange positions by forcing neighboring atoms apart. The interstitial mechanism is shown in Fig. 4(*b*); the atoms migrate through interstitial sites instead of moving from one lattice point to another. This mechanism is unlikely when the solute and solvent atoms are of the same size. The vacant lattice site process as shown in Fig. 4(*c*) occurs when an atom moves into a neighboring vacant lattice site.

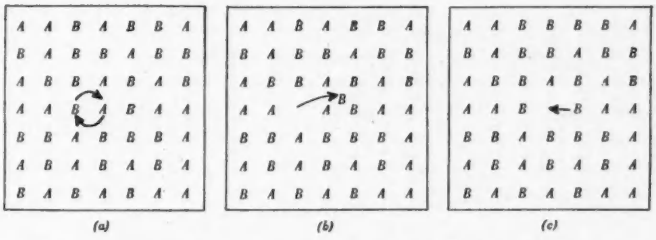

FIG. 4. Three possible mechanisms of volume diffusion (Seitz (12)).

It has recently been shown by Herring (6) that a greater concentration of vacancies exists near the surface than in the interior of the metal. Diffusion by the vacancy mechanism should, therefore, be rapid near the surface. Another possible mechanism for surface diffusion is that in which atoms in the top atomic layer only are moving. This process may occur but it does not appear to be a significant factor in the observed "surface" diffusion for the following reasons: If the diffusion process was the movement of a mono layer, the surface chemistry would be expected to play an important part. From the experiments, it was established that the type of etching solution used made no appreciable difference to the value of *Dx*. Also, if the surface atoms were the only atoms to move, there would seem to be little reason why diffusion should be faster when a change of surface shape is occurring. The movement of a monolayer could hardly explain the large changes in surface shape that do occur in such processes as thermal etching. The change of surface shape can be better explained by a movement of vacancies from concave to convex regions as shown in Fig. 5; this would tend to level the surface.

The vacancies must migrate almost randomly in all directions, but have a slight preference for migration in the direction of *B* to *A*. The net flow of vacancies is shown schematically in Fig. 6. Atoms move preferably in the direction of

FIG. 5. Schematic representation of the surface.

the greater concentration of vacancies. As the diffusion progresses, more vacancies are created and become available for the transport of atoms from *A* to *B*. Thus, self-diffusion near the surface is faster while the creation and subsequent transport of vacancies is occurring.

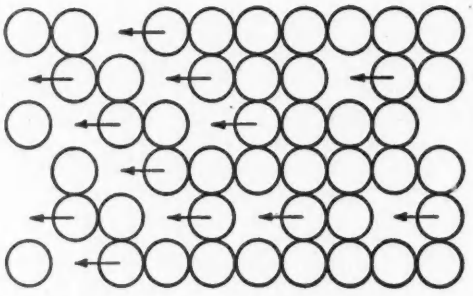

FIG. 6. Schematic representation of the diffusion flow (Kuczynski (8)).

## SUMMARY

The hypothesis presented is that "surface" self-diffusion occurs by a vacancy mechanism. The concentration of vacancies is greater near the surface than in the interior and, therefore, diffusion is faster nearer the surface. Changes of surface shape are explained by the creation and transport of vacancies from concave to convex areas of the surface.

The similarity between the results for surface self-diffusion obtained in these experiments and those for grain boundary diffusion obtained by Hoffman and Turnbull (7) is very striking. The grain boundary may be considered as an array of dislocations (2) which are a potential source of vacancies; hence, the grain boundary diffusion mechanism may also be one of vacancy movement.

The diffusion process is accelerated when a change of surface shape occurs; the diffusion coefficient decreases with time as the surface approaches the equilibrium shape.

## ACKNOWLEDGMENTS

One of the authors (W.C.W.) is indebted to the Department of Veterans Affairs, Canada, and to Russell Industries Limited, Canada, for generous financial assistance.

The Associate Committee on Corrosion Research and Prevention, National Research Council of Canada, has contributed generously to the Radio-active Tracer Laboratory where this work was carried out.

The authors wish to thank Mr. R. S. Davis, M.A.Sc., and Mr. W. R. Thomas, M.A.Sc., for very valuable assistance during the course of the work, and to express their indebtedness to Dr. N. J. Chaplin, Dr. J. W. Rutter, and Dr. G. D. Scott for helpful discussion.

## REFERENCES

1. ANDRADE, E. N. DAC. and MARTINDALE, J. G. Trans. Faraday Soc. 31: 1137. 1935.
2. BURGERS, J. M. Proc. Phys. Soc. (London), 52: 23. 1940.
3. CHALMERS, B. Proc. Roy. Soc. (London), A, 196: 64. 1949.
4. CHALMERS, B., KING, R., and SHUTTLEWORTH, R. Proc. Roy. Soc. (London), A, 193: 465. 1948.
5. GREENOUGH, A. P. and KING, R. J. Inst. Metals, 79: 415. 1951.
6. HERRING, C. Physics of powder metallurgy *edited by* W. E. Kingston. McGraw-Hill Book Company Inc., New York. 1951.
7. HOFFMAN, R. E. and TURNBULL, D. J. Applied Phys. 22: 634. 1951.
8. KUCZYNSKI, G. C. J. Applied Phys. 20: 1160. 1949.
9. LANGMUIR, I. J. Franklin Inst. 217: 543. 1934.
10. NICKERSON, R. A. and PARKER, E. R. Trans. Am. Soc. Metals, 42: 376. 1950.
11. SEITZ, F. Modern theory of solids. McGraw-Hill Book Company Inc., New York. 1940.
12. SEITZ, F. Phase transformations in solids. John Wiley and Sons, Inc., New York. 1951.
13. SENNETT, R. S. and SCOTT, G. D. J. Optical Soc. Am. 40: 203. 1950.
14. STEWART, M. T., THOMAS, W. R., WAUCHOPE, K. L., WINEGARD, W. C., and CHALMERS, B. Phys. Rev. 83: 657. 1951.
15. TEGHTSOONIAN, E. and CHALMERS, B. Can. J. Phys. 29: 370. 1951.
16. WINEGARD, W. C., DAVIS, R. S., THOMAS, W. R., and CHALMERS, B. Metal Progress, 61: 95. 1952.

# SLOW $\pi$-MESONS IN COSMIC-RAY STARS AND THE NEGATIVE–POSITIVE $\pi$-MESON RATIO[1]

By J. Y. Mei[2] and E. Pickup

ABSTRACT

In a survey of mesons ending in the emulsion no $\tau$- or $\kappa$-mesons have been observed so far. The variation of the negative–positive $\pi$-meson ratio with energy shows up the effect of the Coulomb barrier on $\pi$-meson production at very low energies. The variations of this ratio at mountain and balloon altitudes are discussed. Examples have been obtained of the emission of slow $\pi$-mesons in hydrogen collisions in the emulsion, and also in energetic stars with several shower particles and few evaporation particles.

## 1. INTRODUCTION

The results described here were obtained during the course of an attempt to detect $\tau$-and $\kappa$-mesons ending in thick photographic emulsions exposed to cosmic radiation at high altitudes. So far, out of a total of about 500 $\pi$-mesons ending, no $\tau$-or $\kappa_2$-mesons* have been observed. Under the conditions of the examination we would not have detected $\kappa_1$-mesons.

This negative result, however, after allowing for the possibility of missing the odd single event, is not inconsistent with the observations of Fowler *et al.* (10), and O'Ceallaigh (13) who noted only three $\tau$- and $\kappa_2$-mesons in a total of 750 $\pi$-meson ends. Furthermore, as they note, it depends on the exact experimental conditions. However, it is evident that these mesons are either created rarely compared with $\pi$-mesons (e.g. in higher energy events mainly, as would be expected from Fermi's theory (9)) or have an appreciably shorter lifetime. Further work is in progress in the hope of detecting heavy mesons stopping in the emulsion.

It was considered worth while to record the results obtained for the negative–positive $\pi$-meson ratio. Since this work was completed Yagoda (15) has also published some similar results.

Examples have also been found of the creation of single positive $\pi$-mesons in what appear to be proton–hydrogen collisions in the emulsion, although the fact that $\pi$-mesons are created in this way is now quite evident from the cyclotron work at Berkeley. Fig. 3 shows a case of the creation of a slow positive $\pi$-meson in such a nucleon–nucleon collision. One case was observed where a positive $\pi$-meson originated in the emulsion with no sign of other charged tracks, and this is interpreted as $\pi$-meson creation in the interaction of neutral radiation with hydrogen in the emulsion. Slow $\pi$-mesons are also emitted in very high energy stars having few or no "black" (evaporation) tracks, and the implications of this are discussed.

[1] *Manuscript received April 18, 1952.*
*Contribution from the Division of Physics, National Research Council, Ottawa. Issued as N.R.C. No. 2812.*

[2] *Holder of a National Research Council of Canada Fellowship.*

**We use here the nomenclature, i.e. $\tau \rightarrow$ three charged $\pi$-mesons; $\kappa_1 \rightarrow$ high energy, minimum ionization particle; $\kappa_2 \rightarrow \mu$-meson with range about 1200 microns. See References 10 and 13.*

## 2. EXPERIMENTAL TECHNIQUE

### (a). *Exposure*

Ilford G5 emulsions of thicknesses 600, 1000, and 1200 microns were exposed in a balloon flight at about 80,000 ft. for 12 hr.* Fig. 1 shows the time-altitude

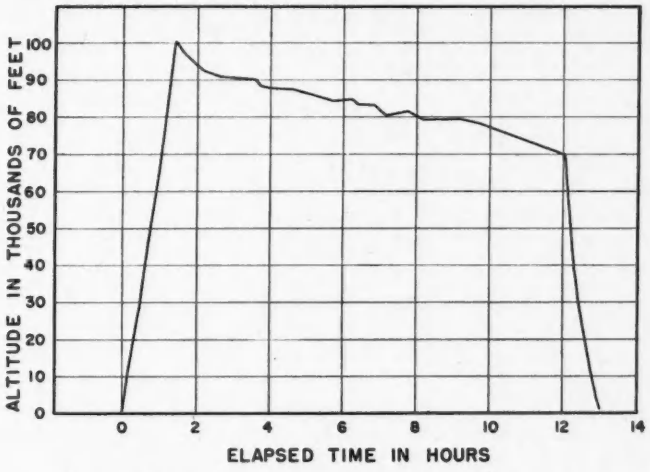


FIG. 1. Time versus altitude graph for balloon flight.

graph for this exposure. The approximate dimensions of the emulsion stack were $8 \times 8 \times 15$ cm., and there was no shielding material. Some emulsions were also exposed for five weeks on the Jungfraujoch.**

### (b). *Development*

The emulsions were much thicker than we had previously used, and needed two to three weeks for complete processing. The method used for developing was the "hot plate" method described by Dilworth, Occhialini, and Vermaesen (8), and that for processing after development was similar to the one described by Bonetti, Dilworth, and Occhialini (5). We introduced small variations to suit our local conditions, but a detailed description will not be given here. Reasonably successful results were obtained, except that there was a fairly big variation of development with depth for the 1200 $\mu$ plates. Detailed measurements indicate that the 600 $\mu$ plates have a small but typical variation of grain count with depth. All plates recorded minimum ionization particles.

## 3. NEGATIVE-POSITIVE π-MESON RATIO

### (a). *π-Mesons Ending in the Emulsion*

The star-size distribution for about 150 negative $\pi$-mesons ending in the emulsions (i.e. they show typical scattering and give small stars) exposed at

*This was obtained with the cooperation of the Bartol Research Foundation and the ONR project, "Skyhook".

**Dr. L. Voyvodic made these exposures for us during a recent visit to Europe.

80,000 ft. is not significantly different from that given by Adelman and Jones (1) for artificially produced mesons, as shown in Table I.

TABLE I

PERCENTAGE OF $\pi^-$ STARS WITH GIVEN NUMBER OF PRONGS FOR ARTIFICIALLY PRODUCED AND FOR COSMIC-RAY MESONS

The results were normalized at zero prong number after this value had been estimated for the cosmic-ray mesons using Adelman and Jones' result that 27% of negative $\pi$-mesons do not give stars

| No. of prongs | 0 | 1 | 2 | 3 | 4 | 5 |
|---|---|---|---|---|---|---|
| Adelman and Jones, % | 27.0 | 23.6 | 24.0 | 14.8 | 8.7 | 1.9 |
| 80,000 ft., % | 27.0 | 24.4 | 24.4 | 17.8 | 5.2 | 1.3 |

Positive $\pi$-mesons were identified by means of $\pi$–$\mu$ decay and 197 $\pi^+$- and 110 $\pi^-$- (giving stars having at least one prong) mesons were observed to enter and end in the emulsion. The emulsion stack was virtually free and, while some of the $\pi$-mesons may come from outside, it is likely that most of them originated in stars within the stack. Thus, considering the dimensions of the stack, their original energy would be less than about 100 Mev.

Correcting for the 27% of negative $\pi$-mesons (1) which do not give stars, and for the about 2.5% of $\mu$-mesons ending in the emulsion and which give stars (12), (using a measured relative number of $\mu$-mesons to negative $\pi$-mesons, in our case $\backsim$ 4/1), we obtain the ratio $N(\pi^-)/N(\pi^+) = 0.66$. The uncorrected ratio was 0.56. This latter value may be compared with similar results by Barbour (2) at 90,000 ft. which give a ratio of 0.59 for the number of $\pi$-mesons giving stars to those giving $\pi$–$\mu$ decays. Yagoda's results (15) for approximately 90,000 ft. give a value of 1.0. The ratio of $\mu$-mesons to $\pi$-mesons (giving stars or $\pi$–$\mu$ decay) that we found, 1.6, was also similar to Barbour's estimate of 1.4. There is a striking difference between these results and those of Fry (11) who gives $N(\pi^-)/N(\pi^+) = 3.27 \pm 0.7$ for emulsions exposed at 60,000 ft. and it would be interesting to know whether this is a real effect.

In our case a selection was also made of those $\pi$-mesons with ranges of at least about 5 mm. in the emulsion, i.e. original energy definitely greater than 20 Mev., giving a corrected ratio $N(\pi^-)/N(\pi^+) = 0.8$. However, owing to the small number of events available (ratio 8/12) this result is subject to a large statistical fluctuation and is not considered significantly different from that for all $\pi$-mesons.

For mountain altitudes Barton, George, and Jason (4) give $N(\pi^-)/N(\pi^+) = 3.25 \pm 0.25$ at 3457 meters (exposure under carbon plate). Bonetti and Tomasini (6) give a ratio of about 2.0 (86/48). From the present work emulsions exposed on the Jungfraujoch under 10 cm. lead gave a ratio 1.1. Previous unpublished airplane results with unshielded emulsions gave a higher value. Thus it seems that at mountain altitudes there is, in general, an excess of slow negative $\pi$-mesons.

(*b*). *$\pi$-mesons Originating and Terminating in the Emulsion*

Seventy cases were observed where $\pi$-mesons with energies up to 35 Mev. came from stars in the emulsion at 80,000 ft. For these $N(\pi^-)/N(\pi^+) = 52/18$

= 2.9. This is similar to a result obtained by Yagoda (15) for emulsions exposed at about 90,000 ft., including π-mesons with energies up to 40 Mev., i.e., $N(\pi^-)/N(\pi^+) = 5.5$, although he indicates that observational corrections may reduce this ratio to 3.1. Both ratios indicate a negative excess as compared with the positive excess found in 3(*a*) for all π-mesons entering and ending in the emulsion. Primarily, this difference appears to be an effect due to the inclusion of more energetic π-mesons (energies up to 100 Mev.) in the latter case.

This change is seen clearly if the 70 π-mesons from stars are divided into energy groups. Fig. 2 shows a plot of $N(\pi^-)/N(\pi^+)$ against energy. Although

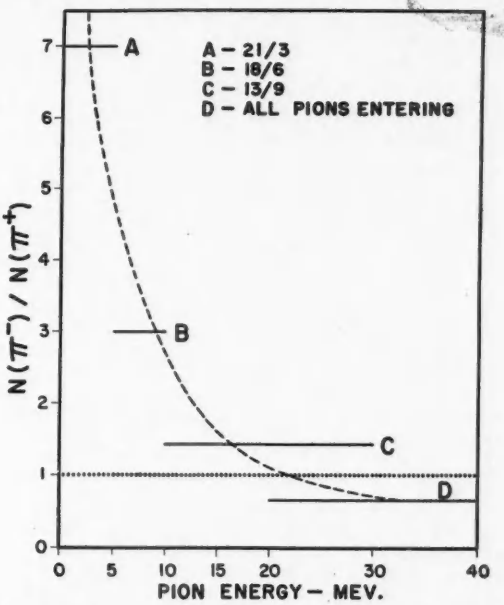


FIG. 2. Variation of negative–positive π-meson ratio with energy for π-mesons from stars.

the absolute numbers involved become small there is a marked variation with energy. It should be noted that this result is independent of any correction due to loss of the more energetic, longer range π-mesons leaving the emulsion before ending their range or undergoing marked scattering, and so not being recognized as π-mesons here. From the 70 π-mesons the 52 classed as negative included 10 π-mesons not giving stars. This number, i.e. 20% of the negative π-mesons, is in reasonable agreement with Adelman and Jones' (1) estimate of 27% with much better statistics.

The stars giving π-mesons were of various types, with and without shower particles, and were formed in both the light and heavy elements in the emulsion. There was a total excess of neutron induced stars, mainly of low energy (less than 1 Bev., i.e. no shower particles). The higher energy stars (with at least one

shower particle) were predominantly proton induced. Grouping the $\pi$-mesons into two energy groups (less than and greater than 10 Mev.) for these different types of stars, however, always gave an increased negative $\pi$-meson excess for the lower energies, although statistics were poor.

(*c*). *Discussion*

The negative–positive $\pi$-meson ratio for low energy disintegrations with only one meson has been discussed theoretically by Chew and Steinberger (7). The first main feature is a negative excess for neutron stars and a positive excess for proton stars, with complications in an actual nuclear collision due to the exclusion principle, giving energy dependent effects. Measurements of the ratio in cyclotron experiments using known targets seem to support the theoretical ideas (6).

Considering the curve of Fig. 2 in 3 (*b*) the initial part can probably be attributed to the effect of the Coulomb barrier in inhibiting the emission of very low energy positive $\pi$-mesons (14). From the composition of the emulsion we would not expect the Coulomb barrier effect to extend much beyond 10 Mev. (3 and 11 Mev. being barrier heights for light and heavy elements respectively in the emulsion), and there is the possibility that the barrier may be reduced in the course of the nuclear disruption, especially for some cosmic-ray events. As pointed out in 3 (*b*) the initial negative excess is shown for both proton and neutron induced stars, thus supporting the view that it is, at least partly, a Coulomb barrier effect. Barkas (3) has also demonstrated this effect using 390 Mev. $\alpha$-particles to produce low energy $\pi$-mesons from different targets. In our case part of the low energy excess may also be due to the predominance of low energy neutron induced stars.

The final positive excess for $\pi$-mesons entering the emulsion (energies about 30–100 Mev.) from elsewhere in the stack can probably be attributed to an excess of somewhat higher energy proton induced stars. The very low energy $\pi$-mesons produced elsewhere, of course, usually terminate before entering the emulsion in question. The effect from the most energetic stars giving several shower particles is more difficult to predict since the final $\pi$-meson emerges after several collisions have occurred.

The negative excess at mountain altitudes is probably to be associated with the large excess of neutron induced stars there, as discussed by Barton, George, and Jason (4).

## 4. SLOW $\pi$-MESONS FROM VERY HIGH ENERGY STARS

During the course of this work we have observed slow $\pi$-mesons ejected from proton stars having many shower particles in a forward cone. Sometimes there are only one or two "black" tracks associated with the star. It is becoming customary to try to treat the showers in this latter type of event as being the result of multiple meson production in single nucleon–nucleon collisions (peripheral nuclear collisions), but the presence of slow $\pi$-mesons is a strong indication that in at least some such events secondary collisions have occurred, and the

shower itself may contain mesons from more than one collision and not be a pure multiple event. Heavy nuclear recoils from the stars may not be detected in the emulsion if their energy is less than 50 Mev. It is not possible at present to give a good estimate for the absolute frequency of these events. They were found here because the search was, primarily, for slow mesons ending in the emulsion, and these are easy to detect. Otherwise the events are easily missed.

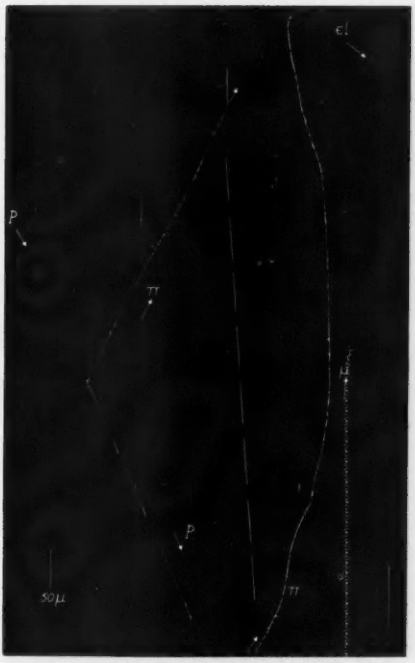


FIG. 3. Microprojection tracing showing emission of positive π-meson, with energy about 20 Mev., in proton–hydrogen collision in G5 emulsion. The positive π-meson shows π–μ–electron decay.

Fig. 4 is a microscope projection tracing showing two such events in which negative π-mesons (giving one-pronged stars) were emitted. Fig. 5 shows an unusual event in which the only low energy particle was a positive π-meson, giving π–μ–electron decay. The total, odd number of tracks (5) precludes the possibility of this being a proton-hydrogen collision with multiple meson production, and we assume it to be the result of a peripheral collision with a heavy nucleus in the emulsion with secondary collisions also occurring. There is no visible nuclear recoil. An event of a similar nature to this has been obtained by Heisenberg (14). Fig. 6 shows the results of a more central collision with a heavy nucleus (Ag or Br in the emulsion) giving a proton star with 12 "black"

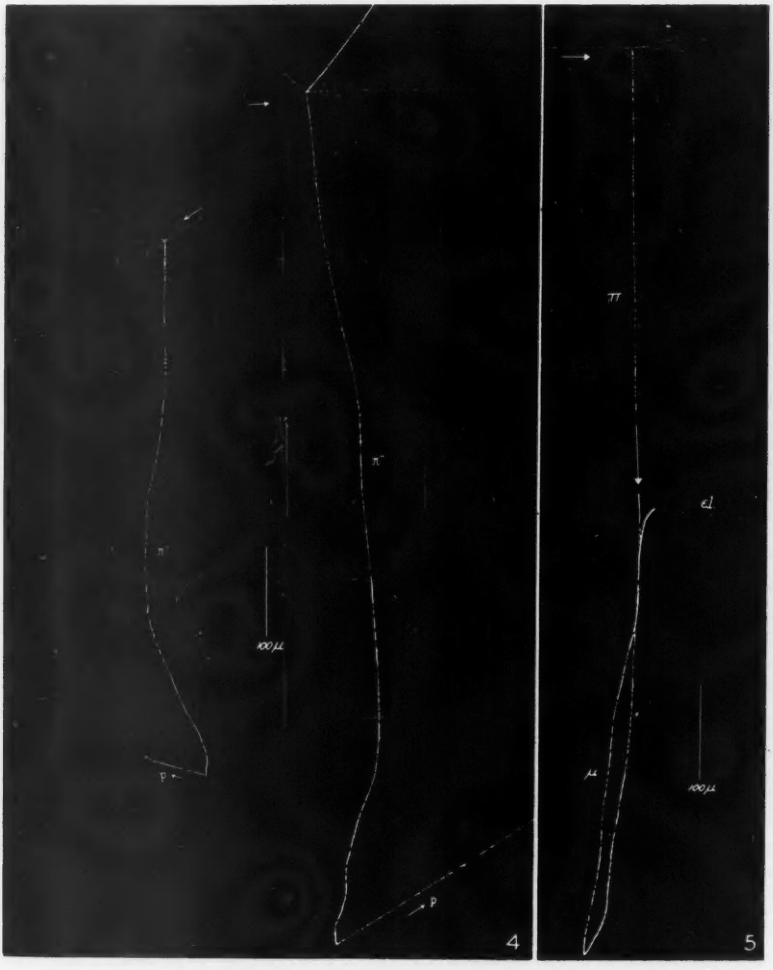


FIG. 4. Energetic stars with very few "black" tracks in which slow negative $\pi$-mesons with energies 3 and 5 Mev. were emitted.

FIG. 5. Unusual star in which only four minimum ionization tracks and a slow positive $\pi$-meson with energy 25 Mev. are produced in a 1200 $\mu$ thick, G5 emulsion.

and 10 shower particles. The wide angle cone of shower particles almost certainly indicates several collisions with the final emission of a slow positive $\pi$-meson which undergoes $\pi$–$\mu$–electron decay.

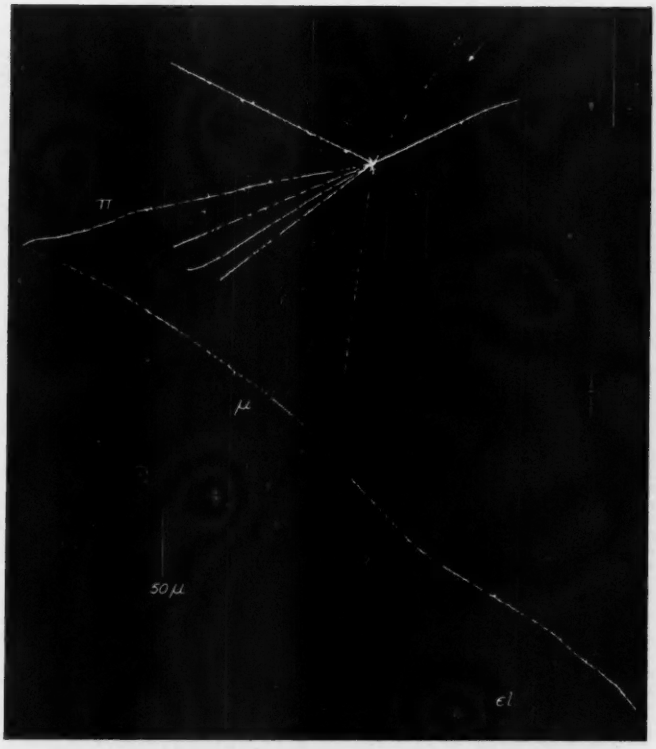


FIG. 6. Energetic star due to disintegration of Ag or Br in the emulsion by incoming proton, in which a 3 Mev. positive π-meson is emitted together with about 10 shower particles.

We are indebted to D. Rushton for making the microprojection tracings.

## REFERENCES

1. ADELMAN, F. L. and JONES, S. B. Phys. Rev. 75: 1468. 1949.
2. BARBOUR, I. Phys. Rev. 78: 518. 1950.
3. BARKAS, W. H. Phys. Rev. 75: 1467. 1949. See also References 14, 15.
4. BARTON, J. C., GEORGE, E. P. and JASON, A. C. Proc. Phys. Soc. (London), 64: 189. 1951.
5. BONETTI, A., DILWORTH, C. C., and OCCHIALINI, G. P. S. Bull. Centre de Physique Nuclaire de Bruxelles N 13b. 1951.
6. BONETTI, A. and TOMASINI, G. Nuovo cimento, 8: 693. 1951.
7. CHEW, G. F. and STEINBERGER, J. L. Phys. Rev. 78: 497. 1950.
8. DILWORTH, C. C., OCCHIALINI, G. P. S., and VERMAESEN, L. Bull. Centre de Physique Nuclaire de Bruxelles N 13a. 1951.
9. FERMI, E. Progress Theor. Phys. 5: 570. 1951.
10. FOWLER, P. H., MENON, M. G. K., POWELL, C. F.. and ROCHAT, O. Phil. Mag. 42: 1040. 1951.
11. FRY, W. F. Phys. Rev. 82: 747. 1951.
12. GEORGE, E. P. and EVANS, G. R. Proc. Phys. Soc. (London), 64: 193. 1951.
13. O'CEALLAIGH, C. Phil. Mag. 42: 1032. 1951.
14. POWELL, C. F. Repts. Progress Phys. 13: 350. 1950. See also report of Heisenberg's event.
15. YAGODA, H. Phys. Rev. 85: 891. 1952.

# SEARCH FOR ANOMALOUS ABSORPTION OF Ra(B + C) $\gamma$ RAYS[1]

By W. R. Dixon and G. N. Whyte

ABSTRACT

The absorption of Ra(B+C) $\gamma$ rays in lead from 13 to 26 cm. has been investigated in a search for the anomalies reported by Sen Chaudhary. No such anomalies were found.

## INTRODUCTION

In 1948 Sen Chaudhary (1) reported an anomalous effect in the absorption of Ra(B + C) $\gamma$ rays in lead. Using a collimated beam of $\gamma$ rays and a Geiger counter shielded by 1 cm. of lead, he found that the linear absorption coefficient dropped from 0.465 cm.$^{-1}$ at around 20 cm. of lead to a minimum of 0.307 at 23 cm. and then increased again to 0.40 at 26 cm. He suggested that this behavior might be due to the formation of positronium with enough energy to penetrate a considerable thickness of lead before annihilating, and later (2) associated it with the second and third Rossi maxima of the cosmic radiation. The only previous work in this region of thicknesses appears to be that of Russell (3) in 1910, which extended to only 22 cm. of lead. Since the statistical uncertainties in Sen Chaudhary's measurements were large, and since the use of only 10 cm. of lead as shielding around the source made it difficult to estimate the contribution of scattered radiation to the background counting rate, it seemed desirable to repeat the experiment using a stronger source and better shielding.

## APPARATUS

The radium used was in the form of three 1-gm. sources housed in cylindrical monel capsules about 1 cm. in diameter, 1 cm. long, and 2 mm. in wall thickness, each of which was contained in a $\frac{3}{4}$ in. diameter hexagonal duraluminum container with 3 mm. walls. The sources were placed side by side in the center of a spherical lead shipping container which provided more than 30 cm. of shielding in all directions (see Fig. 1). The opening in the container was collimated to a diameter of 4.0 cm., so that the angular divergence of the $\gamma$-ray beam was about the same as that used by Sen Chaudhary (half-angle 3.5°). Measurements were also made with this extra collimator removed; the beam then diverged with a half-angle of 12.6°.

The detector was a Geiger counter with a copper cathode 10 cm. long and 2 cm. in diameter housed in a glass envelope. It was used under two different conditions of lead shielding, shown in (*a*) and (*b*) of Fig. 1, and also unshielded and located in a horizontal position above the absorbers. In order to emphasize any effects due to low-energy radiations, measurements were also made with a

[1] *Manuscript received April 10, 1952.*
*Contribution from the Division of Physics, National Research Council of Canada, Ottawa, Canada. Issued as N.R.C. No. 2811.*

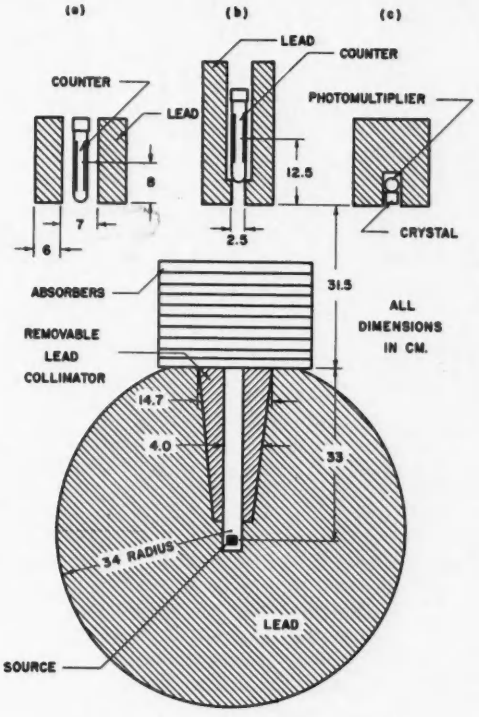


FIG. 1. Experimental arrangement.

sodium iodide crystal mounted on an RCA 931A photomultiplier (see (*c*) of Fig. 1).

The absorbers were in the form of lead sheets 30 cm. square by $1.28_3$ cm. thick, the density of the lead being 11.30 gm. per cm.$^2$ As in Sen Chaudhary's experiment, they were placed directly on top of the source container.

## RESULTS

The counting rates as a function of absorber thickness for a variety of geometrical conditions are shown in logarithmic plots in Fig. 2. Curve 2 corresponds to the conditions used by Sen Chaudhary, curve 1 to better collimation at the detector, curve 4 to a broader γ-ray beam, and curve 5 to the broader beam and a completely unshielded counter. Curve 3 was taken with the scintillation counter.

It is apparent that over the range of thicknesses investigated the experimental points lie very close to a straight line in every case. In particular there is no evidence of the irregularities between 20 and 26 cm. reported by Sen Chaudhary. The linear absorption coefficient of 0.513 cm.$^{-1}$ calculated from the slope of

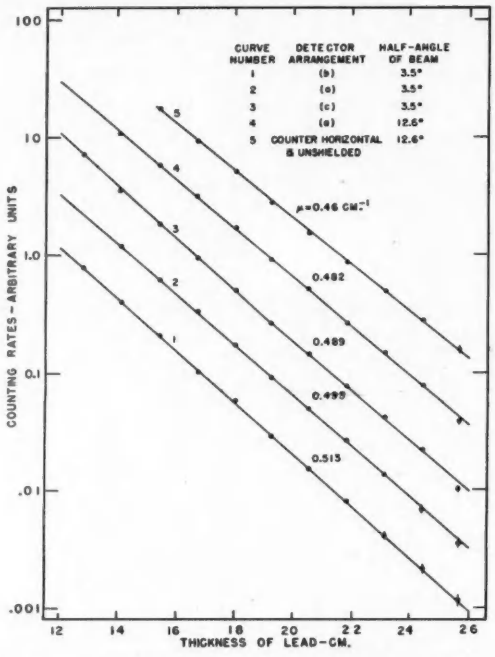


FIG. 2. Counting rate vs. absorber thickness for different geometrical conditions. The relative ordinates of the different curves have no significance.

curve 1 is not far from the value of 0.52 to be expected on the basis of the Ra(B + C) $\gamma$-ray spectrum and the theoretical absorption coefficients. (See the following paper.) In the succeeding curves an increasing fraction of the scattered radiation reaches the detector and the observed coefficient is correspondingly lower.

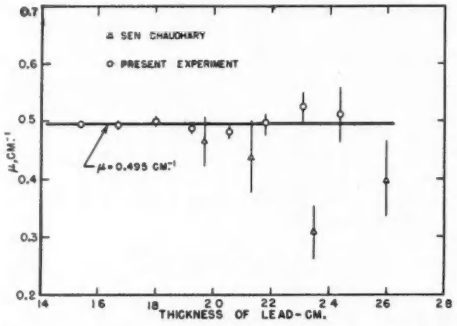


FIG. 3. Comparison of experimental absorption coefficients with those of Sen Chaudhary.

In Fig. 3 the absorption coefficients obtained from successive pairs of points 2.5 cm. apart in curve 2 are compared with those measured by Sen Chaudhary under similar geometrical conditions. The points lie within the statistical error of the constant value of 0.495 cm.$^{-1}$ obtained from the slope of curve 2 in Fig. 2.

From the above measurements we conclude that there is no evidence for anomalous effects in the absorption of Ra(B + C) γ rays in lead.

ACKNOWLEDGMENTS

We wish to express our thanks to Eldorado Mining and Refining (1944) Limited for the loan of the sources and the shipping container, and to Mr. G. M. Keyser of this laboratory for the use of his scintillation counting equipment.

REFERENCES

1. SEN CHAUDHARY, P. K. Indian J. Phys. 22: 106. 1948; 22: 341. 1948.
2. SEN CHAUDHARY, P. K. Phys. Rev. 81: 274. 1951.
3. SODDY, F., SODDY, W. M., and RUSSELL, A. S. Phil. Mag. 19:725. 1910.

# ON THE γ-RAY SPECTRUM OF Ra(B + C)[1]

By G. N. Whyte

ABSTRACT

Measurements of the transmission of Ra(B+C) γ rays through lead between 0 and 26 cm. are described and compared with the transmissions predicted on the basis of a modified version of the γ-ray spectrum of Ellis and Aston and on the basis of the spectrum of Latyshev *et al.* Ellis and Aston's spectrum gives the better agreement. Both the relative and absolute values of the γ-ray intensities given by Ellis and Aston are revised in the light of more recent information. This revised spectrum leads to a predicted value of 0.84 roentgens per hour at a meter for the γ-ray output of a gram of radium and its equilibrium products in 0.5 mm. of platinum, in good agreement with experiment.

## INTRODUCTION

Although the first measurements of the energies of the Ra(B + C) γ rays were made in 1921(7), there is as yet no completely satisfactory γ-ray spectrum for radium in equilibrium with its decay products. In particular, while the energies of the principal γ rays are now well established, the intensities are still uncertain. Where one is concerned with determining nuclear energy levels, it is the energies of the rays that are of primary importance, but where one wishes to calculate the absorption of the γ rays in matter or the dosage rates produced by them, the intensities are equally significant. The purpose of this paper is to reconsider these intensities.

The early experiments of Skobelzyn (24), who examined the Compton recoil electrons in the gas of a cloud chamber, give perhaps the most direct estimate of the relative intensities of the different Ra(B + C) γ rays, but suffer from large statistical uncertainties. The extremely careful measurements of Ellis and Aston (9) and Ellis (8), who analyzed the natural beta spectrum of Ra(B + C) and the photoelectrons ejected from a platinum foil, by means of a 180° focusing spectrograph, still appear to be the most widely accepted (10, 28), despite the occasional doubt that has been cast on their relative intensities, e.g. (12), and despite the more recent work of Latyshev and his co-workers (1, 18, 17). The latter used a magnetic spectrograph to examine both the Compton electrons ejected in the forward direction from a thin target of light material and the internal-conversion positrons. They found a number of γ rays not reported by Ellis and Aston and obtained agreement in the relative intensities derived from the two kinds of measurement; these intensities, however, differ markedly from those of Ellis and Aston. Unfortunately Latyshev's results could not be extended below 1 Mev.

More recently Mann and Ozeroff (20) have tried to verify the findings of Latyshev *et al.*, using a thin-lens spectrometer to analyze the photoelectrons from a lead radiator. They found only the γ-ray energies reported by Ellis and Aston, but it would appear that their resolution was insufficient to distinguish the new

[1] *Manuscript received April 10, 1952.*
*Contribution of the Division of Physics, National Research Council of Canada, Ottawa. Issued as N.R.C. No. 2810.*

lines found by Latyshev *et al.*; also, they did not report the intensities of a few of the weaker lines, their main interest being in the energies. On the other hand Wolfson (29) has carefully examined the region between 2.1 and 2.7 Mev. and has confirmed the presence of the 2.4-Mev. ray found by Latyshev.

Of the determinations of the Ra(B + C) γ-ray spectrum mentioned above, those of Ellis and Aston and of Latyshev *et al.* appear to involve the best estimates of the relative intensities. In what follows the spectrum of Ellis and Aston will be modified on the basis of more recent information, and the transmission curves of the γ rays through lead predicted using this spectrum and also that of Latyshev will be compared with the experimentally determined transmission curve. Finally, the absolute intensities in the modified Ellis and Aston spectrum will be re-evaluated, and the results used to calculate the γ-ray output of a gram of radium in roentgens per hour at a meter.

## EXPERIMENTAL METHOD

The experimental arrangement was the same as that shown in Fig. 1(*b*) of the preceding paper and described there, except that the distance from the center of the counter cathode to the opening in the lead collimator was 18 cm. instead of 12.5 cm. The arrangement was such that the angles of collimation at the source and detector were approximately equal (half-angles of 3.5° and 4.0° respectively) and as small as the requirement of useful counting rates at the large absorber thicknesses would allow. For lead thicknesses between 26 and 13 cm. the 3-gm. radium source described in the previous paper was used; for the range 14 to 5 cm. this was replaced by 100 mgm. of radium encased in 0.5 mm. of platinum and 1 mm. of aluminum; and from 6 to 0 cm. by 5 mgm. of radium in a platinum capsule 2.5 mm. in outside diameter and 0.5 mm. in wall thickness. This last source was placed with its axis at right angles to that of the collimating system so that the absorption of the low-energy rays in the radium salt would be a minimum and the absorption in the platinum wall could be calculated.

The counting rate at each absorber thickness was measured at least twice to give a statistical accuracy of about 1% for thicknesses out to 20 cm.; beyond 20 cm. the low counting rates resulted in somewhat larger uncertainties. After being corrected for the background counting rate and, where necessary, for counter dead time, the curves of counting rate vs. lead thickness for the different source strengths were normalized in the regions where they overlapped, so that a continuous transmission curve from 0 to 26 cm. was obtained.

## SCATTERING CORRECTION

Under the geometrical conditions used, the radiation reaching the counter will include an appreciable amount of secondary radiation scattered in the absorber; the contribution of this scattered radiation must be subtracted from the observed counting rates before the experimental transmissions can be compared with the calculated ones.

Tarrant (26) has estimated the effect of singly scattered radiation under conditions similar to those used here. As corrected by Davisson and Evans (6), his formula reduces at small angles to

$$S/B = N_e x_0 \pi r_0^2 \theta_0^2 [1 - (\theta_0^2/12)(9\alpha + 4)] \tag{1}$$

where $S/B$ is the ratio of the number of singly scattered photons to the number of primary photons detected, $N_e$ is the electron density in the absorber, $x_0$ is the absorber thickness, $\theta_0$ is the maximum angle through which a photon can scatter and still reach the detector, $r_0$ is $e^2/m_0c^2$, and $\alpha$ is the primary photon energy in units of $m_0c^2$. For the conditions of this experiment the term in square brackets is close to unity and can be neglected; the correction is then independent of photon energy. Further, if it is assumed that the scattering cross section for the radiation scattered through a few degrees is the same as for the primary radiation, one may take into account successive small-angle scatterings by writing the correction in the form

$$S/B = \exp N_e x_0 \pi r_0^2 \theta_0^2 - 1. \tag{2}$$

The value of $\theta_0$ in Equation (2) depends on the position of the "effective center" of the counter—that is, where, on the average, a $\gamma$ ray interacts in the counter to produce a count. Since electrons can be ejected both from the cylindrical copper cathode and from the glass end of the counter, this "effective center" will be somewhere between the center of the cathode and the end of the glass envelope, but its exact position is difficult to estimate. For this reason the average value of $\theta_0^2$ for each absorber thickness has been computed on the basis of two extreme assumptions: first, that the "effective center" is at the geometrical center of the cathode, and second, that it is at the end of the glass envelope. The experimental counting rates have been corrected with the aid of Equation (2) for these two assumptions.

It should be noted that since the above correction applies only to the radiation scattered so as to remain within the primary beam and takes no account of radiation scattered out of the beam and then back in again, it will tend, if anything, to underestimate the scattering contribution.* Consequently the use of Equation (2) and the first of the two assumptions mentioned above should give a lower limit for the scattering correction, and the counting rates thus corrected should represent upper limits to narrow-beam rates.

## EXPERIMENTAL RESULTS

The corrected counting rates, expressed as fractional transmissions, are shown in Fig. 1, the open and full circles denoting respectively the rates corrected on the basis of the first and second assumptions discussed in the previous section. The crosses show the results of Davisson and Evans (5, 6), who measured the transmission out to 14 cm. of lead under geometrical conditions that excluded practically all scattered radiation. The two sets of measurements, which in effect are normalized at 0 cm. of lead, diverge slightly with increasing thickness, a fact which may indicate that the scattering has been underestimated in the present experiment.

**The mathematical approximations used in deriving Equation (2) are actually such as to make the correction high, but only by a few per cent for the thickest absorbers used.*

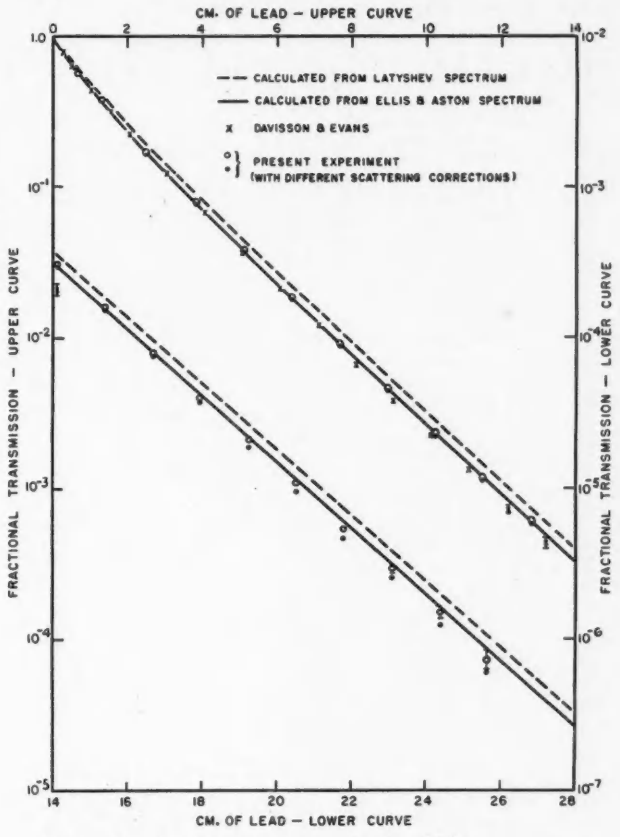


FIG.1. Fractional transmission vs. absorber thickness.

## COMPARISON OF EXPERIMENTAL AND CALCULATED TRANSMISSIONS

### (a) *Relative Intensities in the Ellis and Aston Spectrum*

Before calculating the transmission curve to be expected on the basis of the Ra(B + C) spectrum of Ellis and Aston, it is worth while to examine the basis for the relative intensities given by them. Ellis and Aston measured indirectly the relative numbers of photoelectrons ejected from a platinum foil by the different $\gamma$ rays. This measurement gave them a quantity proportional to $n.\tau_K$, the product of the number of $\gamma$ rays of a given energy emitted per disintegration and the photoelectric absorption cross section in the $K$-shell of platinum for that energy. Using an empirical formula due to L. H. Gray to estimate the $\tau_K$s, they were able to obtain relative values for $n$.

Since Gray's formula appears to fall off too rapidly at high energies, the relative intensities have been recalculated using the theoretical photoelectric

cross sections presented graphically by Davisson (5) from the calculations of Hulme *et al.* (13). The result is a reduction in the intensities of the high energies relative to the lower ones. To complete the spectrum, the $\gamma$ ray found by Wolfson (29) with an energy of 2.452 Mev. and an intensity of 35 to 40% of that of the 2.2-Mev. ray has been included.

The spectrum modified in this manner is presented in Table I. The energies are

TABLE I

REVISED $\gamma$ RAY SPECTRUM OF RADIUM IN EQUILIBRIUM WITH ITS DECAY PRODUCTS

| $h\nu$, Mev. | $n$ Ellis and Aston | $n$ Revised | $n.h\nu$ |
|---|---|---|---|
| 0·184 | — | 0·012 | 0·002 |
| 0·241 | 0·115 | 0·106 | 0·026 |
| 0·294 | 0·258 | 0·240 | 0·070 |
| 0·350 | 0·450 | 0·435 | 0·152 |
| 0·607 | 0·658 | 0·680 | 0·414 |
| 0·766 | 0·065 | 0·067 | 0·051 |
| 0·933 | 0·067 | 0·068 | 0·064 |
| 1·120 | 0·206 | 0·202 | 0·226 |
| 1·238 | 0·063 | 0·060 | 0·074 |
| 1·379 | 0·064 | 0·059 | 0·081 |
| 1·761 | 0·258 | 0·223 | 0·393 |
| 2·198 | 0·074 | 0·060 | 0·132 |
| 2·452 | — | 0·022 | 0·054 |

those remeasured by Ellis (8), with the addition of the 2.452-Mev. $\gamma$ ray from RaC and the 0.184-Mev. $\gamma$ ray emitted by Ra itself; the absolute intensities, $n$, were obtained by normalizing the recalculated relative intensities in a way described below.

(*b*) *Calculation of Transmission Curves*

The spectrum must next be corrected for absorption in the walls of the platinum capsule containing the radium. This has been done by multiplying the absolute intensity of each $\gamma$ ray by $\exp(-\mu'_t t)$, where $\mu'_t$ is the effective absorption coefficient of the $\gamma$ ray in platinum and $t$ is the effective thickness of the cylinder wall (21, 14). Evans and Evans (11) have reported that for lead cylinders placed around a source of $Co^{60}$ $\gamma$ rays (1.17 and 1.33 Mev.) $\mu' = \tau + \kappa + \sigma_a + 0.2\sigma_s$, where the symbols have their usual significance. On the basis of this result and an effective wall thickness of 0.55 mm. the $\gamma$-ray spectrum emerging from the capsule has been estimated.

The transmission curve was calculated using this filtered spectrum, the absorption coefficients in lead for each $\gamma$ ray given by Davisson (5), and the variation of the counter efficiency with quantum energy measured by Bradt *et al.* (2) for a brass counter. The result, shown by the solid line in Fig. 1, follows the experimental points quite closely.

In order to make a similar calculation for the Latyshev spectrum it was necessary to complete it by adding the low-energy $\gamma$ rays measured by Ellis and Aston, in the manner of Davisson (5). The intensities of these were normalized

to those of Latyshev at 1.120 Mev., both because this is the lowest-energy line measured by Latyshev and because it is an unambiguous single line of fairly high intensity. The transmission curve calculated on the basis of this composite spectrum is shown by the dashed line in Fig. 1; it lies considerably above the experimental points.

Since there is little difference in the *energies* of the principal γ-ray lines in the two spectra under consideration, the differences in the predicted transmission curves must be due mainly to the differences in the relative intensities of the rays of different energies. Thus the agreement with experiment of the curve based on the Ellis and Aston spectrum presumably indicates that the relative intensities in that spectrum are not greatly in error, while the fact that the curve based on the Latyshev spectrum lies above the experimental points suggests that the higher-energy rays in that spectrum are overemphasized.*

## EVIDENCE FROM OTHER EXPERIMENTS

Other indirect evidence on the relative intensities exists, but it is mostly inconclusive. L. H. Gray (12) concluded from the absorption curve of Ra(B + C) γ rays in a large block of aluminum that the high-energy components in the spectrum had been underestimated by Ellis and Aston, but his arguments were based on the assumption that the secondary radiation is in equilibrium with the primary after traversing 40 cm. of aluminum, and it has been shown both theoretically (25) and experimentally (27) that under these conditions the ratio of secondary to primary radiation increases indefinitely with increasing absorber thickness. Gray also cited the results of Chalmers (3), who analyzed a transmission curve out to 3 cm. of lead into two components which he attributed to the γ rays from RaB and RaC respectively, and obtained a ratio of 0.10 for the energies in these two components. Since Ellis and Aston's intensities lead to a considerably larger value for this ratio, the implication was again that the high-energy rays had been underestimated. However, in view of the large amount of scattered radiation which could enter Chalmers' electroscope, of the fact that the slope of the transmission curve changes appreciably beyond 3 cm. of lead, and of the complexity of the actual γ-ray spectrum, it is doubtful whether such a breaking-up of the curve can have much significance.

On the other hand, Sizoo and Willemsen (23) have used the spectrum of Ellis and Aston to calculate the transmission through a number of elements as measured in an aluminum ionization chamber, and have compared the results with the experimental data of Kohlrausch (15). They found almost perfect agreement.

## ABSOLUTE INTENSITIES

In a previous section the relative intensities based on the measurements of Ellis and Aston were recalculated. The absolute intensities must now be considered.

**Davisson and Evans made a similar comparison with their experimental data, using the unmodified Ellis and Aston spectrum, making their normalization to the Latyshev spectrum at 2·2 Mev., and assuming that their counter efficiency was proportional to quantum energy. Although both curves lie near the experimental points, it was difficult to make a choice between them.*

The absolute intensities are obtained by normalizing the relative intensities so as to make the total energy emitted in $\gamma$ rays per disintegrating radium atom equal to $Q_0/R$, where $Q_0$ is the total $\gamma$-ray energy emitted per unit time by a gram of radium in equilibrium with its decay products, and $R$ is the number of radium atoms disintegrating per unit time in a gram of radium. For $R$ Ellis and Aston appear to have used $3.70 \times 10^{10}$ disintegrations per gm. per sec., but more recent evidence points to a value somewhere between this and $3.60 \times 10^{10}$ (22, 10, 16). For the present purpose a value of $3.65 \times 10^{10}$ disintegrations per gm. per sec. will be used; this is unlikely to be in error by more than 1%.

The magnitude of $Q_0$ is less certain. Ellis and Aston used a figure of 9.2 cal. per gm. per hr. based on early measurements of L. H. Gray by the ionization method. But Gray's final experiment (12) yielded a value between 8.3 and 8.5 cal. per gm. per hr., whereas the best calorimetric determination (30) is $9.1 \pm 0.15$ cal. per gm. per hr. On the basis of these measurements Gray concluded that the most probable value was 8.75 cal. per gm. per hr.*

Taking $Q_0 = 8.75$ cal. per gm. per hr. and $R = 3.65 \times 10^{10}$ disintegrations per gm. per sec., one obtains for the total $\gamma$-ray energy emitted from radium and its equilibrium products a value of 1.74 Mev. per disintegrating radium atom. Since virtually all this energy is included in the Ra and Ra(B + C) $\gamma$ rays listed in Table I, normalizing the relative intensities of these rays to give a total of 1.74 Mev. per disintegration gives one the absolute intensities, $n$, measured in $\gamma$ rays per disintegrating radium atom. These are the numbers listed in the third column of Table I. On the average they are a few per cent less than those given by Ellis and Aston. The fourth column gives the total energy in each $\gamma$-ray line per radium disintegration.

It is possible to subject the absolute intensities to an indirect comparison with experiment by using them to calculate the number of roentgens per hour to be expected at a meter (rhm) from a gram of radium. This quantity has been measured for the $\gamma$ rays of radium filtered by 0.5 mm. of platinum many times and by a variety of methods; from a survey of the more recent determinations Evans (10) has arrived at a value of $0.84 \pm 0.02$ rhm, which agrees well with an earlier survey of Laurence (19) leading to 0.835 rhm. From empirical data, Evans has also estimated the absorption in the platinum to be $10 \pm 2\%$, so that the value for unfiltered rays should be around 0.93 rhm.

*Dacey, Paine, and Goodman (4) have also reported a mean value of 8·75 cal. per gm. per hr. from a series of ionization measurements in different liquid media, but this figure would seem to require modification. First, the figure includes a correction of about 7% for the difference in the stopping power per electron, for electrons, between the liquid medium and the air in the measuring chamber. But this correction properly applies to the material surrounding the air volume in which the ionization is measured, which in this case was not the medium but the aluminum wall of the chamber used; further, since the chamber had been calibrated to read directly in roentgens, its readings presumably corresponded to the ionization in an air-wall chamber, for which no correction is necessary. Eliminating this correction from the measurements leads to a value of 8·20 cal. per gm. per hr. This figure, however, appears to apply only to the $\gamma$ radiation which was able to penetrate the steel capsule containing the source and a steel shell surrounding it. If account is taken of the curvature of the capsule wall, this amounts to an effective thickness of 0·38 cm. of steel, in which the absorption of the unfiltered radiation will be of the order of 10%. Thus the value of $Q_0$ indicated by these measurements is probably nearer to 8·20/0·90 = 9·1 cal. per gm. per hr. However, in view of the uncertainties in the above figure, the value of 8·75 cal. per gm. per hr. put forward by Gray has been used here.*

The value for unfiltered rays has been calculated, in the manner described by Evans, on the basis of the spectrum of Table I; the result is 0.93 rhm. When the absorption in 0.5 mm. of platinum is included in the calculation the result is 0.84 rhm. Both these figures are in good agreement with experiment. Evans (10) has estimated the unfiltered value on the basis of the intensities given by Ellis and Aston and obtained 0.969 rhm. The disagreement with the experimental figure is not greatly outside the estimated error, but it tends to reinforce the indications that the Ellis and Aston intensities are a few per cent high.

## CONCLUSIONS

Of the two principal determinations of the γ-ray spectrum of Ra(B + C), that of Ellis and Aston, as modified above, leads to better agreement with experiments on the absorption in lead than that of Latyshev *et al.* This does not mean, of course, that only those γ-ray energies found by Ellis and Aston are actually present, but it suggests that the general distribution of energy through the spectrum reported by them is more nearly correct than that found by Latyshev. The spectrum presented in Table I may be expected to give reasonably accurate results in calculations of the absorption of Ra(B + C) γ rays in matter.

## ACKNOWLEDGMENTS

It is a pleasure to thank Mr. W. R. Dixon for numerous helpful discussions.

## REFERENCES

1. ALICHANOW, A. I. and LATYSHEV, G. D. J. Phys. (U.S.S.R.), 3: 263. 1940.
2. BRADT, H., GUGELOT, P. C., HUBER, O., MEDICUS, H., PREISWERK, P.. and SCHERRER, P. Helv. Phys. Acta, 19: 77. 1946.
3. CHALMERS, J. A. Phil. Mag. 6: 745. 1928.
4. DACEY, J. E., PAINE, R. W., and GOODMAN, C. Mass. Inst. Technol., Laboratory of Nuclear Science and Engineering, Tech. Rept. No. 23.
5. DAVISSON, C. M. Massachusetts Institute of Technology, Thesis, 1948.
6. DAVISSON, C. M. and EVANS, R. D. Phys. Rev. 81: 404. 1951.
7. ELLIS, C. D. Proc. Roy. Soc. (London), A, 99: 261. 1921; A, 101: 1. 1922.
8. ELLIS, C. D. Proc. Roy. Soc. (London), A, 143: 350. 1933.
9. ELLIS, C. D. and ASTON, G. H. Proc. Roy. Soc. (London), A, 129: 180. 1930.
10. EVANS, R. D. Nucleonics, 1: 32. October, 1947.
11. EVANS, R. D. and EVANS, R. O. Revs. Modern Phys. 20: 305. 1948.
12. GRAY, L. H. Proc. Roy. Soc. (London), A, 159: 263. 1937.
13. HULME, H. R., MCDOUGALL, J., BUCKINGHAM, R. A., and FOWLER, R. H. Proc. Roy. Soc. (London), A, 149: 131. 1935.
14. KEYSER, G. M. Can. J. Phys. 29: 301. 1951.
15. KOHLRAUSCH, K. W. F. Wien. Ber. 126: 441, 683, 887. 1917.
16. KOHMAN, T. P., AMES, D. P., and SEDLET, J. MDDC 852, Argonne National Laboratory, March 25, 1947.
17. LATYSHEV, G. D. Revs. Modern Phys. 19: 132. 1947.
18. LATYSHEV, G. D., KOMPANEETZ, A. F., BORISOV, N. P., and GUSAK, I. M. J. Phys. (U.S.S.R.), 3: 251. 1940.
19. LAURENCE, G. C. Can. J. Research, A, 15: 67. 1937.
20. MANN, K. C. and OZEROFF, M. J. Can. J. Research, A, 27: 164. 1949.
21. OWEN, E. A. and NAYLOR, B. Proc. Phys. Soc. (London), 34: 92. 1922.
22. PANETH, F. A. Nucleonics, 8: 38. May, 1951.
23. SIZOO, G. J. and WILLEMSEN, H. Physica, 5: 100. 1938.
24. SKOBELZYN, D. Z. Physik, 43: 354. 1927; 58: 595. 1929.
25. SPENCER, L. V. and FANO, U. J. Research Natl. Bur. Standards, 46: 446. 1951.
26. TARRANT, G. T. P. Proc. Cambridge Phil. Soc. 28: 475. 1932.
27. WHITE, G. R. Phys. Rev. 80: 154. 1950.
28. WILSON, C. W. Radium therapy, its physical aspects. Chapman and Hall, Ltd., London. 1945. p. 17.
29. WOLFSON, J. L. Phys. Rev. 78: 176. 1950.
30. ZLOTOWSKI, I. J. phys. radium, 6: 241. 1935.

# MUTUAL INDUCTANCE OF CIRCUITS ON A TWO LAYER EARTH[1]

By James R. Wait[2]

ABSTRACT

A general formula is derived for the mutual inductance of ungrounded insulated wires lying on the surface of a two layer earth with a small conductivity contrast between the layers.

In a previous paper (2) the author has investigated the problem of a magnetic dipole of time varying strength on the surface of a flat horizontally stratified earth. The evaluation of the integrals occurring in the formal solution of this problem is very difficult. Only special cases were treated in detail in that paper.

The case of the magnetic dipole on the two layer earth which has only a small contrast in electrical conductivity between the two regions is another special case of the general problem which yields a solution expressible in tabulated functions. The result is considered to be of interest to geophysicists. This particular solution will be carried out in this paper.

A conventional cylindrical polar coordinate system is employed. The dipole of area $dA$, carrying a circulating $I$, is situated at the origin and oriented in the $z$ direction. The earth's surface is at $z = 0$ and the interface between the upper and lower layers is at $z = -d$. The conductivity of the upper layer is denoted by $\sigma_1$, and that of the lower layer by $\sigma_2$. The magnetic permeability is denoted by $\mu$ and assumed not to vary for any of the regions. All displacement currents are considered to be negligible. This is usually quite valid for frequencies that are used in geophysical prospecting as pointed out in the author's previous paper (2). The tangential electric field component $E_\phi$ and the vertical magnetic field component $H_z$ on the surface of the earth (i.e. $z = 0$) are given in terms of a wave function $F$ as follows:

$$E_\phi = \frac{\partial F}{\partial \rho} \tag{1}$$

and

$$i\mu\omega H_z = \frac{1}{\rho}\frac{\partial}{\partial \rho}\left(\rho \frac{\partial F}{\partial \rho}\right) \tag{2}$$

where

$$F = \frac{i\mu\omega I dA}{2\pi}\int_0^\infty \frac{[(u_1 + u_2) + (u_1 - u_2)\exp(-2du_1)]\lambda\, J_0(\lambda\rho)}{(\lambda+u_1)(u_1+u_2) + (\lambda-u_1)(u_1-u_2)\exp(-2du_1)}\, d\lambda, \tag{3}$$

$$u_1 = (\lambda^2 + \gamma_1^2)^{\frac{1}{2}}, \quad \gamma_1^2 = i\sigma_1\mu\omega,$$

and

$$u_2 = (\lambda^2 + \gamma_2^2)^{\frac{1}{2}}, \quad \gamma_2^2 = i\sigma_2\mu\omega.$$

[1] *Manuscript received February 19, 1952.*
*Contribution from Newmont Exploration Limited, Jerome, Ariz.*
[2] *Research Engineer, Newmont Exploration Limited. Now with Defence Research Board, Ottawa.*

The function $F$ can now be broken into two integrals as follows:

$$F = R - Q \tag{4}$$

where

$$R = \frac{i\mu\omega IdA}{2\pi}\int_0^\infty (\lambda + u_1)^{-1}\lambda\, J_0(\lambda\rho)\, d\lambda = i\omega IdA\, M_1(\rho) \tag{5}$$

$$\text{with } M_1(\rho) = \mu[1 - (1 + \gamma\rho)\exp(-\gamma\rho)]/2\pi\gamma^2\rho^3 \tag{6}$$

and

$$Q = \frac{i\mu\omega IdA}{2\pi}\int_0^\infty \frac{2u_1(u_2 - u_1)\exp(-2u_1d)\lambda\, J_0(\lambda\rho)}{(u_1 + u_2)(\lambda + u_1)^2 - \gamma_1^2(u_1 - u_2)\exp(-2u_1d)}\, d\lambda. \tag{7}$$

The first integral is the form $F$ takes when the earth is homogeneous with conductivity $\sigma_1$. The second integral may be interpreted as the effect of the lower layer at depth $d$.

It will now be assumed that the conductivity contrast between the layers is small such that

$$\sigma_2 = \sigma_1 + \Delta$$

where $|\Delta| \ll \sigma_1$. The following substitution can then be made:

$$u_2 - u_1 \cong \Delta i\mu\omega/2u_1.$$

The integral $Q$ then simplifies considerably to the following form with this approximation:

$$Q = \frac{(i\mu\omega)^2 IdA\Delta}{4\pi}\int_0^\infty \frac{\exp(-2u_1d)}{u_1(\lambda + u_1)^2}\,\lambda\, J_0(\lambda\rho)\, d\lambda. \tag{8}$$

The numerator and denominator of this preceding expression are both multiplied by $(u_1 - \lambda)^2$ to give

$$Q = \frac{IdA\Delta}{4\pi\sigma_1^2}\int_0^\infty (2u_1^2 - 2\lambda u_1 - \gamma_1^2)u_1^{-1}\exp(-2u_1d)\,\lambda\, J_0(\lambda\rho)\, d\lambda. \tag{9}$$

This can be rewritten in terms of derivatives with respect to a parameter $a$ of two known integrals which are referred to in the author's previous paper (2).

$$Q = \frac{IdA\Delta}{4\pi\sigma_1^2}\left\{\left(2\frac{\partial^2}{\partial a^2} - \gamma_1^2\right)P - \left(2\frac{\partial^3}{\partial a^3} - 2\gamma_1^2\frac{\partial}{\partial a}\right)N\right\} \tag{10}$$

where

$$P = \int_0^\infty J_0(\lambda\rho)\, u_1^{-1}\exp(au_1)\,\lambda d\lambda = \exp(-\gamma_1 r)/r \tag{11}$$

and

$$N = \int_0^\infty J_0(\lambda\rho)\, u_1^{-1}\exp(au_1)\, d\lambda = I_0[(\gamma_1/2)(r + a)]\, K_0[(\gamma_1/2)(r - a)] \tag{12}$$

where $r = [a^2 + \rho^2]^{\frac{1}{2}}$ and $a = -2d$.

These differentiations can be carried out to give the following expression for $Q$:

$$Q = i\omega IdA\ M_2(\rho) \tag{13}$$

where

$$\begin{aligned} M_2(\rho) = \frac{\mu\Delta}{4\pi\sigma_1}\Big\{ & 2\gamma_1^{-2}r^{-5}[(3a^2 - r^2)(1 + \gamma_1 r) + \gamma_1^2 r^2 a^2]e^{-\gamma_1 r} \\ & - r^{-1}e^{-\gamma_1 r} + ar^{-4}(3a^2 - r^2)I_0K_0 + 3\rho^2 ar^{-4}I_1K_1 \\ & + [\gamma_1^{-1}r^{-5}(r^2 - 3a^2)(r - a) - \gamma_1\rho^2 ar^{-3}]I_0K_1 \\ & + [\gamma_1^{-1}r^{-5}(r^2 - 3a^2)(r + a) + \gamma_1\rho^2 ar^{-3}]I_1K_0\Big\} \end{aligned} \tag{14}$$

where the arguments of the $I$ and $K$ functions are as given in equation (12). The function $F$ is then given by

$$F = [M_1(\rho) - M_2(\rho)]i\omega IdA. \tag{15}$$

The actual field components $E_\phi$ and $H_z$ on the surface of the two layer earth can then be evaluated by carrying out the operations indicated in equations (1) and (2). The mutual inductance $M$ between two insulated wire circuits lying on the surface of the earth with small contrast in conductivity between the layers can then be written down immediately, employing the general result derived in the previous paper (2).

$$M = \int_{C_1}\int_{C_2} [M_1(\rho) - M_2(\rho)] \cos\epsilon\, dS\, ds. \tag{16}$$

The contours of the circuits are denoted by $C_1$ and $C_2$ respectively. $\epsilon$ is the angle subtended by infinitesimal elements $dS$ and $ds$ of the wires respectively. The functions $M_1(\rho)$ and $M_2(\rho)$ are computable and they involve only elementary transcendental functions and the modified Bessel functions with an argument proportional to the square root of $i$. These latter functions are tabulated by McLachlan (1) and others.

ACKNOWLEDGMENT

The author would like to express his appreciation to Dr. A. A. Brant of Newmont Exploration Ltd. for his permission to publish this paper.

REFERENCES

1. McLachlan, N. W. Bessel functions for engineers. Oxford University Press. 1934.
2. Wait, J. R. Can. J. Phys. 29: 577. 1951.

# SIZE DISTRIBUTION OF COSMIC RAY STARS IN PHOTOGRAPHIC EMULSIONS[1]

By J. Y. Mei[2]

ABSTRACT

In an analysis of cosmic ray stars found in Ilford G5 emulsions exposed at about 85,000 ft. the star-size distribution curve shows a change in slope at a prong number of about 8.5. A similar effect is shown for emulsions exposed at airplane altitudes, and it is assumed that the effect is mainly due to the composition of the emulsions. While the primary particles producing the stars at about 85,000 ft. are mostly protons, about 50% of the low energy stars are produced by nonionizing radiation, presumably neutrons. α-Particles and heavier nuclei produce about 30% of the larger energetic stars. The absolute frequency of star production is given.

## INTRODUCTION

The work now reported resulted from an exposure of Ilford G5 emulsions to cosmic rays at about 85,000 ft. in a balloon flight. Numerous reports dealing with the general statistics of stars at both mountain top and balloon altitudes have appeared (2), but a few specialized aspects are dealt with here. The presence of a break in the star-size distribution curve has been discussed recently by Birnbaum *et al.* (1), their evidence indicating that the effect is due to the presence of a light (carbon, nitrogen, oxygen) and a heavy (silver, bromine) group of nuclei in the emulsion*. The present work confirms the presence of a break with much better statistics than previously obtained. Estimating the relative numbers of stars produced in the two groups of nuclei in the emulsion from the star-size distribution curve and the known emulsion composition it is confirmed that the cross section for star production is of the order of the geometrical cross section.

While the more energetic stars at balloon altitudes are produced predominantly by protons and the low energy stars by neutrons it is shown that primary α-particles and heavier nuclei play an important role in producing the larger and more energetic stars, i.e. those with 40 or more prongs (charged particles). Such stars occur infrequently.

## EXPERIMENTAL TECHNIQUE

The photographic emulsions used were Ilford G5 of 250μ thickness and lateral dimensions 3 × 2 in., and they were exposed in a "Skyhook" balloon flight at 54° N. geomagnetic latitude. The time altitude curve for the flight is shown in Fig. 1. The emulsions were developed in elon by the temperature development method (5), and recorded minimum ionization particles with a grain density of about 30 grains per 100μ. The preliminary microscope scanning was done with a magnification of about 250 times.

[1] *Manuscript received May 20, 1952.*
*Contribution from the Department of Physics, National Research Council, Ottawa. Issued as N.R.C. No. 2813.*

[2] *National Research Laboratories Postdoctorate Fellow.*

**While there is an appreciable amount of hydrogen in the emulsion, its effects are relatively rare because of the small geometric cross section. Also these interactions can be readily distinguished from the others.*

Only stars with more than two prongs were counted, all recognizable prongs of whatever length and density being included. To eliminate the small fraction of background stars due to radioactive contamination, stars were rejected unless

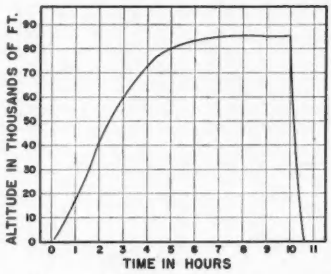


FIG. 1. Time altitude curve for the balloon flight.

at least one prong was longer than $50\mu$. Also the reported number of prongs includes the incident particle even in the cases where this was charged and it was possible to recognize it.

## STAR-SIZE DISTRIBUTION

Fig. 2, curve $A$ shows the variation of the number of stars with at least $n$ prongs, plotted logarithmically, with $n$, the number of prongs, for the balloon flight. The experimental points lie on a smooth line with a significant change of slope when the number of prongs equals 8.5. The fluctuations in the curve for

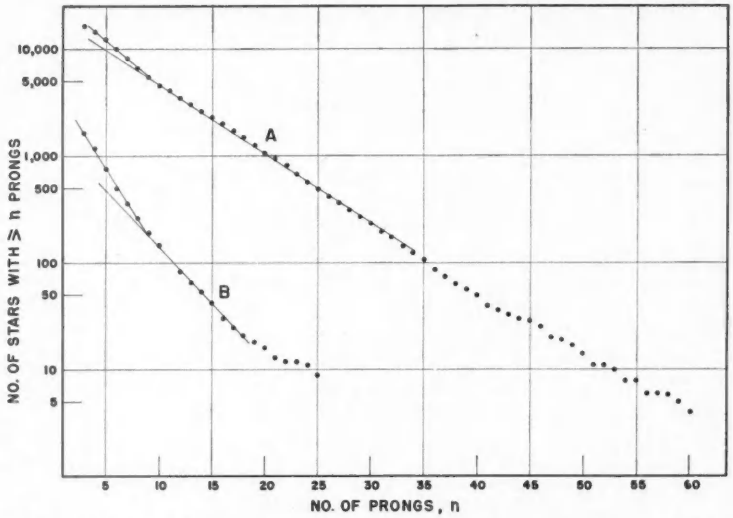


FIG. 2. Rate of variation of numbers of stars with $\geqslant n$ prongs against $n$ for $A$ — balloon flight, and $B$ — airplane flights. Both curves show change in slope at $n \simeq 8.5$.

prong number larger than about 40 are mainly statistical, owing to the small numbers of events. Also the slope of the curve in this region may be influenced by the fact that some mesons are always created in these particular events. Curve *B* is for Ilford G5 emulsions exposed in airplane flights for several hundred hours*. There is a similar change in slope for a prong number of about 8.5.

Such a break has been pointed out by Birnbaum *et al.* (1) and earlier investigators** and the most logical explanation is, as pointed out by Birnbaum *et al.*, that the increase in slope for the lower prong numbers is mainly due to stars formed in the lighter group of nuclei in the emulsions. These light nuclei (carbon, nitrogen, oxygen) in general would not be expected to give stars with more than seven or eight prongs. The present results can be compared most directly with those of Lord (6) from whose measurements the break occurs at about 11 prongs. Birnbaum *et al.* defined the star size by the number of heavy prongs and thus excluded tracks with grain density less than about 1.4 times the minimum value, and this probably explains why their break occurs at 7.5 compared with the present value of 8.5 prongs. A small percentage of high energy protons and mesons is included in the present work, and this would shift the break slightly towards a higher prong number. The fact that the break occurs at about the same prong number for both low and high altitudes supports the view that it is due to emulsion composition, rather than a cosmic ray effect.

Extrapolating the right part of curve *A* beyond the break, back to $n = 3$, should give the number of stars with at least three prongs owing to the heavy elements. The ratio of the total number of stars with at least three prongs to the number of the same stars produced in the heavy group of elements is then nearly 1.3, in agreement with the results of Birnbaum *et al.* (1). A similar result may be calculated from the known composition of the emulsion, assuming the collision cross section to be geometric. This indirect evidence for an approximately geometric cross section is in agreement with direct measurements in emulsions (4).

## NATURE OF STAR PRODUCING PRIMARIES

An analysis of data on two plates (840 stars) from the balloon flight indicates that about 50% of the low energy stars (no shower tracks) are caused by neutral radiation, presumably neutrons, while 30% of stars had at least one shower track, and, of these latter, 70% were proton induced. In this work tracks coming from the stars with less than about 1.5 times minimum ionization were designated as shower particles. Singly charged tracks were assigned as the primary producing radiation if they were opposite a number of shower tracks or, in cases with only a few or no shower tracks, if they were in the upper hemisphere. Recent work by Camerini *et al.* (3) indicates that about 94% of such primaries at balloon flight altitudes are protons, the rest being mesons.

Fig. 3 shows a histogram for all stars in the batch of emulsion plates from the balloon flight, with at least four shower tracks, these being produced by

**From some early unpublished work by E. Pickup. These plates were exposed by the courtesy of Trans-Canada Airlines.*

***See Reference 1 for full bibliography.*

protons, neutrons, relativistic $\alpha$-particles, and heavier nuclei ($Z$ at least 3). These stars are predominantly proton induced, but it is interesting to note that $\alpha$-particles and heavier nuclei produce a considerable fraction of the more energetic stars. The stars induced by $\alpha$-particles and heavier nuclei often have many heavy prongs also. This is to be expected since for incident particles with $Z$ at least 2, more nucleons in general may be involved in a collision with a target nucleus, each contributing to the creation of shower particles (mainly mesons) and to the residual excitation of the target nucleus, which gives the heavy prongs. Forty-four stars having at least 40 prongs included 11 unambiguously produced by particles with $Z$ at least 2, 18 by protons, 7 probably by

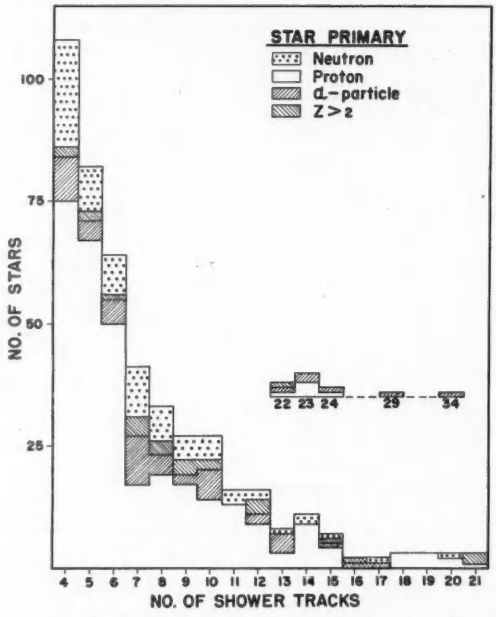


FIG. 3. Histogram showing nature of initiating radiation for stars with increasing number of shower tracks ( $\gtrsim$ 1.5 minimum ionization) for the balloon flight.

neutral particles, and 8 whose primary could not be decided. For some of the proton cases the primary assignment was doubtful since there would be a possible relativistic $\alpha$-particle and one or two shower tracks in the upper hemisphere also, with the forward shower particles lying in a wide cone. In such cases the ambiguity could only be resolved definitely by energy measurements (scattering) but, unfortunately, this is usually impossible because of steepness of tracks. Fig. 4 is a microprojection tracing, illustrating a typical case of a probable proton induced star with about 45 prongs produced in a bromine or silver nucleus in the emulsion and with several shower tracks in the upper hemisphere.

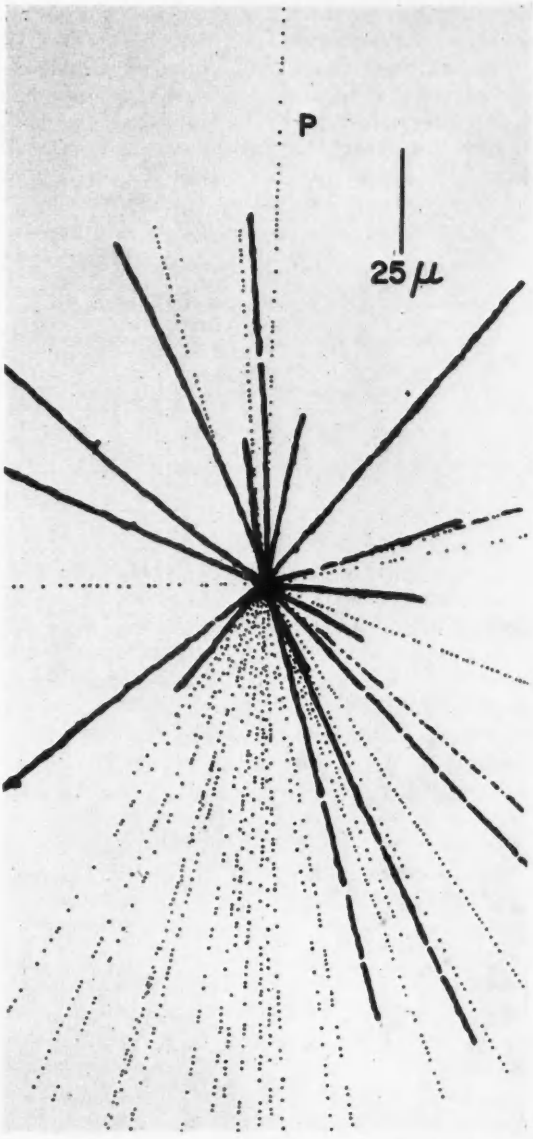


FIG. 4. Large star with shower, formed in silver or bromine in G5 emulsion, caused by probable proton at ~ 85,000 ft., and showing several backward shower tracks.

## RATE OF STAR PRODUCTION

In the present work there were about 500 stars (excluding slow meson events, two-pronged stars, and radioactive contamination stars) per plate. The absolute frequency of events is given in Table I and is based on a total of 840 stars from two plates, a fraction of stars occurring near glass or air being excluded. Also a correction, which would be several per cent, was not made for background stars formed below 85,000 ft. The results are in reasonable agreement with data given by Lord (6) although in the present work there appears to be a greater ratio of proton to neutron stars than in Lord's case. This difference may be caused by different amounts of auxiliary material near the plates in the two experiments.

TABLE I

RATE OF PRODUCTION OF STARS WITH MORE THAN TWO PRONGS PER CC. PER DAY AT 54° N.

| Primary | ~ 85,000 ft. data (assuming 6 hr. flight) | Lord (~90,000 ft.) |
|---|---|---|
| Neutron | 1010 | 1400 |
| Proton | 1360 | 873 |
| $\alpha$-particle | 106 | 107 |
| Heavy nuclei | 11 ($Z > 2$) | 7 ($Z \geqslant 6$) |

## ACKNOWLEDGMENTS

The author is indebted to Dr. E. Pickup for his help and advice in this work, to Misses B. Woodruff, B. Mear, and S. W. Young for scanning, and to Mr. D. Rushton for the drawings and photograph. The emulsions at 85,000 ft. were exposed through a collaborative program of cosmic ray investigations by the Bartol Research Foundation and the National Research Council of Canada with the co-operation of the ONR project "Skyhook". The author is also grateful to the National Research Council of Canada for the award of a fellowship.

## REFERENCES

1. BIRNBAUM, M., SHAPIRO, M. M., STILLER, B., and O'DELL, F. W. Phys. Rev. 86: 86. 1952.
2. BROWN, R. H., CAMERINI, U., FOWLER, P. H., HEITLER, H., KING, D. T., and POWELL, C. F. Phil. Mag. Ser. 7, 40: 862. 1949. (A fuller bibliography will not be given here.)
3. CAMERINI, U., DAVIES, J. H., FOWLER, P. H., FRANZINETTI, C., MUIRHEAD, H., LOCK, W. O., PERKINS, D. H., and YEKUTIELI, G. Phil. Mag. Ser. 7, 42: 1241. 1951.
4. CAMERINI, U., FOWLER, P. H., LOCK, W. O., and MUIRHEAD, H. Phil. Mag. Ser. 7, 41: 413. 1950.
5. DILWORTH, C. C., PAYNE, R. M., and OCCHIALINI, G. P. S. Nature, 161: 120. 1948.
6. LORD, J. J. Phys. Rev. 81: 901. 1951.

# THE DISINTEGRATION OF $Tm^{170}$[1]

By R. L. Graham, J. L. Wolfson, and R. E. Bell


## ABSTRACT

The radiations from the decay of $Tm^{170}$ (127 day) have been studied by means of a lens type $\beta$-ray spectrometer, a scintillation spectrometer, short resolving time ($2\tau_0 = 2 \times 10^{-9}$ sec.) coincidence counting techniques, and a pair of lens type $\beta$-ray spectrometers placed end to end with coincidence counting of the focused radiations from a single source. A disintegration scheme is proposed which is consistent with the experimental results. Decay is found to be by negative $\beta$-ray emission; the spectrum consists of two components, one of maximum energy $968 \pm 4$ kev. (76%) proceeding to the ground state of $Yb^{170}$ and one of maximum energy $884 \pm 4$ kev. (24%) to an excited state in $Yb^{170}$ followed by emission of a $\gamma$ ray or conversion electron to the ground state. The $\gamma$-ray transition in $Yb^{170}$ is found to have an energy of $84.1 \pm 0.1$ kev., a half-life of $(1.57 \pm 0.05) \times 10^{-9}$ sec., and conversion coefficients $\alpha_K = 1.60 \pm 0.15$, $\alpha_L = 4.1 \pm 0.5$, $\alpha_M = 1.2 \pm 0.2$ which show that it is electric quadrupole in character. Upper limits are given for decay by $K$ capture, 0.3%, or positive $\beta$-ray emission, 0.01%, and also for the occurrence of other $\gamma$ rays.


## I. INTRODUCTION

The 127 day $\beta$ activity arising from neutron bombardment of stable $Tm^{169}$ was first identified by Bothe (6). The $\beta$-ray spectrum has been reported to be simple with an upper energy end point near 970 kev. by Ketelle and Boyd (19), Saxon and Richards (36), Graham and Tomlin (14), and Agnew (1). Grant and Richmond (16) reported that the $\beta$-ray spectrum is highly complex with the components ending at 1.00, 0.90, 0.79, and 0.45 Mev. Fraser (10) found that the $\beta$-ray spectrum consisted of two components, one (90%) with an upper energy end point of 970 kev. leading directly to the ground state of $Yb^{170}$ and the other (10%) to an 84 kev. excited state in $Yb^{170}$. All experimenters are agreed that the $\beta$ decay is accompanied by a $\gamma$ transition of about 84 kev. which is highly converted internally in the $L$ shell. Bell and Graham (4) have obtained a value of $T_{1/2} = (1.6 \pm 0.2) \times 10^{-9}$ sec. for the half-life of this transition. It has been classified as an electric quadrupole transition on the basis of its lifetime and of the ratio of $K$ to $L$ conversion coefficients by Goldhaber and Sunyar (18). Grant and Richmond (16) also report evidence for two weaker gamma rays at about 200 and about 430 kev. and more recently (15) report that there are three gamma rays at 198, 360, and 550 kev. The disintegration scheme suggested by Fraser has been tentatively accepted in the tables of Mitchell (27) and Way (40).

Novey (31) reported finding an asymmetry in the $\beta$–$\gamma$ angular correlation, from which he concluded that the lower energy $\beta$-ray spectrum should have the $\alpha$ forbidden shape ($\Delta J = 2$, yes). However, from his later work (32) it appears that the asymmetry might be due, at least in part, to coincidences between $\beta$ rays and inner bremsstrahlung. Also Siegbahn (38) finds no anisotropy in the angular correlation between $L$-conversion electrons of the 84 kev. $\gamma$ transition

[1] *Manuscript received May 12, 1952.*
*Contribution from Atomic Energy of Canada, Ltd., Chalk River Project, Chalk River, Ontario. Issued as A.E.C.L. No. 1.*

and $\beta$ rays. Quite recently Richmond and Rose (34) have examined the lower energy spectrum by coincidence-spectrometer techniques and find it to be nearly allowed in shape.

$Tm^{170}$ has been investigated extensively in this laboratory during the past two years using a wide variety of experimental techniques and sources of high specific activity produced by neutron irradiation in the NRX pile. Preliminary results on the shape and end point of the low energy $\beta$-ray spectrum were reported at the Kingston meeting of the Royal Society of Canada in June 1950 (12).

## II. PRIMARY $\beta$-RAY SPECTRUM

The spectrum of primary $\beta$ rays from $Tm^{170}$ was investigated in a conventional lens spectrometer of focal length 9 cm. normally adjusted for full line width at half intensity of 1.57%. The line width was reduced to 1.25% for one investigation at energies above 500 kev. On this occasion the detector was a scintillation counter consisting of a $\frac{1}{2}$ mm. thick anthracene disk 4 mm. in diameter, masked to 2 mm. diameter, a 1 ft. long lucite light pipe and a magnetically shielded 5819 photomultiplier. For all other investigations the detector was a Geiger counter having a 4 mm. diameter window of 0.3 mgm. per $cm.^2$ quartz or 0.045 mgm. per $cm.^2$ Zapon film supported on a screen of 0.004 in. copper wire.

Sources were prepared from a nitric acid solution of spectroscopically pure $Tm_2O_3$ powder which had been irradiated in the Chalk River reactor to an activity of about 15 mc. per mgm. Some sources were made by evaporating to dryness small amounts of the solution on 20 $\mu$gm. per $cm.^2$ acid-resistant films. As has been found by other workers (22) sources made in this manner tend to have local thicknesses much greater than their average surface density, which give rise to abnormally wide conversion lines. By examining the internal conversion lines it was found that more uniform sources could be prepared by precipitation of the thulium with ammonium hydroxide on a backing of mica, followed by drying and subliming of the ammonium nitrate under heat.

The $\beta$-ray spectrum of $Tm^{170}$ in the region above 500 kev. was examined with a spectrometer resolution of 1.25% in an effort to determine its shape accurately near the end point. The detector was the scintillation counter described above. A source mounted on 2.7 mgm. per $cm.^2$ Al foil was used which had a diameter $\backsim$ 2 mm., an average thickness $\backsim$ 10 $\mu$gm. per $cm.^2$, and an activity $\backsim$ 6$\mu$c. An allowed Fermi plot of the $Tm^{170}$ data, corrected for background and finite spectrometer resolution (33), is shown in Fig. 1, curve *A*. The system was checked for reliability in this energy region by observing the $\beta$ spectrum from a 2 mm. diameter, 0.2 mgm. per $cm.^2$ $Au^{198}$ source. This gave a straight Fermi plot and an extrapolated end point of 962 $\pm$ 4 kev. The internal conversion lines of the accurately known 411.6 kev.* $\gamma$-ray transition in $Hg^{198}$ were used for energy calibration. The extrapolated end point of the $Tm^{170}$ spectrum is 968 $\pm$ 4 kev. and the plot appears to break at about 884 kev., indicating the presence of a lower energy component. Assuming that the lower energy component leads to

**The value of 411·2 ± 0·1 kev. previously assigned by DuMond (9) is now believed to be about 0·1% too low.*

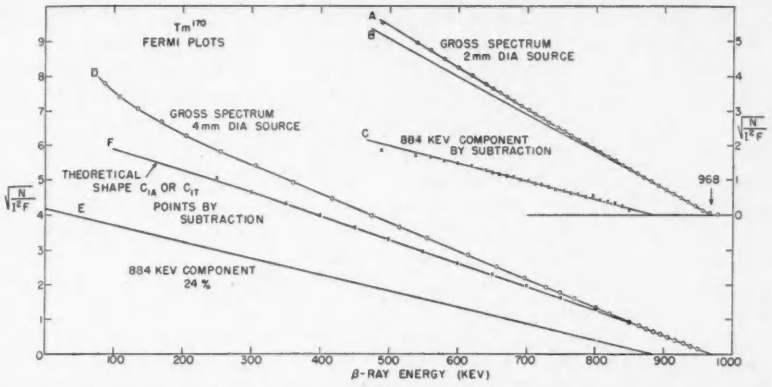


FIG. 1. Fermi plots of the $\beta$-ray spectrum of $Tm^{170}$. The circles on curves $A$ and $D$ represent the experimental data. Standard deviations are less than the radii of the circles. Curve $B$ is the high energy component obtained by extrapolation assuming an allowed shape, and curve $C$ is the low energy component obtained by subtraction. The intensity of the low energy component estimated in this way (16%) is inconsistent with other measurements. Curve $E$ is the low energy component having an allowed shape and an intensity of 24%, as determined by the intensity of the 84.1 kev. $\gamma$ transition in $Yb^{170}$. The points $X$ are obtained by subtracting $E$ from $D$. Curve $F$ is the theoretical shape of a first forbidden 968 kev. component of intensity 76%, assuming either tensor or axial vector interaction, for a $1 \rightarrow 0$ (yes) transition.

the 84.1 kev. excited state of $Yb^{170}$, analysis of the allowed Fermi plot and reconstruction of the two partial spectra lead to an intensity of 16% of the total disintegration rate for the component of lower energy. This may be compared with Fraser's result (10) of about 10%.

The $\beta$-ray spectrum of $Tm^{170}$ from 85 kev. to its upper end point has been examined using a spectrometer resolution of 1.57% and the Geiger counter as detector. The low energy data were taken using the Zapon counter window and the high energy data using the quartz window. These were normalized over the region 130-170 kev. to correct for opacity of the screen supporting the Zapon counter window ( $\backsim$ 15%). Minor corrections were applied for absorption in the window material itself using the data of Saxon (37). A number of spectra were obtained using different sources and source backings. All display a rise at energies below 300 kev. which varies somewhat with source thickness. An allowed Fermi plot of the spectrum obtained using a 4 mm. diameter precipitated source of average thickness $\backsim$ 5 $\mu$gm. per cm.$^2$ mounted on a 0.75 mgm. per cm.$^2$ mica backing is shown by curve $D$, Fig. 1. Analysis of this spectrum as above (not shown in the diagram) again gives a figure of 16% for the intensity of the 884 kev. component. The rise in the Fermi plot below 300 kev. is less than that found when using sources of similar average thicknesses evaporated from solution, and is probably due to scattering within the source rather than to an impurity or a third lower energy component. Evidence for this view is presented in Section VI.

The region of the $\beta$-ray spectrum below 90 kev., which contains internal conversion lines, has been examined in detail using several sources. Low energy

tails on the conversion lines were observed in all cases and were found to vary with the thickness of the source. The best spectrum was obtained using the precipitated source described above and is shown in Fig. 2. Here the counting rate per unit momentum interval $N$ is plotted against electron momentum. Three conversion lines are observed corresponding to the internal conversion of an $84.1 \pm 0.1$ kev. transition in the $K$, $L$, and $M$ shells of Yb. In addition the $K$ and $L$ series Auger lines also appear. The most accurate measurement of the energy of the transition, quoted above, was obtained by comparing the $K$ conversion line with that of the accurately known 411.6 kev. transition following the decay of $Au^{198}$. Because of the presence of the low energy tail, the line positions were taken to be one half line width lower in momentum than the half height positions of the upper edges. The peak of the $L$ line, which consists of the unresolved $L_{\mathrm{I}}$, $L_{\mathrm{II}}$, and $L_{\mathrm{III}}$ lines, occurs at $74.2 \pm 0.25$ kev. and gives an average $K$–$L$ difference of $51.5 \pm 0.3$ kev. From X-ray data the $K$–$L_{\mathrm{I}}$, $K$–$L_{\mathrm{II}}$, and $K$–$L_{\mathrm{III}}$ differences in Yb are 50.84, 51.37, and 52.41 kev. respectively (8). This suggests that $L$ conversion takes place chiefly in the $L_{\mathrm{II}}$ and $L_{\mathrm{III}}$ subshells. This result, which has also been obtained by Mihelich and Church (26) using a spectrograph of higher resolution, indicates the electric quadrupole character of the transition (11). By comparison of line areas in Fig. 2 we obtain for the relative intensities of the internal conversion groups: $K/L = 0.36 \pm 0.04$, $K/(L + M) = 0.28 \pm 0.03$, and $L/M = 3.6 \pm 0.05$. By comparison of these line areas with that of the total $\beta$-ray spectrum (shown only in part in Fig. 2) the absolute intensities of the conversion groups per disintegration are: $I_K = (4.5 \pm 0.8)\%$, $I_{(L+M)} = (16 \pm 2)\%$. The errors

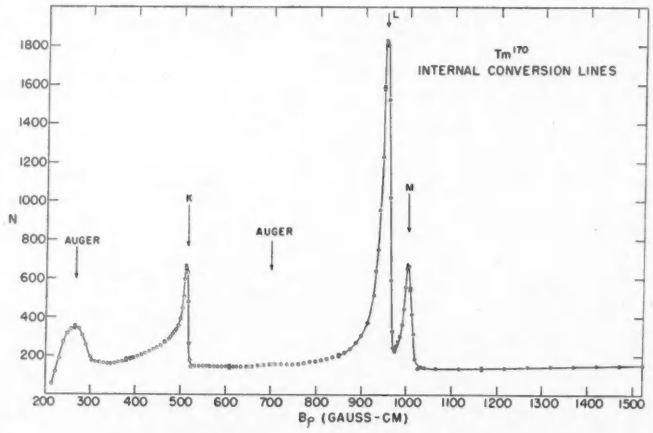


FIG. 2. $\beta$-ray spectrum of $Tm^{170}$ below 170 kev. taken with a spectrometer line width of 1.57%; the counting rate per unit momentum interval is plotted against electron momentum. The lines marked $K$, $L$, and $M$ are internal conversion lines of an $84.1 \pm 0.1$ kev. transition in $Yb^{170}$. The Auger lines result from de-excitation of the Yb atom following internal conversion. The standard deviations are represented by vertical bars on a few of the points.

quoted include an estimate of the uncertainty in the shape of the continuum on which the lines are superposed and in the magnitude of scattering in the source. Using the result for the $K$-conversion coefficient $\alpha_K$ found in Section IV along with these values the incidence of $\gamma$ rays per disintegration is $I_\gamma = (2.8 \pm 0.5)\%$. The sum of these intensities is seen to exceed the estimate of 16% obtained previously for the intensity of the 884 kev. $\beta$ component assuming both $\beta$ components have the allowed shape. Further, no internal conversion lines corresponding to other transitions in $Yb^{170}$ have been observed. It therefore seems likely that one or both of the $\beta$ components has a shape differing slightly from the allowed shape. This will be discussed in Section VII below.

## III. SECONDARY ELECTRON SPECTRA

The $\gamma$ and X radiations arising from decay of $Tm^{170}$ were examined in the same lens spectrometer adjusted for a full line width at half maximum intensity of 1.6%. The detector was a Geiger counter having a 0.3 mgm. per cm.$^2$ quartz window. The source consisted of 1.13 mgm. of spectroscopically pure $Tm_2O_3$ which had been irradiated in the NRX pile to an activity of $\backsim$ 40 mc. This was

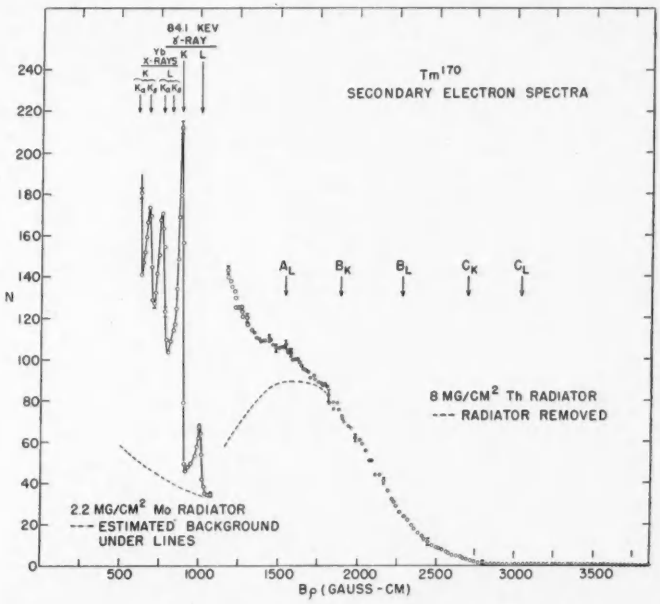


FIG. 3. Secondary electron spectra of a $Tm^{170}$ source using 8 mgm. per cm.$^2$ Th and 2.2 mgm. per cm.$^2$ Mo radiators. The counting rate per unit momentum interval is plotted against electron momentum. Positions marked $K$ and $L$ indicate where photoelectron lines due to X and $\gamma$ radiation appear. The $M$ lines are unresolved from the $L$ lines. Positions marked $A$, $B$, and $C$ indicate where photoelectron peaks due to $\gamma$ rays of energies 198 kev., 360 kev., and 550 kev. would be expected to appear. The standard deviations are shown by vertical bars on a few of the points.

embedded in a cylindrical aluminum container having an outside diameter 0.200 in. and a wall thickness sufficient to stop primary $\beta$ rays. In this investigation three 4 mm. diameter radiators were used: Th of thickness 8 mgm. per cm.$^2$, Ag of thickness 1.4 mgm. per cm.$^2$, and Mo of thickness 2.2 mgm. per cm.$^2$ When using the Ag and Mo radiators, a 0.005 in. thick disk of beryllium was interposed between the aluminum holder and the radiator to absorb photoelectrons ejected from the aluminum. The secondary electron spectra obtained using the Mo and Th radiators are shown in Fig. 3 and that obtained using the Ag radiator in Fig. 4. The counting rate per unit momentum interval

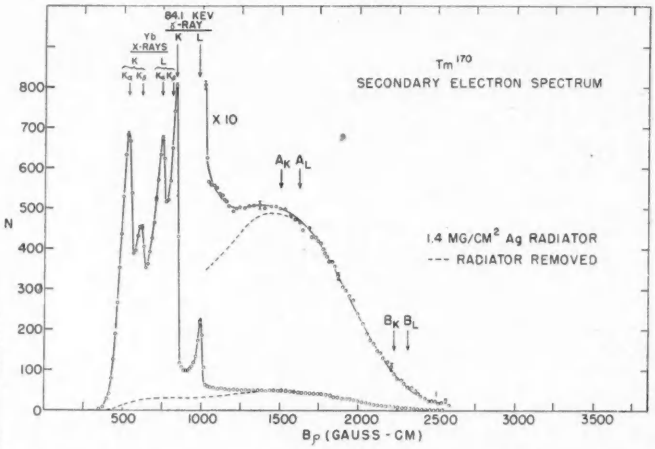


FIG. 4. Secondary electron spectrum of a $Tm^{170}$ source using a 1.4 mgm. per cm.$^2$ Ag radiator. The counting rate per unit momentum interval is plotted against electron momentum. Positions marked $A$ and $B$ indicate where photoelectron peaks due to $\gamma$ rays of energies 198 and 360 kev. would be expected to appear. The standard deviations are shown by vertical bars on a few of the points.

$N$ is plotted against electron momentum. Photoelectron lines ($K$ and $L$) corresponding to only one nuclear $\gamma$ ray are found. For an energy calibration the $Tm^{170}$ source was replaced by a $Au^{198}$ source. Comparing the position of the extrapolated upper edge of the $K$ photoelectron line (Mo radiator) with that obtained from the 411.6 kev. $\gamma$ ray following the decay of $Au^{198}$ gives a value of $84.3 \pm 0.25$ kev. for the $\gamma$-ray energy, which agrees with the energy assigned above. A single set of X-ray peaks is observed, corresponding to transitions which follow internal conversion in the $K$ shell of Yb. Er X-ray lines, which might be expected if $Tm^{170}$ decays by $K$ capture as well as by $\beta$ emission, are not evident and if they occur are less than 10% as intense as the Yb X rays.

Rough estimates may be made of the $K$-conversion coefficient $\alpha_K$ for the 84 kev. transition by a comparison of the intensities of the X-ray and $\gamma$-ray lines converted in the $L$ and $M$ shells of the radiator material. Comparing the areas of X-ray and $\gamma$-ray peaks in Figs. 3 and 4 and making the necessary corrections,

the value $1.6 \pm 0.3$ was obtained from the Mo radiator spectrum and $1.6 \pm 0.4$ from the Ag radiator spectrum. These values are in agreement with the more precise value given in Section IV.

The continuum which extends to higher energies in Figs. 3 and 4 is due to Compton electrons and photoelectrons ejected from the radiator and surrounding material by bremsstrahlung associated with the primary $\beta$ rays. As a check, the bremsstrahlung spectra of $Tm^{170}$ and $P^{32}$ were examined using the scintillation spectrometer described below in Section IV. Above 90 kev. the bremsstrahlung spectra of both nuclides are similar in shape and intensity. Assuming that the $Tm^{170}$ bremsstrahlung spectrum is similar to that of $P^{32}$ below 90 kev. one obtains an intensity figure of $\backsim 1$ quantum ( $>$ 20 kev.) per 100 $\beta$ rays. This intensity is of the right order to account for the continuum observed in the secondary electron spectra.

The higher energy region of the $Tm^{170}$ $\gamma$ spectrum was examined in the $\beta$-ray spectrometer with Ag and Th radiators in a search for the photoelectron peaks of $\gamma$ rays of energies greater than 84 kev. In particular a search was made for $\gamma$ rays of energies 198, 360, and 550 kev. which have been reported by Grant (15). The $K$ and $L$ photoelectron peaks of these quanta would appear at the positions marked $A$, $B$, and $C$ in Figs. 3 and 4. No peaks were detected and from the known sensitivity of the spectrometer it is concluded that the intensities of $\gamma$ rays of energies 198, 360, and 550 kev. are less than $2 \times 10^{-4}$, $6 \times 10^{-4}$, and $2 \times 10^{-4}$ quanta per disintegration respectively. Absence of photoelectron lines corresponding to annihilation radiation shows, similarly, that positon emission to $Er^{170}$ cannot occur in more than $10^{-4}$ of the disintegrations.

## IV. SCINTILLATION SPECTROMETER MEASUREMENTS

A scintillation spectrometer has been used to measure the intensities of the 84 kev. $\gamma$ ray and of the $K$ X radiations. The arrangement of the sodium iodide crystal and the R.C.A. type 5819 photomultiplier is shown in Fig 5($a$). The thickness of the scintillating crystal, 1.0 cm., was great enough to absorb more than 99% of X and $\gamma$ radiations of energy less than 100 kev. Apart from

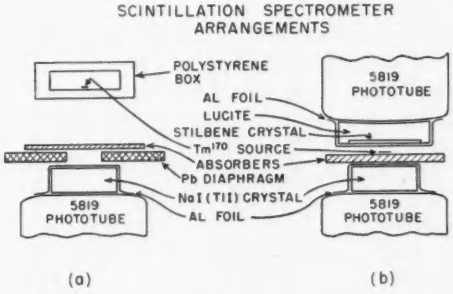


FIG. 5. Arrangement of the scintillation spectrometer ($a$) for $\gamma$-and X-ray scintillation spectrum, ($b$) for observing coincidences with $\beta$ rays.

secondary effects, each monoenergetic radiation gives a single peak in the pulse height spectrum. The pulses from the scintillation counter were amplified and counted on either a 30-channel or a single-channel pulse height analyzer.

The conversion coefficient $\alpha_K$ of the 84 kev. $\gamma$ transition was measured by comparing the areas of the $K$ X-ray and the 84 kev. $\gamma$-ray peaks in the scintillation spectrum, Fig. 6. The results were obtained with the single-channel analyzer. The upper curve is the spectrum obtained with the $Tm^{170}$ source covered with

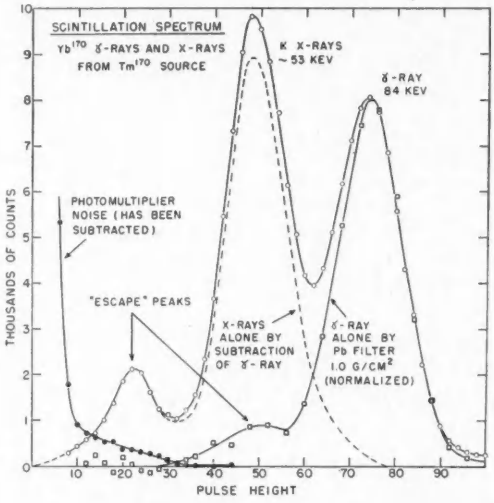


FIG. 6. Scintillation spectrum of the X and $\gamma$ rays from a $Tm^{170}$ source obtained with the counter in Fig. 5(*a*) and a single channel pulse height analyzer. The X-ray peak is slightly attenuated relative to the $\gamma$ peak by a 43 mgm. per cm.$^2$ Pb absorber.

0.3 cm. polystyrene to stop the $\beta$ rays and 43 mgm. per cm.$^2$ Pb to absorb the $Yb^{170}$ $L$ X rays. Two main peaks are visible, corresponding respectively to the 84 kev. $\gamma$ ray and to $\backsim$ 53 kev. $K$ X rays of $Yb^{170}$. The shape of the peak due to the $\gamma$ ray was observed separately by using a 1.0 gm. per cm.$^2$ Pb absorber to reduce the intensity of the $K$ X rays by a factor of $\backsim$ 1000, while reducing the intensity of the 84 kev. $\gamma$ ray by a factor of $\backsim$ 7. As shown in Fig. 6 the shape of the $K$ X-ray peak is then easily obtained by subtraction. Each main peak has associated with it a smaller peak situated about 28 kev. lower in energy, corresponding to photoelectric absorption in the $K$ shell of iodine atoms in the scintillating crystal with the subsequent escape of the X rays from the crystal (42). The area of each "escape" peak must therefore be added to that of the main peak with which it is associated. The total areas must be further corrected for absorption by the polystyrene $\beta$-ray absorber and the 43 mgm. per cm.$^2$ Pb absorber, and, in the case of the $K$ X rays, for the fluorescent yield, here assumed to be 0.92 (7). The ratio of the corrected X-ray peak area to the

corrected $\gamma$-ray peak area is the $K$-conversion coefficient $\alpha_K$. From the results in Fig. 6,

$$\alpha_K = 1.60 \pm 0.15.$$

This value is in good agreement with the theoretical value of about 1.7 for electric quadrupole radiation, which is obtained by interpolating between the relativistic values calculated by Rose *et al.* (35) and the threshold values calculated by Spinrad and Keller (39). It also agrees well with the less precise experimental values deduced in Section III and with the value of $1.5 \pm 0.2$ found by McGowan (24).

The absolute intensity of the X and $\gamma$ radiations from a $Tm^{170}$ source was measured using a scintillation spectrometer having its solid angle defined by a lead baffle with a central hole. The strength of the source used had previously been measured by Mr. R. C. Hawkings of this laboratory by defined-solid-angle beta counting. The counts on this occasion were registered on a 30-channel pulse height analyzer. The spectrum produced was similar in appearance to that of Fig. 6, except that the two main peaks were less well resolved. The sum of the peak areas was therefore evaluated, and the division between them made on the basis of the results given above. In this way, after the usual small corrections, we obtain the absolute intensity per $\beta$ disintegration of the 84 kev. $\gamma$ ray and its $K$ conversion: $I_\gamma = (3.2 \pm 0.4)\%$, $I_K = (5.1 \pm 0.6)\%$. The probable errors quoted in $\alpha_K$, $I_\gamma$, and $I_K$ are several times the statistical errors alone, and are believed to be reasonable estimates of the total probable error.

The possibility that $Tm^{170}$ decays by $K$ capture to $Er^{170}$, which might be expected on energetic grounds (25), has been examined using the $\gamma$-scintillation spectrometer, a $\beta$-scintillation counter, and a conventional coincidence mixer having a resolving time of one microsecond. A one microcurie source of $Tm^{170}$

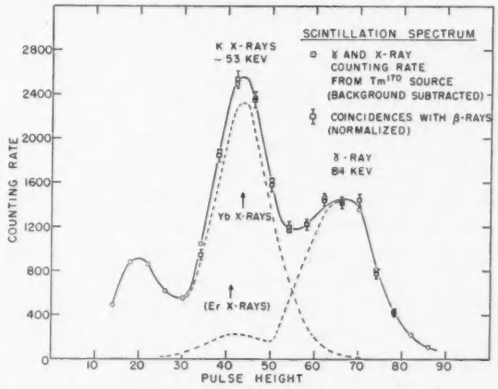


FIG. 7. Scintillation spectrum observed in coincidence with $\beta$ rays from a $Tm^{170}$ source using the counter arrangement shown in Fig. 5 (*b*) and a single channel pulse height analyzer. The similarity between the coincidence spectrum and the total scintillation spectrum observed at the same time shows that Er X rays are not present.

was placed between the two counters as shown in Fig. 5(*b*). A 400 mgm. per cm.$^2$ polystyrene and aluminum absorber prevented $\beta$ rays from reaching the NaI scintillating crystal and a 5 mgm. per cm.$^2$ Al foil prevented $K$-conversion electrons from being counted in the $\beta$ counter. Coincidences with the $\beta$ rays were observed as the scintillation spectrometer was swept over the 84 kev. $\gamma$-ray and 53 kev. X-ray peaks. The experimental results are shown in Fig. 7. The solid line shows the spectrum obtained for the X rays and $\gamma$ rays using the single-channel pulse height analyzer. The coincidence counting rates observed simultaneously have been normalized to the 84 kev. $\gamma$-ray peak and are seen to follow the X-ray peak closely. The energy resolution of the scintillation counter is not sufficient to distinguish between the Er X rays that would arise from $K$ capture and the Yb X rays that arise from internal conversion following $\beta$ decay. If Er X rays did occur they would not give rise to coincidences with the $\beta$ rays and hence the coincidence counting rate per recorded X ray would be less than that per recorded 84 kev. $\gamma$ ray. Using the experimental data of four points on the X-ray peak and five points on the $\gamma$ peak, the coincidence counting rate per recorded X ray is found to be equal within $\pm$ 3% to that per recorded $\gamma$ ray. This means that not more than a maximum of, say, 6% of the X rays can be due to $K$ captures. Since the $K$ X rays occur in only 5% of the disintegrations the probability of $K$ capture per $\beta$ disintegration does not exceed 0.3%.

## V. LIFETIME OF THE 84 KEV. $\gamma$ RAY

The half-life of the 84 kev. $\gamma$-ray transition in $Yb^{170}$ following the $\beta$ decay of $Tm^{170}$ has already been reported in an earlier publication (4). A value of $T_{1/2} = (1.60 \pm 0.2) \times 10^{-9}$ sec. was obtained using the fast coincidence circuit described elsewhere (5) and a single $\beta$-ray spectrometer to focus the 74 kev. $L$-conversion electrons on one of the scintillation counters. Since that time the useful resolving time of this circuit has been greatly improved by the use of *trans*-stilbene crystals in place of the anthracene crystals used in the former experiment and by the use of a motor driven, automatically operated helical transmission line unit (5) which varies the relative time delay between the two 1P21-stilbene scintillation counters in steps as small as $4 \times 10^{-10}$ seconds with 1% accuracy.

Fig. 8 shows resolution curves obtained with the improved equipment. A $Tm^{170}$ source of a few microcuries was placed between the two 1 mm. thick stilbene crystals of the two counters. A 20 mgm. per cm.$^2$ aluminum absorber was placed over one crystal to prevent conversion electrons of the 84 kev. $\gamma$-ray transition from reaching it, while all radiations including the conversion electrons reached the other crystal. In Fig. 8 the coincidence counting rate, corrected for chance coincidences, is plotted on a logarithmic scale against the artificially inserted time delay. The delayed curve $F(x)$ shows the results for $Tm^{170}$. For comparison a prompt curve $P(x)$ was obtained with a Th B source in place of the $Tm^{170}$ source and this is normalized to include the same area.

A least squares analysis of the slope of the tail of $F(x)$ in the region $(2.4 < x < 15.2) \times 10^{-9}$ sec. gives for the half-life: $T_{1/2} = (1.585 \pm 0.021) \times 10^{-9}$ sec., which is in good agreement with the earlier value. In this analysis

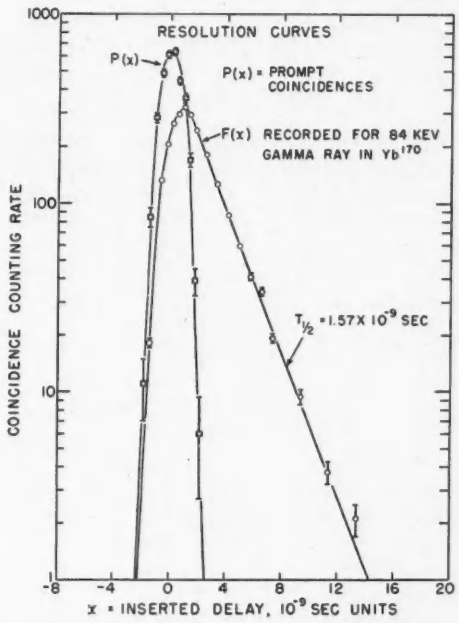


FIG. 8. Coincidence resolution curves. The delayed resolution curve $F(x)$ obtained with a $Tm^{170}$ source and the prompt resolution curve $P(x)$ obtained with a Th B source have been normalized to include equal areas. The slope of the tail taken together with other measurements on the 84.1 kev. $\gamma$ transition gives for the half-life $T_{1/2} = (1.57 \pm 0.05) \times 10^{-9}$ sec. The standard deviations are indicated by vertical bars.

the points were weighted according to the number of counts at each delay position and the standard deviation was calculated according to the method suggested by Behrens (3). Analysis of the same data using Newton's method (29) gives for the half-life: $T_{1/2} = (1.53 \pm 0.04) \times 10^{-9}$ sec. A centroid-shift analysis (2) would be subject to error in this experiment since the energies of the radiations being counted in recording $F(x)$ and $P(x)$ were different. Another less accurate determination has been made using the double spectrometer shown in Fig. 9 to focus the radiations falling on the two counters. Comparison was made with the Th B $F$ line in the manner described elsewhere for the 80 kev. $\gamma$ transition in $Xe^{131}$ (13). A centroid-shift analysis (2) of the two resolution curves so obtained (not shown) makes best use of the data in this case and yields a half-life $T_{1/2} = (1.49 \pm 0.06) \times 10^{-9}$ sec. Taking a weighted average of these three results and increasing the error to include possible systematic errors, we obtain for the 84 kev. $\gamma$ transition

$$T_{1/2} = (1.57 \pm 0.05) \times 10^{-9} \text{ sec.}$$

This half-life is about one hundred times shorter than that calculated for an electric quadrupole transition using the lifetime–energy relation derived by Weisskopf (41). Nevertheless, the agreement is considered to be reasonable and the discrepancy is of the same magnitude as is found for many $E2$ transitions (18).

## VI. COINCIDENCE SPECTRUM

The $\beta$-ray spectrum leading to the 84 kev. excited state in $Yb^{170}$ has been examined using the fast coincidence circuit in combination with two conventional thin-lens $\beta$-ray spectrometers placed end to end. The apparatus is shown schematically in Fig. 9. A thin 6 mm. diameter 200 $\mu$c. source of $Tm^{170}$, mounted

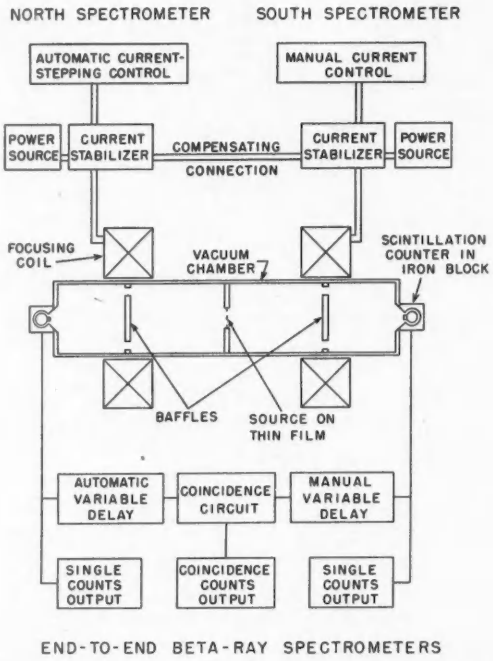


FIG. 9. Pair of end-to-end $\beta$-ray spectrometers and associated equipment. The diagram illustrates schematically the functions of the various components of the system. Short lucite light pipes (not shown above) are used between the scintillating crystals and the 1P21 photomultipliers. The two lens spectrometers are operated at a magnification $\sim 0.7$ in order to minimize the interaction effect between them.

on a 100 $\mu$gm. per cm.$^2$ plastic film, was placed at the center of the vacuum chamber so that radiations could be focused in both spectrometers simultaneously. The source was prevented from charging electrically by bombarding it with a low-voltage $10^{-8}$ ampere beam of electrons from an electron gun mounted on one of the baffles (43). The focused radiations were detected by scintillation counters each consisting of a 1 mm. thick anthracene crystal 6 to 9 mm. in

diameter and an R.C.A. type 1P21 photomultiplier housed in an iron block which shields the photomultiplier from the magnetic field and from light. The position of the counters was adjusted for alignment purposes by sliding the iron blocks about the flat surfaces of the vacuum-chamber end plates on greased O-rings.

Each spectrometer has its own power source and current stabilizer, so that each operates independently of the other. Because of the proximity of the two coils a given current, $i_1$, in one coil requires that the value of the current in the other coil, $i_2$, be reduced by an amount $0.06\,i_1$, for focusing electrons of a given momentum. The compensating connection of Fig. 9 applies this correction automatically. The transmission in one spectrometer is altered slightly by the current in the other spectrometer. Corrections for this effect are made in the observed results.

The gross $\beta$-ray spectrum was observed in the north spectrometer with the south spectrometer turned off, and the $\beta$-ray spectrum leading to the 84 kev. $\gamma$-ray transition was examined by focusing 74 kev. $L$-conversion electrons in the south spectrometer and observing coincidences with $\beta$ rays scanned in the north spectrometer. To ensure that the coincidence circuit had the same efficiency for all $\beta$-ray energies the resolving time was lengthened to $2\tau_o = 1.7 \times 10^{-8}$ sec. This made it unnecessary to correct for the effect of the $\gamma$-ray lifetime as well as for variations of the $\beta$-ray transit time in the north spectrometer, and yielded a flat topped resolution curve which is the criterion of 100% coincidence efficiency (5). All the data for the $Tm^{170}$ coincidence spectrum were recorded automatically on charts over a period of four days. The current in the north $\beta$-ray spectrometer was cycled through a given sequence of current settings by a stepping current control which was automatically advanced at 20-min. intervals. Both the true-plus-chance and chance-alone coincidence counting rates were measured during each 20-min. interval by operating the coincidence circuit for 10 min. at a delay setting near the center of the resolution curve to get the true-plus-chance coincidence rate, and for 10 min. at another delay setting well off the resolution curve to get the chance-alone coincidence rate. The $\beta$ counting rate and conversion line counting rates were monitored by counting rate meters connected to recording milliammeters. These data were used to correct the coincidence counting rates for source decay, variations in spectrometer transmission mentioned above, and slow drifts in counter sensitivity.

Fermi plots of the gross $\beta$-ray spectrum and of the coincidence spectrum are shown in Fig. 10. The gross $\beta$-ray spectrum ends at $970 \pm 10$ kev. while the coincidence spectrum ends at $886 \pm 10$ kev., i.e. about 84 kev. lower. The disintegration of $Tm^{170}$ is therefore complex, consisting of a partial $\beta$-ray spectrum leading directly to the ground state of $Yb^{170}$ and another spectrum leading to an 84 kev. excited state of $Yb^{170}$ as proposed by Fraser (10). Both spectra are similar in shape, having Fermi plots which are nearly straight down to a $\beta$-ray energy of about 300 kev. and rising above the projected straight lines by the same amount at lower energies. Immediately after completing the above experiment a similar coincidence-spectrometer experiment was carried out using

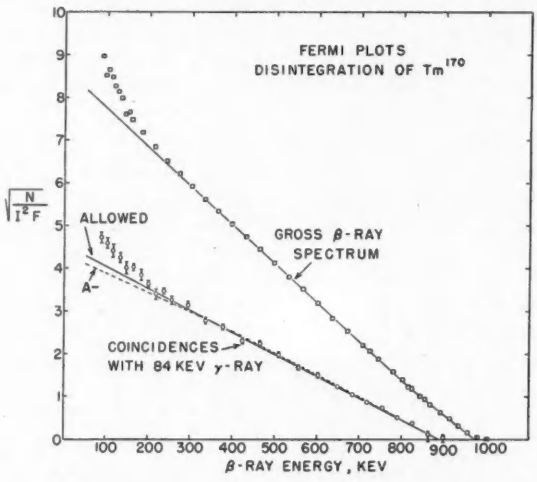


FIG. 10. Fermi plots of the gross $\beta$-ray spectrum of $Tm^{170}$ and of that part of it which is followed by the 84.1 kev. $\gamma$ transition in $Yb^{170}$. The shape of the coincidence spectrum is allowed or very nearly so. The dashed line indicates the theoretical shape ($\Delta J = 1$, yes) for a first forbidden transition if the $A_-$ correction factor applies. The standard deviations on the coincidence spectrum are indicated by vertical bars.

a 4 mm. diameter 200 $\mu$gm. per cm.$^2$ $Au^{198}$ source mounted on thin Al foil in place of the $Tm^{170}$ source, without altering the spectrometer or coincidence apparatus in any way. The conversion electrons of the 411.6 kev. transition following the $\beta$ decay of $Au^{198}$ provided an energy calibration. The $\beta$-ray spectrum was observed in the north spectrometer and coincidences were observed between the scanned $\beta$ rays and $K$-conversion electrons of the 411 kev. $\gamma$ transition focused in the south spectrometer in the same manner as for $Tm^{170}$. Fermi plots (not shown) of both the coincidence spectrum and the $\beta$-ray spectrum were identical in shape and end point, being straight for $\beta$-ray energies above 300 kev. and rising above the expected straight line below 300 kev. by an amount comparable to that observed with $Tm^{170}$. The Fermi plots for $Au^{198}$ are expected to be straight (21) except for a slight rise below 283 kev. due to the presence of a $\beta$-ray component in the disintegration whose intensity is, however, only about 1%. The observed rise below this energy is many times this amount, and is almost certainly due to scattering within the source and from its backing. The $Tm^{170}$ source, made by evaporating a nitric acid solution of thulium oxide to dryness on an acid resistant plastic film about 100 $\mu$gm. per cm.$^2$ thick, had an estimated average surface density of 40 $\mu$gm. per cm.$^2$ As was noted in Section III sources made in this manner tend to have local thicknesses much greater than the average surface density, and it is probable that the effective thickness of the source was comparable with that of the uniform 200 $\mu$gm.per cm.$^2$ $Au^{198}$ source. Consequently it is felt that the excess of electrons at energies

below 300 kev. is due to scattering effects and that the $Tm^{170}$ spectra suffer no appreciable distortion above 300 kev.

The shape of the $Tm^{170}$ coincidence spectrum as determined by the points above 300 kev. is allowed or very nearly so. The data are sufficiently accurate to rule out the first forbidden $\alpha$ shape* suggested by Novey (31) which is unique for spin change $\Delta J = 2$ and a change of parity (yes). Other first forbidden correction factors for $\Delta J = 1$ (yes) do not vary so rapidly with energy and cannot be ruled out. To illustrate this point the shape to be expected from an $A-$ correction factor** is shown by the dashed line in Fig. 10.

## VII. DISCUSSION

The 84.1 kev. $\gamma$ transition in $Yb^{170}$ is electric quadrupole on the basis of the measured conversion coefficients. From Section IV we have for this transition:

$$\alpha_K = 1.60 \pm 0.15$$

and from Section II

$$I_{L+M} = (16 \pm 2)\%.$$

From Sections II and IV weighted mean values are obtained for the following:

$$I_K = (4.9 \pm 0.5)\%,$$
$$I_\gamma = (3.1 \pm 0.3)\%,$$
$$\alpha_L = (4.1 \pm 0.5)\%,$$
$$\alpha_M = (1.2 \pm 0.2)\%.$$

By summation, transitions proceeding from the 84.1 kev. excited state in $Yb^{170}$ occur in $(24.0 \pm 2.1)\%$ of the $\beta$ disintegrations. No other $\gamma$ rays have been detected and it is therefore concluded that there are only two components in the $\beta$-ray spectrum, that of maximum energy $968 \pm 4$ kev. which goes directly to the ground state of $Yb^{170}$ in 76% of the disintegrations and that of maximum energy $884 \pm 4$ kev. which goes to the 84.1 kev. excited state in $Yb^{170}$ in 24% of the disintegrations.

The disintegration scheme shown in Fig. 11 is consistent with the experimental results. Since $Yb^{170}$ is an even–even nucleus its ground state is assigned zero spin and even parity. Thus the excited state at 84.1 kev. has a spin of 2 and even parity since the transition from it to the ground state is electric quadrupole. According to nuclear shell theory the 69th proton, orbit $d_{5/2}$, and the 101st neutron, orbit $p_{1/2}$, will combine in $Tm^{170}$ to form a ground state having odd parity. This is borne out by the log $f_0 t$ values, 9.0 and 9.3 for the higher and lower energy $\beta$-ray spectra respectively, which suggest that both transitions are first forbidden and hence involve a change in parity.

According to the assignments above and Gamow-Teller selection rules for $\beta$ decay, the spin of $Tm^{170}$ could be 0, 1, or 2. A spin of 0 which has been suggested by Novey (31) has been ruled out since the lower energy component of the $\beta$-ray spectrum which was observed separately in coincidence (Section VI) does not have the unique $\alpha$ shape required for first-forbidden transitions of this

*Using Wu's notation (44).
**Using Konopinski's notation (20).

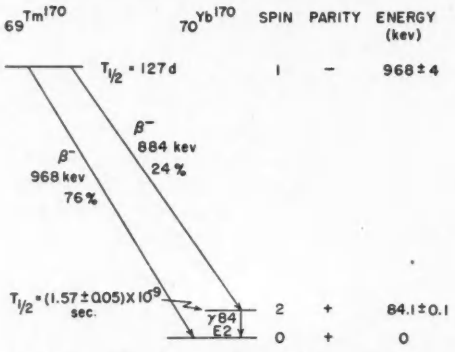


FIG. 11. Proposed disintegration scheme of $Tm^{170}$. No $\gamma$ rays other than the 84.1 kev. transition have been detected. Decay to $Er^{170}$ by $K$ capture or $\beta^+$ emission does not occur in more than $3 \times 10^{-3}$ or $10^{-4}$ of the disintegrations respectively.

type ($\Delta J = 2$, yes). A Tm $^{170}$ ground state spin of 2, which has been predicted on shell theory considerations by Nordheim (30), would require that the high energy component of the $\beta$ spectrum have the $\alpha$ shape. The shape of this component has been deduced, as shown in Fig. 1, by subtracting the low energy component, curve $E$, which is known to have an allowed or nearly allowed shape and an intensity of 24%, from the total spectrum, curve $D$. The Fermi plot of the high energy component obtained in this manner is shown by the points on curve $F$ in Fig. 1 and is seen to be slightly concave towards the energy axis in the energy region above 300 kev. This curve, however, does not possess the type or degree of curvature required for the $\alpha$ type spectrum, which rules out a spin of 2 for $Tm^{170}$. It follows that the ground state of $Tm^{170}$ must have a spin of 1 and odd parity.

The shape of the $\beta$-ray spectrum to the ground state as deduced above is consistent with tensor interaction. The correction factor $C_{1T}$ for this transition ($1 \rightarrow 0$, yes) contains terms involving the matrix elements $\int \vec{\alpha}$, $\int \vec{\sigma} \times \vec{r}$, and their cross product. Following Nakamura *et al.* (28) we assume that the cross product does not vanish, and calculate $C_{1T} / |\int \vec{\sigma} \times \vec{r}|^2$ for particular values of the ratio $k = |\int \vec{\alpha}| / |\int \vec{\sigma} \times \vec{r}|$ using the expressions of Greuling (17). The best fit to the experimental data was found for $k = 9.2$ and the theoretical spectrum shape is shown by curve $F$ in Fig. 1. The correction factor $C_{1A}$, assuming axial vector interaction, is unique and has also been calculated using Greuling's expression. It is interesting that this factor also fits the experimental data well and is almost identical in energy dependence with the factor $C_{1T}(k = 9.2)$. The shape of the high energy component of the $\beta$-ray spectrum deduced in this manner is thus consistent with either tensor or axial vector interaction. If the low energy component is assumed to have a similar first forbidden shape, then after subtraction as above the shape of the deduced high energy spectrum is not altered appreciably and the conclusions are the same. The experimental data are therefore consistent with a spin of 1 for the ground state of $Tm^{170}$. The low value for the intensity of

the lower energy component of the spectrum which was obtained by resolution of the Fermi plot in Section II is due, on these grounds, to the incorrect assumption of an allowed shape for the higher energy component.

The absence of positive $\beta$-ray emission and $K$ capture to $Er^{170}$ suggests that the $Tm^{170} - Er^{170}$ mass difference is very small. Transitions to $Er^{170}$ will be first forbidden, since like $Yb^{170}$ it is an even–even nucleus. Taking the experimental upper limit for the occurrence of $K$ capture and using the theoretical formulae for first forbidden orbital electron capture derived by Marshak (23), one obtains the result that this mass difference is not greater than about 300 kev.

## ACKNOWLEDGMENTS

The authors wish to thank Dr. L. Yaffe for preparing the sources and Dr. L. G. Elliott for many valuable discussions. It is also a pleasure to acknowledge the assistance of Mr. R. C. Hawkings in making the absolute $\beta$ counting measurements.

## REFERENCES

1. AGNEW, N. M. Phys. Rev. 77:655. 1950.
2. BAY, Z. Phys. Rev. 77: 419. 1950.
3. BEHRENS, D. J. A.E.R.E. Report T/R 629. 1951.
4. BELL, R. E. and GRAHAM, R. L. Phys. Rev. 78:490. 1950.
5. BELL, R. E., GRAHAM, R. L., and PETCH, H. E. Can. J. Phys. 30:35. 1952.
6. BOTHE, W. Z. Naturforsch. 1: 173. 1946.
7. BURHOP, E. H. S. and MASSEY, H. S. W. Proc. Roy. Soc. (London), A, 153: 661. 1936.
8. COMPTON, A. H. and ALLISON, S. K. X-rays in theory and experiment. D. Van Nostrand Inc., New York. 1935.
9. DUMOND, J. W., LIND, D. A., and WATSON, B. B. Phys. Rev. 73: 1932. 1948.
10. FRASER, J. S. Phys. Rev. 76: 1540. 1949.
11. GELLMAN, H., GRIFFITH, B. A., and STANLEY, J. P. Phys. Rev. 85: 944. 1952.
12. GRAHAM, R. L. and BELL, R. E. Proc. Roy. Soc. Can., III, 44:193. 1950.
13. GRAHAM, R. L. and BELL, R. E. Phys. Rev. 84: 380. 1951.
14. GRAHAM, R. L. and TOMLIN, D. H. Nature, 164: 278. 1949.
15. GRANT, P. J. Nature, 165: 1018. 1950.
16. GRANT, P. J. and RICHMOND, R. Proc. Phys. Soc. 62: 573. 1949.
17. GREULING, E. Phys. Rev. 61: 568. 1942.
18. GOLDHABER, M. and SUNYAR, A. W. Phys. Rev. 83: 906. 1951.
19. KETELLE, B. H. and BOYD, G. E. Oak Ridge Rept. ORNL-65: 94. 1948.
20. KONOPINSKI, E. J. Revs. Modern Phys. 15: 209. 1943.
21. LANGER, L. M. and PRICE, H. C. JR. Phys. Rev. 76: 641. 1949.
22. LANGER, L. M., MOFFAT, R. D., and PRICE, H. C. JR. Phys. Rev. 76: 1725. 1949.
23. MARSHAK, R. E. Phys. Rev. 61: 431. 1942.
24. MCGOWAN, F. K. Phys. Rev. 85: 142. 1952.
25. METROPOLIS, N. and REITWEISNER, G. Los Alamos Rept. NP-1980. 1950.
26. MIHELICH, J. W. and CHURCH, E. L. Phys. Rev. 85: 690. 1952.
27. MITCHELL, A. C. G. Revs. Modern Phys. 22:36. 1950.
28. NAKAMURA, S., UMEZAWA, M., and TAKEBE, H. Phys. Rev. 84: 865. 1951.
29. NEWTON, T. D. Phys. Rev. 78: 490. 1950.
30. NORDHEIM, L. W. Revs. Modern Phys. 23:322. 1951.
31. NOVEY, T. B. Phys. Rev. 78:66. 1950.
32. NOVEY, T. B. Phys. Rev. 84: 145. 1951.
33. OWEN, G. E. and PRIMAKOFF, N. Phys. Rev. 74: 1406. 1948.
34. RICHMOND, R. and ROSE, N. Phil. Mag. 43: 367. 1952.
35. ROSE, M. E., GOERTZEL, G. H., SPINRAD, B. I., HARR, J., and STRONG, P. Phys. Rev. 83: 79. 1951.
36. SAXON, D. and RICHARDS, J. Phys. Rev. 76: 186A. 1949.
37. SAXON, D. Phys. Rev. 81: 639. 1951.
38. SIEGBAHN, K. Manne Siegbahn. Almqvist and Wiksells, Uppsala, Sweden, 228. 1951.
39. SPINRAD, B. I. and KELLER, L. B. Phys. Rev. 84: 1056. 1951.
40. WAY, K. Nuclear Data, Natl. Bur. Standards (U.S.), Circ. 499. 1950.
41. WEISSKOPF, V. F. Phys. Rev. 83: 1073. 1951.
42. WEST, H. I., MEYERHOF, W. E., and HOFSTADTER, R. Phys. Rev. 81: 141. 1951.
43. WOLFSON, J. L. Rev. Sci. Instruments, 22: 280. 1951.
44. WU, C. S. Revs. Modern Phys. 22:386. 1950.

# THE PHOTONEUTRON CROSS SECTIONS FOR THE REACTIONS $Br^{81}$ $(\gamma,n)$ $Br^{80}$ AND $Br^{81}$ $(\gamma,n)$ $Br^{80*}$ AND AN ANALYSIS OF THE RATIO BETWEEN THESE CROSS SECTIONS[1]

By L. Katz, L. Pease, and H. Moody

ABSTRACT

Cross-section curves have been measured as a function of energy for the reactions $Br^{81}(\gamma,n)Br^{80}$ and $Br^{81}(\gamma,n)Br^{80*}$ and the ratio between these cross sections has been examined critically. The curves exhibit the peaked shape characteristic of photonuclear reactions with maximum cross sections of 88 and 42 millibarns respectively. It is shown that the ratio of the cross sections depends on the spins of the excited levels in which the $Br^{80}$ nucleus is left prior to $\gamma$ cascading and thus on the reaction leading to it. An elementary analysis based on this point of view gives results consistent with the ratio measured for six different types of reactions.

## INTRODUCTION

During the course of our work on the photoneutron cross sections of various elements it was felt desirable to investigate the reactions $Br^{81}(\gamma,n)Br^{80}$ and $Br^{81}(\gamma,n)Br^{80*}$. Besides giving two more photoneutron cross sections these measurements would give the ratio of the cross sections leading to the ground and isomeric states. It was hoped also that a determination of the ratio as a function of photon energy might lead to a better understanding of the nuclear levels in the bromine nucleus.

Numerous measurements of the cross section ratio, $\sigma_{17\text{min.}} / \sigma_{4.4\text{hr.}}$, have been made (2, 3, 4, 6, 20, 21) using slow and fast neutrons, lithium gamma rays, protons up to 4 Mev., and deuterons. Most of the measurements gave values of 2.4 to 3.2 when the $Br^{80}$ nucleus was excited to 7 or more Mev. above its ground state. For other reactions there was a wide variation, from 0.7 in the case of $(n,2n)$ to greater than 15 for the $(p,n)$ reaction. It will be shown later that this ratio depends on the spins $J$ of the excited levels in which the $Br^{80}$ nucleus is left before cascading takes place and thus on the reaction leading to the $Br^{80}$ nucleus. Schiff (18) has suggested that only certain nuclear levels may be excited in nuclear photoabsorption. If this were the case then one might expect that a different cross-section ratio would result, particularly at energies near threshold, even if the same $J$ value levels were excited in $Br^{80}$ by other reactions. In our experiment the ratio has been measured from the photoneutron threshold at 10.2 Mev. (15) to 25 Mev.

The decay scheme of $Br^{80}$ (12) is shown in Fig. 1. In the main this decay scheme agrees with the older data as given in N.B.S. Circular 499 (16) and Reference (19). The spin assignments are from (19). The 4.4 hr. metastable state decays in two steps by gamma emission to the 17.2 min. ground state which then decays by either $\beta^+$ or $\beta^-$ emission or $K$ capture.

[1] *Manuscript received April 28, 1952.*
*Contribution from the Department of Physics, University of Saskatchewan, Saskatoon, Sask.*

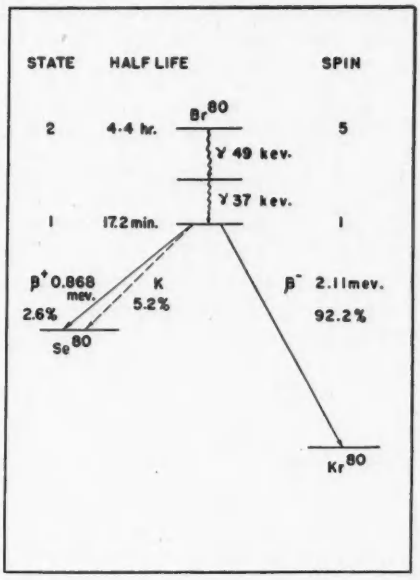


FIG. 1. Decay scheme of $Br^{80}$.

In this paper we report on measurements of the photonuclear cross sections leading to the two states in $Br^{80}$ and in particular examine the ratio of these cross sections as a function of energy. The cross sections are determined from the 4.4 hr. and 17.2 min. activities which result from the photoneutron reactions. Since some of the isomeric state decays to the ground state and some of the ground state decays to $Se^{80}$ during irradiation, the necessary mathematical relations are first derived.

## MATHEMATICAL ANALYSIS

When a mole of some isotope is placed in the X-ray beam of a betatron operating at an energy $E_0$, the number of reactions induced per unit time by the photons is given by

$$a(E_0) = 0.6023 \int_0^{E_0} \sigma(E)\, P(E,E_0)\, dE \tag{1}$$

where $\sigma(E)$ is the cross section in barns for the reaction at an energy $E$ and $P(E,E_0)$ is the number of photons of energy $E$ per cm.$^2$ per Mev. per min. The numerical factor is Avogadro's number divided by $10^{24}$ to convert cross-section units from cm.$^2$ to barns. A mole is defined as one gram atom of the isotope. When an isomeric state is present two cross sections are involved, $\sigma_1(E)$ leading to the ground state and $\sigma_2(E)$ leading to the excited state, and two such integrals

may be written. Actually during irradiation the rate of production of radioactive nuclei in State 2 (isomeric state) is given by

$$\frac{dN_2}{dt} = -\lambda_2 N_2 + a_2(E_0) \tag{2}$$

and the rate of production of radioactive nuclei in State 1 (ground state) is

$$\frac{dN_1}{dt} = -\lambda_1 N_1 + p\lambda_2 N_2 + a_1(E_0) \tag{3}$$

where $p$ is the fraction of nuclei from State 2 decaying to State 1. In the case of $Br^{80*}$, $p = 1$ as will be seen from Fig. 1.

Solving equations (2) and (3) for the boundary conditions $N_1 = N_2 = 0$ at $t = 0$ we find the populations of the two states, $N_{20}$ and $N_{10}$, at the end of an irradiation time $t_R$. These equations are in turn solved for $a_1(E_0)$ and $a_2(E_0)$;

$$a_2(E_0) = \frac{\lambda_2 N_{20}}{1 - e^{-\lambda_2 t_R}}. \tag{4}$$

$$a_1(E_0) = \frac{\lambda_1 N_{10}}{1 - e^{-\lambda_1 t_R}} - \frac{P}{\lambda_2 - \lambda_1}\left\{\lambda_2 - \lambda_1\left(\frac{1 - e^{-\lambda_2 t_R}}{1 - e^{-\lambda_1 t_R}}\right)\right\} a_2(E_0). \tag{5}$$

The populations of the states at a time $t$ after the end of irradiation are given by

$$N_2 = N_{20}\, e^{-\lambda_2 t}, \tag{6}$$

$$N_1 = N_{10}\, e^{-\lambda_1 t} + p\,\frac{\lambda_2 N_{20}}{\lambda_2 - \lambda_1}(e^{-\lambda_1 t} - e^{-\lambda_2 t}). \tag{7}$$

Since decays from the metastable to ground state go by gamma-ray emission and gamma rays are counted with less than 1% efficiency in our Geiger-Müller tubes, it follows that the counting circuit does not observe the gamma rays from the metastable state. Therefore, the observed activity is given by

$$\begin{aligned} C = g\lambda_1 N_1 &= g\lambda_1\left(N_{10} - p\,\frac{\lambda_2 N_{20}}{\lambda_1 - \lambda_2}\right)e^{-\lambda_1 t} + gp\,\frac{\lambda_1\lambda_2 N_{20}}{\lambda_1 - \lambda_2}e^{-\lambda_2 t} \\ &= C_{10}\, e^{-\lambda_1 t} + C_{20}\, e^{-\lambda_2 t} \end{aligned} \tag{8}$$

where $g$ is the fraction of the actual disintegrations recorded by the Geiger counter. A detailed analysis of the evaluation of $g$ will be given in a forthcoming paper by Katz, Baker, and Montalbetti. It should be noted that $C_{10}$ and $C_{20}$ are not constants but functions of the irradiation time $t_R$.

The observed activity consists of two exponential decays with decay constants $\lambda_1$ and $\lambda_2$. Analysis of a decay curve gives $C_{10}$ and $C_{20}$. The initial populations in the two states are then found from

$$\begin{aligned} N_{10} &= \frac{C_{10} + C_{20}}{\lambda_1 g}, \\ N_{20} &= \frac{\lambda_1 - \lambda_2}{\lambda_1\lambda_2 gp} C_{20}. \end{aligned} \tag{9}$$

These are then substituted back into equations (4) and (5) to give the values $a_1(E_0)$ and $a_2(E_0)$. Plots of $a(E_0)$ vs. $E_0$ give the usual activation curves and

may be solved by the photon-difference method (10) for the cross section $\sigma(E)$ after suitable corrections are made for $K$ capture.

The ratio of $a_1(E_0)/a_2(E_0)$ follows directly from equations (4) and (5):

$$R_a = \frac{a_1(E_0)}{a_2(E_0)} = \frac{\lambda_1 P}{\lambda_1 - \lambda_2}\frac{C_{10}}{C_{20}}\left(\frac{1 - e^{-\lambda_2 t_R}}{1 - e^{-\lambda_1 t_R}}\right) + \frac{\lambda_2 P}{\lambda_1 - \lambda_2}. \tag{10}$$

This ratio does not depend on counting geometry, etc. That is, it is independent of the value of the factor $g$, and thus can be determined very accurately. The ratio $R_a$ should not be confused with the ratio of cross sections $R_\sigma$ introduced later. $R_\sigma$ is found by taking the ratio of the cross sections given in Fig. 6. On the other hand $R_a$ is the ratio of the activation curves of Fig. 4 and therefore includes the bremsstrahlung spectrum of the betatron.

## EXPERIMENTAL PROCEDURE

A value of $a_1(E_0)$, $a_2(E_0)$, and $R_a$ may be obtained from a single irradiation at each energy setting of the betatron. It was found, however, that for more accurate results these values should be measured separately. To compute the ratio $R_a$ it was only necessary to measure the irradiation time $t_R$ and the initial counting rates $C_{10}$ and $C_{20}$ and to substitute them into equation (10). In order to obtain high accuracy, large samples were used and counted in cylindrical geometry with cylindrical counters. The values of $a_2(E_0)$ ( 4.4 hr. activity) were obtained from an independent set of experiments. In this case the dosage rate, sample weight, as well as irradiation time were accurately measured and the counting geometry carefully controlled. The beam intensity was monitored with an ionization chamber which was frequently checked against a 100 r. Victoreen thimble chamber in the center of an 8 cm. block of Lucite—the usual monitoring practice followed in our laboratory (9). Finally $a_1(E_0)$ was calculated from $a_2(E_0)$ and $R_a$.

Bromine was obtained in the form of pure sodium bromide. Gamma induced reactions in sodium produced no interference. However, since bromine consists of two isotopes of mass 79 and 81, occurring in very nearly equal abundance, two $(\gamma,n)$ reactions are possible: $Br^{79}(\gamma,n)Br^{78}$ with a half life of 6.4 min. and $Br^{81}(\gamma,n)Br^{80}$ and $Br^{80*}$ with half lives of 17.2 min. and 4.4 hr. respectively. The short-lived 6.4 min. activity dies out quickly and does not interfere with the measurements of the other two activities. The presence of $Br^{79}$ does, however, lead to another difficulty: neutrons which are knocked out of the walls of the donut, lead shield, etc., give rise to the reaction, $Br^{79}(n,\gamma)Br^{80}$ and $Br^{80*}$. The activity ratio resulting from neutron capture in this reaction is about 3(3,6,20) so that, whatever the ratio of the activities from gamma irradiation, as the photothreshold is approached the neutron capture reaction will predominate forcing the ratio to approach 3. This behavior is shown in curve $A$ in the insert of Fig. 2; the ratio rises to about 17 at 10.7 Mev. and then falls rapidly to about 3 at 10.2 Mev. The sodium bromide samples for this experiment were shielded in cadmium during irradiation. To further reduce the effects of neutron capture the cadmium box was then lined with indium. Unfortunately the neutron capture cross section of bromine has not been published so that the best material

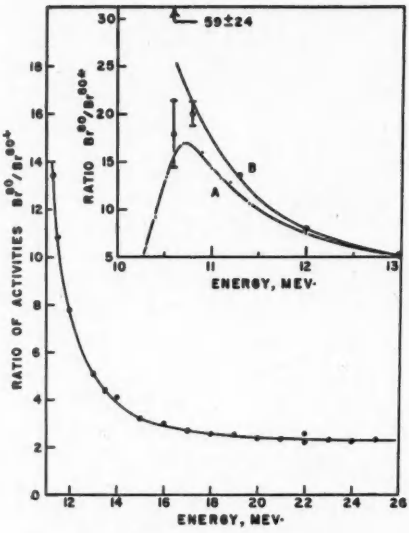


FIG. 2. Ratio of the saturated activities $R_a\left(\frac{17.2 \text{ min. act.}}{4.4 \text{ hr. act.}}\right)$ induced in a bromine sample as a function of the betatron operating energy. The 17.2 min. activity used has been corrected for transitions from the isomeric state during irradiation. Insert shows the ratio near the photoneutron threshold. Curve *A*, using only cadmium shielding on samples. Curve *B*, cadmium and indium shielding as well as a correction for activity induced by fast neutrons determined from the 35 hr. neutron capture activity of $Br^{82}$.

for neutron shielding could not be selected. However, the addition of the indium lining reduced the neutron flux somewhat as the curve rose higher and did not turn over until lower energies, but it did turn over. Finally a further correction was made for the remaining neutron induced activity as follows. An experiment below the $Br^{81}$ photothreshold energy (10.2 Mev.) showed that the 4.4 hr. and the 35 hr. activities resulting from neutron capture in $Br^{79}$ and $Br^{81}$ are about equal. Assuming these are also equal at slightly higher energies it was then possible to correct for neutron capture from the 35 hr. activity remaining after the other activities had died out. Applying this correction and using cadmium and indium shielding the curve shown in Fig. 2 was obtained. The lower energy region is shown on a greatly enlarged scale as curve *B* in the insert.

Instead of evaluating the counting factor $g$ to reduce a given counting rate to an absolute specific activity, a sample of sodium bromide and one of copper were irradiated simultaneously in the betatron beam at 22.4 Mev. The ratio of the 4.4 hr. $Br^{80*}$ activity to the 10.1 min. $Cu^{62}$ activity, when corrected for self-absorption, allowed us to calculate $a_2(22.4)$ as $1.18 \times 10^8$ activations per 100r. per gm-atom of $Br^{81}$ taking the value for $Cu^{62}$ at the same energy to be $2.56 \times 10^8$ activations per 100r. per gm-atom of $Cu^{63}$. In order to obtain the actual correction for self-absorption, curves were plotted of the measured or apparent

specific activity of $NaBr^{80*}$ and $Cu^{62}$ against sample thickness (Fig. 3), care being taken to use the same geometry as in the actual comparison experiment. These curves exhibit the usual initial rise (due to self-scattering) and final

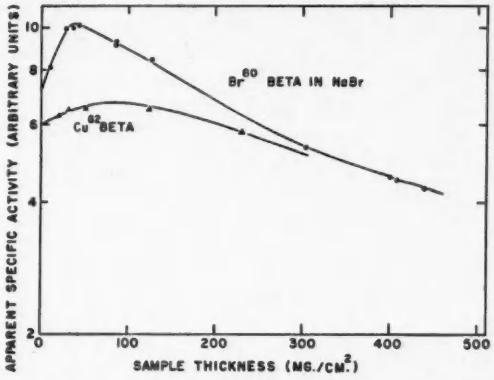


FIG. 3. Self-absorption curves of $Br^{80}$ beta rays in a sodium bromide sample and $Cu^{62}$ beta rays in a copper sample. These were taken in a fairly large geometry ($\sim \pi$ steradians) with planar samples.

exponential dropping off (due to self-absorption) and serve to emphasize the large errors which may be involved when a simple exponential correction is applied.

The activation curve of the isomeric state, $a_2(E_0)$ vs. $E_0$, was obtained by irradiating samples of sodium bromide in a cadmium–indium container and counting the 4.4 hr. activity after the short-lived activities had died out. Extra-

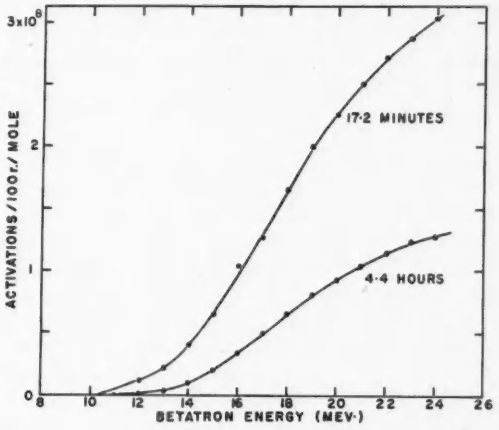


FIG. 4. Activation curves for the 17.2 min. and 4.4 hr. activities induced by the reactions $Br^{81}(\gamma,n)Br^{80}$ and $Br^{81}(\gamma,n)Br^{80*}$.

polation of this curve to zero time gave $C_{20}$, and $a_2(E_0)$ was calculated with the aid of equations (4) and (9). The 4.4 hr. activation curve and the 17.2 min. activation curve obtained from $a_1(E_0) = R_a a_2(E_0)$ are shown in Fig. 4. These curves have been corrected for $K$ capture and are expressed in activations induced in a gram atom of parent isotope when irradiated with a 100 roentgen of betatron flux as measured by a Victoreen thimble chamber in the center of an 8 cm. cube of Lucite (9).

During the course of this work it was found that the ground state decayed with a half life somewhat shorter than the usually accepted value of 18 min. The average of several measurements followed out for eight half lives gave an average value of 17.2±0.2 min. in good agreement with the value of 17.4± 0.25 min. reported by DuBridge *et al.* (4). One of these decay curves is reproduced in Fig. 5.

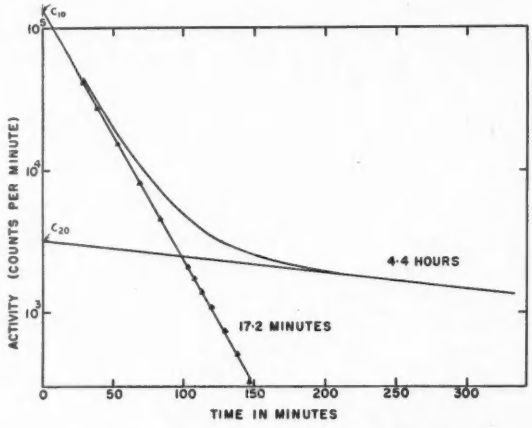


FIG. 5. Decay curve of $Br^{80}$. The intercepts of the extrapolations of the straight portions with the zero time ordinate (end of betatron irradiation) give $C_{10}$ and $C_{20}$ as indicated.

## RESULTS

The activation curves of Fig. 4 were analyzed by the photon-difference method of Katz and Cameron (10) resulting in the cross-section curves shown in Fig. 6. Both these curves have their maximum cross sections at about 18 Mev. The peak cross sections for the ground and isomeric states are 0.088 barn and 0.042 barn respectively, each curve has a width at half maximum of about 8 Mev. The integrated cross sections are 0.72 Mev-barn for the 17.2 min. activity and 0.36 Mev-barn for the 4.4 hr. activity, a total of 1.08 Mev-barns for photon energies up to 24 Mev.

From our activation curves we find that the total neutron yield per gram atom of $Br^{81}$ per roentgen is $2.30 \times 10^6$ at 18 Mev. and $3.85 \times 10^6$ at 22 Mev. Price and Kerst (17) have measured the neutron yields from natural bromine (both isotopes) directly and find $2.15 \times 10^6$ and $3.90 \times 10^6$ at the same energies

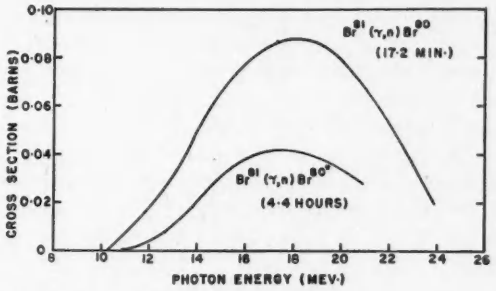


FIG. 6. The cross sections for the two reactions involved as determined from the activation curves of Fig. 4 using the photon difference method.

—values which are in surprisingly good agreement. Because $Br^{79}$ and $Br^{81}$ occur in approximately equal abundance one must assume that the photoneutron cross sections of the two isotopes are also about equal in order to explain this agreement. McDaniel, Walker, and Stearns (14) have measured the total cross section of natural bromine using lithium gamma rays and find it to be 0.08 barn. Wäffler and Hirzel (22) have measured the total cross section for the $Br^{81}$ isotope also using lithium gamma rays and find it to be 0.83 relative to $Cu^{63}(\gamma,n)\,Cu^{62}$. The lithium gamma rays consist of a 14.8 Mev. and a 17.6 Mev. component with intensities in the ratio of 1 to 2 respectively. Using our published cross-section curve for the above copper reaction, we find the copper cross section as measured with lithium gamma rays should be 0.086 barn, so that the value of Wäffler and Hirzel for $Br^{81}$ actually corresponds to 0.072 barn (compared to the above mentioned value of 0.08 barn found by McDaniel *et al.*). Taking the sum of our cross sections from Fig. 6 at 14.8 and 17.6 Mev. and giving them

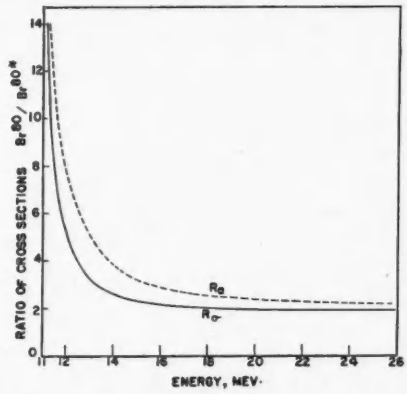


FIG. 7. Ratio of the cross sections $R_\sigma = (\sigma$ 17.2 min./$\sigma$ 4.4 hr.) as a function of photon energy. The ratio of the activities $R_a$ is shown by the dashed line for comparison. Since the threshold for the 4.4 hr. activity is 0.086 Mev. above that for the 17.2 min. activity (10.2 Mev.) the ratios should become infinite at $\sim$ 10.3 Mev.

weights of 1 to 2 we find an average value of 0.12 barn. Wäffler and Hirzel used an exponential correction for self-absorption and some of the discrepancy with their value may stem from this. It is difficult to explain the large discrepancy with the value of McDaniel *et al.*

The ratio of the cross sections, $R_\sigma = \sigma_1/\sigma_2$, as a function of photon energy is shown in Fig. 7. This ratio increases rapidly as the threshold for the 4.4 hr. activity is approached. The ratio $R_a$ is shown for comparison, the abscissa scale representing maximum energy of the bremsstrahlung spectrum in this case.

All the previously published values of the ratio of cross sections have been collected in Table I. Some of the values found in the literature give only the

TABLE I

| Reaction | Ref. | Incident radiation, Mev. | $Br^{80}$ Excitation energy, Mev. | $R'$ | $R$ |
|---|---|---|---|---|---|
| $Br^{79}(n,\gamma)Br^{80}$ | 6 | $E_n = 0$ | $\sim 7$ | 2·18 | 2·4 |
| $Br^{79}(n,\gamma)Br^{80}$ | 20 | $E_n = 0$ | $\sim 7$ | 2·3 | 2·5 |
| $Br^{79}(n,\gamma)Br^{80}$ | 3 | $E_n = 0$ | $\sim 7$ | 2·95 | 3·2 |
| $Br^{79}(n,\gamma)Br^{80}$ | 8 | $E_n = 0$ | $\sim 7$ | | 3·0 |
| $Br^{79}(n,\gamma)Br^{80}$ | 8 | $E_n = 1$ | $\sim 8$ | | 2·1 |
| $Br^{79}(d,p)Br^{80}$ | 20 | $E_d = 5$ | $\sim 12$ | 2·1 | 2·3 |
| $Se^{80}(p,n)Br^{80}$ | 4 | $E_p = 4$ | 1·2 | 15 | 16 |
| $Br^{81}(\gamma,n)Br^{80}$ | 2 | $E_\gamma = 17·6$ | 6·8 | 0·9 | 1·0 |
| $Br^{81}(\gamma,n)Br^{80}$ | 2 | $E_\gamma = 12$ | 1·8 | $>2·6$ | $>2·8$ |
| $Br^{81}(n,2n)Br^{80}$ | 20 | $E_n \leqslant 14$ | $\leqslant 4$ | 0·8 | 0·9 |
| $Br^{81}(n,2n)Br^{80}$ | 21 | $E_n \leqslant 14$ | $\leqslant 4$ | 0·6 | 0·7 |

ratio of the observed initial activities after correction to saturation (infinite length of irradiation time). Say we call this ratio $R'$. Now the observed initial activities are precisely $C_{10}$ and $C_{20}$, as indicated by equation (8), and correction to saturation gives

$$R' = \frac{C_{10}}{C_{20}}\left(\frac{1 - e^{-\lambda_2 t_R}}{1 - e^{-\lambda_1 t_R}}\right).$$

Since only monochromatic radiation is involved we have $R_a = R_\sigma$ and thus we find from equation (10) that

$$R_\sigma = \frac{\lambda_1}{\lambda_1 - \lambda_2} R' + \frac{\lambda_2}{\lambda_1 - \lambda_2} \tag{11}$$

$$= 1.07R' + 0.07.$$

In Table I the published value $R'$ is listed along with the value of $R_\sigma$ computed from it.

## ANALYSIS OF CROSS-SECTION RATIOS AND THE CASCADE BRANCHING RATIO

It is seen from Table I that the ratio of the cross sections leading to the ground and excited states in $Br^{80}$ depends strongly on the reactions involved. The most obvious difference between the various reactions is in the spins of the

excited levels to which they lead in the $Br^{80}$ nucleus prior to cascading. Qualitatively at least, the difference in spins is sufficient to account for the results listed in Table I, as the following elementary analysis will show.

The spins of the levels in $Br^{80}$ which result from any reaction may be estimated from the spins of the interacting particles and the angular momenta carried by the incoming and outgoing waves. In the case of neutron absorption by $Br^{79}$ the spins may be calculated as follows: the cross section for the formation of a compound nucleus by that part of the incident neutron plane wave of angular momentum $l$ and energy $E$ is given by (5)

$$\sigma_c^{(l)}(E) = \tfrac{1}{2}(2l+1)\,\lambda^2\,T_l(E) \tag{12}$$

where $\lambda$ is the wave length of the incident neutron and $T_l(E)$ is the transmission coefficient of the nuclear surface for neutrons of angular momentum $l$ and energy $E$. Graphs of $T_l(E)$ are given in Reference (5). An examination of these graphs shows that for thermal neutrons $\sigma_c^{(1)}$ is less than 1% of $\sigma_c^{(0)}$. Thus for thermal neutron absorption we can assume $l = 0$. On the other hand for 1 Mev. neutrons we find from the same graphs that the relative cross sections are $\sigma_c^{(0)}$ (21%), $\sigma_c^{(1)}$ (47%), $\sigma_c^{(2)}$ (29%), and $\sigma_c^{(3)}$ (3%) so that on the average one unit of angular momentum is carried in by 1 Mev. neutrons. Similar calculations for 10 Mev. neutrons give $l_{av.} = 3.3$. The spin of $Br^{79}$ is 3/2 (16): combining this with $l = 0$ and $s = 1/2$ for slow neutrons, the only possible levels excited in $Br^{80}$ on slow neutron capture by $Br^{79}$ are those of spin 1 and 2. Assigning weights to these according to their multiplicity, the level of spin 1 has a weight of 0.375 and the level of spin 2 a weight of 0.625. In the case of 1 Mev. neutrons $l = 1$, and the resulting spins in the same reaction are 0(0.042), 1(0.250), 2(0.416), and 3(0.292) where the weight of each is written in parenthesis.

We now assume that from a statistical point of view the branching ratio leading from any level in the excited $Br^{80}$ nucleus, by $\gamma$ cascading, to the isomeric and ground states, is a function of the spin of that level. (We shall name this the "cascade branching ratio" and designate it by $r_j$.) Levels of small spin, i.e. 0, 1, will predominantly feed into the ground state whose spin is 1 (see Fig. 1) and levels of large spin, 4 or larger, will predominantly feed into the isomeric state whose spin is 5. Thus, in the case of fast neutron absorption, the presence of some levels with spin 3 will favor the formation of the isomeric state and give a value of $R_\sigma$ which is smaller for fast neutrons than for slow neutrons. This is in agreement with the measurements of Hughes *et al.* (8), Table I, who gave the ratios for the cross sections as 3.0 and 2.1 for thermal and $\backsim$1 Mev. neutrons.

Spins resulting from the $(\gamma,n)$ reaction were calculated as follows: according to recent photonuclear theories (7, 13) high energy photoreactions proceed mainly by electric dipole photon absorption ($l = 1$). However, the angular momentum carried by the emitted neutron is difficult to determine. An estimate for this was obtained as follows: a $Br^{81}$ nucleus was assumed to be excited by the absorption of 17 Mev. photons (corresponding to the same $Br^{80}$ excitation energy as in thermal neutron absorption by $Br^{79}$). The energy distribution of the emitted neutrons was then calculated on the basis of the statistical formula

due to Weisskopf and Ewing (1,23) and the average value of $l$ for each neutron energy evaluated as previously outlined. This allowed us to calculate the angular momentum averaged over all neutron energies and a value of $l_{av.} = 0.56$ was obtained. As a first approximation we assume that 44% of the photoneutron reactions emit neutrons with $l = 0$ and 56% with $l = 1$. Taking the spin of $Br^{81}$ as 3/2 (16), the first of these ($l = 0$) results in levels of spin 0(0.42), 1(0.250), 2(0.416), and 3(0.292), the second ($l = 1$ neutrons) gives $Br^{80}$ with spin 0(0.028), 1(0.208), 2(0.348), 3(0.291), and 4(0.125).

The three other reactions listed in Table I, $Se^{80}(p,n)Br^{80}$, $Br^{79}(d,p)Br^{80}$, and $Br^{81}(n,2n)Br^{80}$, were treated as follows. The first two were assumed to have all particles react with $l = 0$, and in the last reaction, where incident neutron energies up to 14 Mev. are involved, it was assumed that on the average $l = 3$ for the incident neutrons, with $l = 0$ for one of the emitted neutrons and 1 for the other, an average of 1/2 for the emitted neutrons, similar to the value used in the $(\gamma,n)$ reaction. All results are summarized in Table II, where we have listed the weights of the various level spins corresponding to the different reactions.

TABLE II

| Spin of level / Reaction | 0 | 1 | 2 | 3 | 4 | 5 | 6 | 7 | $R_\sigma$ Calc. | $R_\sigma$ Meas. |
|---|---|---|---|---|---|---|---|---|---|---|
| $Se^{80}(p,n)Br^{80}$ | 0·250 | 0·750 | | | | | | | 12 | 16 |
| $Br^{79}(n,\gamma)Br^{80}$ Thermal neutrons | | 0·375 | 0·625 | | | | | | 3·1 | 3·2 |
| $Br^{79}(n,\gamma)Br^{80}$ 1 Mev. neutrons | 0·042 | 0·250 | 0·416 | 0·292 | | | | | 2·2 | 2·1 |
| $Br^{81}(\gamma,n)Br^{80}$ $l = 0$ | 0·042 | 0·250 | 0·416 | 0·292 | | | | | 2·24 (44%) | 2·1 |
| $Br^{81}(\gamma,n)Br^{80}$ $l = 1$ | 0·028 | 0·208 | 0·348 | 0·291 | 0·125 | | | | 1·74 (56%) | |
| | | | | | | | | | 2.00 | |
| $Br^{79}(d,p)Br^{80}$ | 0·042 | 0·250 | 0·416 | 0·292 | | | | | 2·2 | 2·3 |
| $Br^{81}(n,2n)Br^{80}$ | 0·006 | 0·054 | 0·141 | 0·229 | 0·255 | 0·196 | 0·097 | 0.0224 | 0·58 | 0·9 |
| | | | | | | | | | | 0·7 |
| Assumed cascade branching ratio* $r_J$ | 1/0 | 9/1 | 2/1 | 1/1 | 1/2 | 1/9 | 0/1 | 0/1 | | |

$$*r_J = \frac{\textit{No. of transitions to State 1}}{\textit{No. of transitions to State 2}}.$$

With the data of Table II in mind and assuming that the cascade branching ratios, $r_J$, are independent of excitation energy over the region of interest it is possible to assign a reasonable set of values to them to give all the measured ratios $R_\sigma$. These assumed cascade branching ratios are also shown in the table as well as the calculated and measured values of $R_\sigma$. It must be emphasized that the branching ratios were chosen simply to give the desired values $R_\sigma$ and the validity of this choice must await further proof. On the other hand there was comparatively little leeway in this choice, for example, equal or nearly equal branching had to be assumed for the spin 3 level. In fact the best results

were obtained with branching ratios symmetric about this spin 3 level, which is intermediate between the spins of the ground and isomeric states. The smaller values for the ratio found in (6 and 20) are believed to be due to an admixture of fast neutrons during the measurements. An admixture of slow neutrons in the $(n,2n)$ reactions or neutron capture by $Br^{79}$ would explain the somewhat larger experimental results in this case.

It is of interest to note that $R_\sigma$ for the photoneutron reaction is relatively constant, being independent of the energy at energies greater than 4 Mev. above threshold (Fig.7). This would imply that $r_J$ is not materially changed as the number of levels available for cascading is varied. An analysis of this "cascade saturation" (this name was suggested to the authors by Dr. L. Trainer) phenomena would be rather difficult to carry out as can be seen from the difficulty of analyzing the simpler problem of cascade multiplicity (5).

## ACKNOWLEDGMENTS

The authors would like to thank the National Research Council of Canada for making available to two of them, L. P. and H. M., scholarships which enabled them to carry out this work. They would also like to thank A. G. W. Cameron for many helpful suggestions and enlightening discussions and Dr. L. Trainer of the National Research Council of Canada for helpful criticism.

## REFERENCES

1. BLATT, J. M. and WEISSKOPF, V. F. The theory of nuclear reactions. M.I.T. Tech. Rept. No. 42. May 1, 1950.
2. BOTHE, W. and GENTNER, W. Z. Physik, 112: 45. 1939.
3. CAPRON, P. C. and VERHOEVE-STOKKINK, A. J. Phys. Rev. 81: 336. 1951.
4. DUBRIDGE, L. A., BARNES, S. W., BUCK, J. H., and STRAIN, C. V. Phys. Rev. 53: 477. 1938.
5. FELD, B. T., FESHBACK, H., GOLDBERGER, M. L., GOLDSTEIN, H., and WEISSKOPF, V. F. Final Report of the Fast Neutron Data Project NYO-636.
6. FLEISHMANN, R. Z. Physik, 107: 204. 1937.
7. GOLDHABER, M. and TELLER, E. Phys. Rev. 74: 1046. 1948.
8. HUGHES, D. J., SPATZ, W. B., and GOLDSTEIN, N. Phys. Rev. 75: 1781. 1949.
9. JOHNS, H. E., KATZ, L., DOUGLAS, R. A., and HASLAM, R. N. H. Phys. Rev. 80: 1062. 1950.
10. KATZ, L. and CAMERON, A. G. W. Can. J. Phys. 29: 518. 1951.
11. KATZ, L., MCNAMARA, A. G., FORSYTH, P. A., HASLAM, R. N. H., and JOHNS, H. E. Can. J. Research, A. 28: 113. 1950.
12. LABERRIQUE-FROLOW, J. Compt. rend. 232: 1201. 1951.
13. LEVINGER, J. S. and BETHE, H. A. Phys. Rev. 78: 115. 1950.
14. MCDANIEL, B. D., WALKER, R. L., and STEARNS, M. B. Phys. Rev. 80: 807. 1950.
15. MCELHINNEY, J., HANSON, A. O., BECKER, R. A., DUFFIELD, R. B., and DIVEN, B. C. Phys. Rev. 75: 542. 1949.
16. National Bureau of Standards, U.S.A. Bulletin No. 499.
17. PRICE, G. A. and KERST, D. W. Phys. Rev. 77: 806. 1950.
18. SCHIFF, L. I. Phys. Rev. 73: 1311. 1948.
19. SEGRÈ, E. and HELMHOLZ, A. C. Revs. Modern Phys. 21: 271. 1949.
20. SNELL, A. H. Phys. Rev. 52: 1007. 1937.
21. SOLTEN, A. and WESTENSTEIN, L. Nature, 141: 76. 1938.
22. WÄFFLER, H. and HIRZEL, O. Helv. Phys. Acta, 21: 200. 1948.
23. WEISSKOPF, V. F. and EWING, D. H. Phys. Rev. 57: 472. 1940.

# FURTHER OBSERVATIONS ON DENDRITIC GROWTH IN METALS[1]

By F. Weinberg[2] and Bruce Chalmers[3]

ABSTRACT

The direction of dendrite growth has been determined as a function of crystallographic orientation for high purity tin and zinc, using a single crystal decanting technique. Measurements are reported on the rate of dendrite growth in lead, and the spacing between dendrite rows of a lead crystal for varying amounts of supercooling. The initial formation of dendrite stalks appears related to a cell structure observed on the exposed solid liquid interface.

A mechanism of dendrite growth is advanced and compared with the experimental observations. It is shown that dendritic growth occurs only during the initial part of solidification. The remainder is a result of the nondendritic advance of a solid liquid interface with some thickening of the existing branches.

## INTRODUCTION

An investigation into the dendritic growth of lead crystals was reported in a previous paper (4). The same techniques of growing crystals and measuring temperatures have been used for further observations on tin and zinc as well as on lead. These three metals were chosen because of their low melting points, which permits the use of simple techniques for growing single crystals, and because of their crystallographic structures, the three being representative of the structures of many of the common metals.

Observations are reported on the crystallographic direction of dendrite growth for tin and for zinc. These results, used in conjunction with those previously obtained for lead (4), provide three different sets of observations on which to base an explanation of the results.

The rate of dendrite growth and the average separation of the dendrite rows as a function of supercooling are examined to provide further data on the process of dendritic growth. Brief mention is made of the apparent development of spikes from a cell structure that is observed on the exposed solid liquid interface. This point, although believed to be important, is not discussed further, as the cell structure itself is discussed elsewhere.

A qualitative mechanism of dendrite formation is advanced and compared with the experimental observations.

## EXPERIMENTAL OBSERVATIONS

### *Direction of Dendrite Growth: Tin*

A decanted single crystal of tin of 99.98% purity is shown in Fig. 1, photographed from above and to one side. The crystal was grown from the right from a point outside the photograph. The *c* crystallographic axis is perpendicular to

[1] *Manuscript received April 15, 1952.*
*Contribution from the Department of Metallurgical Engineering, University of Toronto, Toronto, Ont.*

[2] *Mines Branch, Bureau of Mines and Technical Surveys, Ottawa.*
[3] *Professor of Physical Metallurgy, Department of Metallurgical Engineering, University of Toronto.*

FIG. 1. Decanted tin single crystal grown from the right showing dendrite stalks. FIG. 2. Zinc dendrite (× 20). FIG. 3. The decanted surface showing the development of some cells at the beginning of a dendrite row. The crystal was grown from the left (× 50).

the general direction of solidification and is in a horizontal plane, i.e., parallel to the top surface of the crystal. The *a* and *b* axes are at 45° to this horizontal plane.* The photograph shows a number of dendrite rows which have grown parallel to the direction of solidification and have large vertical secondary branches.

Other tin crystals were grown in which the *c* axis was vertical and with the *a* and *b* axes at 45° to the direction of solidification. In this case, vertical secondary branches were not observed. However, if the temperature of the liquid was recorded during growth, and the liquid decanted just after showing supercooling, then large flat dendrites were observed. These had grown parallel to the direction of solidification with slight traces of growth along the *c* axis. As growth proceeded, these flat dendrites were covered over by the advancing solid liquid interface. This interface shows no dendritic growth.

In tin, therefore, it appears that dendrite branches grow predominantly in the [110] and [1$\bar{1}$0] directions with very slight growth in the [001] direction.

*Direction of Dendrite Growth: Zinc*

In contrast to lead and tin, large single crystals of zinc could not be obtained under the conditions required for dendritic growth. However, sufficiently large dendrites were obtained to allow back reflection X-ray photographs to be taken on the dendrites themselves, so that their crystallographic orientation could be determined.

The decanted surface of a high purity (99.999%) polycrystalline zinc specimen showed dendrites in the form of flat branches. The flat branches for any one crystallite were all in one plane, the position of that plane, with respect to the specimen axis, depending on the orientation of the crystallite. An example is shown in Fig. 2, in which the plane containing the dendrite branches is very nearly horizontal, and where six-fold symmetry of the branches about a vertical axis is evident. Zinc has a close-packed hexagonal structure.

The back reflection X-ray photograph of the branches showed that they were in the (0001) plane, and growing in the [10$\bar{1}$0] and equivalent directions. The orientation of the branches is shown in the photograph by the arrows drawn parallel to the axial [2$\bar{1}\bar{1}$0] directions. Fig. 2 also shows slight traces of dendrite stalks perpendicular to the flat dendrite branches, that is, in the [0001] direction. In this case, their growth could have been inhibited by the upper surface of the liquid. However, for other orientations where there is no interference from the surface of the liquid, these perpendicular stalks are no larger.

For zinc, therefore, it appears that dendrite branches grow in the [10$\bar{1}$0] and equivalent directions, with slight growth in the [0001] direction.

## RATE OF SOLIDIFICATION IN LEAD

In examining the dendritic solidification of lead, it was noted that two processes appeared to be operating concurrently as the crystal solidified. First, following removal of the furnace, a roughly vertical solid liquid interface ad-

*Tin has an interlacing body centered tetragonal structure.

vanced at an accelerating rate, continuing to advance until the crystal had completely solidified. Secondly, a short period after the furnace had been removed, large dendrites commenced growing near the bottom of the boat to points well ahead of the interface; this could not happen unless the rate of advance of the dendrites is greater than that of the interface. To obtain more specific information regarding the relative rates of the two processes, measurements were made on a number of crystals in which the position of the general interface was recorded at known times by ripple marks on the top surface of the crystal, while temperature measurements of the metal were made near the bottom of the boat with five thermocouples.

The thermocouples were inserted through the walls of the boat, 1 mm. above the boat bottom and 10, 40, 55, 70, and 85 mm. (for couples 1 to 5 respectively) from the point at which solidification started. A switching mechanism successively connected each thermocouple for five-second intervals to the potentiometer and speedomax recorder system described previously (4). The crystals were 5 mm. thick and had a [100] direction parallel to the direction of solidification. From previous observations dendritic growth was expected to begin at approximately 12 mm. from the point at which solidification started.

The temperature measurements for one crystal are shown in Fig. 4. In each curve, the heavy lined portions are the parts actually recorded, corresponding to the period during which the couple was connected to the recorder by the

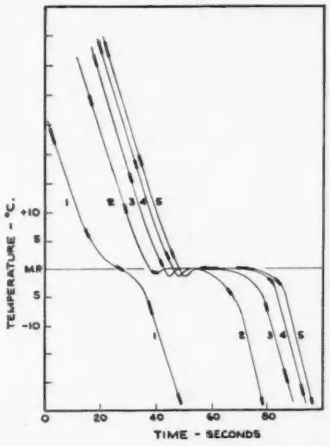


FIG. 4. Cooling curves taken simultaneously for five positions of one crystal during growth. The heavy lines are the parts actually recorded.

switching mechanism. Supercooling is shown in the drawn portion of the curves for couples 2 to 5, since growth proceeds dendritically in this part of the crystal. In the earlier paper (4) it was shown that dendritic growth is accompanied by supercooling of the liquid.

A decrease in supercooling of the liquid surrounding a thermocouple should indicate the presence of a solid liquid interface in this region. Knowing the spacing between the couples and the recorder chart speed, we can, therefore, approximately determine the position of the solid liquid interface from the curves in Fig. 4. This is shown in curve *N* of Fig. 5. For this curve, the points

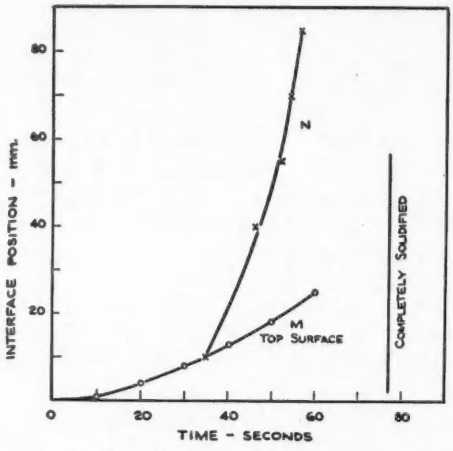


FIG. 5. Position of the solid liquid interface as observed on the top surface (curve *M*) and determined from the curves of Fig. 4 (curve *N*) during the growth of the same crystal.

at which the cooling curves of Fig. 4 first crossed the freezing point were used to indicate the presence of a solid liquid interface at the thermocouple, since the point of minimum supercooling was not actually recorded. Curve *M* of Fig. 5 shows the position of the general solid liquid interface, observed from ripple marks on the top surface of the same crystal.

Since growth proceeds dendritically along the bottom surface of the crystal for couples 2 to 5, curve *N* can be interpreted as indicating the approximate position of the advancing ends of the dendrite rows, as a function of time. The rate of growth of the dendrite rows, as given by the slope of curve *N*, reaches the value of 7 mm. per sec. The corresponding rate of the general solid liquid interface, from curve *M*, reaches 0.6 mm. per sec.

*Variation of Dendrite Spacing with Supercooling*

For these measurements lead crystals were grown in the manner normally adopted throughout this work, namely removing the furnace and, after a specific time interval, decanting the remaining liquid. In this particular case, the temperature of the liquid at the center of the dendrite region was recorded, and the liquid decanted during the constant temperature portion of the cooling curve.

If the liquid metal supercools, the amount of supercooling depends upon the ratio of the lateral heat loss from the liquid, to that lost longitudinally through

the solid metal. Accordingly, the amount of supercooling can be varied by sharply reducing the current through the furnace, then placing the furnace either round the liquid metal or seed crystal during growth; the supercooling is decreased or increased respectively.

After decantation, measurements were made of the relative positions of *all* the dendrite rows which were present on both sides of the thermocouple. Crystals having dendrite rows terminating at the couple were rejected. The measurements were made with a low powered traveling microscope using only the smaller vertical branches to indicate the position of the rows, since many of the larger vertical stalks were bent in the decanting process. The corresponding supercooling for each crystal was obtained from the recorder trace.

The results of the measurements are shown in Fig. 6, in which each point indicates the average spacing for one crystal. Regrowing a crystal a number of

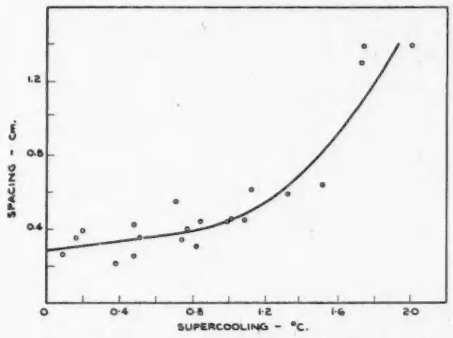


FIG. 6. Average separation of the dendrite rows of lead crystals as a function of the supercooling of the liquid metal.

times under apparently similar conditions does not produce exactly the same dendrite pattern, as shown by the considerable scatter of the points. However, a general relationship between spacing and supercooling does appear to exist, the spacing increasing as the supercooling increases. The curve also indicates that with progressively smaller amounts of supercooling, the average spacing approaches a value of 3 mm. for crystals grown in the present manner.

The large vertical secondary branches along any one dendrite row did not show any marked change in spacing as the supercooling was increased, remaining approximately 1 mm. apart.

## CELL STRUCTURE

When the decanted solid liquid interface of a lead crystal is examined under a microscope, a cell structure similar to that reported in tin by Rutter and Chalmers (3) is observed on the entire interface. Fig. 3 shows the lower part of a crystal interface, decanted during the early stage of dendritic growth, at the beginning of a small dendrite row. It is seen, as one proceeds from left to right

along the center of the photograph, that some of the cells are larger than their neighbors, both laterally and vertically.

Further to the right, past the region shown in the photograph, they grow sufficiently large to be seen without a microscope, and are recognized as the beginning of a dendrite row.

It therefore appears that the growth of dendrite stalks is closely related to the fine cell structure shown.

## SUMMARY OF OBSERVATIONS

The principal observations are summarized below, in order to present the facts which must be accounted for by a mechanism of dendrite formation. For completeness, the summary includes the observations reported in the earlier paper (4) on dendritic growth in lead.

(1) Dendrite stalks develop from an initially plane solid liquid interface when conditions are such that the interface advances at a high increasing rate. Secondary, tertiary, and higher order branches then form; some of them continue to grow. The resultant dendrite patterns are not exactly reproducible for crystals grown under apparently similar conditions.

(2) For the three metals examined, dendrites grow only in the crystallographic directions listed below. The directions are independent of the direction of solidification.

| Material | Crystal structure | Direction of dendrite growth | |
|---|---|---|---|
| | | Major growth | Minor growth |
| Lead | F.C.C. | ⟨100⟩ | None |
| Tin | B.C. Tet. (interlacing) | [110], [1$\bar{1}$0] | [001] |
| Zinc | H.C.P. | [10$\bar{1}$0] and equivalent directions | [0001] |

(3) It has been shown (4) that rapidly grown crystals of lead are divided into large regions of slightly different orientations; this effect is not observed in slowly grown crystals. A similar effect has also been observed in tin. It is attributed to the bending by convective disturbances of the small dendrites from which the substructure develops.

(4) Dendrites grow at very rapid rates, considerably greater than the advance of the general solid liquid interface.

(5) Supercooling of the liquid is a necessary condition for dendritic growth.

(6) The average separation of the dendrite rows of a crystal is greater with increased supercooling of the liquid. Secondary branch spacings appear to be independent of supercooling.

(7) A cell structure, possibly related to dendritic growth, is observed on the decanted surface of the crystal.

## MECHANISM OF DENDRITE FORMATION

In proposing a mechanism of dendrite formation in a pure metal, we shall consider as our starting point a slowly advancing, approximately plane solid liquid interface, exhibiting a cell structure similar to that shown in Fig. 3 and described in detail by Rutter and Chalmers (3).

### THERMAL CONSIDERATIONS

We shall assume that the following statements apply to crystals of pure metals, growing from the melt:

(*a*) A thin layer of supercooled liquid always precedes an advancing solid liquid interface.

When the solid and liquid phases of a pure metal are in equilibrium, then, by definition, the temperature of the metal is at its freezing point. With an advancing interface, however—a nonequilibrium case—the temperature of the liquid at the interface must be less than the equilibrium freezing point, that is, it must be supercooled, if growth is to continue.

(*b*) Growth proceeds by a mechanism similar to that described by Volmer for growth from the vapor, namely, by the nucleation and lateral growth of monolayers of atoms on a crystal surface, called two-dimensional nucleation. A summary of this mechanism is given by Buckley (1). At very slow rates the manner of growth may be that described by the Frank dislocation mechanism (2). This is assumed to become insignificant at the more rapid rates.

(*c*) The probability of a three-dimensional nucleus forming in the supercooled liquid layer of (*a*) is considerably less than that of a two-dimensional nucleus forming on the interface.

(*d*) The probability of a two-dimensional nucleus forming on the interface increases rapidly with increased supercooling at the interface.

At slow rates of growth, therefore, a slight amount of supercooling exists in the liquid layer, and the interface advances as a result of a continuous process of nucleation and spreading of layers of atoms. Three-dimensional nucleation, which would produce stray crystallites, does not occur, since the probability of formation of three-dimensional nuclei is small for small amounts of supercooling.

Consider first the temperature distribution around a slowly advancing plane interface, for the case of unidirectional heat flow parallel to the direction of solidification. From assumption (*a*) the liquid layer ahead of the interface must be supercooled. Then the solid metal at the interface must also be below the equilibrium freezing point temperature, since a thermal discontinuity cannot exist at the boundary between solid and liquid. The temperature distribution at the interface would then be of the form shown in Fig. 7(A).

If we extend the unidirectional heat flow case to one in which heat is lost laterally from the liquid as well as by conduction through the solid, then the temperature of parts of the liquid could be lower than that at the interface. The temperature distribution would then be of the form shown in Fig. 7(B). The latent heat evolved at the interface is now conducted into the liquid as well as through the solid (as shown by the two arrows).

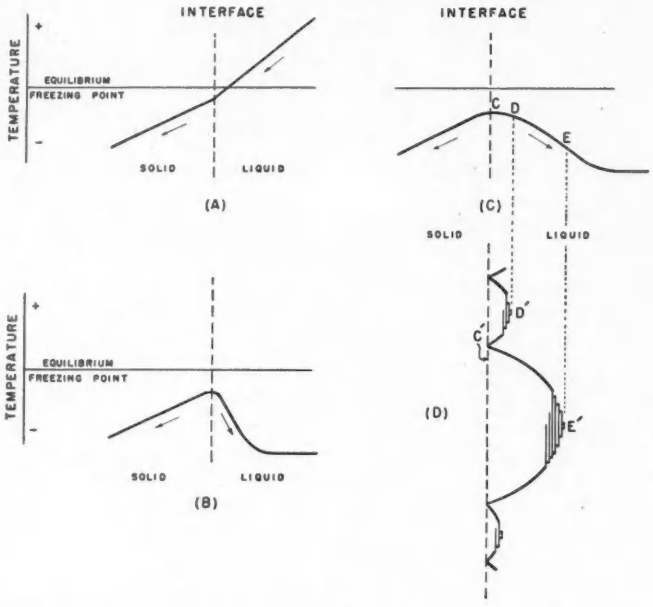


FIG. 7. (A), (B), (C). Interface temperature distributions for different growth conditions; (D). Schematic representation of interface contour (see text).

With an increase in the rate of growth, larger amounts of latent heat are evolved per unit time. This would tend to raise the temperature of the metal adjacent to the interface, resulting in the temperature distribution shown in Fig. 7(C).

Consider the actual case of an approximately plane advancing interface exhibiting a cell structure. The cells observed on the interface are of slightly varying dimensions and have surfaces convex towards the liquid, as shown schematically in Fig.7(D). The presence of the cells would tend to raise and extend the flattened portion, *CD*, of curve (C) in Fig. 7, but would not change the general shape of the curve. Then taking Fig. 7(C) as representing the temperature distribution of the interface shown in 7(D), it is apparent that the temperature at point $E'$ on the interface is slightly less than that at $D'$.

From assumption (*b*) growth proceeds by the nucleation and spreading of layers of atoms; from assumption (*d*) the probability of a nucleus forming is sensitive to small temperature differences. It therefore seems probable that nuclei will form more readily on $E'$ than $D'$, that is, $E'$ will advance at a more rapid rate than $D'$, increasing the separation $D'E'$, and therefore increasing the temperature difference. As this separation increases, the latent heat evolved by the larger cell will tend to raise the temperature at $D'$, further increasing the

temperature difference between $D'$ and $E'$. As a result, initially small differences in cell thickness will be accentuated as the interface advances.

Under these conditions, the largest cells will be advancing at the most rapid rate. Their presence raises the temperature of the liquid ahead of the smaller cells, reducing the rate of heat flow from the smaller cells into the general mass of supercooled liquid. The rate of advance of the smaller cells (interface $D'$) will then be increasingly controlled by the external conditions governing the rate at which heat is removed from the solid. On the other hand, the larger cells (interface $E'$) can continue advancing independently of heat lost from the system, as long as the liquid into which they grow remains supercooled. Their latent heat is absorbed in raising the temperature of the surrounding liquid to the equilibrium freezing point.

The latent heat evolved by the spreading layer of atoms, or disks, which have nucleated at $E'$ controls their radial growth in the following way. Consider the liquid ahead of plane $C'$ in Fig. 7(D) to be divided into thin equal sections by planes perpendicular to the direction of growth. Solidification will then continue in each section, independently of external heat losses from the system, until the temperature of the metal in the section has reached the equilibrium freezing point. For 1 gm. of liquid lead supercooled by 1 C.°, the percentage of metal that must solidify to raise the temperature of the lead to the equilibrium freezing point is:

$$\frac{\text{specific heat}}{\text{latent heat}} \times 100\% = \frac{0.0338}{6.26} \times 100\% = 0.5\%.$$

Accordingly, in each of the liquid sections considered above, only a small amount of metal need solidify in that section to prevent further growth without additional heat losses from the section. In the section of the liquid adjacent to interface $C'$, a number of disks are spreading. It is expected that the supercooling at this point is much less than 1 C.° Therefore, the radial growth of the disks will be arrested long before their total surface area is comparable to the area of plane $C'$.

In the next liquid section, the supercooling is greater and the number of disks smaller. The average radius of the disks in this section would be larger than in the first. Then, as we consider the third, fourth, and succeeding sections, we will obtain progressively fewer and wider disks present in that section, until the supercooling becomes approximately constant. The disk radii will then approach a constant value. Once the disks in a later section have grown radially to a size sufficient to remove supercooling in that section, then the disks can no longer advance. If all the liquid metal is supercooled, then we have no limiting condition on the thickness of the few cells which have advanced ahead of the others. They will then become macroscopic in size and take on a rod appearance.

At this stage of growth, we then have a number of macroscopic rods projecting into the liquid ahead of a general interface and growing at a rapid rate. The ends of these rods are roughly of a conical shape, nucleation occurring near the peak of the cone. The rate at which the rods lengthen is independent of the heat lost externally from the system. The diameter of the rods is dependent upon the supercooling of the liquid into which the rods grow, the number of rods which have managed to survive, and the rate at which heat is conducted away from the rods into the liquid.

As the rods become thicker, the amount of latent heat evolved for a unit increase in diameter becomes larger, and since radial growth depends on the rate at which heat is conducted into the liquid, the radial growth rate of the rods will decrease. With only a relatively few rods surviving, a condition will be reached in which the temperature distribution of the liquid surrounding the rod will approach that previously discussed for the general interface. Much of the liquid will still be supercooled. A cell structure will then form on the rod walls and the same process of preferential growth of some of the cells will take place resulting in another set of rod structures, that is, lateral branches would grow in the same manner as the initial rods. These in turn would branch again, and so on, forming a skeletal structure of branching stalks away from the general interface.

## EFFECTS OF CRYSTAL STRUCTURE

Consider, for a moment, one of the cells present on a slowly advancing interface. On an atomic scale, the solid liquid boundary of the cell likely consists of segments of many different crystallographic planes. Then as growth continues, one would expect (following Bravais (1, p.178)) that the low index segments would increase in size at the expense of the neighboring high index planes. Eventually, the boundary would consist entirely of planes characteristic of the surface of the idiomorphic form of the crystal as grown from the melt. Assuming Bravais Law applies in this case, these planes would be those in the system having the closest packing.

Accordingly, for the present case of a cellular interface advancing at an accelerating rate, each cell boundary should develop into some form of pyramid or wedge as defined by the number of equivalent closely packed planes.

The schematic diagram of the cell boundaries shown in Fig. 7(D) must then be modified. Instead of the boundary being smoothly convex toward the liquid with nucleation and growth of layers of atoms on planes perpendicular to the general direction of solidification, as shown, the boundary should be pictured as a pyramid or wedge pointing into the liquid. The axis of the pyramid would not generally be parallel to the general direction of solidification but would form an angle with this direction as determined by the orientation of the crystal. Two-dimensional nuclei would then form on the walls of the pyramid, most probably near the pyramid peak where the temperature of the boundary is lowest. The nuclei would spread on the pyramid wall on which they formed.

As growth continues at an accelerating rate, the peaks of some of the pyramids would project progressively further into the liquid ahead of the average solid

liquid interface, with the corresponding pyramid bases becoming larger. In effect, some of the cells (which now have a pyramid shaped solid liquid boundary) develop into rods in the manner described in the preceding section, except that the rods now grow in directions determined by the orientation of the crystal and not the general direction of solidification.

In order that the rods be propagated, we require fresh nucleation on each face of the pyramid. If nucleation stopped on one of the surfaces, the result would be a lateral translation of that part of the rod growing after this point, with respect to the first part. The rod would still grow parallel to its initial direction of growth. However, one would expect that, on the average, the same number of nuclei would form on all the sides, therefore the macroscopic rod would appear straight, being sufficiently large to make the slight lateral displacements which occur unobservable. Also, if one surface did stop growing, the temperature gradient of the liquid layer adjacent to it would become greater, and strongly increase the probability that new nuclei would form.

## COMPARISON WITH OBSERVATIONS

The points listed in the summary of observations may now be considered in relation to the proposed mechanism.

(1) *Development of Dendrite Stalks*

The development of spikes projecting ahead of a relatively smooth solid liquid interface, as well as the progressive growth and branching of the resultant dendrites, is accounted for by the above mechanism, when the liquid in which they grow remains supercooled. Many of the initial small spikes which do not continue to grow would be covered by the advancing general interface and thus would not be visible on the exposed interface after decanting. The variations of the dendrite pattern observed for crystals grown under apparently similar conditions would be expected since the dendrite stalks are the result of the chance development of some cells to a size slightly larger than their neighbors.

It has been mentioned previously that many texts on metallurgy, in discussing the dendritic solidification of a metal, state that dendrites continue to grow and branch until all the liquid metal is used up. If this were the case, then from Fig. 6, it is difficult to account for the long interval required for complete solidification after dendrites have commenced growing, noting that dendrites grow at the rate of approximately 7 mm. per sec. Further, for the tin crystal having the [001] direction perpendicular to the top surface of the crystal, the dendrites initially formed did not continue to grow but were covered over by the general interface as solidification proceeded. Finally, one would expect that the shrinkage cavity of a large crystal allowed to solidify completely would be distributed along the boundaries of the existing dendrite rows, which was not the case for the lead crystals examined.

What is believed to happen, when the liquid metal becomes supercooled, is that very rapid dendritic growth takes place from a solid liquid interface, if one exists, or from a solid nucleus. Because the liquid is supercooled, it is not necessary that heat be conducted away from the metal in order that freezing may occur. The latent heat evolved as the dendrites grow, however, spreads through

the liquid by conduction and convection; this allows the dendrites to grow at the rapid rates observed. At any point where the temperature of the liquid reaches the melting point, dendritic growth stops, and further growth takes place by the nondendritic advance of a solid liquid interface, at a rate governed by the rate at which heat is removed from the metal, and in a direction governed by the direction of heat flow. Some thickening of the existing dendrite branches would be expected as a result of heat conducted along the dendrite stalks, but this would be small since the stalks have a small cross-sectional area.

It has been noted that some secondary branches are much larger and thicker than others. The larger branches grow at approximately periodic intervals; the smaller branches more randomly and with a wider range of size. This may be attributed to the latent heat, evolved during growth, producing an interaction between neighboring branches. Consider first an isolated growing secondary branch. As it lengthens and thickens, its latent heat spreads radially in the supercooled liquid about it. As a result, when a second secondary branch starts to grow close to the first, the liquid into which it grows is not supercooled as in the first case, and it grows more slowly. This difference is accentuated as the first branch grows thicker, until finally the second branch stops advancing completely. As one considers a third and fourth branch, the effects of the latent heat from the first branch decrease. A point will then be reached when a branch grows to the same size as the first, creating the same conditions as the first for the branches following it. We thus obtain a secondary dendrite pattern similar to that observed.

(2) *Direction of Dendrite Stalks*

From the mechanism postulated, the direction in which dendrite branches grow should be defined by the position of the most closely packed planes. Picturing the pyramid structure described, the branch will grow in the direction of the axis of the pyramid, that is, parallel to the line bisecting the angles formed at the peak of the pyramid, the peak being at the intersection of the maximum number of equivalent closely packed planes.

In lead (face centered cubic) the {111} planes are the most closely packed. The maximum number of equivalent planes which intersect at a point is four, forming a four sided pyramid whose axis is a ⟨100⟩ direction. Dendrites should then grow in the ⟨100⟩ direction, as is observed.

In tin (interlacing body centered tetragonal), {100} are the most closely packed planes. The maximum number intersecting at a point is two, forming a wedge. The line bisecting the wedge, defining the direction of dendrite growth, is either [110] or [1$\bar{1}$0], agreeing with the experimental results. The slight dendritic growth observed in the [001] direction could be the result of planes not quite as closely packed as {100}; these combining with the wedge to form a pyramidal structure. The next set of planes in order of packing is of the (110) type, which will not do as they contain the line of intersection of the {100} planes. The (112) type planes, which are next, can form the remaining two sides of the pyramid. Following the same procedure as before, these planes would define dendrite growth in the observed [001] direction.

In zinc (hexagonal close packed) the basal plane (0001) is the most closely packed, but does not intersect with another equivalent plane. From the mechanism postulated, nucleation and spreading of layers of atoms takes place on the most closely packed planes. In this case, therefore, if large dendrites grow, they can only result from an anisotropic spreading of the layers of atoms in the (0001) plane. The next most closely packed planes are those of the $(11\bar{2}0)$ type, which have two equivalent planes intersecting. These equivalent planes intersect in two ways, forming an acute and obtuse angle respectively. Two possible bisecting lines, and therefore dendrite directions of growth, would be expected to exist, the $[11\bar{2}0]$, $[10\bar{1}0]$, and equivalent directions; both would produce dendrite branches growing in the basal plane having six-fold symmetry about the $c$ axis.

To decide between the two possible directions, consider the manner in which individual atoms are added to the periphery of a disk of spreading layers of atoms in the (0001) plane. If the disk is initially considered as bounded by a circle, then following the earlier argument, as growth continues, the most closely packed planes would grow at the expense of their neighbors. The circle would then become a hexagon, the sides consisting of planes of the $(11\bar{2}0)$ form. The corners of the hexagon would be at a slightly lower temperature than the center of the faces and, therefore, would favor nucleation at the more rapid rates of growth. The corners would then develop, leading to dendrites pointing in the $[10\bar{1}0]$ and equivalent directions, which is the observed direction of dendrite growth.

The latent heat evolved by the spreading layers of atoms in the basal plane would reduce the rate of radial growth of succeeding layers. With nucleation continuing on the basal plane, this could result in the appearance of small dendrite stalks similar to those observed, growing in the [0001] direction.

(3) *Rate of Dendrite Growth*

The observed rapid rate of dendrite growth, as compared to the rate of advance of the general solid liquid interface, is consistent with the mechanism proposed above. The rate of advance of a dendrite stalk growing well ahead of the general interface is governed by the rate of two-dimensional nucleus formation and, therefore, by the degree of supercooling of the liquid at the stalk tip. Accordingly, a primary stalk will advance at a more rapid rate than a secondary or tertiary stalk, since the latent heat of the primary has raised the temperature of the liquid near the tip of the secondary, and so on. The relative rates of the stalks are determined by the temperature dependence of two-dimensional nuclei formation. All can grow independently of external heat losses from the system.

The rate of advance of the general interface, however, is determined entirely by the direction and rate at which heat is removed from the system. It is inherently less than the rate of advance of a primary dendrite stalk, if the mechanism proposed is a real description of the solidification process.

(4) *Dendrite Row Spacing*

It was observed that the average separation of the dendrite rows of a crystal was greater with increased supercooling of the liquid. Average spacings as large

as 1.4 cm. were measured, corresponding to supercooling of 1.8 C.° The average separation of the large secondary branches, of approximately 1 mm., appeared to be independent of supercooling.

These observations do not appear to be consistent with the mechanism proposed, in which the spacing between neighboring branches should be determined by the radial spread of the latent heat evolved by the earliest branch.

Increased supercooling of the liquid would result in a larger average temperature gradient between the surface of a growing stalk and the general liquid. The rate of radial spread of the latent heat should then be greater and thus spacing between neighboring branches greater. The extent of this difference is not known without a detailed mathematical analysis. It may be small enough, however, to be unnoticed in the rough observations of secondary branch spacings, but could not account for the observed relatively large separation of the primary stalks (dendrite rows).

A closer examination of a decanted lead crystal, for example Fig. 5 in the earlier paper (4), shows that another factor may contribute to the large separation of the dendrite rows. If one dendrite row is a little ahead of its neighbor, then the transverse secondary branches of the leading row could grow ahead of the second, preventing any further growth of the second. This would depend upon the lag between the two dendrite rows and the relative rate of growth of the secondary branches as compared to the primary stalk.

The three dendrite rows on the left of Fig. 5 of (4) show that the transverse secondary branches become progressively smaller near the advancing end of the row, outlining a wedge in the horizontal plane. If at higher supercooling of the liquid, the secondary branches grow at a more rapid rate than the corresponding primary stalk, then the wedge angle would become larger. This would then reduce the distance that one dendrite row can lag behind its neighbor and still survive. On the average then, the spacing between dendrite rows would increase with increased supercooling.

## ACKNOWLEDGMENTS

The authors gratefully acknowledge financial aid received from the School of Engineering Research of the University of Toronto, and from the National Research Council of Canada.

## REFERENCES

1. BUCKLEY, H. E. Crystal growth. John Wiley and Sons, N.Y. 1951.
2. FRANK, F. C. Discussions of the Faraday Society "Crystal Growth" 5: 48. 1949.
3. RUTTER, J. and CHALMERS, B. Unpublished.
4. WEINBERG, F. and CHALMERS, B. Can. J. Phys. 29: 382. 1951.

# NOTE ON THE RESOLVING POWER OF MASS SPECTROMETERS[1]

By Larkin Kerwin

ABSTRACT

In calculating the resolving power of a homogeneous field mass spectrometer, one must consider the dispersion and the beam width of the instrument. The latter is the sum of at least 10 components, which are discussed. Formulae giving the resolving power of three types of spectrometer of current interest are developed, as well as formulae for positioning the exit slits.

There is a convenient rule of thumb for determining the approximate resolving power of a mass spectrometer. It is:

$$\text{(1)} \qquad \text{R.P.} = \frac{\text{radius of ion beam trajectory in magnetic field}}{\text{entrance slit width} + \text{exit slit width}}.$$

Although useful, this rule does not agree with experimental values, because factors other than those mentioned enter into a correct formula.

Since 1947, several authors have published papers on magnetic lenses of better focusing power than those previously known (2, 6, 7, 9, 16). Several inflection type spectrometers (3, 8, 10), and at least one normal-circle type (13), have been constructed. Because of the superior focusing of these instruments, the factors neglected in equation (1) assume greater importance, and so the rule of thumb becomes inadequate. It is not generally appreciated that almost a dozen effects may have to be considered in calculating resolving power. It is the purpose of this note to enumerate them, and to give the formulae required.

## A. RESOLVING POWER—GENERAL

In an ideal spectrometer, each component of the analyzed beam would reach the detector as a point. In practice, several factors result in ions having the same mass-to-charge ratio ( $= A$) being spread out into a beam having a certain width at the detector. We shall consider the total width $W_t$ as being the sum total of all possible effects including those of the exit slit and detector.

Two ion beams having different mass-to-charge ratios will be focused by the lens action of the spectrometer at different places. The displacement $x$ of one beam from another per change of mass-to-charge ratio is called the dispersion $D$ of the instrument. Thus:

$$\text{(2)} \qquad D = \frac{x}{\Delta A}.$$

Speaking generally, the resolving power of a focusing instrument is the limit of its ability to distinguish one focused beam from another. In the case of mass spectrometry, if a beam of particles of ratio $A$ is just resolved from a beam of particles differing in ratio by $\Delta A$, then the resolving power is defined as:

$$\text{(3)} \qquad \text{R.P.} = \frac{A}{\Delta A}.$$

[1] *Manuscript received April 15, 1952.*
*Contribution from Département de Physique, Université Laval, Quebec, Que.*

Equations (2) and (3) give:

$$\text{R.P.} = \frac{DA}{x}. \tag{4}$$

Two beams are just resolved when the distance separating them approaches zero. This means that the separation $x$ becomes the total beam width $W_t$ at the limit of resolution, and so:

$$\text{R.P.} = \frac{DA}{W_t}. \tag{5}$$

### B. DISPERSION

The dispersion produced by a homogeneous magnetic field bounded by any shape of boundary may be calculated by the methods of the references cited. Formulae for three symmetrical types of current interest may be developed (7) and simplified as follows:

Normal Case (NC): $D_n = 2\Delta R/\Delta A$,
Inflection Case (IC): $D_f = 4\Delta R/3\Delta A$,
Normal Circle Case (NCC): $D_c = (2\Delta R/\Delta A)\ (1 + n)$

where $n = (\Delta R/R)\tan^2\theta$, $\theta$ being the half-angle of deviation. We assume here that the dispersion is measured normally to the central ion beam. If measured otherwise (as in spectrographs) the ratios are not so simple. In the three cases cited, $\Delta R/R = \Delta A/2A$, as is well known. In the normal-circle case, $n$ is usually small. Therefore we may write:

$$D_n = D_c = R/A, \tag{6}$$

$$D_f = 2R/3A. \tag{7}$$

### C. TOTAL WIDTH $W_t$

The following factors enter into the calculation of the total effective beam width $W_t$:

(*a*) $I$ —the image of the finite source,
(*b*) $Ab$ —the aberration due to imperfect focusing in the plane of the magnet pole face,
(*c*) $G$ —the aberration caused by beam divergence normal to the pole face plane,
(*d*) $E$ —the dispersion caused by variations in energy of the beam particles,
(*e*) $SC$ —the defocusing effect of space charge,
(*f*) $F$ —the fringing field effect,
(*g*) $S$ —the exit slit width,
(*h*) —the fact that the line of focus of different beams does not lie normal to the central ion beam,
(*i*) $t$ —the exit slit thickness,
(*j*) $T$ —the effect of detector time response.

(*a*) *Image of Source—I*

The component of the total width $W_t$ which is an image of a finite source is, in the normal and inflection cases, equal in width to the source (7). In the normal-circle case the image is slightly larger, the magnification differing very little from one however. So:

$$I_n = I_f = I_c = I. \tag{8}$$

In spectrometry, the source is usually a slit through which a divergent beam of ions emerges, and the source width is taken as this slit width. Although sufficiently accurate for most purposes, a strict analysis must take into account the slit thickness (beveled slits eliminate this), and the effective narrowing of the slit by the electric field used between it and the previous slit. This effect seems to be very small in most cases.

(*b*) *Aberration in Pole Plane—Ab*

Formulae for this component of the total width $W_t$ are given in the references cited (7), and may be simplified as follows:

$$\text{NC} : Ab_n = R\alpha^2, \tag{8}$$

$$\text{IC} : Ab_f = 2\alpha^3(3a - 2x)/3\cos\theta, \tag{9}$$

$$\text{NCC}: Ab_c = R\alpha^3 \tag{10}$$

where $a$, $x$, and $\theta$ are related to $R$ by the following expressions (7):

$$R^2 = x(3a - x)/2, \tag{11}$$

$$x = R\sin\theta, \tag{12}$$

and $\alpha$ is the half-angle of divergence of the ion beam. In the normal case, the aberration is large, and even in the other type instruments it definitely may not be neglected when the components of the total beam width are properly proportioned. Persson discusses an asymmetric inflection type (13) whose aberration is given as being smaller than that of the symmetric type discussed in this paper. Actually, the aberration may be made as small as the designer wishes by use of an appropriate field shape (7). However the three types discussed here are convenient to build.

(*c*) *Aberration Normal to Pole Plane—G*

The trajectories of the ions passing between the pole faces of the analyzing magnet do not all lie in the median plane or in planes parallel to it. For those ions whose trajectory plane lies at an angle to these, the magnetic field acts only on the component of their momentum parallel to the median plane. This has the same effect as if the velocity of the ions were reduced, and hence an aberration is produced. This aberration is given by:

$$\text{NC} : G_n = R\beta^2, \tag{13}$$

$$\text{IC} : G_f = 2R\beta^2/3, \tag{14}$$

$$\text{NCC: } G_c = R\beta^2(1 + n') \tag{15}$$

where $\beta$ is the maximum angle that any ion beam makes with the median plane. We assume here that the beam width is very small compared with the total ion trajectory, and note that in the normal-circle case $n'$ is usually small.

(*d*) *Energy Dispersion—E*

Generally speaking, the ions in a spectrometer beam are assumed to possess the same energy. However the mechanism of sources commonly used is such that a small variation of the average energy $E$ of the ions may be present. This factor $\Delta E/E$ gives rise to a corresponding $2\Delta R/R$, and therefore to a component of the total width $W_t$. This component is, for the three cases considered:

$$\text{NC} : E_n = R\Delta E/E, \tag{16}$$

$$\text{IC} : E_f = 2R\Delta E/3E, \tag{17}$$

$$\text{NCC: } E_c = R\Delta E/E. \tag{18}$$

The normal-circle case is subject to the usual small correction.

(*e*) *Space Charge—SC*

When the ion beam in a spectrometer is very intense and finely focused, the ions repel each other at the exit slit to such an extent that the beam may be broadened. This addition to the total width we shall designate by *SC*. It will be proportional to the beam intensity and the fineness of the focusing. The effect may be reduced by operating the spectrometer at higher pressures than used to be considered advisable (11). The ionization of the residual gas molecules helps to neutralize the defocusing space charge. Measurements on the resolving power of the Laval inflection spectrometer indicate that the effect is small when the operating pressure is between $5 \times 10^{-6}$ and $10^{-5}$ mm. Hg.

(*f*) *Fringing Field—F*

The fringing magnetic field extending beyond the pole gap has three effects on the ion beam, one of which affects the effective beam width. The first is a displacement of the focal point. This has been discussed by several authors (15). The second effect is due to the curvature of the fringing field lines. This results in a small component of the field being normal to both the ion beam and the main field, when the ion beam is not normal to the pole edge. Thus the beam emerges to the exit slit longer than it entered, and unless the exit slit is made correspondingly longer, there is a loss of intensity, which does not, however, affect the beam width (7). The third effect is also caused by the curved fringing field, and corresponds to an effect mentioned by Aston in discussing deflection by electric fields (1). Ions which are not in the central plane are deflected by a component of the fringing field, and therefore will not be deviated by exactly the same amount as the central ion beam (14). The image will thus be widened by a component which we shall designate *F*. It cannot be eliminated for a finite beam, but is usually small, particularly for normal spectrometers. It may be

reduced by reducing the curvature of the fringing lines—by making the pole edges obtuse angles instead of the usual right angles. Such a procedure would aggravate the focal point displacement.

(*g*) *Exit Slit Width—S*

As is well known, the exit slit adds its width $S$ to the effective total width, and so we have for this component:

$$S_n = S_f = S_c = S. \tag{19}$$

(*h, i*) *Line of Focus and Exit Slit Thickness — t*

It has been pointed out by Persico and Geoffrion (12) for $\beta$-ray spectrometers, and by Persson (13) for mass spectrometers that, if the exit slit is properly located, the ion beam is at best focus only when it is at the center of the slit. As it sweeps to one side of the slit, the beam does not remain in focus, because the line of focus for beams of different radii does not lie in the plane of the slit but at an angle to it, as shown in the figure. Therefore if any part of the beam can pass through the exit slit when the beam is not perfectly focused the effective beam width is increased. This effect is complicated by the use of slits whose thickness is not neglible compared to their width. From the figure, drawn for a particular case, we can define:

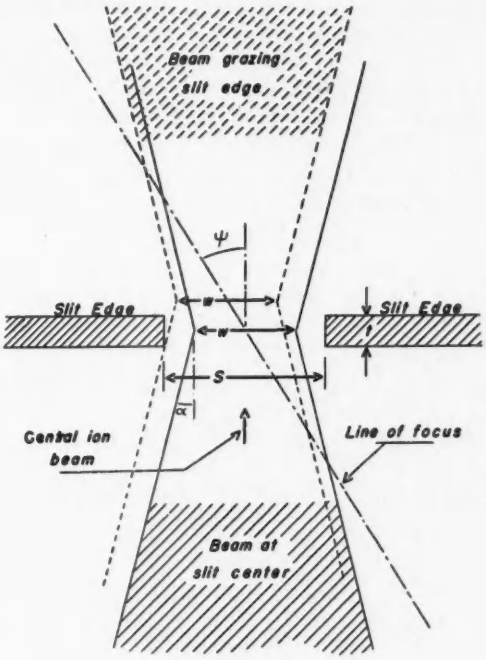


FIG. 1.

$S$ = the exit slit width,

$t$ = the exit slit thickness,

$\psi$ = the angle between the central ion beam at focus and the line of focus (13),

$\alpha$ = the half-angle of divergence of the ion beam,

$w$ = the width of the ion beam at perfect focus,

or: $w = I + Ab + G + E + SC + F$.

The factors contributing so far to the total width $W_t$ make up the sum $S + w$. If the thickness of the exit slit is negligible (beveled edges), and if the plane of the slit is such as to lie approximately along the line of focus (the effective width $S$ being then the projection of the actual width on a plane normal to the central ion beam), then the contribution remains $S + w$. However if these conditions are not met, the expression becomes:

(20) NC: $$\frac{(S + w)(1 - \tan \alpha/2 \tan \psi) - (t \tan \alpha)/2}{1 - \tan \alpha/\tan \psi},$$

(21) IC and NCC: $$\frac{(S + w) - t \tan \alpha}{1 - \tan \alpha/\tan \psi}.$$

The effect is larger in the case of the higher-order focusing instruments. This is because their beams, at the exit slit, diverge $\pm\alpha$ from the central ion beam, as shown in the figure. This fact is expressed analytically by the term $\alpha$ being given in the expression for the aberration as a third power. In the normal case, the angle $\alpha$ is contained in the aberration expression (equation (8)) as a second power. This indicates, as is well known, that the beam at focus diverges only $+\alpha$ from the central ion beam; therefore the effect discussed in this section is found for only one side of the beam.

The equations are valid for $S$ wider or narrower than $w$.

(*j*) *Detector — T*

The automatic scanning of spectrometer ion beams involves the use of a detector whose response time is not zero. This effect may be considered as adding a component $T$ to the total width $W_t$.

*Résumé—*$W_t$

The total effective image width $W_t$ is given by:

(22) NC: $$\frac{(S+I+Ab+G+E+SC+F)(1-\tan \alpha/2\tan\psi)-(t \tan\alpha)/2}{1 - \tan \alpha/\tan \psi} + T,$$

(23) IC and NCC: $$\frac{(S + I + Ab + G + E + SC + F) - (t \tan \alpha)}{1 - \tan \alpha/\tan \psi} + T.$$

## D. RESOLVING POWER

The application of the various formulae for dispersion (B) and total image width (C) allow us to write equation (5) for the resolving power in the various cases as:

(24) NC:

$$\frac{R(1-\tan\alpha/\tan\psi)}{(S+I+Ab+G+E+SC+F)(1-\tan\alpha/2\tan\psi)-(t\tan\alpha)/2+T(1-\tan\alpha/\tan\psi)},$$

(25) IC: $$\frac{2R(1-\tan\alpha/\tan\psi)}{3(S+I+Ab+G+E+SC+F)-3(t\tan\alpha)+3T(1-\tan\alpha/\tan\psi)},$$

(26) NCC: $$\frac{R(1-\tan\alpha/\tan\psi)}{(S+I+Ab+G+E+SC+F)-t\tan\alpha+T(1-\tan\alpha/\tan\psi)}.$$

Most contemporary spectrometers should consider almost all of these factors in calculating resolving power. However proper design can eliminate some of them and improve the resolution. Thus, if beveled slits are used, the exit slit plane placed approximately along the focus line, the sweep time sufficiently slow, and space charge effects reduced, then the equations become:

(27) NC and NCC: $$\frac{R}{S+I+Ab+G+E+F},$$

(28) IC: $$\frac{2R}{3(S+I+Ab+G+E+F)}.$$

In order to obtain high resolving power, it has been customary to design so as to make $Ab$ and $G$ negligible, by using very small slits. However these quantities also enter into the expression for beam intensity, and reducing them involves a sacrifice of beam strength. Geoffrion has shown (4, 5) that an optimum choice of parameters exists which ensures a maximum beam intensity for a given resolving power.

### E. MEASUREMENTS

Determination of the actual resolving power of a spectrometer usually involves making measurements on a spectrogram record or photograph. For this purpose, certain formulae are useful:

(*a*) The base of a "mass peak" is, of course, the total effective width $W_t$ given by equations (22) and (23). Regardless of the height of any particular peak, the base widths are all the same width if the sweep is linear. This may not always appear to be the case, owing to the tails of small peaks disappearing into the base line. Another exception is the case of very intense beams, where the space charge $SC$ and the detector effect $T$ are functions of beam intensity.

(*b*) The width of the mass peak at half intensity is exactly equal to $S$ when $S$ is greater than $w$, regardless of intensity distribution in the beam. The only exception to this is the improbable case of the intensity being zero for a finite distance within the beam, i.e. there being effectively *two* beams.

When $S$ is smaller than $w$, the peak width at half intensity is equal to $w$, when the ion beam intensity is homogeneous.

(*c*) When the exit slit $S$ is wider than $w$, and the sweep time is sufficiently slow, the peaks will have flat tops. The width of the flat top is a function of the difference between $S$ and $w$. The equations for flat-top width are:

(29) NC: $$\frac{(S-w)(1+\tan\alpha/2\tan\psi)-(t\tan\alpha)/2}{1+\tan\alpha/\tan\psi},$$

(30) IC and NCC: $$\frac{(S-w)-t\tan\alpha}{1+\tan\alpha/\tan\psi}.$$

Here the effect of the tails may be to cause smaller peaks to appear to have wider tops than the intense peaks.

## F. SLIT LOCATION

It was mentioned in previous sections that the effect of the line of focus not being normal to the central ion beam could be avoided by placing the plane of the exit slit approximately along the line of focus. More precisely, the slit edges should be staggered so that their remote faces are separated by a normal distance equal to (for the inflection and normal-circle cases):

(31) $$d_{f,nc}=\frac{S+w}{\tan\psi}.$$

The two edges are located symmetrically on each side of the point of central focus. In the normal case, only the slit edge nearest the source is moved, so that the final separation is given by:

(32) $$d_n=\frac{S+w}{2\tan\psi}+\frac{t}{2}.$$

If this is done, and the other conditions mentioned are met, then the resolving power will be given by equations (27) and (28).

However this staggering of the slit edges also affects another measurement—that of the flat-top width, which is reduced. Under conditions described in this section, the flat-top width will be given by:

(33) NC: $$(S-w)-w/((\tan\psi/\tan\alpha)-1),$$

(34) IC and NCC: $$(S-w)-2w/((\tan\psi/\tan\alpha)-1).$$

## G. CONCLUSION

The equations presented in this note refer specifically to the three types of homogeneous magnetic lens of current interest. They may be adapted to the various other types of lenses (6, 7, 9) by calculating the dispersion of each type and the various factors entering into the total image width. The methods of calculating these factors are given in the references cited. However although many suggestions for improving resolution involve reducing the various aberrations, it is worth remembering that optimum operating conditions generally dictate a more or less even distribution of the total image width among the various components. Therefore in a well-designed instrument, none of the aberrations contributing to beam intensity will be negligible.

I am glad to acknowledge interesting discussions on this subject with Professors Claude Geoffrion and Gerard Nadeau, and am particularly grateful to Father Ernest Clarke who critically reviewed the manuscript.

## REFERENCES

1. ASTON, F. W. Phil. Mag. 39: 611. 1920.
2. BAINBRIDGE, K. T. 7th Solvay Congress. 1947.
3. CUTLER, PAUL. Private Communication.
4. GEOFFRION, C. Rev. Sci. Instruments, 20: 638. 1949.
5. GEOFFRION, C. Rev. Sci. Instruments, 23: 224. 1952.
6. HINTENBERGER, H. Z. Naturforsch. 3: 125, 669. 1948. Rev. Sci. Instruments, 20: 748. 1949.
7. KERWIN, LARKIN. Rev. Sci. Instruments, 20: 36. 1949.
8. KERWIN, LARKIN. Rev. Sci. Instruments, 21: 96. 1950.
9. KERWIN, L. and GEOFFRION, C. Rev. Sci. Instruments, 20: 381. 1949.
10. LEGER, E. Thése de doctorat, Université Laval, Quebec, Que. 1952.
11. NIER, A. O. and BERNAS, R. H. Rev. Sci. Instruments, 19: 895. 1948.
12. PERSICO, E. and GEOFFRION, C. Rev. Sci. Instruments, 21: 945. 1950.
13. PERSSON, R. Arkiv Fysik, 3: 455. 1951.
14. PLOCH, W. and WALCHER, W. Z. Physik, 127: 274. 1950.
15. REUTERSWARD, C. Arkiv Fysik, 3: 53. 1951.
16. SPIGHEL, M. J. phys. radium, 8: 10, 207. 1949.

# ELECTROMAGNETIC FIELDS OF CURRENT-CARRYING WIRES IN A CONDUCTING MEDIUM[1]

By James R. Wait[2]

ABSTRACT

The fields of a finite wire carrying a harmonically time varying current are calculated for the case of the wire contained in an infinite conducting medium. The insulation of current-carrying wires in a conducting medium is discussed. It is concluded that the insulation characteristics need not usually be considered.

The fields of a finite current-carrying vertical wire within a horizontal slab are calculated. The mutual impedance between two finite circuits, one being vertical and within the slab and one horizontal and on the surface of the slab, is calculated for limiting values of the lower medium conductivity. The results are thought to be applicable to electrical methods of well logging in geophysical exploration.

## INTRODUCTION

The essence of geophysical well testing is a determination of physical properties *in situ*. The purpose is to detect commercial minerals or to determine data required in the interpretation of geophysical surface measurements. Geophysical well-testing methods (2) may be divided into the following categories: electrical logging, temperature measurements, seismic measurements, magnetic measurements, radioactive measurements, and possibly a few others. This paper is an analysis of an electrode system which is essentially suited to alternating current measurements in wells and comes within the general category of electrical logging.

Usually electrical logging in wells is equivalent to a mapping of the electrical resistivity of the medium adjacent to the well. Direct currents are supplied to electrodes which are usually spaced at distances equal to 10 or 20 times the diameter of the hole. Resulting electric fields or potentials are then measured by two additional electrodes which are placed in the well or on the surface but in the region of influence of the current electrodes. The analysis of the mutual or transfer resistance between these pairs of electrodes for various geological formations is well known and an account is given in the above mentioned reference (2).

Very often however the current used is commutated direct or alternating current. The experimental advantages are numerous over the older direct current methods. It is generally assumed however for purposes of analysis that the currents and fields in the medium are governed by static or potential theory. However as will be evident from the following analysis the currents and fields must be generally analyzed by wave theory which should reduce to the well-known static cases as the frequency approaches zero.

The analysis of an electrode system subjected to alternating currents should then provide a definite criterion as to the range of frequencies and associated

[1] *Manuscript received in original form October 1, 1951, and as revised June 16, 1952. Contribution from the Department of Electrical Engineering, University of Toronto, Toronto, Ont.*

[2] *Now with Defence Research Board, Ottawa, Canada.*

parameters that may be employed and yet still be correctly analyzed by methods of potential theory. In addition the following analysis by wave theory suggests an obvious extension to the well-known static method. That is, a spectrum of frequencies is employed for the source current. For any particular configuration of the electrodes within the well a transfer impedance can be calculated for all significant frequencies. As the frequency approaches zero this impedance, of course, should reduce to the well-known transfer resistance as calculated from potential theory. The behavior of this frequency spectrum of the mutual impedance then should give additional information as to the electrical properties of the rock media in the neighborhood of the electrodes.

The analysis will be carried out for the fields of an insulated grounded circuit of finite length which is situated in what is assumed to be an infinite and homogeneous conducting medium. The circuit is to be supplied an alternating current by a generator which is either contained within the well or is situated on the surface. In the latter case the contribution to the fields from the twisted-pair line to the upper electrode in the well is considered negligible.

Some idea as to the effect of the well on the radiated fields from the current-carrying linear circuit is obtained by the analysis of an infinite current-carrying wire with a concentric cylindrical insulation contained in a conducting medium of infinite extent. This analysis is carried out in the second section of this paper.

Since for many purposes the crust of the earth may be represented by horizontally stratified layers it is of considerable practical interest to extend the analysis to the case where the electrode arrangement is contained within a horizontal slab of contrasting conductivity and dielectric constant to the semi-infinite external regions above and below the slab. The analysis is then carried out in the third section of this paper for the fields of a vertical grounded circuit contained within the horizontal slab. The formal solution for this problem is obtained by a straightforward but tedious application of Maxwell's field equations. A workable solution is only obtained if certain limiting values of the electrical constants of the external regions are chosen. For example, the upper semi-infinite region above the slab may represent the atmosphere where the conductivity is essentially zero. The lower region may be very highly conducting to represent saline water, or on the other hand, it may be very poorly conducting to represent certain oil bearing sands. Furthermore since the slab medium is to be a moderate earth conductor displacement currents will play a negligible role compared to the conduction currents at audio frequencies.

The starting point for the analysis is the well-known Maxwell's equations. For a homogeneous and isotropic medium of conductivity $\sigma$, permeability $\mu$, and dielectric constant $\epsilon$, these equations are:

$$\text{curl}\,\mathbf{H} = (\sigma + i\omega\epsilon)\mathbf{E} + \mathbf{J}, \tag{1}$$

$$\text{curl}\,\mathbf{E} = -i\mu\omega\mathbf{H}. \tag{2}$$

The electric field vector $\mathbf{E}$ and the magnetic field vector $\mathbf{H}$ here vary as $\exp(i\omega t)$. $\mathbf{J}$ is the impressed current density vector.

## THE FINITE CURRENT ELEMENT

Formulas will now be derived for the fields of a finite insulated linear wire which is carrying a harmonically time varying current. The amplitude and phase of the current is considered to be constant throughout its length. The propagation effects along the wire are neglected; this is justified only at low frequencies. A cylindrical reference system is chosen with the $z$ axis parallel to the wire. The wire extends from a point $A$ to the point $B$ on the $z$ axis.

The electric fields $E_z$ and $E_\rho$ at the point $P$ due to an element $dS$ of the wire carrying a current $I$ are given by the well-known dipole formulas by Stratton (5):

$$E_z = I\left[P(r) + \frac{\partial^2}{\partial S \partial z} Q(r)\right] dS, \tag{3}$$

and

$$E_\rho = I \frac{\partial^2 Q(r)}{\partial S \partial \rho}\, dS$$

where $S$ here is taken as the coordinate in the $z$ direction to specify a point on the wire.

The functions $P(r)$ and $Q(r)$ are given by:

$$P(r) = \frac{i\mu\omega}{4\pi} \frac{\exp(-\gamma r)}{r},$$

and

$$Q(r) = \exp(-\gamma r)/4\pi\sigma r \tag{4}$$

where

$$\gamma = (i\sigma\mu\omega - \epsilon\mu\omega^2)^{\frac{1}{2}} \simeq (i\sigma\mu\omega)^{\frac{1}{2}}$$

and

$$r = [\rho^2 + (S - z)^2]^{\frac{1}{2}}.$$

The fields at point $P$ due to current throughout the length $L$ of the element are then obtained by an integration with respect to $S$.

$$E_z = I\int_A^B P(r)\, dS + I\left[\frac{\partial Q(r)}{\partial z}\right]_{S=A}^{B} \tag{5}$$

and

$$E_\rho = I\left[\frac{\partial Q(r)}{\partial \rho}\right]_{S=A}^{B}.$$

The integral in equation (5) will be evaluated

$$\int_A^B P(r)\, dS = \frac{i\mu\omega}{4\pi}\int_{A-z}^{B-z} \frac{\exp[-\gamma[(S-z)^2 + \rho^2]^{\frac{1}{2}}]}{[(S-z)^2 + \rho^2]^{\frac{1}{2}}}\, d(S-z).$$

This can be written in the following form:

$$\int_A^B P(r)\, dS = \frac{i\mu\omega}{4\pi}\int_{\beta(A-z)}^{\beta(B-z)} \frac{\exp[-(1+i)u]}{u}\, dx$$

where

$$u = (a^2 + x^2)^{\frac{1}{2}}, \quad x = \beta(S - z),$$

$$\beta = (\sigma\mu\omega/2)^{\frac{1}{2}}, \quad \text{and } a = \beta\rho.$$

The integral can now be broken down into the following integrals:

$$\int_A^B P(r)\,dS = \frac{i\mu\omega}{4\pi}\left[\int\frac{1}{u}\,dx - \int\frac{1-e^{-u}\cos u}{u}\,dx - \int\frac{e^{-u}\sin u}{u}\,dx\right]$$

where the limits of integration of $x$ are $\beta(A-z)$ to $\beta(B-z)$. The first integral is well known and the second and third are respectively equal to the tabulated, generalized cosine and sine integrals (1). The integral involving $P(r)$ is finally given by

$$\int_A^B P(r)\,dS = \frac{i\mu\omega}{4\pi}\left[\sinh^{-1}x/a - E_c(a,x) - E_S(a,x)\right]_{x=\beta(A-z)}^{\beta(B-z)}$$

where now the integration limits of $x$ can be substituted directly.

Employing this result, the fields $E_z$ and $E_\rho$ for the current $I$ in the linear grounded wire element can be written

$$\begin{aligned}\frac{E_z}{I} = \frac{i\mu\omega}{4\pi}\Bigg[&\Big\{\sinh^{-1}\frac{B-z}{\rho} - \sinh^{-1}\frac{A-z}{\rho}\\ &+ E_c[\beta\rho,\beta(A-z)] - E_c[\beta\rho,\beta(B-z)]\Big\}\\ &+ i\{E_S[\beta\rho,\beta(A-z)] - E_S[\beta\rho,\beta(B-z)]\}\Bigg]\\ &+ \frac{\exp(-\gamma r_1)}{4\pi\sigma r_1^3}(1+\gamma r_1)(z-A) - \frac{\exp(-\gamma r_2)}{4\pi\sigma r_2^3}(1+\gamma r_2)(z-B)\end{aligned} \tag{6}$$

and

$$\frac{E_\rho}{I} = \frac{\exp(-\gamma r_1)}{4\pi\sigma r_1^3}(1+\gamma r_1)\rho - \frac{\exp(-\gamma r_2)}{4\pi\sigma r_2^3}(1+\gamma r_2)\rho \tag{7}$$

where

$$r_1 = [(z-A)^2+\rho^2]^{\frac{1}{2}}$$

and

$$r_2 = [(z-B)^2+\rho^2]^{\frac{1}{2}}.$$

These general formulas can be simplified somewhat for certain conditions. At low frequencies where $\beta r_1$ and $\beta r_2$ are much less than one the fields can be written simply

$$\frac{E_z}{I} = \frac{i\mu\omega}{4\pi}\left[\sinh^{-1}\frac{B-z}{\rho} - \sinh^{-1}\frac{A-z}{\rho}\right] + \frac{z-A}{4\pi\sigma r_1^3} - \frac{z-B}{4\pi\sigma r_2^3} \tag{6a}$$

and

$$\frac{E_\rho}{I} = \frac{\rho}{4\pi\sigma}\left(\frac{1}{r_1^3} - \frac{1}{r_2^3}\right). \tag{7a}$$

The general formula can also be simplified somewhat if the observation point becomes very near the wire so that the end points are at a relatively great distance. The fields are

$$E_z/I = -\frac{i\mu\omega}{2\pi}K_0(\sqrt{i\sigma\mu\omega}\,\rho) \tag{6b}$$

and

$$E_\rho / I = 0. \tag{7b}$$

This formula was given by Rudenberg (3) as the field due to a current-carrying wire of infinite length. $K_0$ is the modified Bessel function of the third kind of zero order.

## EFFECT OF THE INSULATION

The presence of the insulation on the current-carrying wires has not been considered up to this point. This insulation is necessary to assure that the current flows in a substantially uniform manner throughout the length of the wire. The theory of propagation of electrical current along an infinite wire with a cylindrical insulated covering is quite difficult. Sunde (6) gives an approximate analysis for the two cases when the insulated wire lies on the surface of a flat earth and when the wire is immersed in an infinite dissipative medium.

Sunde's (6) equations Nos. 5.33 and 5.34 would indicate that the propagation constant for low frequency currents on an insulated wire in a conducting medium is determined largely by the electrical characteristics of the insulation. In fact, the propagation constant $\Gamma$ of a current $I(x)$ at point $x$ from the current $I_0$ at the generator terminals is given approximately by

$$I(x) \simeq I_0 \exp(-\Gamma x) \tag{7}$$

where

$$\Gamma \simeq i(\epsilon_0 \mu_0 \omega^2)^{\frac{1}{2}}$$

where $\epsilon_0$ and $\mu_0$ are the dielectric constant and the permeability of the insulation material. It would then seem justified to assume that the current on the finite current element is essentially uniform if the parameter $|\Gamma L|$ is much less than one where $L$ is the length of the current element. In other words, the current supplied by the generator flows into the surroundings by conduction paths alone from the ends of the wire, the displacement current paths from the wire to the medium through the insulation are offered a relatively high impedance at low frequencies.

The electric and magnetic fields at some exterior point in the medium due to current from this insulated current-carrying wire will now be shown to be essentially unaltered by the presence of the insulation for a specified uniform current on the wire. The fields of an infinite insulated current-carrying wire in a dissipative medium will be calculated. The current will be given by $I \exp(i\omega t)$. The radius of the insulated covering is $b$, the electrical properties of the insulation are $\sigma_1$, $\epsilon_1$, and $\mu_0$. The external medium is assumed to be infinite with electrical properties $\sigma_2$, $\epsilon_2$, and $\mu_0$. Cylindrical coordinates $(\rho, \phi, z)$ with axial symmetry are chosen.

The fields in this case can be derived from a Hertz vector in the $z$ direction,

$$E_z = -\gamma^2 \Pi_z,$$
$$H_\phi = -(\sigma + i\omega\epsilon)\frac{\partial \Pi_z}{\partial \rho}. \tag{8}$$

The primary field of the wire within the insulation is given by

$$E_z^0 = -\frac{i\mu_0\omega I}{2\pi} K_0(\gamma_1\rho). \tag{9}$$

This can be checked readily since it is an axially symmetrical solution of the wave equation and behaves in a proper manner as $\gamma_1\rho$ approaches zero in accord with equation (6*b*). The total Hertz vectors $\Pi_{1z}$ and $\Pi_{2z}$ inside and outside the insulation are given* respectively by

$$\begin{aligned} \Pi_{1z} &= g\,K_0(\gamma_1\rho) + A\,I_0(\gamma_1\rho), \\ \Pi_{2z} &= B\,K_0(\gamma_2\rho) \end{aligned} \tag{10}$$

where

$$g = I/2\pi(\sigma + i\omega\epsilon)$$

and

$$\gamma_1 = (i\sigma_1\mu_0\omega - \epsilon_1\mu_0\omega^2)^{\frac{1}{2}},$$

$$\gamma_2 = (i\sigma_2\mu_0\omega - \epsilon_2\mu_0\omega^2)^{\frac{1}{2}}.$$

The boundary conditions require that $E_z$ and $H_\phi$ are continuous across the interface at $\rho = b$. This leads to two equations to solve for $A$ and $B$. They are given as follows:

$$A = \frac{B(\sigma_2 + i\omega\epsilon_2)K_0(\gamma_2 b) - g(\sigma_1 + i\omega\epsilon_1)K_0(\gamma_1 b)}{I_0(\gamma_1 b)}$$

and

$$B = \frac{g(\sigma_1 + i\omega\epsilon_1)}{b(\sigma_2 + i\omega\epsilon_2)[\gamma_1 I_1(\gamma_1 b)K_0(\gamma_2 b) + \gamma_2 I_0(\gamma_1 b)K_1(\gamma_2 b)]}.$$

For lower frequencies where $|\gamma_1 b|$ and $|\gamma_2 b|$ are much less than one the coefficient $B$ simplifies to

$$B \cong g\frac{\sigma_1 + i\omega\epsilon_1}{\sigma_2 + i\omega\epsilon_2}.$$

The electric field $E_z$ in the exterior region is then given by

$$E_z \cong -\frac{i\mu_0\omega I}{2\pi} K_0(\gamma_2\rho). \tag{11}$$

It is apparent that the insulation characteristics need not be considered in calculating the field due to an insulated current-carrying wire of infinite length, for all reasonable frequencies.

It would then seem reasonable to ignore the insulation characteristics of finite wires if the radius of the insulation $b$ and the propagation constants $\gamma_1$ and $\gamma_2$ are such that $|\gamma_1 b|$ and $|\gamma_2 b|$ are much less than one.

## THE VERTICAL RADIATOR WITHIN A HORIZONTAL CONDUCTING SLAB

The medium up to this point has been considered to be infinite and homogeneous. A special problem of an inhomogeneous region will now be considered. A vertical current-carrying wire element which is insulated throughout its length

**It has been pointed out by the reviewer that the expression set up for $\Pi_{1z}$ in equation (10) is only approximate, in the sense that it implies that $|\gamma_1 a| \ll 1$ where $a$ is the wire radius.*

will be placed within a horizontal conducting slab. Calculations will be made for the cases when the lower region is either highly conducting or highly insulating.

It is convenient to start with the vertical current element $Idh$ at a depth $h$ from the upper surface of the slab of thickness $d$. The slab has electrical properties $\sigma_1$, $\epsilon_1$, and $\mu_0$. The upper region and the lower region have electrical properties $\sigma_0$, $\epsilon_0$, $\mu_0$ and $\sigma_2$, $\epsilon_2$, $\mu_0$, respectively. It is assumed that the media have no magnetic permeability contrast. The situation is indicated in Fig. 1 with respect to conventional cylindrical coordinates. The polar symmetry about the $z$ axis is evident.

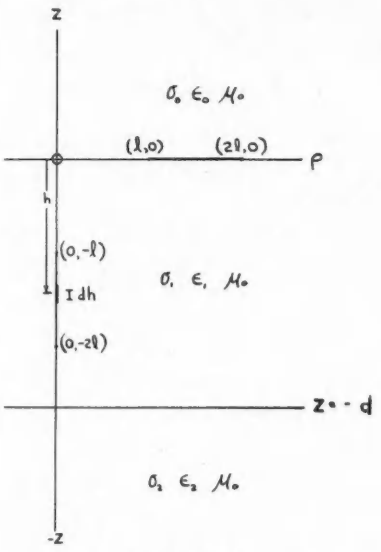


FIG. 1. The coordinate system for the vertical dipole element within a horizontal slab. The finite grounded circuits are also shown.

When the depth $d$ of the slab approaches infinity the problem is formally equivalent to that of Weyl's (7). The primary radiation from the current element $Idh$ can be written in terms of a Hertz vector $\Pi$ which has only a component in the $z$ direction and is given by

$$\Pi = \frac{Idh}{4\pi(\sigma_1 + i\omega\epsilon_1)} \frac{\exp(-\gamma_1 r_1)}{r_1} \tag{12}$$

where

$$r_1 = [(z+h)^2 + \rho^2]^{\frac{1}{2}}.$$

The electric and magnetic fields are given by

$$E_\rho = \frac{\partial^2 \Pi_i}{\partial \rho \partial z}, \qquad H_\rho = 0,$$

$$E_z = \frac{\partial^2 \Pi_i}{\partial z^2} - \gamma_i^2 \Pi_i, \quad H_z = 0, \tag{13}$$

$$E_\phi = 0, \qquad H_\phi = -(\sigma_i + i\omega\epsilon_i)\frac{\partial \Pi_i}{\partial \rho}$$

where $\gamma_i = (i\sigma_i \mu_0 \omega - \epsilon_i \mu_0 \omega^2)^{\frac{1}{2}}$.

The subscript $i$ in the above expressions takes the value 0, 1, or 2 to designate the particular medium.

Solutions of the wave equation that have axial symmetry and are finite at the origin and infinity are given by

$$\exp\left[\pm (\lambda^2 + \gamma_i^2)^{\frac{1}{2}} z\right] J_n(\lambda\rho). \tag{14}$$

The general solutions for the Hertz vectors $\Pi_i$ are then given by

$$\Pi_0 = k \int_0^\infty f_1(\lambda) J_0(\lambda\rho) \exp(-u_0 z)\, d\lambda \tag{15}$$

for $z \geqslant 0$,

$$\Pi_1 = k \exp(-\gamma_1 r_1)/r_1 + k \int_0^\infty [f_2(\lambda) \exp(u_1 z) + f_3(\lambda) \exp(-u_1 z)]\, J_0(\lambda\rho)\, d\lambda \tag{16}$$

for $0 \geqslant z \geqslant -d$, and

$$\Pi_2 = k \int_0^\infty f_4(\lambda) \exp(u_2 z)\, J_0(\lambda\rho)\, d\lambda \tag{17}$$

for $z \leqslant -d$ where $k = \dfrac{Idh}{4\pi(\sigma_1 + i\omega\epsilon_1)}$ and $u_i = (\lambda^2 + \gamma_i^2)^{\frac{1}{2}}$.

The well-known Sommerfeld (4) integral representation for $\exp(-\gamma_1 r_1)/r_1$ must be used,

$$\exp(-\gamma_1 r_1)/r_1 = \int_0^\infty \lambda/u_1\, J_0(\lambda\rho) \exp[\pm u(z + h)]\, d\lambda. \tag{18}$$

The positive sign in the exponent is used for $(z + h) \leqslant 0$, and the negative sign is used for $(z + h) \geqslant 0$.

The boundary conditions require that the $E_\rho$ and the $H_\phi$ components be continuous across the interfaces at $z = 0$ and $z = -d$. The boundary equations can then be written down:

$$\left.\begin{aligned} \frac{\partial \Pi_0}{\partial z} &= \frac{\partial \Pi_1}{\partial z} \\ \gamma_0^2 \Pi_0 &= \gamma_1^2 \Pi_1 \end{aligned}\right\} \text{ at } z = 0, \tag{19}$$

$$\left.\begin{aligned} \frac{\partial \Pi_1}{\partial z} &= \frac{\partial \Pi_2}{\partial z} \\ \gamma_1^2 \Pi_1 &= \gamma_2^2 \Pi_2 \end{aligned}\right\} \text{ at } z = -d. \tag{20}$$

The solution of these equations yields:

$$(21)\quad f_2(\lambda) = \frac{\frac{\lambda}{u_1}\left(1 - \alpha\frac{u_0}{u_1}\right)e^{-u_1 h}\left(\beta\frac{u_1}{u_2} + 1\right)e^{2u_1 d} + \frac{\lambda}{u_1}\left(\beta\frac{u_1}{u_2} - 1\right)e^{u_1 h}\left(1 - \alpha\frac{u_0}{u_1}\right)}{\Delta}$$

and

$$(22)\quad f_3(\lambda) = \frac{\frac{\lambda}{u_1}\left(1 + \alpha\frac{u_0}{u_1}\right)\left(\beta\frac{u_1}{u_2} - 1\right)e^{u_1 h} - \left(1 - \beta\frac{u_1}{u_2}\right)\frac{\lambda}{u_1}\left(1 - \alpha\frac{u_0}{u_1}\right)e^{-u_1 h}}{\Delta}$$

where $$\Delta = \left(1 + \alpha\frac{u_0}{u_1}\right)\left(1 + \beta\frac{u_1}{u_2}\right)e^{2u_1 d} + \left(1 - \beta\frac{u_1}{u_2}\right)\left(1 - \alpha\frac{u_0}{u_1}\right)$$

and $\alpha = \gamma_1^2/\gamma_0^2$ and $\beta = \gamma_2^2/\gamma_1^2$.

This is the formal solution of the problem with no approximations. A great simplification is effected when all the displacement currents in the three media are assumed to be negligibly small. That is, the conduction currents are assumed to predominate.

The first special case is when the lower region is very highly conducting and the upper region is highly insulating. The following inequalities will be assumed to be valid for all values of the integration variable $\lambda$.

$$\alpha\frac{u_0}{u_1} = \frac{\gamma_1^2(\lambda^2 + \gamma_0^2)^{\frac{1}{2}}}{\gamma_0^2(\lambda^2 + \gamma_1^2)^{\frac{1}{2}}} \gg 1,$$

$$\beta\frac{u_1}{u_2} = \frac{\gamma_2^2(\lambda^2 + \gamma_1^2)^{\frac{1}{2}}}{\gamma_1^2(\lambda^2 + \gamma_2^2)^{\frac{1}{2}}} \gg 1,$$

and $$\sigma_1 \gg \epsilon_1\omega.$$

The coefficients then simplify considerably to

$$(23)\quad f_2 = -\frac{\lambda}{u_1}\left[\frac{\exp\left[-u_1(h - 2d)\right] - \exp\left(u_1 h\right)}{1 + \exp\left(2u_1 d\right)}\right]$$

and

$$(24)\quad f_3 = \frac{\lambda}{u_1}\left[\frac{\exp\left(u_1 h\right) - \exp\left(-u_1 h\right)}{1 + \exp\left(2u_1 d\right)}\right].$$

The denominator of the preceding two expressions can be expanded in a binomial series. The Hertz potential in the slab is then given by the following when the expressions for $f_2$ and $f_3$ are inserted in (16):

$$\begin{aligned}(25)\quad \Pi_1 = {} & k\exp\left(-\gamma_1 r_1\right)/r_1 - k\int_0^\infty \exp\left[u_1(z - h)\right] J_0(\lambda\rho)\,\lambda/u_1\,d\lambda \\ & + k\int_0^\infty \Big\{\sum_1^\infty (-1)^n \exp\left[u_1(z - h - 2nd)\right] \\ & - \sum_1^\infty (-1)^n \exp\left[u_1(z + h - 2nd)\right] \\ & + \sum_1^\infty (-1)^n \exp\left[-u_1(z + h + 2nd)\right] \\ & - \sum_1^\infty (-1)^n \exp\left[-u_1(z - h + 2nd)\right]\Big\} J_0(\lambda\rho)\,\lambda/u_1\,d\lambda.\end{aligned}$$

These are all integrals of the following form:

$$\int_0^\infty \exp(-au_1)\, J_0(\lambda\rho)\, \lambda/u_1\, d\lambda = \frac{\exp[-\gamma(a^2+\rho^2)^{\frac{1}{2}}]}{(a^2+\rho^2)^{\frac{1}{2}}}.$$

The required integrations can thus be carried out

$$\Pi_1/k = \sum_{n=-\infty}^{\infty} (-1)^n [F(h+2nd) - F(-h+2nd)] \tag{25a}$$

where

$$F(w) = \frac{\exp\{-\gamma_1[(z-w)^2+\rho^2]^{\frac{1}{2}}\}}{[(z-w)^2+\rho^2]^{\frac{1}{2}}}.$$

It is interesting to note that these terms represent images of the primary dipole and they are situated at appropriate positions on the $z$ axis.

The electric fields within the slab are given by

$$E_z = -\gamma_1{}^2\Pi_1 + \frac{\partial^2\Pi_1}{\partial z^2}$$

(26)

and

$$E_\rho = \frac{\partial^2\Pi_1}{\partial\rho\partial z}$$

The electric fields along the surface of the slab (i.e. $z = 0$) can be written

$$E_\rho = \frac{\partial^2 Q_1}{\partial h\partial\rho} Idh \tag{27}$$

where

$$Q_1 = \frac{1}{2\pi\sigma_1}\left\{\frac{\exp[-\gamma_1(h^2+\rho^2)^{\frac{1}{2}}]}{(h^2+\rho^2)^{\frac{1}{2}}} + \sum_1^\infty (-1)^n [F_0(h+2nd) - F_0(-h+2nd)]\right\} \tag{28}$$

and

$$F_0(w) = \frac{\exp[-\gamma_1(w^2+\rho^2)^{\frac{1}{2}}]}{(w^2+\rho^2)^{\frac{1}{2}}}.$$

When the lower layer becomes highly insulating such that

$$\frac{\gamma_1{}^2}{\gamma_2{}^2}\left[\frac{\lambda^2+\gamma_2{}^2}{\lambda^2+\gamma_1{}^2}\right]^{\frac{1}{2}} \gg 1$$

a similar analysis can be carried out. The function corresponding to $Q_1$ is here given by $Q_2$ where

$$Q_2 = \frac{1}{2\pi\sigma_1}\left\{\frac{\exp[-\gamma_1(h^2+\rho^2)^{\frac{1}{2}}]}{(h^2+\rho^2)^{\frac{1}{2}}} - \sum_1^\infty (-1)^n [F_0(h+2nd) - F_0(-h+2nd)]\right\}. \tag{29}$$

It is of interest now to apply this result to calculate the mutual impedance between a vertical grounded wire element of length $l$ in the slab and a horizontal

grounded wire element of length $l$ on the surface of the slab. The coordinates $(\rho, z)$ of the end points of the vertical element are $(0, -l)$ and $(0, -2l)$. The coordinates of the end points of the surface element are $(l, 0)$ and $(2l, 0)$. The circuits are considered to be coplanar.

The mutual impedance $Z$ is defined as the line integral of the electric field along one circuit due to unit current throughout the other circuit. The calculation follows directly from integrations with respect to $h$ and $\rho$ of equation (27).

$$Z = \int_l^{2l}\int_l^{2l} \frac{\partial^2 Q_m(\rho, h, d)}{\partial\rho\partial h}\, dh\, d\rho$$

$$= Q_m(2l, 2l, d) + Q_m(l, l, d) - Q_m(l, 2l, d) - Q_m(2l, l, d). \tag{30}$$

The subscript $m$ takes the value 1 or 2 to designate the highly conducting or the highly insulating lower region respectively. The functions $Q_m$ as a function of $\rho$, $h$, and $d$ are given by equations (28) and (29) respectively.

The function $2\pi\sigma l \mid Z \mid$ is plotted in Fig. 2 against the parameter $(\sigma\mu\omega/2)^{\frac{1}{2}}l$ for the case when the slab has an infinite depth and the two cases of the highly

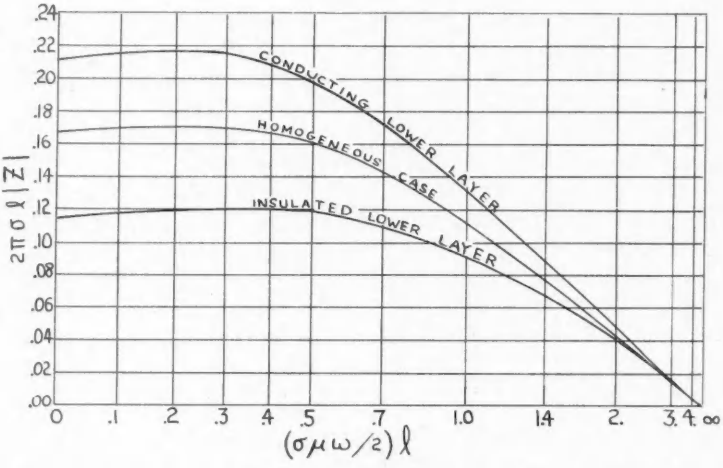


FIG. 2. The magnitude of the mutual impedance between the two grounded circuits for the case of a homogeneous conducting half space and the two cases when the slab is terminated by a highly conducting and a highly insulating lower medium.

conducting and the highly insulating lower region for the depth $d$ of the slab equal to $2l$. It is quite apparent that the impedance amplitude decreases with increasing frequency or conductivity due to the increased attenuation with the slab medium.

This calculation and other similar calculations of the fields of a vertical radiator within the slab, if based on the general formula of equation (25), neces-

sarily assume that all the displacement currents in the media are negligible compared to the conduction currents in the slab. This implies that the normal current density at the upper surface of the slab is zero. This also implies that the equation of Laplace is the governing equation in the highly insulating region.

## REFERENCES

1. Annals of the Computation Laboratory of Harvard University. Vol. 21. 1949.
2. HEILAND, C. A. Geophysical exploration. Chap. 11. Prentice-Hall, Inc., New York. 1946.
3. RUDENBERG, R. Z. angew. Math. Mech. 5: 361. 1926.
4. SOMMERFELD, A. Ann. Physik, 81: 1135. 1926.
5. STRATTON, J. A. Electromagnetic theory. McGraw Hill Book Company, Inc., New York and London. 1941. p.435.
6. SUNDE, E. Earth conduction effects in transmission systems. Chap. 5. Van Nostrand Company, Inc., New York. 1949.
7. WEYL, H. Ann. Physik, 60. 1919.

# DESIGN AND PERFORMANCE OF A FUSED SILICA MICROBALANCE[1]

By Hugh Carmichael

ABSTRACT

The construction and the use of a robust microbalance with a fused silica beam are described. The design is such that the microbalance is undisturbed by convection even in surroundings where it would be impossible to use an ordinary microbalance; nevertheless the instrument is very convenient to operate. A comprehensive theoretical treatment of the silica torsion balance and of the effects of constructional imperfections is given and shown to be in good agreement with experiment. The performance of the microbalance is illustrated by means of an example from the microchemical work of B. G. Harvey, where four samples of americium oxide, of masses between two and six micrograms, were weighed on 100 mgm. scale pans, with a proven accuracy better than 0.3%. The precautions that were taken to minimize the harmful effects of adsorption and dust are described. A commercial version of this microbalance is now available.

## 1. INTRODUCTION

### 1.1 *Historical*

Microbalances of the conventional type, in which the beam and the scale pans are supported by knife edges, can be operated only with difficulty with a precision of more than two or three micrograms. It has long been known that for work of greater precision than this it is desirable not to use knife edges; in microbalances of greater precision, filaments of a highly elastic substance such as clear fused silica (quartz) have been used with success to replace knife edges.

The first beam microbalance of the elastic filament type appears to have been constructed by W. Weber (12) in 1841 using very thin strips of metal. The first beam microbalance constructed entirely of fused silica was described in 1909 by B. D. Steele and K. Grant (11). In this instrument the scale pans were suspended by silica fibers but the beam rested on a knife edge. An improved form of the Steele–Grant microbalance, in which the beam also was suspended by vertical silica fibers, was described in 1914 by H. Pettersson (10) and his dissertation contains a detailed account of the development of microbalances up to that date. His account of the theory and performance of his own instrument is very complete and includes discussion of its behavior *in vacuo*. He could adjust the temperature of specimens in the range −190°C. to 700°C. while they were being weighed. He used his balance to study the absorptive and hygroscopic qualities of surfaces, the vaporization of refractory solids, the density of gases and vapors, and the magnetic susceptibility of gases. He looked for a possible influence of temperature on weight and even discussed the possibility of directly verifying the mass–energy relation with a sensitive microbalance. He was aware of the errors that arose from the presence of static electric charges on the balance and, following Steele and Grant, he used the ionizing radiation from uranium oxide to dissipate them.

[1] *Manuscript received April 15, 1952.*
*Contribution from the Physics Division, Atomic Energy of Canada Limited, Chalk River, Ontario. Issued as A.E.C.L. No. 3.*

The smallest detectable mass difference claimed by Pettersson was $10^{-9}$ gm. with loads of 20 mgm., and of the order of twice this amount with loads of $\frac{1}{4}$ gm.

In the measurement of these very small mass differences it is not possible to use the conventional method of manipulating weights. Such weights would be almost invisible and their mass would be liable to change appreciably from pickup of foreign matter such as dust. It is desirable also, when weighing, to be able to bring the beam exactly to a preset balance point. It is therefore necessary to have a smoothly variable means of bringing the beam to balance and to have this means calibrated in terms of mass. In the Steele–Grant and Pettersson microbalances the variable agent was the air pressure in the case. The beam had on one side a hollow airtight silica bulb whose buoyancy depended on the air pressure.

Comparatively recently Neher (8) introduced the very convenient method of applying a variable torque to the beam by a silica fiber in torsion. The angle through which the torsion fiber must be twisted to restore balance after the addition of a mass to one side of the beam is proportional to this mass. Thus the instrument may be calibrated with a single standard weight of convenient size.

The best features of the microbalances of Steele and Grant (11), Pettersson (10), and Neher (8) were incorporated by Kirk, Craig, Gullberg, and Boyer (7) in an instrument which was much better adapted for routine use than the previous instruments. This microbalance was seen by the writer in Chicago in 1945 and details of the silica suspension became available (9) in 1946. The construction, theory, and use of this and other fused silica microbalances have been summarized in a recent article by B. B. Cunningham (3).

1.2 *General*

Early in 1947 the writer was given the responsibility of producing microbalances for the Canadian and British Atomic Energy Projects. He had no previous experience with very sensitive balances, but, at the Chalk River Laboratory, he had the benefit of watching the microchemical work of B. G. Harvey who had constructed fused silica microbalances for his own use (4). The writer had made silica electroscopes (1) of such stable performance that the Brownian motion limit of sensitivity was reached.

The beam structure of the microbalance made by Kirk, Craig, Gullberg, and Boyer (7) could not be greatly improved. On the other hand the general design of their microbalance, which followed conventional practice in that the beam was enclosed in a rectangular protecting case of considerable volume, allowed unnecessary thermal convection arising from temperature differences. They mentioned (7) the need for a second case placed over the first "to minimize the effects of temperature change".

The microbalance described below has substantially the same beam but it is otherwise of quite unconventional design. It has a protecting housing in the form of a solid block and the beam swings in a cavity in the block, which is as narrow as possible and of such a shape that large-scale convection is prevented.

The housing is made of metal of good heat conductivity, so that the time taken for the temperature to become uniform after a disturbance is short. No additional thermal protection is required. This microbalance can be used in ordinary laboratory surroundings and seems to be unaffected by the proximity of the operator or by the radiant heat from common laboratory sources.

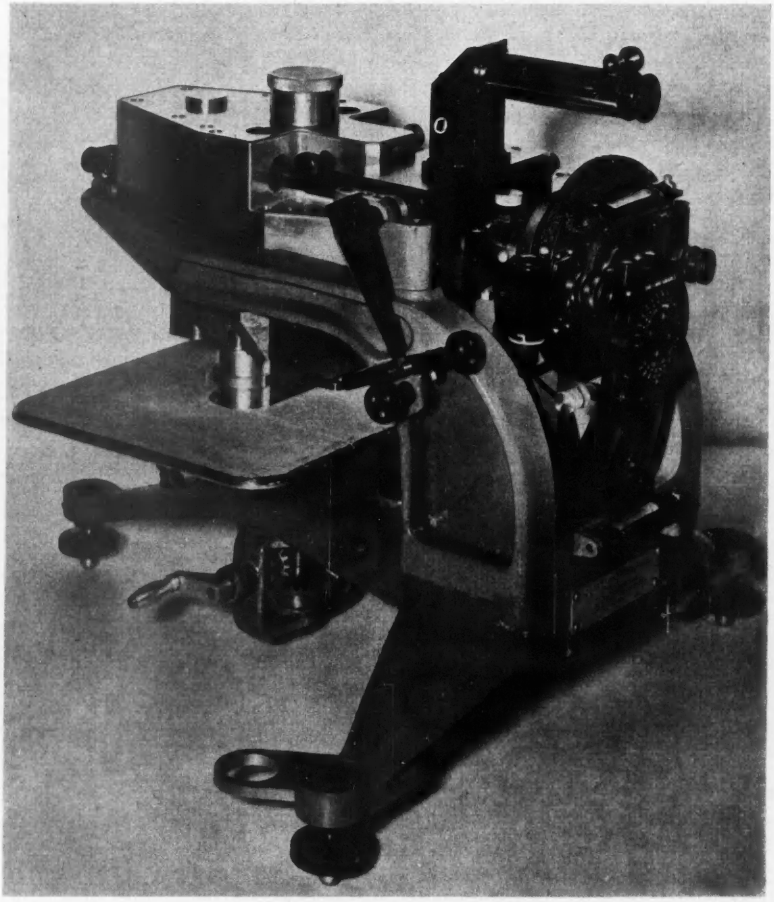

FIG. 1. The Microbalance Mark I constructed at the Chalk River Laboratory of the National Research Council of Canada.

In addition the new design is such that the microbalance is convenient to operate, is resistant to damage by clumsy operation, is easily fitted with a new suspension should a breakage occur, and is suitable for quantity production.

A propotype was tested in summer 1948 and more than 12 microbalances of this Mark I design (Fig. 1) were made at Chalk River in the following year. A

Mark II form of the same instrument (Fig. 2), having several improvements including projection reading, has since been made by the Watts Division of the London firm of Hilger and Watts Ltd. and this instrument is now commercially available. The basic design of Mark II was evolved (2) in September and November 1949 at Chalk River during a visit by Mr. V. W. H. Towns, Technical Director of Hilger and Watts.

Generally, in both microbalances, a sensibility (the smallest detectable mass difference) of about $10^{-8}$ gm. is provided. With this sensibility, mass differences

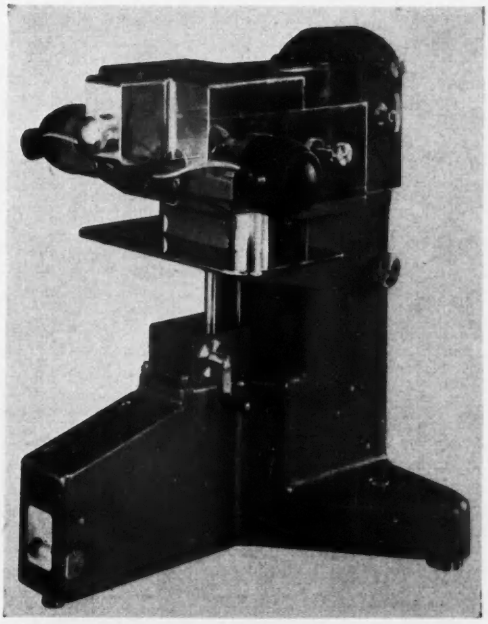

FIG. 2. The Microbalance Mark II constructed by Messrs. Hilger and Watts, Limited, London, England. (Photo by courtesy of Hilger and Watts Ltd.)

up to about 2 mgm. can be compensated and determined by means of the torsion fiber. Larger masses, up to 300 mgm. on each side (including scale pans), can be carried safely by the microbalance. Comparisons of such larger masses may be made by substitution or interchange. With finer torsion fibers smaller sensibilities can be achieved.

While no errors directly attributable to defects of the microbalance itself have been detected, it is found that, when the microbalance has to be opened and closed for loading, errors arising from hygroscopy and dust tend to be troublesome. If a microbalance can be kept closed during a series of readings, for example when measuring magnetic susceptibilities, there seems no reason why a beam with a sensibility of $10^{-10}$ gm. or less may not be used with success.

## 2. DESIGN

### 2.1 *The Beam*

The beam structure of the Mark I microbalance is shown in Fig. 3, in which the numbers on the various parts of the beam represent their thicknesses in microns. The beam is suspended by two substantially horizontal 25$\mu$ silica fibers under tension. These fibers are fused to the axle of the beam and at their

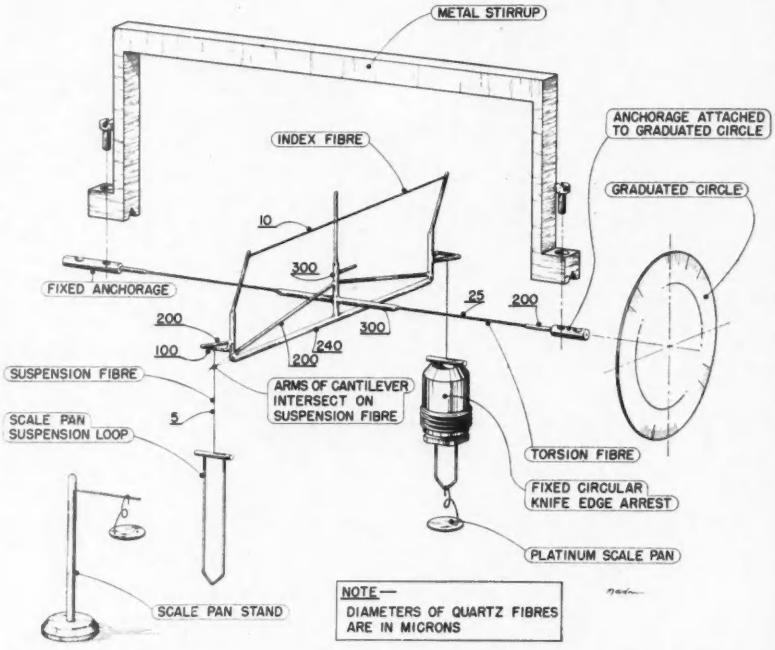


FIG. 3. The fused silica beam suspension of the Microbalance Mark I with the diameters of the fibers in microns. One of the fixed circular knife edge arrests, two platinum scale pans, and the carrying stirrup are also shown.

other ends to silica rods which are cemented into metal holders. One of these holders forms a fixed anchorage in the microbalance and the other is attached to the center of a graduated circle. The graduated circle is used to adjust the torque applied to the beam through one fiber and hence to bring the beam to a preset angle of balance. A small mass to be weighed can then be added on one side and the beam again brought to balance by means of the circle. The angular difference of the two positions of the graduated circle is a measure of the weight of the added mass and can be converted directly into mass by calibrating the balance on the same side with a known mass.

A detailed account of the method of constructing fused silica beams, which is somewhat different from that described in Reference 9, may be published in

due course. The beam is constructed on a jig, using clear, uniform silica rods and fibers and all joints are made by fusing the silica, as described in Reference 9, with a small oxygas flame. All the important dimensions are controlled by the jig so that the arms of the balance are equal in length to within one part in 1000 and the points of attachment of the scale pan suspension fibers are at the correct height, to within one or two thousandths of an inch, with respect to the torsion fibers which support the beam. When new beams are being tested, a final slight adjustment of this height may have to be made. The center of gravity of each beam is adjusted to coincide with the torsion axis, while the beam is still on the jig and before the scale pan suspensions are attached, by balancing the beam on the torsion fibers in two directions at right angles to each other.

Before the construction of a beam is started, the silica fibers and the thicker silica rods from which it is to be made are freshly drawn on an automatic machine. An important feature of the method of construction is that the torsion fibers and the scale pan suspension fibers never come into contact with anything except the air in the room and the joints to which they are fused. Silica fibers which have been handled or touched against anything are more readily broken; evidently the strength of a fiber depends on the condition of its surface.

When not installed in the microbalance the beam is held by the metal stirrup shown in Fig. 3. The metal holders at the ends of the torsion fiber are attached to the stirrup with small screws. After the beam has been fixed in the microbalance the stirrup is removed. Beams can be shipped either clamped to the stirrup or clamped in position in the microbalance.

The beam suspension of the Mark I microbalance differs from that of the Kirk, Craig, Gullberg, and Boyer microbalance in the following respects. The beam cantilever is more rigid, the rectangular silica spring at the end of one of the torsion fibers has been omitted as unnecessary, the index fiber is at a greater height above the torsion axis, the scale pan suspension fibers are attached by fusing at right angles to short horizontal rods because such joints are easier to locate and to make, and the scale pan hooks are in the form of loops of fairly thick rod with a long crosspiece at the top. When a heavy weight is placed on one side of the balance or when a scale pan loop is accidentally pulled this crosspiece descends onto a circular arrest (shown in Fig. 3) and this prevents breakage of the fine suspension fiber.

### 2.2 *General Layout*

A perspective drawing of the microbalance, partly cut away to show the internal structure, is reproduced in Fig. 4: the viewpoint corresponds to that of the photograph in Fig. 1. Another drawing, Fig. 5, shows the various units separately: the base, the frame, the torsion head and beam, the twin optical unit, the housing, the loading platform, and the screw jack with the scale pan cups.

A variety of angle-measuring devices which might be adapted for use in a torsion balance are made commercially and enquiries were instituted with several firms specializing in spectrometers, theodolites or transits, refractom-

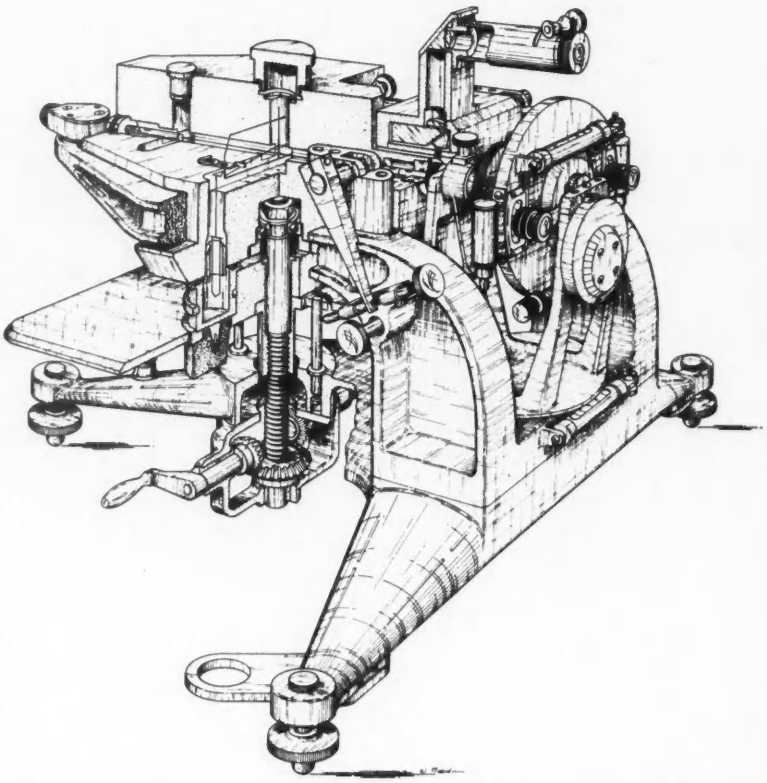

FIG. 4. A perspective drawing of the Microbalance Mark I partly sectioned to show the internal structure.

eters, and clinometers. Messrs. E. R. Watts & Son (now Hilger and Watts) recommended the upper circle of their $4\frac{1}{2}$ in. Standard Theodolite, reading by verniers to 20 sec. of arc, or the glass circle of the Hilger-Chance Refractometer, reading by optical micrometer to 10 sec. in the Medium form, or 1 sec. (by estimation) in the Precision form, and they were prepared to modify these instruments to suit a microbalance. The Mark I microbalance was based upon the Watts Standard Theodolite and the Mark II microbalance on the Medium Refractometer system which was completely redesigned to suit this application.

A disadvantage of the theodolite upper circle, with its magnifying lenses for reading the verniers, is that it has to be in the middle of the front of the microbalance. Thus the operator, when using the Mark I microbalance, can reach the loading platform only around the sides of the theodolite. In practice this has not been found a serious disadvantage. Sometimes it is convenient for the

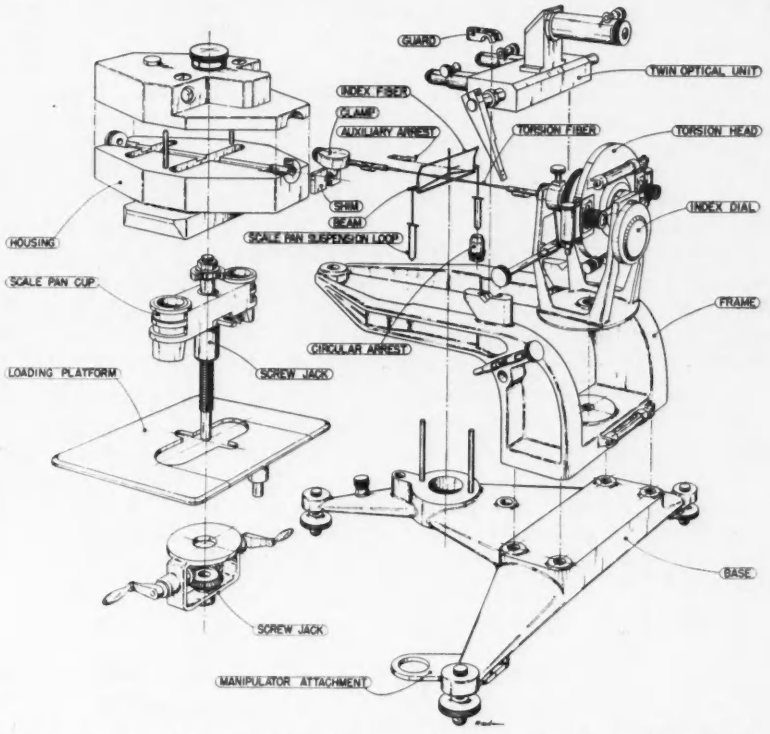


FIG. 5. The separated parts of the Microbalance Mark I seen from the same viewpoint as that of the perspective drawing of Fig. 4 and the photograph of Fig. 1.

microbalance to be set on a square plinth so that the operator can walk around to one side or the other. In the Mark II design the use of the glass circle, with projection reading visible from the front, has enabled the torsion head in this instrument to be placed at the rear so that the loading platform is open to the front, as seen in Fig. 2.

In the Mark I microbalance the beam is mounted between a short extension of the axle of the theodolite at one end and a spindle with provision for rotation, tension adjustment, and clamping at the other end. The theodolite and the clamp, Fig. 5, are mounted on a strong brass casting, the frame, which is screwed to a tripod base fitted with leveling screws. Two vee slots in the frame locate the transverse axle of the optical unit, allowing it to be tilted by a lever and tangent screw to center the images of the index fiber in the field of view. This facility is necessary because the sag of the beam with the heaviest permissible load is about one sixteenth of an inch. The optical unit is easily removable to leave the top of the microbalance clear for the operation of inserting a new suspension.

The parts just mentioned (illustrated on the right-hand side of Fig. 5) constitute a complete working microbalance which could be used in perfectly still surrounding conditions. The parts shown on the left of Fig. 5 provide protection, and facilities for loading. The lower part of the housing is attached to the frame; the lid of the housing is located on the lower part by means of dowel pins and fixed by screws, so that it can be readily taken off to expose the beam. The beam swings freely in the cavity in the housing and when the lid is off it can be easily removed, by lifting straight upwards with the stirrup already mentioned, after two fixing screws have been undone. The fixed and movable anchorages of the suspension enter the housing through loosely fitting brass bushes which are made airtight with rubber O-rings. The lid of the housing fits the lower part sufficiently tightly in the Mark I microbalance for satisfactory operation at atmospheric pressures. In Mark II, the design of the housing has been slightly modified to permit operation under vacuum.

The scale pan suspensions hang down through vertical holes in the lower part of the housing and their ends protrude some distance beneath. The holes are closed by two metal cups, large enough to surround small scale pans. The cups can be raised and lowered by a screw jack and make an airtight seal against the bottom of the housing with O-rings. The transverse slot in the housing and the two vertical holes terminated by the cups constitute a cavity in the shape of an inverted U, in which large-scale air circulation which might disturb the balance is impossible.

The jack for lowering the scale pan cups is operated by either of two handles located beneath the loading platform. The cups descend through holes in the platform and can be easily removed for recovery of dropped weights or for cleaning. The rest of the controls and adjustments can readily be identified in Figs. 1, 4, and 5.

### 2.3 *The Torsion Head*

Tests on a number of 25$\mu$ torsion fibers $1\frac{7}{8}$ in. long showed that most of them could be twisted seven revolutions either way without breakage. In order to give a good factor of safety, it was decided to limit the torsion head to three revolutions in either direction from zero. An index dial on the theodolite, with stops limiting the number of complete revolutions of the circle to six, was provided by Hilger and Watts and, to simplify the readings, a round number of graduations of the circle was used. The standard centesimal figuring of 100 grades to each quarter revolution, with verniers reading to 0.01 grad (32.4 sec. of arc), was provided and, on the index dial, the quarter revolutions were numbered 1 to 24. The torsion fiber is initially attached to the circle so that the figure 12 on the index dial corresponds to zero twist and this condition then cannot be altered except by means of a small and rather inaccessible clamping screw. Operation of the normal slow and fast motions of the circle does not alter this setting. In the Mark II microbalance the circle has been divided in 1000 with single side reading by optical micrometer to 0.01 division (12.96 sec. of arc) and the revolutions are numbered 1 to 6 on the index dial.

The theodolite torsion head behaved very satisfactorily in the first model of the Mark I microbalance but subsequently, in other Mark I microbalances, there was erratic behavior which was traced to the natural end-play of the theodolite axle. This end-play caused changes of tension of the torsion fibers which had no effect on a well-made suspension but affected suspensions in which the torsion fibers were not quite straight (see Section 4.5). To prevent end-play, all Mark I microbalances were fitted with a brass shim (Fig. 5), between a flange on the theodolite axle and the end of the housing, thick enough to spring the theodolite standards slightly. In Mark II the torsion head is bolted directly to the housing and the torsion axle is spring-loaded longitudinally to prevent end-play. Apart from these precautions it is important that beams which are as nearly perfect as possible be used, lest change of tension of the torsion fiber, due to differential thermal expansion of the housing and the silica, cause a change of zero.

2.4 *The Clamp*

Details of the clamp and the fixed end of the suspension are shown in Fig. 6. The fixed anchorage of the suspension and the spindle of the clamp are joined

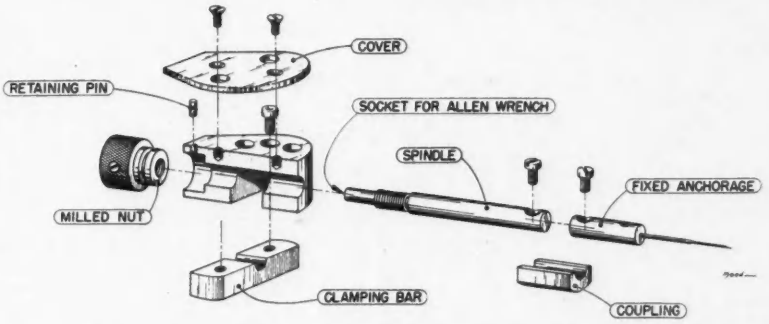


FIG. 6. Details of the device for pre-adjusting the tension and the angle of the passive end of the suspension and for clamping it.

by a well-fitting half-round coupling which enables the suspension to be removed by means of the stirrup as already described. Adjustments of the spindle are (*a*) tension, by turning the milled nut with its grub screw loosened (holding the spindle stationary) until the sag of the unloaded beam is reduced to 0.007 in. and (*b*) zero, by rotating the milled nut, with its grub screw tight and the theodolite circle set at 1200.00 grades, until the unloaded beam balances. After the spindle has been adjusted in position it is positively fixed by tightening the clamping bar.

2.5 *The Frame and Base*

The frame and the base are yellow-brass castings rigidly joined by four bolts. The part of the base beneath the housing is narrow enough to permit the scale pan suspensions of the beam to be extended, if necessary, within vertical pro-

tecting tubes, below the level of the base. Also the frame can be fixed to the base in the opposite direction to that shown, for applications in which the microbalance may have to overhang other equipment. The base stands on three standard theodolite leveling screws and has a terminal for attachment of a grounding wire. Lugs are provided to carry standard three-way micromanipulators, but it has been found that most users prefer to load the balance directly by hand. A leveling bubble, of sensitivity one division = 0.01 grad, is fixed transversely to the base.

2.6 *The Housing*

The most important property of the metal of which the housing is made is its heat transfer coefficient. If this coefficient has a high value, the thick metal walls surrounding the cavity in the housing will reach a uniform temperature quickly after a local temperature disturbance and thermal convection in the cavity will then cease. Silver has a heat transfer coefficient three times, and copper twice, that of aluminum. However, considerations of expense, weight, and ease of fabrication favored the choice of aluminum and experience with the microbalance has indicated that a hard aluminum alloy is satisfactory. The following experimental test of the properties of the housing was made.

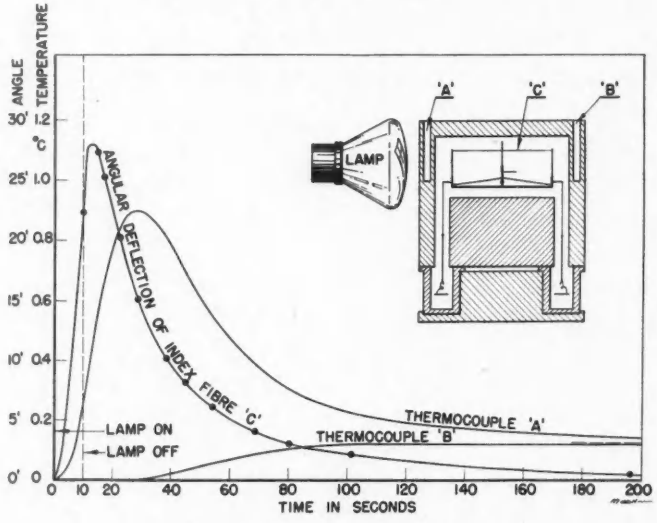


FIG. 7. Thermal test of the housing.

A heat lamp was placed close to one side of the housing of a working microbalance as shown in the inset in Fig. 7. The side of the housing irradiated by the lamp was painted black to increase its rate of absorption of heat and thermojunctions were placed in the holes marked *A* and *B*. When the lamp was switched on for an interval of 10 sec. the sequence of events was as plotted. The index

fiber was deflected as shown by curve *C*, reaching a maximum deflection of 28 min. of arc three seconds after the light was switched off, and recovering so that in two minutes it showed 2% of its maximum deflection and after four to five minutes it was back to zero. The temperature on one side of the housing at position *A* reached a maximum of 0.9°C. above room temperature about 20 sec. after the light was extinguished and after four to five minutes became substantially constant at 0.12°C. The temperature at the other side of the housing at position *B* began to rise after some 30 sec. and leveled off after three to five minutes at 0.12°C. It is clear that 0.12°C. above room temperature was the uniform temperature of the housing corresponding to the quantity of heat that was injected by the lamp. This temperature reverted to normal only slowly and it did not affect the balance.

The disturbance of the beam produced by this very severe test was not unduly large. A high polish is always given to the outside of the housing to minimize absorption of radiant heat from the surroundings and it is found that the balance is quite unaffected by radiant heat from the operator or from all ordinary laboratory equipment. It is affected by direct handling of the housing but after such disturbance it is not necessary to wait longer than five minutes before taking a reading.

Airtight glass windows are provided in the housing opposite the objectives of the optical viewing unit and also vertically above the index fiber so that the latter can be observed by dark ground illumination from a cold fluorescent light placed immediately above the microbalance. Two inspection windows are also provided and are shown on Fig. 4, but these were found to be quite unnecessary since a fault can be readily deduced from the behavior of the protruding scale pan suspensions. A slot in the housing to accommodate a rectangular quartz spring at one end of the suspension is also shown but, as already mentioned, this spring was found to be unnecessary. The slot and the inspection windows have been omitted in the Mark II design.

In the Mark II microbalance the plane interface between the lower and upper halves of the housing has been placed some distance above the level of the torsion fiber. This enables the axles supporting the suspension to be brought into the housing through vacuum tight bearings in the lower half of the housing and the interface itself to be made vacuum tight by means of a separate rubber seal. Much additional work becomes possible with a microbalance which can be evacuated or filled with noncorrosive gases.

### 2.7 *The Screw Jack and Scale Pan Cups*

The scale pan cups (Fig. 5) are carried in recesses at each end of a thick metal bar which tends to keep them at the same temperature. To avoid the possibility of damaging the suspension the cups can be taken off only when they are beneath the level of the table. The upper end of the screw jack is held by a thrust and journal bearing mounted in the lower half of the housing and the lower end of the screw is free to slide in the bevel gear. The thrust bearing takes the full force of the screw when the scale pan cups are pressed against the

bottom of the housing, so that the screw exerts two opposed clamping forces on the housing and the possibility of disturbing the balance by flexure of the frame due to thrust against the base is avoided.

Immediately beneath the scale pan cups are containers made of lead for holding two small gamma radiation sources. These serve to dissipate electrostatic charges on the beam or the scale pans. Because of possible harm to the operator from gamma radiation, later Mark I models and the Mark II microbalance make use of beta radiation sources suitably located inside the housing. Thallium isotope 204, which has a half life of three years and produces no gamma radiation, is used.

2.8 *The Beam Arrests*

Movable beam arrests have not been provided because they are not necessary with a balance of this type. The beam, unloaded, requires only 10 sec. to come completely to rest and, with the maximum load of 0.3 gm. on each side, the beam is at rest after about three minutes (a skillful operator can bring a loaded beam to rest in much less than three minutes by counteracting the movements of the beam with the torsion head). These times are shorter than the time (five minutes) which should be allowed, whenever possible, for the attainment of temperature equilibrium of the housing after loading.

There are four fixed arrests of which two are the circular arrests already mentioned. These two arrests support the scale pan loops while they are being loaded and effectively protect the beam from damage. The vertical clearance between the suspension and the circular arrests is about one sixteenth inch on each side at no load. At maximum load the clearance is quite small. The other two arrests are located above the arms of the beam and act as auxiliary arrests only. They do not touch the beam at all as it swings normally between the limits set by the circular arrests but they prevent abnormal overswing of the beam. All the arrests are in the form of stainless steel knife edges to minimize trouble from sticking.

2.9 *The Optical Unit*

The beam is said to be at balance when its angular position is brought into a fixed relationship with a datum line in the frame. An accurate means of determining this relationship has to be provided. The center of rotation of the beam is not fixed with respect to the frame because of the increased sag under load and because the end of the torsion fiber usually will not be exactly on the axis of the theodolite circle and therefore will describe a small circle as it rotates. There are two standard optical methods for such a system. One method uses a plane mirror fixed to the beam, and the other, as in optical theodolites, brings images of diametrically opposite graduations into juxtaposition. For a beam microbalance the second of these methods can be shown to be the more powerful one and it was first applied to this instrument by Kirk, Craig, Gullberg, and Boyer (7).

The optical unit of the Mark I microbalance is illustrated in Fig. 8. The principal component is a large composite prism with two sets of parallel silvered

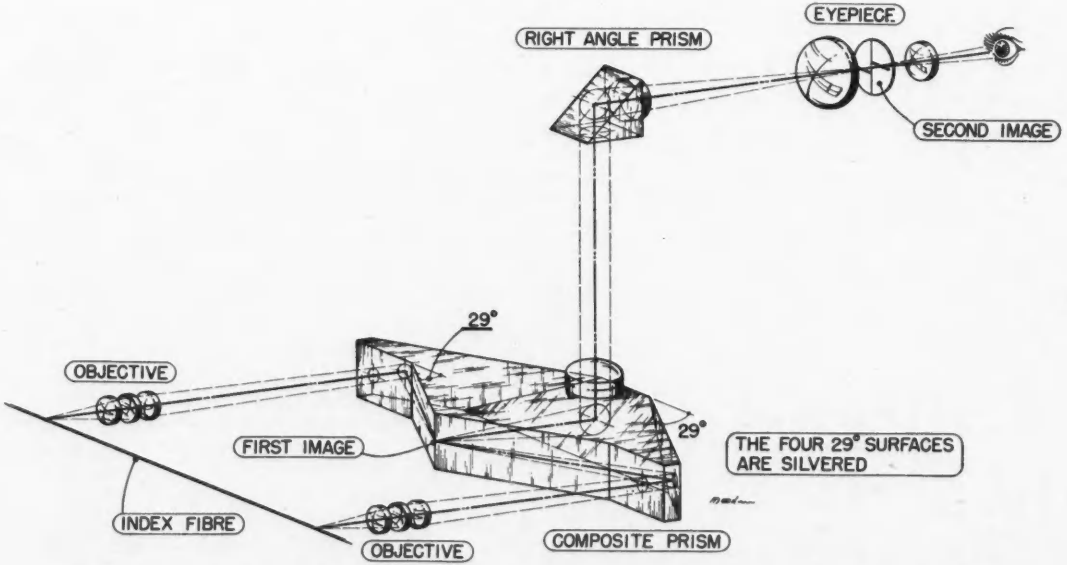


FIG. 8. The twin optical viewing system designed and made by Canadian Arsenals Limited, Leaside, Toronto.

reflecting surfaces making a 29° angle with the axis. Images of parts of the index fiber near each end are formed in the separate halves of a vertically split field and can be lined up with each other by rotating the torsion head. When the images are in line the beam is considered to be at balance. A sharp vertical dividing line is produced in the field of view and the images move in the same direction as the oscillation of the beam. The two objectives can be rotated independently for focusing and have clamps which must be tightened after focusing. The design and fabrication of this unit was carried out by Canadian Arsenals Ltd., Leaside, Toronto, and the writer acknowledges his gratitude to J. Bain and J. Consitt who were responsible for the work.

The optical system can be tilted as a whole by means of a tangent screw to keep the index fiber in view as the beam sags under load. The axle of the optical unit rests by gravity in vee slots in the frame and is loosely located transversely by a collar which fits in a slot. The guards (see Fig. 5) above the vee slots have a substantial clearance but keep the optical unit from being knocked off accidentally. The Kirk, Craig, Gullberg, and Boyer microbalance (7) had a fixed optical system and relied upon its wide field to keep the index fiber in view when the microbalance was heavily loaded.

Focusing of the objectives of the optical unit is an important adjustment because the fused silica beam of the microbalance is not a rigid structure and it usually bends or twists slightly when heavily loaded. The deformation is perfectly elastic and reproducible and in no way affects the accuracy of the microbalance, but it is sometimes so large as to make it difficult to work accurately at different values of the gross load without readjustment of the focus of one or both objectives.

When the optical unit of the Mark I microbalance is refocused by turning the objectives, the datum line of the balance, as determined by the centers of the objectives, is liable to be changed. This does no harm as long as the focus does not have to be changed during any given set of weighings.

A better way of mounting the optical unit was tested on one of the Mark I microbalances and is used on Mark II. In this, as shown in Fig. 9, the transverse axle of the optical unit rests on horizontal flats instead of in vee slots. Refocusing to allow for a change in the plane of movement of the index fiber is done by sliding the unit as a whole along these flats. The end of the tilting screw also

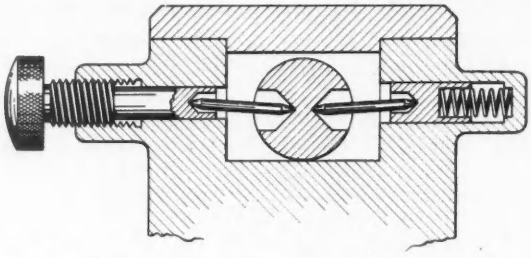

FIG. 9. Preferred method of focusing the optical system (diagrammatic only).

rests on a horizontal flat so that the tilt is not disturbed when the unit is moved for focusing. Sideways motion of the axle at each end is accomplished by opposed, spring-loaded and screw-driven, floating pins which locate in conical holes in the sides of the axle. These floating pins are arranged to keep the axle pressed downwards on the flats. Gross upward movements of the axle are prevented by the guard plates above it. The center of the axle is level with the index fiber when the balance is unloaded. With this accurate kinematic arrangement for moving the unit as a whole, the objectives of the optical system do not have to be moved and a constant datum line is preserved.

In the above discussion it has been tacitly assumed that the optical magnifications of the two sides of the optical system are equal. The objectives are selected so that this is nearly so, but it is usually impossible to obtain an exact match. The user can estimate the discrepancy by noting how well the images of the index fiber keep in line with each other as the tilt of the optical system is varied. If the mismatch is appreciable, the balance point should always be determined with the images near the middle of the field of view.

The appearance of the index fiber, the circle graduations, and the optical micrometer scale on the projection screen is shown in Fig. 10 for the Mark II

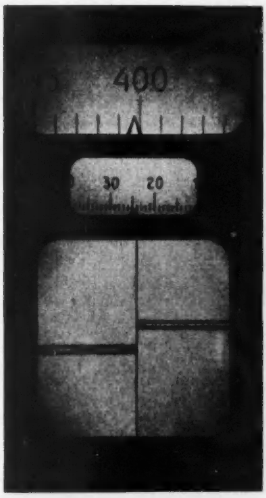


FIG. 10. The optical presentation on the ground glass screen of the projection system of the Microbalance Mark II. (Photo by courtesy of Hilger and Watts Ltd.)

microbalance. The illumination of the index fiber in Mark II is direct and not transverse as in Mark I.

In order to estimate the angular precision of balancing let us assume that the telemicroscopes of the optical system have a linear resolving power of $p$ cm. Then, if the distance between the axes of the objectives is $D$ cm., the smallest

detectable angular movement of the beam is $p/D$ radians. Now, in the optical system of the Mark I microbalance, $p = 1.5\mu$ and $D = 7.62$ cm. so the angular precision of balancing is $1.97 \times 10^{-5}$ radians or 4.1 sec. A rectangular reflecting mirror of comparable resolving power would have aperture $d$ such that $\lambda/d = 2\ p/D$ which, for a wave length $\lambda = 5 \times 10^{-5}$ cm., gives $d = 1.27$ cm. The attachment of such a large mirror to the beam would seriously impair its performance.

It will be noted that the balance point of the beam can be determined with an angular precision (4.1 sec.) eight times better than that provided for the angle of twist of the torsion fiber (0.01 grad = 32.4 sec.). The necessity for this difference will become apparent in Section 3.

## 3. THEORY

### 3.1 *General*

The theory of a balance with vertical elastic suspension was given by Weber (12) in 1841 and extended by Pettersson (10) in 1914. A theoretical expression for the optical sensibility of the present form of microbalance, with a rigid beam supported on torsion fibers and having vertical elastic scale pan suspensions, has recently been given by Cunningham (3). It is desirable to discuss theory here in somewhat greater detail than was done in Cunningham's article.

It is necessary to treat the torsion circle and the optical unit separately. Mass is determined by the torsion circle with which the beam is always brought to a preset angle of balance; the accuracy with which the beam can be set to this point of balance is determined by the optical unit. However, the angular response of the beam to a given movement of the torsion circle is not a constant. With change of the gross load on the microbalance the response of the beam may vary by a factor of three or more. It is preferable and in line with standard instrumental practice, that the optical unit, which is essentially acting as the detector of a null point, should at all times be capable of determining the balance point with an accuracy equal to or greater than that corresponding to the smallest measurable change of torsion.

The performance of the microbalance will be described by two mathematical expressions one of which applies to the torsion circle and the other to the optical unit. These expressions give explicitly the torsion circle and the optical sensibilities of the microbalance, that is the masses which added to one side would produce minimum measurable effects. The sensibility is the simplest and most useful quantity to use because the mathematical expression for the optical sensibility is the sum of a number of terms, each one of which arises from a separate effect, and any one of which can be varied by the designer, independently of the others, to produce a desirable change in the over-all characteristics of the microbalance.

### 3.2 *The Optical Sensibility*

Referring to the diagram in Fig. 11 let us assume that the arms of the balance, $BD$ and $DC$, are of approximately equal lengths $L_1$ and $L_2$ and that the beam balances, about the center of the axle $O$, with load masses $M_1$ and $M_2$ of mean

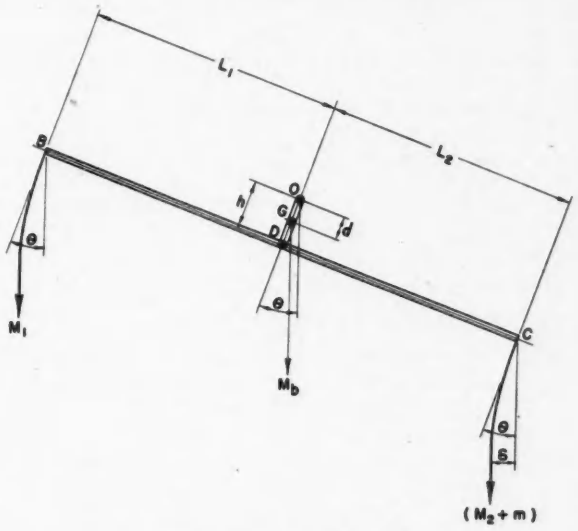


FIG. 11. Parameters for use in the formulae.

mass $M$. Let the beam be deflected, through a small angle $\theta$ from the horizontal position of equilibrium, by the addition of a small mass $m$ on the right-hand side. Assume that the mass of the beam $M_b$ acts through the center of gravity of the beam $G$ at a distance $d$ beneath $O$ and that the load suspension fibers are attached to the beam at $B$ and $C$ at a distance $h$ beneath $O$. Assume that the beam is flexible so that under load, $h = h_0 + Mk$ where $k$ is the change of $h$ corresponding to unit change of $M$ and $h_0$ is the value of $h$ for $M$ zero.

The moment due to the mass $m$ on the right-hand side is balanced by four moments:

(1) the moment produced by $M_b$ the mass of the beam acting through the center of gravity; $M_b g.d \sin\theta = M_b g.d.\theta$, since $\theta$ is small,

(2) the turning couples of the horizontal torsion fibers, assumed each of length $l$, radius $r_t$, and modulus of rigidity $n_t$; $2(n_t \pi r_t^4/2l)\theta$,

(3) the moment produced by the suspended mass $2M$ because the points of suspension of the fibers at $B$ and $C$ are below the torsion axis; $2Mg\,(h_0+Mk)\theta$,

(4) the moment, $2Mg\delta$, which arises, because of the stiffness of the suspension fibers, from the displacement of both the suspended masses through a distance $\delta$ from positions vertically underneath their points of attachment at $B$ and $C$. Weber (12) has shown that for a cylindrical fiber supporting a mass $M$,

$$\delta = \sqrt{\frac{E_s \pi r_s^4}{4Mg}}\,\theta,$$

where $E_s$ is Young's modulus for the fiber and $r_s$ is its radius.

Hence we have,

$$mg(L_2 - \delta - h\theta) = \theta\left\{M_b gd + \frac{2n_t\pi r_t^4}{2l} + 2Mgh_0 + 2M^2gk + 2Mg\sqrt{\frac{E_s\pi r_s^4}{4Mg}}\right\}.$$

Or, neglecting $mg\delta$ and $mgh\theta$,

$$(1) \qquad m = \frac{\theta}{L_2}\left\{M_b d + \frac{n_t\pi r_t^4}{lg} + \sqrt{M}\sqrt{\frac{E_s\pi r_s^4}{g}} + 2Mh_0 + 2M^2k\right\}.$$

This expression corresponds to the one given by Cunningham (3) except for the additional term in $M^2$ due to the assumption of a nonrigid beam. When $\theta$ is replaced by $\Delta\theta$, the smallest change of angle that can be detected by the optical system, $m$ is the optical sensibility.

*3.3 The Torsion Circle Sensibility*

Assume that the beam is deflected from a horizontal position of equilibrium by the addition of a small mass $m$ on the right-hand side and let the beam be brought back to its original position by rotating the theodolite circle through the angle $\phi$. Only the torque of the front torsion fiber has altered so that the moment due to the mass $m$ must be equal to the turning couple of the front torsion fiber,

$$mgL_2 = \phi\frac{n_t\pi r_t^4}{2l}.$$

Therefore

$$(2) \qquad m = \frac{\phi}{L_2}\frac{n_t\pi r_t^4}{2lg}.$$

In this expression when $\phi$ is replaced by $\Delta\phi$, the smallest change of angle that can be detected by the torsion circle, $m$ is the torsion circle sensibility. It is evident that the magnitude of the smallest mass difference which can be detected with the microbalance will be given by either the optical sensibility of equation (1) or the torsion circle sensibility of equation (2), whichever is the larger.

*3.4 Relation of the Sensibilities*

As a very simple case let us consider a microbalance beam having no scale pan suspensions and let the center of gravity of the beam coincide with the center of the axle so that $d = 0$. Let the beam be deflected through a small angle $\theta$ from a horizontal position of equilibrium by the addition of a small mass $m$. We then obtain from equation (1),

$$(3) \qquad m = \frac{\theta}{L_2}\frac{n_t\pi r_t^4}{lg}.$$

Now suppose that $\Delta\theta$ is the smallest angle that can be detected by the optical unit and let $\phi_{\Delta\theta}$ be the rotation of the circle required to restore balance from a deflection $\Delta\theta$. Then, eliminating $m$ in equations (2) and (3),

$$(4) \qquad \phi_{\Delta\theta} = 2\Delta\theta.$$

Alternatively, this relation follows simply from the fact that the beam is mounted between two equal torsion fibers. It is evident that in this case, for equal optical and torsion circle sensibilities, the optical unit should have an angular precision better by a factor of two than that of the torsion circle.

In the general case, eliminating $m$ in equations (1) and (2), we obtain

$$(5) \qquad \phi_{\Delta\theta} = 2\Delta\theta\left[\frac{lg}{n_t\pi r_t^4}\left\{M_0 d + \frac{n_t\pi r_t^4}{lg} + \sqrt{M}\sqrt{\frac{E_s\pi r_s^4}{g} + 2Mh_0 + 2M^2k}\right\}\right].$$

The optical unit and the torsion circle can now be matched only at a particular value of $M$. If it is arranged that the largest value of $\phi_{\Delta\theta}$ within the permissible range of $M$ be made equal to $\Delta\phi$, the smallest angle that can be detected by the torsion circle, then, at all other values of $M$, the optical unit will be more than adequate to determine the balance point and the effective sensibility of the microbalance will be that of the torsion circle. This is given by equation (2) with $\phi$ replaced by $\Delta\phi$, i.e.,

$$(6) \qquad m = \frac{\Delta\phi}{L_2}\frac{n_t\pi r_t^4}{2lg}.$$

3.5 *Calculated Sensibility of the Standard Beam*

For an ideal beam made to the specifications of Fig. 3, in the Mark I microbalance, the quantities on the right-hand side of equation (6) are:

$\Delta\phi = 1.57 \times 10^{-4}$ radians (0.01 grad),
$L_2 = 5.08$ cm. (2 in.),
$l = 4.76$ cm. ($1\frac{7}{8}$ in.),
$r_t = 1.25 \times 10^{-3}$ cm. (25$\mu$ diameter fiber),
$n_t = 3.7 \times 10^{11}$ (for 25$\mu$ diameter).*

Hence the torsion circle sensibility, $m$ of equation (6), is

$$m = 0.94 \times 10^{-8}\text{gm}.$$

Similarly the optical sensibility, which is a function of $M$, may be calculated from equation (1) with $\theta$ replaced by $\Delta\theta$. The additional constants used are:

$\Delta\theta = 1.97 \times 10^{-5}$ radians (1.5 $\mu$ per 7.6 cm.),
$d = 0$ (c. of g. coincides with torsion axis),
$h_0 = -0.005$ cm.,
$r_s = 2.5 \times 10^{-4}$ cm. (5$\mu$ fiber),
$E_s = 9.8 \times 10^{11}$ (for 5$\mu$ diameter),
$k = 0.018$ cm. per gm. (by direct measurement).

It is not easy to calculate a reliable value for $k$ and so the value adopted is an average obtained from direct measurements of the flexibilities of a number of beams.

The two calculated sensibilities are shown as a function of the load $M$ in Fig. 12 and it can be seen that in accordance with Section 3.4 the optical sensibility is less than the torsion circle sensibility for all $M$ except a short range near the maximum permissible load.

Also shown in Fig. 12 by broken curves are the separate terms of equation (1) which are added together to produce the optical sensibility and it is clear that any one of these terms may be altered independently of the others to produce a predictable change in the sensibility curve.

**The value of $n_t$ is taken from the table of experimental values quoted on Page 191 of Reference 4. The elastic moduli of fused silica fibers vary with the diameter.*

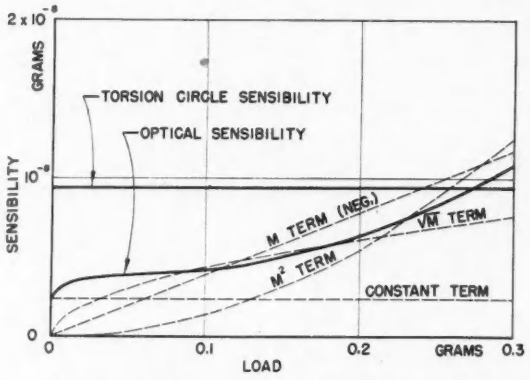


FIG. 12. The sensibilities of an ideal standard beam as a function of the load on one side.

The values adopted for $k$, $r_t$, and $r_s$ have to be fixed prior to the construction of a beam, but $h_0$ can be changed after it is made and after it has been installed in the microbalance. This facility is very valuable since $h_0$ must be adjusted to within extremely narrow limits—a change of only 0.005 cm. in $h_0$ is sufficient to make the standard beam unstable at the maximum load.

3.6 *Measurement of the Sensibilities*

The torsion circle sensibility of equation (6) is easily measured because of the long linear range of the torsion circle. If the smallest measurable angle, 0.01 grad, corresponds to approximately $10^{-8}$ gm., the permissible six revolutions of the torsion circle correspond to $240{,}000 \times 10^{-8} = 2.4 \times 10^{-3}$ gm. Thus standardized weights of 2, 1, or 0.5 mgm. which are commercially available may be used for this calibration.

The optical sensibility of equation (1) can be measured directly by adding a weight to one side of the balance and measuring the angular displacement of the beam on a scale in the eyepiece of the optical unit, but the field of view of the optical unit is so small that such a weight has to be inconveniently small—not larger than 3 or 4 $\mu$gm. Some tests of this kind were made using for a weight a short length of fine silica fiber, the mass of which was then determined on the microbalance itself. However, this process is physically indistinguishable from one in which, without using a weight at all, the angular change in the torsion head, corresponding to a given angular displacement of the beam, is directly measured. For, when $\phi$ is replaced by $\phi_{\Delta\theta}$ in equation (2),

$$m = \frac{n_t \pi r_t^4}{2lL_{2g}} \phi_{\Delta\theta} \tag{7}$$

and the constant of this equation is that of equation (6). The determination of this constant has just been described.

The optical sensibility curve of a beam is therefore determined as follows. A series of paired weights of say 0.01, 0.03, 0.06, 0.1, 0.15, 0.2, 0.25, and 0.3 gm.

is prepared. These weights should have small hooks so that they can be hung directly onto the scale pan suspension loops and the individual pairs of weights need be matched in weight only sufficiently well to allow the beam to be balanced somewhere in the 2 mgm. weighing range of the torsion circle. Then, with each pair of weights in turn, the beam is put out of balance by a fixed amount, say 20 divisions on a suitable eyepiece scale put into the ocular of the optical unit, and the amount of rotation of the torsion circle required to bring the beam to balance is measured. A plot of these angles against load provides a relative sensibility curve of the beam.

This is as far as the user need go in checking the sensibility of a beam, but, for comparison with the theory, an absolute sensibility curve is required. We recall that $\phi_{\Delta\theta}$ of equation (7) is the angle of torsion corresponding to $\Delta\theta$ which in turn corresponds to a $1.5\mu$ deflection of the beam. Since the measured magnification of the optical unit is $\times$ 9.5, and the eyepiece scale divisions are 0.01 cm., $1.5\mu$ corresponds to 0.142 eyepiece scale divisions. To obtain the absolute sensibility curve, the angles of the relative sensibility curve are therefore divided by $20/0.142 = 141$ and converted to mass using the measured value of the constant of equation (7).

### 3.7 *Comparison of Calculated and Measured Sensibilities*

For the measured optical sensibility curve of the standard beam we adopt the average of the last eight beams constructed at Chalk River. The relative sensibilities of these beams, obtained by the method of Section 3.6, are given* in Table I and the average, converted to absolute measure, is plotted in Fig. 13.

TABLE I

TORSION CIRCLE ANGLES IN GRADES CORRESPONDING TO A BEAM DEFLECTION OF 20 EYEPIECE SCALE DIVISIONS

| Beam No. | Load in mgm. | | | | | | | |
|---|---|---|---|---|---|---|---|---|
| | 0 | 30.5 | 52.5 | 76 | 128.5 | 190 | 252.5 | 290 |
| 25 | 0.61 | 1.28 | 1.48 | 1.76 | 1.95 | 2.52 | 2.48 | 2.65 |
| 26 | 0.59 | 1.20 | 1.39 | 1.58 | 1.81 | 2.08 | 2.13 | 2.26 |
| 27 | 0.57 | 1.23 | 1.42 | 1.56 | 1.80 | 1.96 | 2.24 | 2.34 |
| 28 | 0.51 | 1.04 | 1.27 | 1.45 | 1.79 | 2.28 | 2.63 | 2.82 |
| 29 | 0.68 | 1.28 | 1.54 | 1.70 | 1.86 | 2.01 | 2.00 | 2.05 |
| 31 | 0.47 | 1.17 | 1.42 | 1.72 | 2.00 | 2.20 | 2.32 | 2.32 |
| 32 | 0.64 | 1.18 | 1.32 | 1.42 | 1.52 | 1.61 | 1.70 | 1.84 |
| 33 | 0.51 | 1.02 | 1.21 | 1.37 | 1.66 | 1.92 | 2.20 | 2.43 |

It is apparent that the optical sensibility curve of these beams does not agree at all well with the calculated sensibility curve of Fig. 12. The discrepancy is to be attributed to an unavoidable difference between the ideal standard beam specified in Fig. 3 and the real beam. When the $5\mu$ suspension fibers are fused

**The readings of Table I are only rough routine measurements and the accuracy of the microbalance must not be judged from them. Also one of the settings has to be made with the index fiber images separated by 20 eyepiece scale divisions. The table is given only to show the reproducibility with which beams can be made.*

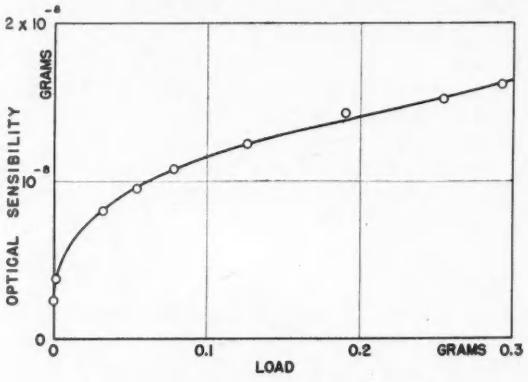


FIG. 13. The average measured optical sensibility of eight standard beams as a function of the load on one side.

to the ends of the beam, to ensure a strong joint, a short length of the fiber is allowed to shrink into the joint while it is hot. Thus the diameter of the 5$\mu$ fiber increases in the vicinity of the join in an exponential fashion rather like the horn of a trumpet, whereas in the calculation it was assumed that the 5$\mu$ fiber was a uniform cylinder up to the point of attachment. This difficulty has already been mentioned by Pettersson (10).

To check the theory experimentally several special beams were constructed in which the suspension fibers were very lightly fused to the beam so that their diameter remained practically unchanged even close to the point of fusion. The measured torsion circle and optical sensibilities of one of these beams are plotted

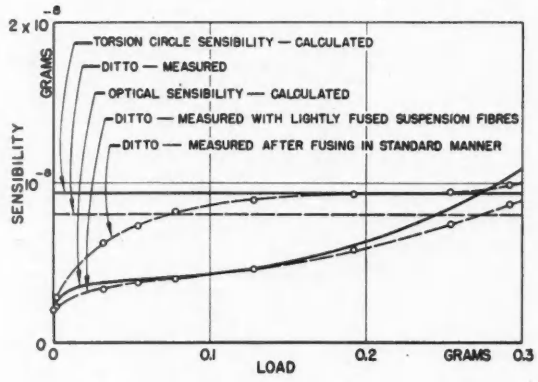


FIG. 14. The optical and torsion circle sensibilities of a standard beam with the scale pan suspension fibers lightly and then more strongly fused to the beam compared with the calculated curves of Fig. 12.

in Fig. 14 in comparison with the calculated curves of Fig. 12. The agreement is reasonably good. The diameters of the torsion and suspension fibers were measured with a sensitive micrometer. Since the mass of the scale pan suspension loops is not negligible (each one weighs approximately 2 mgm.) the special beams were also measured with no scale pan suspensions to give experimental points at $M = 0$. These points, provided that the two torsion fibers on a beam are equal, depend only upon the simple geometrical relationship of equation (4). Apart from the scale factor introduced by the constant of equation (7), they would differ from the calculated value only if the center of gravity of the beam was not at the middle of the axle so that $M_b d$ was not zero. They provided an independent check of the value of the magnification of the optical unit.

Other special beams were constructed in which the suspension fibers were attached by means of globules of shellac so that it was quite certain that there was no change of their diameter, but it was found that satisfactory measurements could not be made with these beams on account of elastic hysteresis due to the shellac.

Now the particular beam used for Fig. 14 was removed from the microbalance and the scale pan suspension fibers were replaced by new ones of the same diameter properly fused to the beam. The beam was put back into the microbalance and $h$ was adjusted till the optical sensibility at maximum load was about the same as it had been before. The optical sensibility curve was remeasured and is shown in Fig. 14. The marked difference of shape between this curve and the previous one obtained with the same beam is evidently due to the configuration of the quartz at the points where the scale pan suspension fibers are joined to the beam.

Probably not much would be gained by trying to evolve a more elaborate formula which would include the effect of tapered suspension fibers, but it is of interest to fit the simple formula to the experimental sensibility curve of the standard beam and find effective values for $r_s$, $k$, and $h$.

The solid curve drawn through the experimental points of Fig. 13 is a calculated curve obtained by increasing the $r_s$ term by a factor of 3, diminishing the $k$ term by a factor of 3, and increasing the $h$ term by a factor of 1.1. These changes indicate an effective diameter of the suspension fibers of $8.6\mu$ instead of $5\mu$ and a beam cantilever apparently three times as rigid as it actually is.

It will be realized that the measured optical sensibility curve (Fig. 13) of the standard beams of Table I could easily have been changed by alteration of $h$ to make it lie below or coincident with the torsion sensibility for all values of the load, in accordance with the criterion mentioned in Section 3.4. This was not done for two reasons. One is that these beams were to be used chiefly for work with scale pans and specimens of weight less than 100 mgm. and the other is that it seems to be possible in practice to set the separate images of the index fiber in line considerably more accurately than has been assumed in the above calculation which was based upon the conventional resolving power of the telemicroscopes for overlapping images.

## 4. IMPERFECTIONS OF BEAMS

### 4.1 *General*

The optical sensibility of the microbalance, which varies with load as shown by equation (1), is, as has already been mentioned, only a measure of the precision with which the point of balance can be set; weighing depends upon the simpler relation of equation (2) in which the mass $m$ being weighed and the corresponding change of torque $\phi$ are related by a constant of proportionality which is independent of the load. However, in the derivation of equation (2), the stretching of the torsion fiber under load was neglected.

Since the axle of the beam at one end and the supporting silica rod at the other end of the torsion fiber remain parallel when the beam sags, there will be no change of the turning couple due to a given torque, when the axle is out of alignment with the support, except that arising from the increased length and reduced diameter of the torsion fiber. The unstretched length of the torsion fiber is 1.87 in. and, when the beam is unloaded, the sag is adjusted to be 0.007 in. At the maximum load (0.3 gm. on each side) the measured sag of the beam is 0.065 in. and the torsion fiber will therefore be longer by 0.06%. If Poisson's ratio for fused silica is taken as 0.2, the radius $r$ of the torsion fiber will be smaller by 0.012%. Therefore, the factor $r^4/l$ in equation (2) will be smaller at maximum load by about one part in 1000. If a change in the torsion circle sensibility of more than this amount is found when a beam is calibrated at different values of the load it may be assumed that there are defects in the construction of the beam.

Here it may be noted that the mass of the beam and suspensions is 35 mgm. and that the tensions of the torsion fibers at no load and at maximum load are 4.7 gm. and 8.7 gm. respectively. This is far less than the breaking tension, about 100 gm., of a good 25$\mu$ fiber. The breaking tension of a 5$\mu$ suspension fiber is about 10 gm.

### 4.2 *Unequal Arms*

If the microbalance is to be used only for weighing within the range of the torsion head ($\backsim$2 mgm.) or for comparisons of larger masses by substitution on one side, the arms need not be of equal length. It will have been noted that the length of the arm on only one side of the microbalance appears in the sensibility equations (1) and (2).

If the arms are of nearly equal length, masses can be compared by interchange. For example, equal loads of 0.3 gm. will balance within the range of the torsion circle ($\pm$ 1 mgm.) if the arms of the balance do not differ in length by more than one part in 300. In fact, however, the arms of the beams made on the jig seldom differ by more than one part in 2000.

Let $m$ be the observed difference between two masses $M_1$ and $M_2$ which are being compared by interchange and let $\epsilon$ be the error arising from any cause other than incorrect balance calibration or incorrect weighing. Then,

$$M_1 = M_2 + m + \epsilon.$$

Let $m'$ be the difference, measured in the same sense on the same side of the microbalance, when $M_1$ and $M_2$ are interchanged, giving

$$M_2 = M_1 + m' + \epsilon.$$

It follows that

$$M_1 - M_2 = \frac{m - m'}{2}. \tag{8}$$

4.3 *Bent Suspension Fibers*

The sensibility equations have been derived assuming that the effective lengths of the arms of the beam are independent of the load. At balance the suspension fibers have been assumed to hang vertically from their points of attachment to the beam. If, however, a suspension fiber is not fused to the beam at the correct angle, or if it has a bend near the point of attachment, it will hang in an elastic curve which will alter with the load and so the effective length of that arm of the balance will not be independent of the load. This fault has not been detected in any of our beams. When a suspension fiber is being attached to the beam it is automatically positioned in the correct direction by the jig and it is perpendicular to its supporting rod so that it is possible to keep the flame directed from the opposite side of the rod in line with the fiber while the joint is being made.

The 5$\mu$ suspension fibers are so flexible that the performance of the balance is quite unaffected by the position of weights on the scale pans, or by imperfect joints where the fibers are fused to the scale pan suspension loops. This was checked experimentally by attaching weights unsymmetrically to the scale pan loops so that the loops were forced to hang far out of the vertical.

4.4 *Unsymmetrical Axle*

In deriving the sensibility equations it has been assumed that the axis about which the beam swings passes through the center of the axle of the beam. This implies that the axle is round and straight, and that the torsion fibers at the ends are attached axially. It does not require that the axle be rigid. The axle bends appreciably under load but this bending is harmless if the axle is symmetrical since then the bend of the axle is in the vertical plane whatever the angle of deflection of the beam. However, if the axle is not symmetrical it may bend in a nonvertical plane and, when the load is changed, there will be an alteration of the effective lengths of the arms.

As an example, which has been verified experimentally, suppose that with the intention of strengthening the axle, two struts are added to it in the vertical plane as shown in Fig. 15. The axle is now very rigid in the plane of the struts, but is still flexible at right angles to this plane. Let the angle of deflection of the beam be $\theta$ and the gross load $2M$. Then, neglecting the mass of the beam, there will be a force $2M \sin\theta$ acting through the middle of the axle at right angles to the plane of the struts. If the length of the axle is $a$, the radius of the rods forming

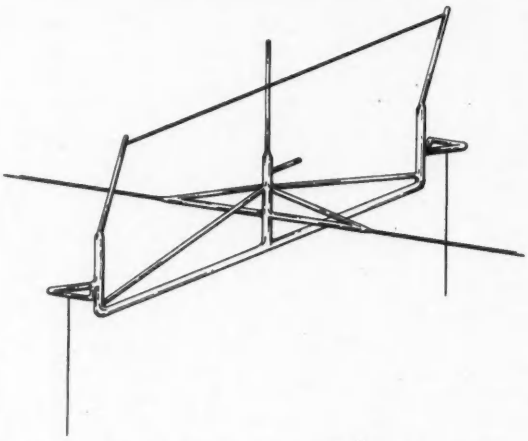

FIG. 15. Experimental fused silica beam with a cantilever axle. This is not a recommended modification.

the axle and struts $r_a$, and the modulus of elasticity $E_a$, the displacement of the axle at the middle is

$$\frac{1}{12}\frac{Mga^3}{\pi E_a r_a^4}\theta$$

for $\theta$ small. This introduces a moment which varies as $M^2$ and is always negative,

$$-2Mg\cdot\frac{1}{12}\frac{Mga^3}{\pi E_a r_a^4}\theta = -\frac{1}{6\pi}\frac{g^2a^3}{E_a r_a^4}M^2\theta.$$

Addition of this term to equation (1), using $r_a$ equal to 100$\mu$ (and $a$ = 4.1 cm.), shows that a beam constructed in this manner would be unstable for all loads above 0.1 gm.

4.5 *Bent Torsion Fibers*

The most difficult joints to make satisfactorily in the construction of the beam are those between the torsion fibers and the ends of the axle. The flame has necessarily to be applied from the side and so it is quite difficult to ensure that the torsion fiber is centrally attached, straight, and in line with the axle. A fault of alignment or a bend in the torsion fiber close to the axle is liable to affect the relative lengths of the arms of the balance by an amount which depends upon the tension of the torsion fibers and which therefore changes with the load and with any other agent causing a change of the tension. For example, the balance point of a beam with this type of fault would probably change with the temperature of the microbalance.

The existence of this fault in a beam can be very readily detected in the Mark I microbalance by removing the shim (Section 2.3) and pulling or pushing the torsion head in the direction of the torsion axis so as to alter the tension o

the fiber. With a good beam only a moderate alteration of the balance point (a few eyepiece scale divisions) should occur. When the shim is in position the alteration should be smaller and the balance should always return exactly to its former position when the torsion head is released.

As a numerical example consider a beam with a torsion fiber making an angle with the axle in the horizontal plane. The displacement of the end of the axle under tension $T$ is given by the expression for $\delta$ quoted in Section 3.2, with $r_t = 12.5\mu$, $E_t = 7.4 \times 10^{11}$, and $Mg$ replaced by $T$. Evaluation of this expression for the unloaded beam ($T$ equal to 4.7 gm. weight) gives a displacement $\delta$ of $3\mu$ per degree of misalignment. Now, let the torsion fibers be extended by moving the anchorage of the suspension 0.001 in. This can be shown to increase the tension by 1 gm. weight and the displacement $\delta$ becomes $2.7\mu$ per degree. The change of $\delta$ is therefore $0.3\mu$ per degree.

Now, if care is not exercised in the construction of beams, imperfections of alignment of several degrees at the points of attachment of the torsion fibers may easily occur so that a displacement of the central fulcrum of these beams of the order of one micron may be expected, when the torsion head is moved one thousandth of an inch. A change of one micron in the position of the fulcrum will produce an alteration of the balance point corresponding to an apparent mass difference of $10^{-6}$ of the load. This is a relatively enormous effect and very great care in the construction of beams has to be taken in order to minimize it as much as possible. Nevertheless, it is possible for a skilled operator to make beams such that this effect is of little practical significance.

### 4.6 *Eccentric Anchorage*

After a new beam has been installed in the microbalance it is advisable to rotate the circle and watch the torsion fiber near its point of attachment to the rotating anchorage. If the torsion fiber rotates eccentrically, the plane of oscillation of the index fiber will vary with the angular position of the circle and this movement may be large enough to spoil the sharpness of focus of the optical unit. This fault may be recognized by focusing the optical unit accurately and then adding weights on one side of the beam sufficient to obtain four new balance points with the circle turned through four quarter revolutions in succession. If the index fiber is out of focus at some positions of the circle and in focus again after a complete revolution there is eccentricity at the rotating anchorage.

When a new beam is tested and adjusted one of the routine operations is the correction of eccentricity of the torsion fiber anchorage. This is done by bending the silica rod to which the torsion fiber is fused. Therefore, any eccentricity seen by the user when a new suspension is put into a microbalance is probably due to imperfect alignment at the coupling and this should be checked.

## 5. PERFORMANCE

### 5.1 *Installation*

The microbalance should be installed on a rigid pillar, preferably built on the ground independently of the floor of the laboratory. Vibration from traffic or machinery is not harmful unless it happens to coincide with some natural

frequency of the suspension, for example a transverse vibration of the index fiber. Then the optical image of the index fiber may appear diffuse and impossible to focus. This defect can be cured by alteration of the supporting pillar so as to prevent transmission of the troublesome vibration, by alteration of the tension of the index fiber (a skilled operation), by alteration of the load, or by use of another beam.

5.2 *Electrification, Adsorption, and Dust*

On a good support in reasonably constant temperature surroundings the balance point of the microbalance is found to remain perfectly constant except when disturbed by electrostatic forces, or by real changes of mass due to adsorption of vapor or pickup of dust particles.

The microbalance should never be used without a grounding wire and the metal forceps with which the scale pans and the specimens are manipulated should also be grounded by means of a flexible wire. If this is not done it may be found that the readings are erratic because of electrostatic charges generated on the scale pans or specimens. Even when strong ionizing sources are used to dissipate them, these charges take quite a long time to disappear. After a new beam has been installed it is advisable to allow it to settle down overnight under the influence of ionizing radiation.

If a small piece of damp paper is enclosed in one of the scale pan cups, the balance (even with no scale pans) will drift for several hours at a rate of about one-half microgram per hour. Most of the weight gained in this way by adsorption of water vapor disappears rapidly after the balance is opened in a dry atmosphere. The normal zero is recovered more slowly if the balance is kept closed, even when a drying agent is placed in each of the scale pan cups. It seems best practice not to use drying agents inside the balance, but rather to use the beam in hygroscopic equilibrium with a fairly dry laboratory atmosphere.

If, during a series of successive determinations of weight, a scale pan or specimen is carried around in the laboratory, or merely laid on a supposedly clean surface while the zero reading of the balance is being taken, there is a high probability that discrete changes of weight which are usually about 0.1 or 0.2 $\mu$gm., but which may be as much as 1$\mu$gm., will be observed. Such changes once they have occurred tend to persist, the succeeding determinations being quite consistent for a few readings until the next change which may be either an increase or a decrease. Occasionally also a similar sudden change may occur in the zero reading of the unloaded beam. These changes are attributable to the pickup or loss of a single particle of dust and very great care has to be taken to avoid their occurrence. One of the most effective precautions is to arrange the work so that scale pans or specimens, when not on the balance, are always hung from a wire as shown in Fig. 3 and never laid down on surfaces. Suitable stands with wires should be provided on the loading platform and in the desiccators in which scale pans or specimens are stored.

Therefore, if the specimens are fairly large, and the work is such that occasional errors of the order of one microgram can be tolerated, the microbalance may be

installed on a pillar in an ordinary laboratory room. Considerably better work can be done if the air in the room is kept at a constant low relative humidity and as far as possible dust-free. The temperature also should be reasonably constant. Realization of the highest accuracy of which the microbalance is capable may require more elaborate precautions as described in the next section.

5.3 *Highly Accurate Work*

The most accurate weighing so far done with the microbalance was carried out in connection with a recent determination (5, 6) of the alpha half life of americium 241 and, since a detailed description of this weighing technique has not yet been published, B. G. Harvey has very kindly supplied the following particulars for inclusion in this report. For a general description of microweighing and microchemical methods, the reader is referred to the excellent article (3) entitled *Microchemical Methods Used in Nuclear Research* by B. B. Cunningham.

The alpha half life of americium was to be determined by finding the rate of emission of alpha particles from a known mass of americium. About 5 μgm. of americium was the maximum quantity which could be used in the alpha counter without introducing a large correction for counting losses. It was desirable to weigh and alpha-count the same sample of americium so that errors in the measurement of aliquot portions could be avoided. The americium was to be carried on a platinum disk which fitted the alpha-particle counter and which could also be used as a scale pan on the microbalance. Therefore, 5 μgm., on a scale pan weighing about 100 mgm., had to be weighed with an error of $\pm 0.02$ μgm. or better.

The microbalance was completely enclosed in an airtight "drybox" with transparent panels and long-sleeved rubber gloves sealed to ports in the box. The air in the box was kept dry with calcium chloride (silica gel may be dangerously dusty and should be avoided). The balance room was maintained at a temperature of 82°F.

The scale pans were disks of mirror-finish platinum foil, 9 mm. in diameter and 0.001 in. thick. A length of platinum wire, 0.015 in. in diameter, was welded to the edge of each disk with a microtorch and the weights of the scale pans were equalized to within 0.1 mgm. by clipping the platinum wires. The wires were then bent as shown in Fig. 3 to form hooks for suspending the scale pans and small rings beneath the hooks to enable the scale pans to be manipulated with a platinum wire.

The scale pans were cleaned in hot nitric acid followed by distilled water and then double-distilled water. They were then heated in a gas flame and stored in a desiccator until required. Alternatively, scale pans may be heated in an electric furnace (but not above 900°C.) and they should be supported on silica, since platinum at this temperature sticks to many substances but not to silica.

One of the scale pans, acting only as a counterpoise, was hung from the left-hand side of the microbalance and the scale pan to be used was hung from the right-hand side. The left-hand scale pan was not interfered with further.

The protecting cup on the right-hand side was removed from the microbalance and the coil of a small induction heater was passed up through the loading platform till it surrounded the platinum disk of the scale pan. The coil was run for 20 sec. (accurately timed) during which the platinum disk reached a temperature of about 850°C. The coil was removed and the scale pan was allowed to cool for 30 sec. before the balance was closed after replacing the protecting cup. A reading was taken $2\frac{1}{2}$ min. later. This cycle of operations was repeated until the scale pan reached a constant weight of four consecutive readings differing by not more than 0.02 μgm. With a new scale pan, constant weight was obtained after some 12 cycles, but subsequent work with the same pan usually required only six cycles.

Accurate timing of the heating and weighing operations was necessary for the following reasons: (*a*) if temperatures of more than 900°C. are used the platinum pans lose some weight with each successive heating, and (*b*) after being heated the platinum pans slowly gain weight for several hours. The rate of increase of weight seems to be rapid at first, but it is difficult to measure because the microbalance needs some time to settle down. Three minutes after the platinum has been heated the rate has dropped to less than 0.20 μgm. per hr. and an accurate balance point can then be determined.

The right-hand scale pan was now removed from the microbalance using a fine platinum wire mounted on a mechanical manipulator inside the dry box. About 3 μl. of the americium solution ($Am(NO_3)_3$ in 0.5 *M* nitric acid)was placed on the scale pan and evaporated with the induction coil at low power, after which the scale pan was heated to 850°C. to drive off volatile substances and convert the $Am(NO_3)_3$ to $AmO_2$.

The scale pan was now replaced on the microbalance and the heating and weighing cycle carried out until constant weight was obtained. A typical set of readings is shown in Table II.

TABLE II

A TYPICAL SET OF READINGS OBTAINED BY B. G. HARVEY IN THE DETERMINATION OF THE ALPHA HALF LIFE OF AMERICIUM

| Scale pan empty | | Scale pan with $AmO_2$ | |
|---|---|---|---|
| Readings, grades | Average, grades | Readings, grades | Average, grades |
| 926.105 | | | |
| .105 | | | |
| .13 | | | |
| .16 | | | |
| .145 | | 921.04 | |
| .12 | | .08 | |
| .115 | 926.115 | .10 | 921.092 |
| .115 | | .10 | |
| .11 | | .09 | |

Weight of sample = 926.115 − 921.092
= $5.02_3$ grades
= $4.67_2$ μgm.

Two different preparations of americium were used and two samples of each of these were weighed and then counted in the alpha-particle counter. The four separate values obtained for the number of alpha particles per minute per microgram of $AmO_2$ were $6.18_3$, $6.15_1$, $6.18_5$, and $6.21_0 \times 10^6$. The root-mean-square deviation of these numbers from the mean is 0.34%, part of which is due to the statistical probable error of the counting, which was 0.1%. It is evident from this example that the microbalance, when skillfully operated, is capable of determining 1 μgm. of material with 1% accuracy on a scale-pan weighing 100 mgm.

## 6. ACKNOWLEDGMENTS

It is a pleasure to thank Miss Marjorie M. Hughes for her skillful and patient work on the construction of nearly 200 silica beams and the measurement of their characteristics in the microbalance. The automatic machine for drawing silica fibers was perfected by Mr. P. G. Salmon. Mr. V. Lynn carried out the drafting of the Mark I microbalance and Mr. W. McAlpin that of the beam constructing jig and the basic Mark II design, and both made valuable suggestions which were adopted. The writer acknowledges a contribution to the theory from Dr. D. G. Hurst and many indispensable discussions of the calculations and other aspects of the work with Mr. J. F. Steljes. Dr. B. B. Cunningham very kindly supplied much interesting information and typical sets of readings obtained from his own experience with microbalances of this type.

## REFERENCES

1. CARMICHAEL, H. Proc. Phys. Soc. (London), 46: 169. 1934.
2. CARMICHAEL, H. and TOWNS, V. W. H. Provisional design and specification of Quartz Microbalance Mark II. N.R.C. Chalk River Report, GPI-1. 1949.
3. CUNNINGHAM, B. B. Nucleonics, 5: 62. 1949.
4. HARVEY, B. G. A simplified quartz torsion fibre ultramicrobalance. N.R.C. Chalk River Report, CI-167. 1948.
5. HARVEY, B. G. Paper presented at the International Congress of Pure & Applied Chemistry. New York. September, 1951.
6. HARVEY, B. G. Phys. Rev. 85: 482. 1952.
7. KIRK, P. L., CRAIG, R., GULLBERG, J. E., and BOYER, R. Q. Anal. Chem. 19: 427. 1947.
8. NEHER, H. V. *in* Procedures in experimental physics *by* J. Strong. Prentice-Hall, Inc., New York. 1942.
9. O'DONNELL, T. J. Drawing and working of quartz fibres. Metallurgical Laboratory, Ryerson Instrument Shop, University of Chicago. March, 1946.
10. PETTERSSON, H. New microbalance and its use. Dissertation. University of Stockholm. Goteberg, Sweden. 1914.
11. STEELE, B. D. and GRANT, K. Proc. Roy. Soc. (London), A, 82: 580. 1909.
12. WEBER, WILHELM. Wilhelm Webers Werke. Bd. 1. Springer, Berlin. 1892. p. 499.

# INITIAL DISTRIBUTION OF COMPTON ELECTRONS[1]

By H. E. Johns, D. V. Cormack, S. A. Denesuk, and G. F. Whitmore

ABSTRACT

Modifications of the Klein-Nishina formula for the Compton effect are presented which give the energy distribution and the angular distribution of the recoil electrons. Electron distributions have been calculated for photon energies from 10 kev. to 30 Mev. The distributions of the electrons produced by $Co^{60}$ $\gamma$ rays have been determined.

## INTRODUCTION

The ordinary form of the Klein-Nishina formula for the Compton effect gives the differential cross section, $d\sigma(\phi)/d\omega$, for the number of photons scattered into unit solid angle at angle $\phi$ per photon per cm.$^2$ per electron of material:

$$(1) \qquad \frac{d\sigma(\phi)}{d\omega} = \frac{r_0^2}{2}\left(\frac{1}{1+\alpha \operatorname{vers}\phi}\right)^2\left\{1+\cos^2\phi+\frac{\alpha^2 \operatorname{vers}^2\phi}{1+\alpha \operatorname{vers}\phi}\right\}$$

where $r_0$ is the classical electronic radius $e^2/m_0c^2$, $\alpha$ is the energy parameter $h\nu/m_0c^2$, and $\operatorname{vers}\phi = 1 - \cos\phi$. The differential cross section, $d\sigma(\phi)/d\phi$, for the number of photons scattered into unit angle at angle $\phi$ is then given by:

$$(2) \qquad \frac{d\sigma(\phi)}{d\phi} = 2\pi \sin\phi \frac{d\sigma(\phi)}{d\omega}.$$

Values for this cross section have been computed to an accuracy of four significant figures and are given in Table I. This table is divided into three parts, covering the energy ranges 10 to 300 kev., 0.35 to 3.0 Mev., and 3.5 to 30 Mev. The physical constants used were taken from Dumond and Cohen (2).

For small photon energies ($h\nu \to 0$) this distribution has the form $\pi r_0 \sin\phi(1+\cos^2\phi)$ which has two peaks which occur at about $\phi = 55°$ and $\phi = 125°$. For larger photon energies the second peak disappears. The single remaining maximum moves towards smaller values of the angle $\phi$ as the energy is increased.

## ENERGY DISTRIBUTION OF COMPTON ELECTRONS

The cross section, $d\sigma(\phi)$, for photons scattered between cones of half angle $\phi$ and $\phi + d\phi$ will be equal to the cross section, $d\sigma(E)$, for the production of Compton electrons with energies between $E$ and $E + dE$. The differential cross section, $d\sigma(E)/dE$, for the number of electrons per unit energy interval at energy $E$ will then be given by:

$$(3) \qquad \frac{d\sigma(E)}{dE} = \frac{d\sigma(\phi)}{d\phi}\frac{d\phi}{dE}$$

[1] *Manuscript received January 18, 1952.*
*Contribution from the Physics Department, University of Saskatchewan, Saskatoon, Sask.*

## TABLE I

DIFFERENTIAL CROSS SECTION FOR THE ANGULAR DISTRIBUTION OF SCATTERED PHOTONS

The table gives the number of photons scattered per unit angle (radians) at angle $\phi$ per electron of material per photon per cm.$^2$ Multiply table values by $10^{-27}$ to obtain $d\sigma(\phi)/d\phi$ in cm.$^2$ per electron.

| $\phi$ \ $h\nu$, kev. | 10 | 20 | 40 | 60 | 80 | 100 | 120 | 150 | 200 | 250 | 300 |
|---|---|---|---|---|---|---|---|---|---|---|---|
| 0 | 0 | 0 | 0 | 0 | 0 | 0 | 0 | 0 | 0 | 0 | 0 |
| 10 | 85.32 | 85.26 | 85.16 | 85.06 | 84.96 | 84.86 | 84.76 | 84.61 | 84.36 | 84.11 | 83.87 |
| 20 | 160.3 | 160.0 | 159.2 | 158.5 | 157.7 | 157.0 | 156.3 | 155.2 | 153.4 | 151.7 | 150.0 |
| 30 | 217.2 | 216.1 | 213.9 | 211.7 | 209.5 | 207.4 | 205.4 | 202.3 | 197.4 | 192.8 | 188.3 |
| 40 | 252.2 | 250.0 | 245.5 | 241.2 | 236.9 | 233.0 | 229.1 | 223.5 | 214.7 | 206.5 | 198.8 |
| 50 | 266.4 | 262.8 | 255.8 | 249.1 | 242.8 | 236.8 | 231.0 | 222.9 | 210.5 | 199.3 | 189.3 |
| 60 | 265.0 | 260.0 | 250.5 | 241.4 | 233.4 | 225.7 | 218.5 | 208.5 | 193.8 | 181.1 | 170.0 |
| 70 | 255.4 | 249.1 | 237.4 | 226.8 | 217.1 | 208.3 | 209.4 | 189.1 | 173.4 | 160.4 | 149.4 |
| 80 | 245.2 | 237.8 | 224.2 | 212.1 | 201.3 | 191.7 | 183.0 | 171.5 | 155.6 | 142.9 | 132.4 |
| 90 | 240.2 | 231.5 | 215.9 | 202.3 | 190.5 | 180.1 | 171.0 | 159.1 | 143.1 | 130.6 | 120.6 |
| 100 | 242.1 | 231.9 | 214.0 | 198.7 | 185.7 | 174.4 | 164.6 | 152.0 | 135.5 | 122.9 | 112.9 |
| 110 | 248.9 | 237.0 | 216.4 | 199.2 | 184.7 | 172.3 | 161.7 | 148.2 | 130.8 | 117.7 | 107.4 |
| 120 | 255.1 | 241.6 | 218.5 | 199.4 | 183.5 | 170.0 | 158.6 | 144.2 | 125.9 | 112.2 | 101.6 |
| 130 | 253.8 | 239.2 | 214.3 | 194.0 | 177.3 | 163.2 | 151.3 | 136.6 | 117.9 | 104.1 | 93.29 |
| 140 | 238.0 | 223.3 | 198.5 | 178.5 | 162.1 | 148.4 | 136.9 | 122.7 | 104.8 | 91.73 | 81.74 |
| 150 | 203.4 | 190.2 | 168.0 | 150.2 | 135.7 | 123.7 | 113.6 | 101.2 | 85.76 | 74.51 | 65.99 |
| 160 | 149.3 | 139.2 | 122.4 | 109.0 | 98.11 | 89.12 | 81.59 | 72.34 | 60.96 | 52.68 | 46.44 |
| 170 | 79.16 | 73.71 | 64.62 | 57.39 | 51.54 | 46.72 | 42.69 | 37.78 | 31.69 | 27.30 | 24.00 |
| 180 | 0 | 0 | 0 | 0 | 0 | 0 | 0 | 0 | 0 | 0 | 0 |

| $\phi$ \ $h\nu$, Mev. | 0.35 | 0.4 | 0.5 | 0.6 | 0.8 | 1.0 | 1.2 | 1.5 | 2.0 | 2.5 | 3.0 |
|---|---|---|---|---|---|---|---|---|---|---|---|
| 0 | 0 | 0 | 0 | 0 | 0 | 0 | 0 | 0 | 0 | 0 | 0 |
| 5 | 43.12 | 43.08 | 43.02 | 42.93 | 42.83 | 42.70 | 42.57 | 42.39 | 42.12 | 41.77 | 41.46 |
| 10 | 83.62 | 83.37 | 82.87 | 82.41 | 81.45 | 80.54 | 79.58 | 78.25 | 76.12 | 74.10 | 72.17 |
| 15 | 119.3 | 118.5 | 117.0 | 115.5 | 112.7 | 110.0 | 107.4 | 103.7 | 97.98 | 92.86 | 88.18 |
| 20 | 148.4 | 146.7 | 143.6 | 140.5 | 134.8 | 129.4 | 124.5 | 117.6 | 107.7 | 99.24 | 92.03 |
| 25 | 170.0 | 167.3 | 161.9 | 156.8 | 147.6 | 139.3 | 131.9 | 121.9 | 108.4 | 97.45 | 88.50 |
| 30 | 184.0 | 179.9 | 172.2 | 165.0 | 152.1 | 141.3 | 131.8 | 119.6 | 103.6 | 91.47 | 81.93 |
| 40 | 192.0 | 185.4 | 173.1 | 162.5 | 144.8 | 130.6 | 119.0 | 105.2 | 88.47 | 76.63 | 67.80 |
| 50 | 180.3 | 172.1 | 157.8 | 145.8 | 126.9 | 112.6 | 101.5 | 88.81 | 74.05 | 63.92 | 56.45 |
| 60 | 160.4 | 151.8 | 137.4 | 125.9 | 108.3 | 95.71 | 86.12 | 75.33 | 63.14 | 54.33 | 47.98 |
| 70 | 140.0 | 132.0 | 118.8 | 108.5 | 93.28 | 82.51 | 74.38 | 65.19 | 54.54 | 47.06 | 41.50 |
| 80 | 123.7 | 116.4 | 104.5 | 95.45 | 82.19 | 72.80 | 65.66 | 57.53 | 47.86 | 41.27 | 36.27 |
| 90 | 112.4 | 105.5 | 94.59 | 86.25 | 74.12 | 65.49 | 58.91 | 51.38 | 42.62 | 36.37 | 31.80 |
| 105 | 101.9 | 95.14 | 84.52 | 76.47 | 64.84 | 56.64 | 50.44 | 43.46 | 35.04 | 29.93 | 25.69 |
| 120 | 93.06 | 86.12 | 75.33 | 67.26 | 55.83 | 47.98 | 42.19 | 35.89 | 28.68 | 23.95 | 20.55 |
| 135 | 79.86 | 73.19 | 62.96 | 55.42 | 45.06 | 38.12 | 33.04 | 27.72 | 21.86 | 18.07 | 16.04 |
| 150 | 59.30 | 53.92 | 45.61 | 39.86 | 31.85 | 26.61 | 22.90 | 18.97 | 14.79 | 12.13 | 10.28 |
| 165 | 31.74 | 28.72 | 24.16 | 20.91 | 16.52 | 13.70 | 11.52 | 9.631 | 7.467 | 6.096 | 5.158 |
| 180 | 0 | 0 | 0 | 0 | 0 | 0 | 0 | 0 | 0 | 0 | 0 |

| $\phi$ \ $h\nu$, Mev. | 3.5 | 4 | 5 | 6 | 8 | 10 | 12 | 15 | 20 | 25 | 30 |
|---|---|---|---|---|---|---|---|---|---|---|---|
| 0 | 0 | 0 | 0 | 0 | 0 | 0 | 0 | 0 | 0 | 0 | 0 |
| 2 | 17.26 | 17.24 | 17.20 | 17.16 | 17.08 | 17.00 | 16.92 | 16.81 | 16.61 | 16.42 | 16.24 |
| 4 | 33.61 | 33.45 | 33.14 | 32.84 | 32.25 | 31.68 | 31.12 | 30.32 | 29.08 | 27.90 | 26.85 |
| 6 | 48.23 | 47.75 | 46.80 | 45.89 | 44.16 | 42.66 | 41.03 | 38.93 | 35.62 | 33.19 | 30.87 |
| 8 | 60.59 | 59.56 | 57.59 | 55.73 | 52.32 | 49.28 | 46.55 | 42.94 | 38.08 | 34.01 | 30.78 |
| 10 | 70.38 | 68.62 | 65.33 | 62.31 | 57.00 | 52.72 | 48.50 | 43.67 | 37.34 | 32.60 | 29.53 |
| 15 | 83.94 | 80.06 | 73.24 | 67.45 | 58.18 | 51.13 | 45.61 | 39.27 | 31.96 | 27.01 | 23.43 |
| 20 | 85.72 | 80.12 | 70.67 | 63.66 | 52.86 | 45.28 | 39.65 | 33.51 | 26.76 | 22.34 | 19.22 |
| 25 | 81.07 | 74.81 | 64.86 | 57.32 | 46.67 | 39.50 | 34.32 | 28.77 | 22.76 | 18.88 | 16.16 |
| 30 | 74.26 | 67.96 | 58.25 | 51.09 | 41.22 | 34.69 | 30.02 | 25.05 | 19.69 | 16.25 | 13.85 |
| 40 | 60.94 | 55.44 | 47.14 | 41.13 | 32.93 | 27.54 | 23.71 | 19.64 | 15.29 | 12.54 | 10.63 |
| 50 | 50.68 | 46.06 | 39.16 | 34.00 | 27.08 | 22.54 | 19.31 | 15.91 | 12.31 | 10.05 | 8.487 |
| 60 | 43.05 | 39.08 | 33.06 | 28.68 | 22.71 | 18.81 | 16.06 | 13.18 | 10.15 | 8.248 | 6.949 |
| 70 | 37.15 | 33.65 | 28.35 | 24.50 | 19.29 | 15.91 | 13.54 | 11.07 | 8.486 | 6.886 | 5.767 |
| 80 | 32.35 | 29.21 | 24.48 | 21.08 | 16.49 | 13.55 | 11.50 | 9.369 | 7.160 | 5.793 | 4.967 |
| 90 | 28.23 | 25.42 | 21.19 | 18.16 | 14.13 | 11.57 | 9.790 | 7.956 | 6.064 | 4.899 | 4.250 |
| 100 | 24.60 | 22.05 | 18.28 | 15.61 | 12.08 | 9.853 | 8.320 | 6.746 | 5.129 | 4.136 | 3.466 |
| 120 | 18.04 | 16.26 | 13.22 | 11.17 | 8.569 | 6.949 | 5.845 | 4.720 | 3.574 | 2.876 | 2.406 |
| 140 | 11.93 | 10.59 | 8.600 | 7.253 | 5.523 | 4.460 | 3.741 | 3.012 | 2.274 | 1.826 | 1.526 |
| 160 | 5.953 | 5.253 | 4.256 | 3.578 | 2.713 | 2.185 | 1.829 | 1.470 | 1.108 | .8887 | .7420 |
| 180 | 0 | 0 | 0 | 0 | 0 | 0 | 0 | 0 | 0 | 0 | 0 |

The energy of the recoil electron $E$ corresponding to a photon scattered through an angle $\phi$ is given by:

$$E = h\nu \frac{\alpha \text{ vers } \phi}{1 + \alpha \text{ vers } \phi}. \tag{4}$$

Differentiation of (4) gives

$$\frac{dE}{d\phi} = h\nu \frac{\alpha \sin \phi}{(1 + \alpha \text{ vers } \phi)^2}. \tag{5}$$

Substituting equations (5) and (2) into equation (3) we obtain

$$\frac{d\sigma(E)}{dE} = \frac{\pi r_0^2}{\alpha h\nu}\left\{1 + \cos^2\phi + \frac{\alpha^2 \text{ vers}^2 \phi}{1 + \alpha \text{ vers } \phi}\right\}. \tag{6}$$

This expression, which gives the energy distribution of the recoil electrons, is simpler than equation (2) which gives the angular distribution of the scattered photons. When one is primarily concerned with the energies of the electrons set in motion by the Compton process, equation (6) may be used directly. By eliminating $\phi$ from equations (4) and (6) the variation of $d\sigma(E)/dE$ with the energy $E$ of the electron may be determined. However in order to present the cross sections in tabular form it is convenient to express the energy of the electron as a fraction $f$ of the maximum energy which an electron can receive. From equation (4) the maximum electron energy is

$$E_{\max} = \left(\frac{2\alpha}{1 + 2\alpha}\right) h\nu \tag{7}$$

and the fraction, $f$, is given by

$$f = \frac{E}{E_{\max}} = \left(\frac{1 + 2\alpha}{2\alpha}\right)\left\{\frac{\alpha \text{ vers } \phi}{1 + \alpha \text{ vers } \phi}\right\}. \tag{8}$$

Equation (8) may be rearranged to yield

$$\text{vers } \phi = \frac{2f}{1 + 2\alpha - 2\alpha f}. \tag{9}$$

Vers $\phi$ was determined from (9) and equation (6) evaluated for values of $f$ from 0 to 1, to yield the data given in Table II. $E_{\max}$ determined from (7) is given in the first line of the table. As $\alpha$ becomes small compared to 1, equation (6) and (9) yield as a limit the following expression,

$$\frac{d\sigma(E)}{dE} = \frac{\pi r_0^2}{\alpha h\nu}(1 + \cos^2\phi) = \frac{\pi r_0^2}{\alpha h\nu}(1 + (1 - 2f)^2), \tag{10}$$

a distribution which is symmetrical about the minimum value at $f = .5$. As the value of $\alpha$ is increased the minimum in the distribution is shifted towards $f = 0$ and for values of $\alpha \gg 1$ the distribution shows a very sharp peak at $f = 1$. This peak value approaches $2\pi r_0^2/h\nu$ or $4.99 \times 10^{-25}/h\nu$ for very large values of $\alpha$.

These facts are illustrated in Table II and Fig. 1. Fig. 1 shows the electron distribution function for photon energies in the range 100 to 200 kev. The dotted curves correspond to constant values of $f = E/E_{\max}$ from 0.1 to 1.0.

## TABLE II

DIFFERENTIAL CROSS SECTION FOR THE ENERGY DISTRIBUTION OF COMPTON ELECTRONS

The table gives the number of Compton electrons per Mev. interval at energy $E$, per electron of material per photon per cm.$^2$ Multiply by the values indicated to obtain $d\sigma(E)/dE$ in cm.$^2$ per electron.

*Multiply by* $10^{-26}$

| $E/E_{max}$ | $h\nu$ (kev.) | | | | | | | | | | |
|---|---|---|---|---|---|---|---|---|---|---|---|
| | 10 | 20 | 40 | 60 | 80 | 100 | 120 | 150 | 200 | 250 | 300 |
| | $E_{max}$ | | | | | | | | | | |
| | .3768 | 1.452 | 5.417 | 11.41 | 19.08 | 28.14 | 38.36 | 55.50 | 87.84 | 123.7 | 162.0 |
| 0 | 2551 | 637.4 | 159.3 | 70.82 | 39.83 | 25.50 | 17.71 | 11.33 | 6.374 | 4.079 | 2.833 |
| .1 | 2106 | 529.5 | 133.9 | 60.10 | 34.12 | 22.01 | 15.40 | 9.953 | 5.676 | 3.674 | 2.575 |
| .2 | 1754 | 442.7 | 112.8 | 51.04 | 29.18 | 18.96 | 13.34 | 8.700 | 5.026 | 3.289 | 2.327 |
| .3 | 1497 | 378.1 | 96.61 | 43.85 | 25.17 | 16.42 | 11.61 | 7.616 | 4.446 | 2.938 | 2.098 |
| .4 | 1337 | 336.7 | 85.67 | 38.79 | 22.24 | 14.51 | 10.26 | 6.756 | 3.968 | 2.641 | 1.900 |
| .5 | 1277 | 319.6 | 80.48 | 36.15 | 20.60 | 13.38 | 9.442 | 6.195 | 3.636 | 2.426 | 1.752 |
| .6 | 1318 | 327.9 | 81.57 | 36.26 | 20.48 | 13.20 | 9.256 | 6.029 | 3.511 | 2.334 | 1.684 |
| .7 | 1464 | 362.7 | 89.51 | 39.49 | 22.14 | 14.18 | 9.779 | 6.384 | 3.679 | 2.427 | 1.744 |
| .8 | 1717 | 425.4 | 104.9 | 45.18 | 25.91 | 16.57 | 11.52 | 7.427 | 4.262 | 2.801 | 2.006 |
| .9 | 2079 | 517.1 | 131.7 | 57.04 | 32.15 | 20.68 | 14.46 | 9.385 | 5.438 | 3.602 | 2.596 |
| 1.0 | 2553 | 639.3 | 161.0 | 72.40 | 41.32 | 26.90 | 19.03 | 12.56 | 7.470 | 5.067 | 3.731 |

*Multiply by* $10^{-27}$

| $E/E_{max}$ | $h\nu$ (Mev.) | | | | | | | | | | |
|---|---|---|---|---|---|---|---|---|---|---|---|
| | 0.35 | 0.4 | 0.5 | 0.6 | 0.8 | 1.0 | 1.2 | 1.5 | 2.0 | 2.5 | 3.0 |
| | $E_{max}$ | | | | | | | | | | |
| | .2023 | .2441 | .3309 | .4209 | .6064 | .7965 | .9894 | 1.282 | 1.773 | 2.268 | 2.765 |
| 0 | 2081 | 1593 | 1020 | 708.2 | 398.4 | 254.9 | 177.0 | 113.3 | 63.74 | 40.79 | 28.33 |
| .1 | 1907 | 1470 | 972.5 | 666.0 | 379.3 | 244.8 | 171.1 | 110.2 | 62.45 | 40.15 | 27.97 |
| .2 | 1738 | 1349 | 883.5 | 624.7 | 360.9 | 235.3 | 165.7 | 107.6 | 61.54 | 39.81 | 27.85 |
| .3 | 1579 | 1235 | 819.4 | 585.6 | 343.9 | 226.9 | 161.2 | 105.8 | 61.18 | 39.87 | 28.04 |
| .4 | 1440 | 1135 | 762.2 | 550.8 | 329.3 | 220.3 | 158.2 | 105.1 | 61.63 | 40.52 | 28.76 |
| .5 | 1335 | 1057 | 718.1 | 524.5 | 319.4 | 216.9 | 157.7 | 106.2 | 63.34 | 42.14 | 30.08 |
| .55 | 1301 | 1035 | 704.1 | 516.6 | 317.4 | 217.2 | 158.9 | 107.9 | 64.92 | 43.47 | 31.18 |
| .60 | 1285 | 1020 | 697.8 | 513.9 | 318.3 | 219.4 | 161.5 | 110.5 | 67.19 | 45.32 | 32.68 |
| .65 | 1291 | 1025 | 702.2 | 518.5 | 323.2 | 224.3 | 166.2 | 114.7 | 70.43 | 47.86 | 34.71 |
| .70 | 1327 | 1052 | 721.0 | 533.1 | 334.1 | 233.2 | 173.8 | 120.9 | 75.04 | 51.41 | 37.52 |
| .75 | 1400 | 1109 | 759.4 | 561.9 | 353.4 | 248.0 | 185.8 | 130.2 | 81.70 | 56.46 | 41.50 |
| .80 | 1523 | 1206 | 825.2 | 610.9 | 385.3 | 271.5 | 204.4 | 144.3 | 91.58 | 63.89 | 47.32 |
| .85 | 1710 | 1355 | 929.2 | 689.2 | 436.5 | 309.1 | 233.9 | 166.4 | 106.9 | 75.39 | 56.36 |
| .90 | 1982 | 1577 | 1088 | 811.0 | 518.2 | 369.9 | 282.0 | 202.8 | 132.4 | 94.71 | 71.69 |
| .95 | 2367 | 1897 | 1325 | 999.0 | 650.5 | 471.8 | 364.9 | 267.5 | 179.7 | 131.7 | 101.9 |
| 1.00 | 2906 | 2355 | 1681 | 1292 | 871.3 | 652.5 | 520.0 | 397.7 | 285.0 | 221.9 | 181.7 |

*Multiply by* $10^{-28}$

| $E/E_{max}$ | $h\nu$ (Mev.) | | | | | | | | | | |
|---|---|---|---|---|---|---|---|---|---|---|---|
| | 3.5 | 4 | 5 | 6 | 8 | 10 | 12 | 15 | 20 | 25 | 30 |
| | $E_{max}$ | | | | | | | | | | |
| | 3.262 | 3.760 | 4.757 | 5.755 | 7.752 | 9.751 | 11.75 | 14.75 | 19.75 | 24.75 | 29.75 |
| 0 | 208.1 | 159.3 | 102.0 | 70.82 | 39.84 | 25.49 | 17.70 | 11.33 | 6.374 | 4.079 | 2.833 |
| .2 | 205.7 | 158.2 | 101.8 | 71.00 | 40.16 | 25.78 | 17.94 | 11.51 | 6.489 | 4.158 | 2.890 |
| .4 | 213.9 | 165.6 | 107.7 | 75.62 | 43.14 | 27.86 | 19.46 | 12.53 | 7.090 | 4.554 | 3.170 |
| .6 | 247.0 | 193.3 | 127.8 | 90.74 | 52.55 | 34.24 | 24.07 | 15.60 | 8.886 | 5.731 | 4.000 |
| .7 | 286.3 | 225.9 | 151.0 | 108.15 | 63.33 | 41.56 | 29.36 | 19.12 | 10.95 | 7.084 | 4.956 |
| .8 | 365.5 | 291.2 | 197.8 | 143.3 | 85.29 | 56.57 | 40.26 | 26.43 | 15.26 | 9.921 | 6.964 |
| .82 | 390.7 | 312.1 | 212.9 | 154.7 | 92.45 | 61.49 | 43.86 | 28.85 | 16.69 | 10.87 | 7.640 |
| .84 | 421.2 | 337.3 | 231.1 | 168.5 | 101.2 | 67.55 | 48.29 | 31.85 | 18.48 | 12.06 | 8.483 |
| .86 | 458.4 | 368.3 | 253.6 | 185.7 | 112.2 | 75.16 | 53.89 | 35.65 | 20.76 | 13.57 | 9.561 |
| .88 | 504.9 | 407.2 | 282.1 | 207.5 | 126.2 | 84.98 | 61.13 | 40.61 | 23.74 | 15.56 | 10.98 |
| .90 | 564.2 | 457.0 | 318.9 | 236.0 | 144.8 | 98.07 | 70.88 | 47.31 | 27.81 | 18.29 | 12.94 |
| .92 | 642.2 | 523.0 | 368.3 | 274.6 | 170.4 | 116.4 | 84.62 | 56.86 | 33.67 | 22.26 | 15.81 |
| .94 | 748.6 | 614.0 | 437.8 | 329.7 | 207.9 | 143.6 | 105.4 | 71.50 | 42.83 | 28.52 | 20.36 |
| .96 | 901.2 | 746.9 | 542.2 | 414.5 | 267.7 | 188.3 | 140.2 | 96.72 | 59.05 | 39.85 | 28.72 |
| .98 | 1136 | 956.8 | 715.0 | 560.7 | 377.8 | 275.0 | 210.5 | 150.2 | 95.59 | 66.44 | 48.96 |
| 1.00 | 1537 | 1332 | 1052 | 868.7 | 644.4 | 512.2 | 425.0 | 338.5 | 252.8 | 201.7 | 167.8 |

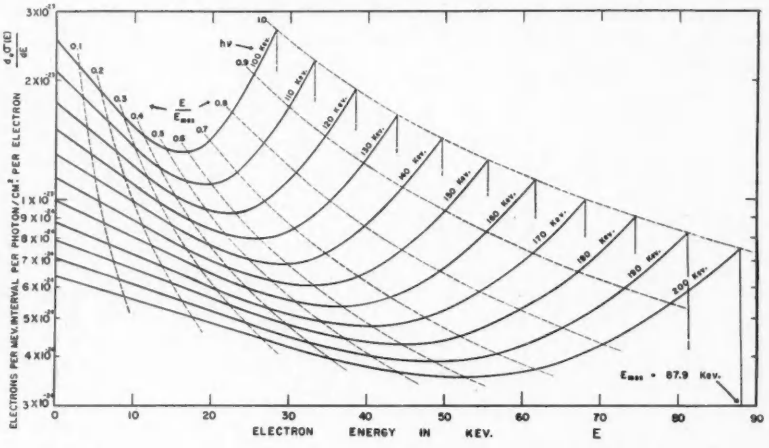


FIG. 1. Differential cross section for the number of Compton electrons produced by photons with energies 100 kev. to 200 kev. The dotted curves are for $E/E_{max}$ values from 0.1–1.0.

## ANGULAR DISTRIBUTION OF COMPTON ELECTRONS

In many problems the angular distribution of the Compton recoil electrons is required. The differential cross section for the production of a Compton electron projected at angle $\theta$ to the original photon direction may be found by a method similar to that used to find the cross section, $d\sigma(E)/dE$, given in equation (6). The angles of scattering of the photon $\phi$ and the electrons $\theta$ are related by the equation

$$(1 + \alpha) \tan \theta = - \cot \phi/2. \tag{11}$$

$$\text{then } \frac{d\phi}{d\theta} = \frac{2(1 + \alpha)}{1 + (\alpha + \tfrac{1}{2}\alpha^2) \text{ vers } 2\theta}. \tag{12}$$

The differential cross section $d\sigma(\theta)/d\theta$ is then given by

$$\frac{d\sigma(\theta)}{d\theta} = \frac{d\sigma(\phi)}{d\phi}\left(\frac{d\phi}{d\theta}\right). \tag{13}$$

Equation (13) may be expressed in terms of $\theta$ as follows

$$\frac{d\sigma(\theta)}{d\theta} = \frac{8\pi r_0^2(1 + \alpha)}{1 + (\alpha + \tfrac{1}{2}\alpha^2) \text{ vers } 2\theta} \frac{b}{(1 + b^2 + 2\alpha)^2}\left(\frac{b^4 + 1}{b^2 + 1} + \frac{2\alpha^2 - 2}{(1 + b^2 + 2\alpha)}\right) \tag{14}$$

where $b = (1 + \alpha)\tan\theta$.

Equation (14) was evaluated and the results given in Table III for photon energies from 10 kev. to 30 Mev. For low energy photons $d\sigma(\theta)/d\theta$ shows a double maximum at about 25° and 65°. As $\alpha \to 0$ the distribution approaches the form $2\pi r_e^2 \sin 2\theta(1 + \cos^2 2\theta)$. For large values of $\alpha$ the distribution shows a single maximum at small values of $\theta$.

## TABLE III

DIFFERENTIAL CROSS SECTION FOR THE ANGULAR DISTRIBUTION OF COMPTON ELECTRONS

The table gives the number of Compton recoil electrons projected per unit angular interval (radians) at angle $\theta$, per electron of material per photon per cm.$^2$ Multiply table values by $10^{-27}$ to obtain $d\sigma(\theta)/d\theta$ in cm.$^2$ per electron.

| $\theta$ \ $h\nu$, kev. | 10 | 20 | 40 | 60 | 80 | 100 | 120 | 150 | 200 | 250 | 300 |
|---|---|---|---|---|---|---|---|---|---|---|---|
| 0 | 0 | 0 | 0 | 0 | 0 | 0 | 0 | 0 | 0 | 0 | 0 |
| 5 | 163.9 | 158.8 | 149.6 | 142.4 | 136.7 | 132.1 | 128.5 | 124.4 | 120.1 | 118.2 | 117.4 |
| 10 | 309.0 | 298.0 | 279.6 | 265.1 | 253.5 | 244.0 | 236.4 | 227.6 | 217.2 | 210.9 | 207.1 |
| 15 | 418.7 | 402.7 | 375.6 | 354.3 | 336.7 | 322.3 | 310.3 | 295.8 | 278.2 | 266.1 | 257.4 |
| 20 | 486.5 | 466.5 | 432.0 | 405.0 | 382.3 | 363.5 | 347.6 | 328.0 | 303.9 | 284.8 | 272.8 |
| 25 | 515.1 | 492.5 | 454.3 | 423.2 | 397.5 | 376.0 | 357.9 | 335.6 | 307.6 | 287.3 | 272.2 |
| 30 | 514.4 | 491.3 | 452.0 | 420.1 | 393.8 | 371.9 | 353.4 | 330.8 | 302.7 | 282.6 | 267.7 |
| 35 | 499.3 | 477.5 | 440.4 | 410.4 | 385.7 | 365.3 | 348.2 | 327.2 | 301.4 | 283.0 | 269.1 |
| 40 | 484.6 | 465.3 | 432.5 | 406.0 | 384.2 | 366.2 | 351.0 | 332.3 | 308.8 | 291.4 | 277.7 |
| 45 | 480.7 | 464.2 | 436.1 | 413.1 | 394.0 | 377.9 | 364.0 | 346.6 | 323.6 | 305.3 | 289.9 |
| 50 | 490.6 | 476.4 | 451.6 | 430.8 | 412.9 | 397.4 | 383.6 | 365.5 | 340.2 | 318.9 | 300.2 |
| 55 | 509.7 | 496.3 | 472.6 | 451.9 | 433.5 | 416.9 | 401.7 | 381.3 | 351.5 | 325.9 | 303.2 |
| 60 | 526.0 | 512.5 | 487.7 | 465.4 | 445.1 | 426.5 | 407.9 | 385.6 | 351.0 | 321.1 | 295.0 |
| 65 | 526.1 | 510.9 | 484.2 | 459.9 | 437.5 | 417.0 | 397.8 | 371.7 | 333.7 | 301.4 | 273.5 |
| 70 | 493.5 | 478.7 | 451.1 | 426.0 | 402.9 | 382.8 | 362.2 | 335.7 | 297.5 | 265.6 | 238.5 |
| 75 | 438.6 | 425.3 | 398.7 | 373.6 | 352.5 | 332.4 | 314.0 | 289.2 | 253.9 | 224.7 | 200.3 |
| 80 | 309.9 | 299.0 | 278.8 | 260.6 | 244.2 | 228.6 | 215.6 | 197.3 | 171.7 | 150.7 | 133.4 |
| 85 | 164.3 | 158.3 | 147.2 | 137.1 | 128.1 | 120.0 | 112.2 | 102.7 | 88.92 | 77.73 | 68.53 |
| 90 | 0 | 0 | 0 | 0 | 0 | 0 | 0 | 0 | 0 | 0 | 0 |

| $\theta$ \ $h\nu$, Mev. | 0.35 | 0.4 | 0.5 | 0.6 | 0.8 | 1.0 | 1.2 | 1.5 | 2.0 | 2.5 | 3.0 |
|---|---|---|---|---|---|---|---|---|---|---|---|
| 0 | 0 | 0 | 0 | 0 | 0 | 0 | 0 | 0 | 0 | 0 | 0 |
| 2 | 48.81 | 49.32 | 50.90 | 52.98 | 57.11 | 63.38 | 69.11 | 77.88 | 92.51 | 106.8 | 120.5 |
| 4 | 95.41 | 95.70 | 98.87 | 102.4 | 110.8 | 120.0 | 129.3 | 143.0 | 164.0 | 182.2 | 197.3 |
| 6 | 137.9 | 138.8 | 141.4 | 144.8 | 154.9 | 165.0 | 174.8 | 187.8 | 206.1 | 218.1 | 225.8 |
| 8 | 174.4 | 174.5 | 176.7 | 178.5 | 186.4 | 196.6 | 204.1 | 213.3 | 222.8 | 226.0 | 224.6 |
| 10 | 204.9 | 203.9 | 204.0 | 205.7 | 210.5 | 215.4 | 219.3 | 222.9 | 223.3 | 218.5 | 210.8 |
| 15 | 251.0 | 246.2 | 239.6 | 235.1 | 229.2 | 224.5 | 219.8 | 212.3 | 198.3 | 183.3 | 168.7 |
| 20 | 262.5 | 254.3 | 241.9 | 225.7 | 219.7 | 209.6 | 200.6 | 187.8 | 167.7 | 149.3 | 133.0 |
| 25 | 260.4 | 248.7 | 256.6 | 226.8 | 211.8 | 199.6 | 188.5 | 172.8 | 149.0 | 128.6 | 111.6 |
| 30 | 266.0 | 247.0 | 233.1 | 222.4 | 205.4 | 190.6 | 176.9 | 157.9 | 130.8 | 109.3 | 92.31 |
| 40 | 266.3 | 256.3 | 239.1 | 224.0 | 197.4 | 174.4 | 154.5 | 129.7 | 99.25 | 78.05 | 62.64 |
| 50 | 283.4 | 268.2 | 241.1 | 217.7 | 179.5 | 150.0 | 126.9 | 100.9 | 72.13 | 54.05 | 41.98 |
| 60 | 272.0 | 251.5 | 230.7 | 188.7 | 146.6 | 116.9 | 95.39 | 72.68 | 49.44 | 35.79 | 27.09 |
| 70 | 215.3 | 195.4 | 163.0 | 138.0 | 102.6 | 79.22 | 63.00 | 47.13 | 30.68 | 21.70 | 16.16 |
| 80 | 118.8 | 106.6 | 87.11 | 72.54 | 52.55 | 39.83 | 31.19 | 22.72 | 14.66 | 10.23 | 7.548 |
| 90 | 0 | 0 | 0 | 0 | 0 | 0 | 0 | 0 | 0 | 0 | 0 |

| $\theta$ \ $h\nu$, Mev. | 3.5 | 4 | 5 | 6 | 8 | 10 | 12 | 15 | 20 | 25 | 30 |
|---|---|---|---|---|---|---|---|---|---|---|---|
| 0 | 0 | 0 | 0 | 0 | 0 | 0 | 0 | 0 | 0 | 0 | 0 |
| 0.5 | 36.50 | 40.62 | 48.86 | 57.04 | 73.12 | 88.72 | 103.7 | 125.0 | 156.7 | 183.2 | 204.5 |
| 1.0 | 71.63 | 79.43 | 94.66 | 109.3 | 136.5 | 160.6 | 181.3 | 206.1 | 232.4 | 243.7 | 245.0 |
| 1.5 | 104.3 | 114.3 | 134.9 | 153.5 | 184.2 | 207.7 | 224.4 | 238.7 | 242.7 | 233.4 | 218.8 |
| 2.0 | 133.6 | 145.9 | 168.1 | 187.0 | 215.1 | 235.0 | 239.9 | 240.6 | 226.1 | 205.4 | 184.8 |
| 3 | 179.9 | 192.3 | 212.0 | 225.4 | 237.4 | 236.3 | 227.8 | 210.5 | 179.6 | 153.3 | 132.3 |
| 4 | 209.4 | 218.8 | 230.5 | 234.8 | 229.7 | 215.7 | 199.0 | 174.8 | 141.6 | 117.1 | 98.89 |
| 5 | 224.7 | 229.6 | 232.1 | 228.2 | 210.9 | 190.1 | 169.4 | 154.7 | 113.8 | 92.30 | 76.94 |
| 6 | 229.3 | 229.7 | 224.3 | 214.3 | 189.9 | 166.1 | 146.0 | 121.8 | 93.48 | 74.77 | 61.72 |
| 8 | 217.5 | 213.8 | 198.4 | 182.0 | 152.3 | 128.5 | 109.9 | 89.45 | 66.49 | 52.17 | 42.42 |
| 10 | 201.6 | 191.4 | 171.4 | 153.2 | 123.6 | 101.8 | 85.64 | 68.20 | 49.77 | 38.41 | 30.79 |
| 12 | 181.4 | 169.7 | 148.2 | 130.0 | 102.2 | 82.71 | 68.63 | 53.83 | 38.49 | 29.20 | 23.06 |
| 15 | 154.9 | 141.3 | 120.9 | 103.8 | 79.13 | 62.63 | 51.06 | 39.15 | 27.15 | 20.08 | 15.51 |
| 20 | 118.9 | 106.8 | 87.35 | 72.82 | 53.05 | 40.55 | 32.10 | 23.73 | 15.68 | 11.16 | 8.306 |
| 25 | 97.51 | 85.87 | 65.86 | 55.24 | 38.61 | 26.93 | 22.04 | 15.79 | 10.03 | 5.023 | 5.094 |
| 30 | 78.75 | 62.65 | 52.37 | 43.13 | 27.94 | 20.11 | 15.18 | 10.56 | 6.550 | 4.446 | 3.215 |
| 40 | 51.72 | 43.27 | 31.57 | 24.05 | 15.29 | 10.51 | 7.747 | 5.240 | 3.122 | 2.070 | 1.472 |
| 50 | 33.42 | 27.41 | 19.29 | 14.30 | 8.765 | 5.917 | 4.261 | 2.839 | 1.653 | 1.083 | .7639 |
| 60 | 21.22 | 17.06 | 11.73 | 8.550 | 5.121 | 3.404 | 2.429 | 1.596 | .9223 | .6001 | .4213 |
| 70 | 12.49 | 9.949 | 6.736 | 4.861 | 2.872 | 1.894 | 1.343 | .8770 | .5037 | .3265 | .2286 |
| 80 | 5.795 | 4.589 | 3.083 | 2.213 | 1.298 | .8517 | .6021 | .3920 | .2244 | .1452 | .1015 |
| 90 | 0 | 0 | 0 | 0 | 0 | 0 | 0 | 0 | 0 | 0 | 0 |

The relation (11) between the angle of electron scattering $\theta$ and of photon scattering $\phi$ is shown graphically in Fig. 2. Corresponding values of $\theta$ and $\phi$ have been plotted on a square root scale for photon energies of 0, 0.1, 0.2, 0.4,

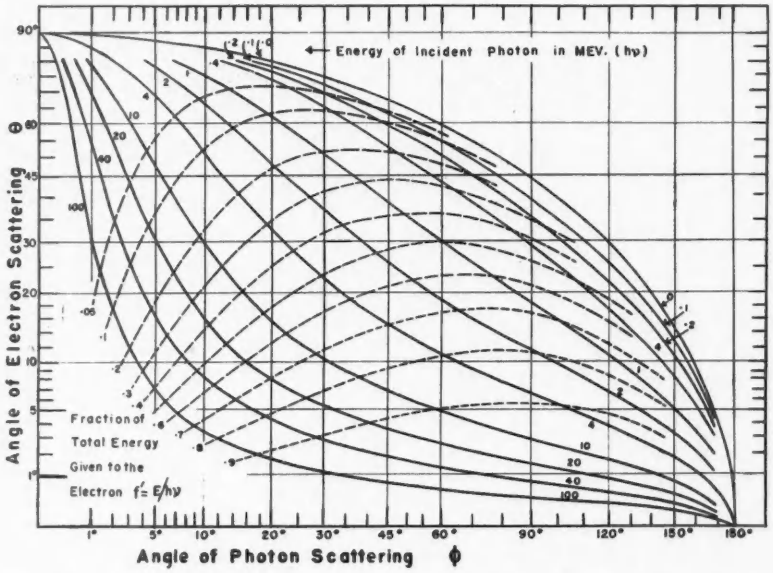


FIG. 2. Graph showing the relation between the angle of photon scattering $\phi$ and the angle of electron scattering $\theta$. The angles $\theta$ and $\phi$ have been plotted on a square root scale to expand the small angle region. The solid lines show the variation of $\theta$ with $\phi$ for constant values of the incident photon energy from 0 to 100 Mev. On the "cross-plot" the broken lines show $\theta$ as a function of $\phi$ for constant values of the quantity $f' = E/h\nu$ from 0.05 to 0.9. Thus the graphs relate the angles of photon and electron scattering, the energy of the incident photon, and the energy given to the scattered Compton electron. If any two of these quantities are given the remaining quantities can be found from the graph.

1, 2, 4, 10, 20, 40, and 100 Mev. The family of cross plot broken lines correspond to a constant fraction $f'$ of the total energy given to the electron. Curves have been plotted for $f' = .05, .1, .2, .3, .4, .5, .6, .7, .8$, and .9. By eliminating the energy parameter $\alpha$ from equations (4) and (11) the relation between $\theta$ and $\phi$ for constant values of $f' = \dfrac{\alpha \operatorname{vers} \phi}{1 + \alpha \operatorname{vers} \phi}$ can be shown to be

$$\cot \theta \sin \phi - \operatorname{vers} \phi = \frac{f'}{1 - f'}. \tag{15}$$

Fig. 2 may be used to relate the three variables $\theta$, $\phi$, and $f'$. For example, we see that for a 1 Mev. photon the electron is given 0.2 of the total energy (200 kev. of energy) when it is scattered at 53° and the photon which receives 800 kev.

of energy is scattered at about 30°. Each of the cross plot broken lines of Fig. 2 passes through $\phi = 180°$. At $\phi = 180°$ the curve is tangent to the member of the main set of curves for which $f' = 2\alpha/(1 + 2\alpha)$.

## DISTRIBUTION OF ELECTRONS PRODUCED BY $Co^{60}$ GAMMA RAYS

As an illustration of the use of Tables I, II, and III the energy and angular distributions of the electrons produced in water by primary $Co^{60}$ gamma rays have been determined. 50% of the $\gamma$ rays from $Co^{60}$ have an energy of 1.17 Mev. and the other 50% have an energy of 1.33 Mev. The differential cross sections $d\sigma(E)/dE$ and $d\sigma(\theta)/d\theta$ were found for these photon energies by interpolation between values from Tables II and III. Using the method of energy flux, the number of photons of each energy required to give a dose of 1 roentgen was found to be $7.85 \times 10^8$ photons per cm.[2] The number of electrons produced with energies in each energy interval was determined for the photon energies 1.17 and 1.33 Mev. using the $d\sigma(E)/dE$ values of Table II and they were added together to give the double peaked curve shown in Fig. 3. The angular distri-

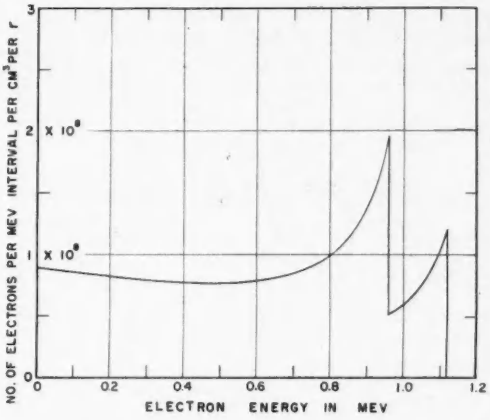


FIG. 3. Initial energy distribution of Compton electrons produced in water by 1 roentgen of $Co^{60}$ $\gamma$ rays. (1.17 and 1.33 Mev.).

bution of electrons from $Co^{60}$ was found in a similar way, but using the values of $d\sigma(\theta)/d\theta$ from Table III. This angular distribution is shown in Fig. 4.

It should be noted that the distributions given in Figs. 3 and 4 consider only electrons set in motion by the primary $Co^{60}$ $\gamma$ rays and disregard the effects of scattered radiation. It should be noted, also, that the energy distribution in Fig. 3 gives the energies with which electrons are projected from their point of origin in the water. It does not give the distribution of the energies which electrons possess at a point in the water. The difference between these energy distributions has been discussed by Cormack and Johns (1).

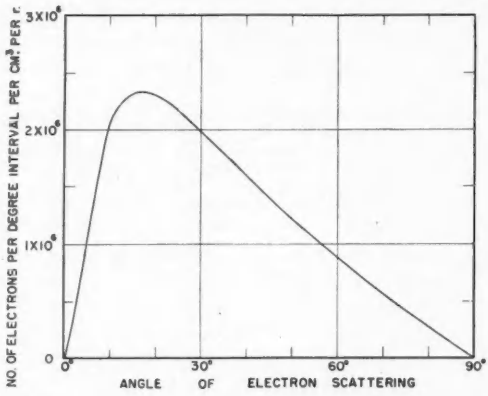


FIG. 4. Initial angular distribution of Compton electrons from $Co^{60}$ $\gamma$ rays.

## ACKNOWLEDGMENTS

The authors wish to express their thanks to the National Cancer Institute for financial assistance given to some of the authors (S.A.D., G.F.W.). One of the authors (D.V.C.) is the holder of a studentship from the National Research Council.

## REFERENCES

1. CORMACK, D. V. and JOHNS, H. E. Brit. J. Radiology, 25: 369. 1952.
2. DUMOND, J. M. and COHEN, E. R. Revs. Modern Phys. 20: 82. 1948.

# HIGH FREQUENCY GAS DISCHARGE BREAKDOWN IN NEON[1]

By A. D. MacDonald and D. D. Betts[2]

ABSTRACT

Electrical breakdown of neon at high frequencies has been treated theoretically on the basis of the Boltzmann transport equation. Exciting and ionizing collisions are accounted for as energy loss terms in the Boltzmann equation and measured values of the ionization efficiency are used in the integral determining the ionization rate. Electrons are lost to the discharge by diffusion. The equations are treated separately for the cases in which the collision frequency is much less than or much greater than the radian frequency of the applied field. The electron energy distribution functions are expressed in terms of Bessel functions, confluent hypergeometric functions, and simple exponentials. The ionization rate and the diffusion coefficient are calculated using these distribution functions in kinetic theory formulas, and combined with the diffusion equation to predict breakdown fields. The theoretically predicted fields are compared with experiment at 3000 Mc. per sec. The breakdown equations, calculated from kinetic theory and using no gas discharge data other than collision cross sections, predict breakdown electric fields within the limits of accuracy determined by these cross sections over a large range of experimental variables.

Phenomena in gas discharges excited by microwave electric fields have been studied extensively in recent years (1, 6, 7, 8, 15). The relative simplicity of the high frequency discharge has permitted theory to predict accurately the breakdown electric field (at which the gas becomes conducting and starts to glow), for helium and hydrogen (11, 12). The breakdown condition is that the number of electrons produced by ionization equals the number diffusing to the walls of the container. It is necessary to know the electron energy distribution function in order to calculate theoretically the rates of ionization and diffusion.

This distribution function is derived as a solution of the Boltzmann transport equation for electrons, and a knowledge of it permits calculation of all properties of the discharge. Helium and hydrogen have elastic collision cross sections for electrons which vary with electron energy such that the ratio of velocity to mean free path, i.e. the collision frequency, is practically constant. This property simplifies considerably the mathematical problem of finding the distribution function. In neon the elastic collision cross section does not vary in the same manner, but to a sufficient degree of approximation the mean free path is the same for all energies (2) and it is this approximation which will be used in this paper. The distribution functions are determined from the appropriate differential equations. From these functions are calculated ionization rates and diffusion coefficients which are combined in an equation which predicts breakdown.

## I. THE BOLTZMANN EQUATION

The derivation of the differential equation for the distribution function presented here is similar to that in Reference 12 but is included because of the difference caused by a different variation of mean free path with electron energy.

[1] *Manuscript received May 5, 1952.*
*Contribution of the Physics Department, Dalhousie University, Halifax, N.S.*
[2] *Holder of Studentship under National Research Council, 1951-52.*

The phase space continuity equation for electrons is (4, 14, 17)

$$C = \frac{\partial f}{\partial t} + \mathbf{v}\cdot\nabla f + \mathbf{a}\cdot\nabla_v f \tag{1}$$

where $f$ is the electron velocity distribution function; $C$ is the net rate at which electrons appear in an element of phase space and is calculated in terms of $f$ by determining velocity changes produced by collisions; $v$ is the velocity; $a$ the acceleration; $t$ the time; and $\nabla_v$ the gradient operator in velocity space.

The distribution function may be expanded in spherical harmonics in velocity

$$f = f_0 + \frac{\mathbf{v}\cdot\mathbf{f}_1}{v} + \ldots . \tag{2}$$

The spherically symmetric term is predominant because collisions tend to disorder any directional motion of the electrons. The series is rapidly convergent and we shall consider only those cases where the first two terms represent a good approximation to the actual distribution function. A consideration of the values of the experimental parameters for which such a theory is valid has been given, with special reference to hydrogen (3). The extension of these results to neon is straightforward.

The term $C$ arising from collisions may also be expanded in spherical harmonics, since it may be represented in terms of integrals over the distribution function. The r.m.s. value of the electric field is $\mathbf{E}$, and a variable of the units of voltage, $u = mv^2/2e$, is introduced; $m$ being the mass and $e$ the charge of the electron. Equation (1) becomes, on substitution of these terms and separation of the vector and scalar parts,

$$C_0 = \frac{\partial f_0}{\partial t} - \frac{v}{3u}\frac{\partial}{\partial u}(u\mathbf{E}\cdot\mathbf{f}_1) + \frac{v}{3}\nabla\cdot\mathbf{f}_1 \tag{3}$$

and

$$\mathbf{C}_1 = \frac{\partial \mathbf{f}_1}{\partial t} + v\nabla f_0 - v\mathbf{E}\frac{\partial f_0}{\partial u}. \tag{4}$$

It has been shown by Morse, Allis, and Lamar (17) that elastic collisions may be accounted for in the differential equations as energy loss terms which may be included in the $C$'s. They have shown that

$$C_{0,\,\mathrm{el}} = \frac{2m}{M}\frac{v}{u}\frac{d}{du}\left(\frac{u^2 f_0}{l}\right), \tag{5}$$

$$\mathbf{C}_{1,\,\mathrm{el}} = -\frac{v}{l}\mathbf{f}_1 \tag{6}$$

where $l$ is the electronic mean free path and $M$ is the mass of the molecule. The remainder of the $C_0$ term results from inelastic collisions and may be represented by $-(h_x + h_i)\frac{v}{l}f_0$ where $h_x$ and $h_i$ are efficiencies of excitation and ionization respectively. Inelastic collisions have no angular dependence and therefore do not enter the higher order terms in the distribution function.

Each term in the distribution function may be expanded in a Fourier series in time

$$f_n = f_n^0 + f_n^1 e^{j\omega t} + \dots \tag{7}$$

where $\omega$ is the radian frequency of the applied electric field.

The electric field may be written $\sqrt{2}\, E\, e^{j\omega t}$ and in the expansion of $E f_n$ we must replace the exponential notation by its real part before taking the product, so that

$$\sqrt{2} E f_n = 2 E f_n^0 e^{j\omega t} + E f_n^1 (1 + 2e^{2j\omega t}) + \dots . \tag{8}$$

Combining the results of Equations (5), (6), and (8) with Equations (3) and (4), and equating terms in like exponents of $t$, we have

$$-(h_x + h_t)\frac{v}{l} f_0^0 = \frac{v}{3}\nabla \cdot \mathbf{f}_1^0 - \frac{v\mathbf{E}}{3u}\cdot\frac{\partial}{\partial u}(u\mathbf{f}_1^1) - 2\frac{mv}{Mu}\frac{\partial}{\partial u}\left(\frac{u^2 f_0^0}{l}\right), \tag{9}$$

$$\mathbf{f}_1^0 = -l\nabla f_0^0, \tag{10}$$

$$\left(\frac{v}{l} + j\omega\right)\mathbf{f}_1^1 = v\mathbf{E}\frac{\partial f_0^0}{\partial u}. \tag{11}$$

The $f_0^1$ term has been dropped in this derivation because it represents the first harmonic of the spherically symmetric part of the distribution function and cannot be generated physically unless there is either a d-c. field or the amplitude of oscillation of the electric field is sufficient to sweep out electrons from the container each half cycle.

Equations (10) and (11) may be substituted in Equation (9) to derive an equation for $f_0^0$. From this point on we shall be concerned only with the $f_0^0$ term and shall drop the subscript and superscript; understanding by $f$ the zero order term $f_0^0$. We may use the diffusion equation to replace the Laplacian of $f$ by $-f/\Lambda^2$, where $\Lambda$ is the characteristic diffusion length depending only on the geometry of the container (6) and defined in the case in which we are at present interested, a cylinder of radius $R$ and length $L$, by the equation

$$1/\Lambda^2 = (\pi/L)^2 + (2.405/R)^2. \tag{12}$$

On making these substitutions we arrive at the energy balance equation which must be solved to find the distribution function

$$-(h_x + h_t)f + \frac{2m}{Mu}\frac{d}{du}(u^2 f) = \frac{l^2}{3\Lambda^2} f - \frac{E^2 l^2}{3u}\frac{d}{du}\left\{\frac{u(v/l)^2}{[(v/l)^2 + \omega^2]}\frac{df}{du}\right\}. \tag{13}$$

Dependence on the space variables having been eliminated by use of the diffusion equation, the distribution function is now a function of $u$ only so that the partial differentials become total differentials in Equation (13).

## II. DISTRIBUTION FUNCTIONS: LOW $p\Lambda$

Inspection of Brode's data (2) indicates that the mean free path of electrons in neon is approximately constant for all energies above 3 or 4 ev. and that it may be represented by $l = 1/10p$ if $p$ is the pressure in mm. of Hg and $l$ is the

mean free path in cm. The effect of the deviation below 4 ev. from our approximation will be considered later. We shall study separately the cases where $(v/l)^2$ is much less than or much greater than $\omega^2$ and neglect the appropriate term in Equation (13) in each case.

If $(v/l)^2 \ll \omega^2$, which corresponds approximately to $p\lambda \ll 130$, if $\lambda$ is the free space wave length of the electric field in cm., then Equation (13) becomes

$$(14)\quad \frac{2e}{3m}\left(\frac{E}{\omega}\right)^2 u\frac{d^2f}{du^2} + \left[\frac{4e}{3m}\left(\frac{E}{\omega}\right)^2 + \frac{2mu}{M}\right]\frac{df}{du} + \left[\frac{4m}{M} - \frac{l^2}{3\Lambda^2}\right]f = (h_x + h_i)f.$$

Inspection shows that for frequencies up to many times those used in the present work the term $2mu/M$ is insignificant as compared to the other part of the $df/du$ term and it is therefore dropped at this point.

We introduce a new independent variable through the relation

$$(15)\quad w = \int_0^u \frac{3m}{M}\frac{du}{u_c},$$

where

$$u_c = \frac{e}{m}\frac{E^2}{(\omega^2 + (v/l)^2)}$$

is the average energy an electron gains between collisions. The variable is transformed in this manner because the one relation between $u$ and $w$ is suitable for both the high $p\lambda$ and the low $p\lambda$ approximations. It should also be noted that $w$ as defined above is the exponent in the Margenau distribution (14).

For low $p\lambda$, $u_c$, the average energy in units of voltage gained between collisions, is equal to $eE^2/m\omega^2$, or twice the energy of oscillatory motion of a free electron. Therefore, the relationship between $u$ and $w$ becomes

$$w = \frac{3m}{M}\frac{m}{e}\left(\frac{\omega}{E}\right)^2 u.$$

The differential equation may then be written

$$(16)\quad \frac{2m}{M}\left(w\frac{d^2f}{dw^2} + 2\frac{df}{dw}\right) - \left(\frac{2}{3}\frac{l^2}{\Lambda^2} - 8\frac{m}{M}\right)f = (h_x + h_i)f.$$

The terms multiplying $f$ in this equation represent the energy loss mechanisms since the $\frac{l^2}{3\Lambda^2}u$ is the diffusion loss per collision, $\frac{2m}{M}u$ is the recoil loss per collision, and $(h_x + h_i)u$ is the inelastic collision loss.

For $u < u_x$, $u_x$ being the lowest excitation potential, $h_x + h_i$ is zero. If we now let

$$x = \left(\frac{2M}{3m}\frac{l^2}{\Lambda^2} - 8\right)w,$$

$x$ is a dimensionless variable and Equation (16) is transformed to

$$\frac{1}{x}\frac{d}{dx}\left(x^2\frac{df}{dx}\right) - \frac{f}{4} = 0$$

the solution of which is

$$f = \frac{1}{\sqrt{x}}[K_1(\sqrt{x}) + C\, I_1(\sqrt{x})] \tag{17}$$

where $K_1$ and $I_1$ are first order Bessel functions of imaginary argument, following the notation of Watson (19).

When $u > u_x$ we use the value of $(h_x + h_i)$ as measured by Maier-Leibnitz (13), using a linear approximation and setting

$$h_x + h_i = h_{x0}(u - u_{x0})$$

where

$$h_{x0} = 5.6\ 10^{-3}(\text{volts})^{-1} \text{ and } u_{x0} = 16.0 \text{ volts.}$$

The differential equation (16) then becomes

$$w\frac{d^2f}{dw^2} + 2\frac{df}{dw} - \frac{1}{4}\left(\frac{2M}{3m}\frac{l^2}{\Lambda^2} - 8\right)f - \frac{M}{2m}[h_{x0}(u - u_{x0})]f = 0$$

which may be transformed by use of the dimensionless variable

$$y = u\left(\frac{m\omega}{ME}\right)\sqrt{\frac{6m}{e\,h_{0x}}}$$

to

$$y\frac{d^2f}{dy^2} + 2\frac{df}{dy} - f(y - \beta) = 0 \tag{18}$$

where

$$\beta = \frac{\omega}{E}u_{0x}\sqrt{\frac{3h_{0x}m}{2e}}\left\{1 - \frac{1}{h_{0x}u_{0x}}\left(\frac{l^2}{3\Lambda^2} - 4\frac{m}{M}\right)\right\}.$$

The above equation may be solved exactly in terms of the confluent hypergeometric equation (9). However a relatively simple approximation is permissible for the experimental conditions usually encountered in microwave discharges and since the breakdown fields predicted by the approximate method are not greatly different to those predicted by the exact solution, the approximation will be given here.

Because $\beta$ is somewhat smaller than $y$ for most values of the variables a logical first approximation is $f = e^{-y}/y$. We multiply this by $(1 + Dy)$ and adjust $D$ to give an exact solution at the ionization potential. The distribution function is then given by

$$f = Ae^{-y}\left(\frac{1}{y} + \frac{D}{y^2}\right) \qquad u > u_x \tag{19}$$

where $D = -\dfrac{\beta y_i^2}{(3+\beta)y_i + 4}$, the term in $D$ constituting a small correction to the main part of the distribution function.

Equations (17) and (19) then give the distribution function, the two constants of integration $A$ and $C$ being determined by equating the distribution functions

in value and in slope at the excitation potential. This procedure gives for the constants

$$(20)\qquad \begin{cases} C = \dfrac{K_2(\sqrt{x}) - \phi K_1(\sqrt{x})}{I_2(\sqrt{x}) + \phi I_1(\sqrt{x})}, \\ A = \dfrac{K_1(\sqrt{x}) + CI_1(\sqrt{x})}{\sqrt{x}e^{-y}(1/y + D/y^2)} \end{cases} \qquad u = u_x$$

where

$$\phi = \frac{2r\sqrt{x}}{s}\,\frac{[y^2 + (1+D)y + 2D]}{Dy + y^2},\ y = ru, \text{ and } x = su.$$

We must now compute the ionization rate and the diffusion coefficient using these distribution functions. The ionization rate is given by (11)

$$(21)\qquad n\nu_i = 8\pi\frac{e^2}{m^2}\int_{u_i}^{\infty}\frac{u}{l}h_i f\,du$$

where $h_i$ is the ionization efficiency and may be written from Maier-Leibnitz' data

$$h_i = h_{i0}(u - u_{i0}) = 4.48\,10^{-3}(u - 21.5).$$

On substituting this value along with the distribution function of Equation (19) in Equation (21), and carrying out the simple integrations, we have

$$(22)\qquad n\nu_i = 8\pi\frac{e^2}{m^2}\frac{h_{i0}}{r^3 l}\{e^{-y_i}(1+D) + Dy_i\mathrm{Ei}(-y_i)\}$$

where $\mathrm{Ei}(-y_i)$ is the exponential integral $\int_{y_i}^{\infty} e^{-t}/t\,dt$, tables of which are available in Jahnke and Emde. The diffusion coefficient is given by a similar integral (11)

$$nD = \frac{8\pi l e^2}{3m^2}\int_0^{\infty} uf\,du$$

$$(23)\qquad = \frac{8\pi l e^2}{3s^2m^2}\left[\int_0^{x_x}\sqrt{x}\,Z_1(x)\,dx + A\frac{s^2}{r^2}\int_{y_x}^{\infty}e^{-y}(1+Dy)\,dy\right]$$

where

$$Z_1(x) = K_1(\sqrt{x}) + C\,I_1(\sqrt{x}).$$

The integration of Equation (23) yields

$$(24)\quad nD = \frac{8\pi l e^2}{3s^2m^2}\{2x_x[CI_0(x) - K_0(x)] - 4\sqrt{x_x}\,Z_1(x_x) + 4 + \frac{s^2}{r^2}A\,[e^{-y_x} - D\,\mathrm{Ei}(-y_x)]\}.$$

The breakdown condition may be stated as follows, $\nu/D = 1/\Lambda^2$ (6, 11), so that setting $1/\Lambda^2$ equal to the ratio of Equations (22) and (24) gives us an equation from which breakdown fields may be calculated

$$(25)\quad \frac{\nu}{D} = \frac{1}{\Lambda^2} = \frac{3s^2}{r^3 l^2}\,\frac{A\,h_{i0}[e^{-y_i}(1+D) + D\,y_i\mathrm{Ei}(-y_i)]}{\{2x_x[CI_0(x) - K_0(x)] - 4\sqrt{x_x}\,Z_1(x_x) + 4 + A\,(s^2/r^2)[e^{-y_x} - D\,\mathrm{Ei}(-y_x)]\}}.$$

At this point we list the variables entering Equation (25) in terms of the experimental parameters

$$h_{i0} = 4.48\ 10^{-3}, \qquad l = 1/10p,$$

$$x = us = u\left(1 - \frac{(p\Lambda)^2}{30.8}\right)\left(\frac{636}{E\Lambda p\lambda}\right)^2,$$

$$y = ur = u\,\frac{412}{E\lambda},$$

$$D = -\frac{\beta y_i^{\,2}}{(3+\beta)y_i + 4} \quad \text{where } \beta = \frac{412}{E\lambda}\left[16 - \frac{0.595}{(p\Lambda)^2}\right].$$

## III. DISTRIBUTION FUNCTIONS: HIGH $p\lambda$

When $p\lambda$ is so high that $(v/l)^2 \gg \omega^2$ the differential equation for the distribution function becomes

$$\frac{1}{u}\frac{d}{du}\left(u\frac{df}{du}\right) + \frac{6m}{M\,E^2l^2u}\frac{d}{du}(u^2f) - f\left[\frac{1}{E^2\Lambda^2} + \frac{3}{E^2l^2}(h_x + h_i)\right] = 0.$$

We must first consider the case where $u < u_x$, so that the excitation and ionization terms are zero. We again introduce the variable $w$ as defined in Equation (15), i.e.,

$$w = \int_0^u \frac{3m}{M}\frac{du}{u_c}.$$

Because for high $p\lambda$ the electron suffers many collisions per oscillation of the electric field, the energy gained between collisions, $u_c$, is determined by the collision frequency and is equal to $eE^2l^2/mv^2$ or $E^2l^2/2u$. To prevent confusion with the earlier form of $w$ we shall let the form used in this case be denoted by $z$ from this point. Thus the dimensionless variable $z$ is defined for this case by

$$z = \frac{\mu u^2}{2}, \text{ where } \mu = \frac{6m}{M}\frac{1}{E^2l^2}.$$

In terms of this variable the equation may be written

$$z\frac{d^2f}{dz^2} + (1+z)\frac{df}{dz} + (1-\delta)f = 0 \tag{26}$$

where

$$\delta = \frac{M}{12m}\frac{l^2}{\Lambda^2}.$$

The solution of Equation (26) is

$$f = e^{-z}[M(\delta;1;z) + F\,W(\delta;1;z)] \tag{27}$$

where $M(\delta;1;z)$ and $W(\delta;1;z)$ are two solutions of the confluent hypergeometric equation, properties and tables of which are available (9, 10). It is interesting to note that the predominant term in the distribution is an exponential in the square of the electron energy, in view of the results of Margenau and his coworkers (5, 15) who also obtained distribution functions in which the principal variable was the square of the energy, in cases where the mean free path was

constant. Margenau's work differed from that reported here in that he assumed a different electron removal mechanism.

When $u > u_x$ the differential equation is altered by the inclusion of the inelastic collision term. Experimental values of $h_x + h_i$ are such that it is difficult to discriminate between several possible analytic forms so we may use

$$h_x + h_i = h_{x0}(u^2 - u_{x0}^2) = 1.40\ 10^{-4}(u^2 - 16^2).$$

Substituting this relation in Equation (25) and again transforming the independent variable to $z$, we have

$$z\frac{d^2f}{dz^2} + (1+z)\frac{df}{dz} + \left(\frac{\sigma}{2\mu} - \frac{\rho z}{\mu^2}\right)f = 0 \tag{28}$$

where

$$\sigma = \frac{3}{E^2 l^2}\left[h_{0x}u_{0x}^2 + \frac{4m}{M}(1-\delta)\right]$$

and

$$\rho = \frac{3}{E^2 l^2}h_{x0}.$$

If we now let $f = e^{-\sigma z/2\mu}g$, the equation for $g$ is

$$z\frac{d^2g}{dz^2} + \left[1 - z\left(\frac{\sigma}{\mu} - 1\right)\right]\frac{dg}{dz} + z\left(\frac{\sigma^2}{4\mu^2} - \frac{\sigma}{2\mu} - \frac{\rho}{\mu^2}\right)g = 0. \tag{29}$$

Inspection of the terms shows that for all cases of practical interest in the high frequency region the term 1 in the coefficient of $dg/dz$ is insignificant in comparison with the other term. On dropping the 1, $g$ is easily seen to be a simple exponential with the two possible solutions having positive and negative exponents. Because the physics of the problem dictates a finite value for large $z$ we choose the exponentially decaying solution. Combining this with the relation between $f$ and $g$ we have

$$f = B\,e^{-az} \tag{30}$$

where

$$a = \tfrac{1}{2}(1 + \sqrt{1 + 4\rho/\mu^2}).$$

Thus the values of the distribution functions are given by

$$f = e^{-z}[M_1(z) + F\,W_1(z)] \qquad u < u_x$$

$$= B\,e^{-az} \qquad u > u_x$$

where we use the notation $M_1(z)$ for the confluent hypergeometric function $M(\delta; 1; z)$, with a similar notation for the second solution.

The values of the constants $B$ and $F$ are again determined by equating the values and first derivatives of the function at $u = u_x$; which procedure yields

$$(31)\qquad \begin{cases} F = -\dfrac{\dfrac{d}{dz}M_1(z) + (a-1)\,M_1(z)}{\dfrac{d}{dz}W_1(z) + (a-1)\,W_1(z)}, \\ B = e^{(a-1)z}[M_1(z) + F\,W_1(z)]. \end{cases} \qquad z = z_z$$

The definition of the ionization rate of Equation (20) gives us

$$n\nu_i = 16\pi\frac{e^2}{m^2\mu^2 l}\,Bh_{i0}\int_{z_i}^{\infty} e^{-az}(z - z_{i0})\,dz$$

$$(32)_i \qquad = \frac{16\pi e^2}{m^2\mu^2 a^2 l}\,Bh_{i0}\,e^{-az_i}.$$

Similarly

$$nD = \frac{8\pi}{3}\frac{e^2 l}{m^2\mu}\int_0^{\infty} f\,dz$$

$$(33)\qquad = \frac{8\pi}{3}\frac{e^2}{m^2}\left[\int_0^{z_z} e^{-z}[M_1(z) + F\,W_1(z)]\,dz + B\int_{z_z}^{\infty} e^{-az}\,dz\right].$$

The integration of Equation (33) is accomplished by making use of the indefinite integral (9)

$$\int e^{-z}M(a;\gamma;z)\,dz = \frac{e^{-z}}{(a-\gamma+1)}\left\{z\frac{a}{\gamma}M(a+1;\gamma+1;z) + (\gamma-1)\,M(a;\gamma;z)\right\}.$$

If now we write $M_2(z_z)$ for $M(\delta+1;\,2;\,z_z)$, the integral is

$$(34)\qquad nD = \frac{8\pi e^2 l}{3m^2\mu}\left\{z_z e^{-z_z}[M_2(z_z) + F\,W_2(z_z)] - \frac{F}{\delta} + \frac{B}{a}e^{-az_z}\right\}.$$

Combining the results of Equations (32) and (34) with the breakdown condition we arrive at an implicit expression for the breakdown field

$$(35)\qquad 1/\Lambda^2 = \frac{6B}{a^2\mu l^2}\,h_{i0}\,\frac{e^{-az_i}}{[z_z e^{-z_z}[M_2(z_z) + F\,W_2(z_z)] - F/\delta + (B/a)e^{-az_z}]}.$$

For convenience we collect at this point the meanings of the symbols in Equation (35) in terms of the experimental parameters

$$h_{i0} = 0.90\,10^{-4}, \qquad \mu = 1.62\left(\frac{p}{10E}\right)^2,$$

$$z = u^2\left(\frac{p}{E}\right)^2/123.4, \qquad \delta = \frac{30.8}{(p\Lambda)^2},$$

$$\rho = 4.2\left(\frac{p}{10E}\right)^2, \qquad a = \tfrac{1}{2}(1 + \sqrt{1 + 4\rho/\mu^2}).$$

$F$ and $B$ are defined in terms of these in Equation (31).

Equations (25) and (35) are implicit expressions for the breakdown electric field as a function of pressure, container size, and frequency of applied field. The breakdown fields are computed in practice by successive approximations.

## IV. CORRECTION FOR COLLISION CROSS-SECTION APPROXIMATION

The collision cross section is smaller than that used in the theory when the electron energy is less than 4 ev. The effect of the different cross section is most important at high pressure because when the pressure is high there is a relatively large number of low energy electrons. The breakdown field has been computed considering the cross section below 4 ev. to be different to that above by a factor somewhat greater than Brode's data indicates. The computed breakdown field does not differ at most by more than 2% from the uncorrected field. This indicates that the effect on breakdown of the electrons whose energy is below 4 ev. is in general very small, as was found to be the case in helium (11). Because, in all cases considered, the error introduced by neglecting this discrepancy below 4 ev. energy is smaller than other errors, correction has not been made in the breakdown curves.

## V. EXPERIMENTAL RESULTS

The experimental apparatus used in measuring the breakdown electric fields is similar to that used in previous measurements (11, 12). A schematic diagram of the equipment is shown in Fig. 1. Microwave power at a frequency of approxi-

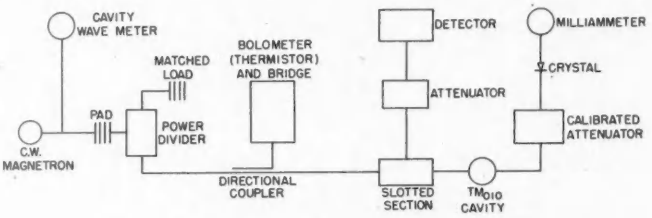


FIG. 1. Block diagram of the microwave equipment used.

mately 3000 Mc. generated by a CW magnetron is coupled to a resonant cavity by coaxial transmission lines. A known fraction of the power delivered is measured by a bolometer. The power absorbed by the cavity is combined with the cavity $Q$ and the known field configuration to determine the electric field by

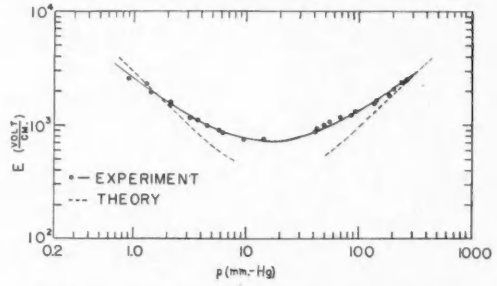


FIG. 2. Comparison of measured breakdown fields in neon with theory. The frequency of the electric field is 2810 Mc. and the characteristic diffusion length, $\Lambda$, is 0.101 cm.

standard methods (16, 18). The cavities in which breakdown takes place are made of oxygen-free high conductivity copper and connected through Kovar to an all glass vacuum system. The vacuum system holds at a pressure of less than $10^{-6}$ mm. of Hg with the pumps shut off for a period longer than that

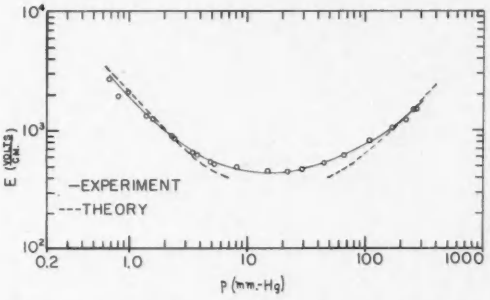


FIG. 3. Comparison of measured breakdown fields in neon with theory. The frequency of the electric field is 2810 Mc. and the characteristic diffusion length, $\Lambda$, is 0.202 cm.

necessary to make a series of measurements. Air Reduction Company spectroscopically pure neon was used. Measurements were made in cylindrical cavities having heights of 0.3172 and 0.6344 cm., the radius being such that the resonant frequency corresponded to a free space wave length of 10.7 cm. The experimental data are presented in Figs. 2 and 3, which give breakdown electric field as a function of pressure. On the figures are also shown the theoretical breakdown fields as calculated from Equations (24) and (35).

## VI. SUMMARY

High frequency breakdown electric fields have been derived theoretically by kinetic theory using measured values of the collision cross sections of neon. The idealization of these cross sections as simple functions of electron energy combines with the experimental error to introduce uncertainty into the theory, although the percentage error introduced in the electric fields is not as high as that in the quantities themselves. The elastic collision cross section used in this theory is probably correct to about 15% introducing errors of approximately 10% in breakdown fields. The measurement of excitation and ionization efficiencies is extremely difficult and laborious, and errors may be of the order of 15% introducing possibly 10% in the field. This indicates the need for more accurate collision cross-section data. The maximum error in the measured electric field is 5%; relative field measurements are however much more accurate than this. The error in the pressure measurement is less than 1%.

Comparison of theory and experiment shows that Equations (25) and (35) predict the breakdown fields in their ranges of validity. In the theory it was assumed in one case that the collision frequency was much higher than the radian frequency of the field and in the other case that it was much smaller. In the intermediate region it is possible to use an average value of the smaller term in

the relation below $w$ and $u$, instead of neglecting it entirely, and thus to extend the ranges of validity somewhat. This has been done in the calculations.

## ACKNOWLEDGMENTS

The authors wish to express their thanks to the Defence Research Board of Canada for a grant-in-aid which made this research possible. The stimulating and helpful discussions with Professors W. P. Allis and S. C. Brown of the Massachusetts Institute of Technology are gratefully acknowledged.

## REFERENCES

1. Biondi, M. A. and Brown, S. C. Phys. Rev. 75: 1700. 1949.
2. Brode, R. B. Revs. Modern Phys. 5: 257. 1933.
3. Brown, S. C. and MacDonald, A. D. Phys. Rev. 76: 1629. 1949.
4. Chapman, S. and Cowling, T. G. The mathematical theory of non-uniform gases. Cambridge University Press, London. 1939.
5. Hartmann, L. M. Phys. Rev. 73: 316. 1948.
6. Herlin, M. A. and Brown, S. C. Phys. Rev. 74: 291. 1948.
7. Herlin, M. A. and Brown, S. C. Phys. Rev. 74: 1650. 1948.
8. Holstein, T. Phys. Rev. 70: 367. 1946.
9. MacDonald, A. D. J. Math. Phys. 28: 183. 1949.
10. MacDonald, A. D. Can. J. Research, A, 28: 175. 1950.
11. MacDonald, A. D. and Brown, S. C. Phys. Rev. 75: 411. 1949.
12. MacDonald, A. D. and Brown, S. C. Phys. Rev. 76: 1634. 1949.
13. Maier-Leibnitz, H. Z. Physik, 95: 499. 1935.
14. Margenau, H. Phys. Rev. 69: 508. 1946.
15. Margenau, H. Phys. Rev. 73: 303. 1948.
16. Montgomery, C. G. Microwave techniques. McGraw-Hill Book Company, Inc., New York. 1948.
17. Morse, P. M., Allis, W. P., and Lamar, E. S. Phys. Rev. 48: 412. 1935.
18. Rose, D. J., Kerr, D. E., Biondi, M. A., Everhart, E., and Brown, S. C. Mass. Inst. Technol., Research Lab. Electronics, Tech. Rept. 140. 1950.
19. Watson, G. N. Theory of Bessel functions. Cambridge University Press, London. 1922.

# RAMAN SPECTROSCOPY OF LOW PRESSURE GASES AND VAPORS[1]

By H. L. Welsh, M. F. Crawford, T. R. Thomas,[2] and G. R. Love[3]


## ABSTRACT

Raman spectra of gases and vapors at pressures of a few atmospheres were obtained with a carefully diaphragmed Raman tube of large volume, irradiated by five high intensity mercury lamps with water-cooled electrodes. Frequencies and intensity contours of 32 of the 35 fundamental bands of $CH_4$, $CH_3Cl$, $CH_2Cl_2$, $CHCl_3$, $CCl_4$, and $CH_3Br$ were measured. Vibrational assignments, based on the intensity contours of the bands, showed no discrepancies in previous assignments. The integrated intensities of the bands, determined on the same intensity scale for all compounds of the series, show the inadequacy of the bond polarizability theory of Raman intensities. Depolarization factors, calculated from the intensity distribution in totally symmetric bands, are somewhat greater than those measured for the liquid. Asymmetries in the $Q$ branches of some totally symmetric bands are explained quantitatively in terms of anharmonicity and isotope effect.


## INTRODUCTION

Since its discovery the Raman effect has been used, with only few exceptions, in the study of substances in the condensed phases. The lack of systematic investigations on compounds in the gaseous state is due to the experimental difficulties in obtaining satisfactory Raman spectograms when the density of the scattering substance is low. Nevertheless, it is important to study the spectra of gases at low pressures, since the present theories of molecular structure and of Raman scattering are strictly applicable only to molecules which are free from the perturbing influence of neighboring molecules. In addition, the comparison of the Raman spectra of a substance in the gaseous and the condensed phase can lead to some understanding of the effect of intermolecular forces on the vibration and rotation of molecules.

With the experimental methods developed in the present investigation reasonably complete Raman spectra can be obtained for gases at pressures of a few atmospheres. Special attention was directed to the accurate measurement of intensities since intensity data are important in the development of molecular spectroscopy. The relative integrated intensities of the bands of a given molecule and of chemically related molecules furnish data for testing theories of Raman intensities. Also, the contours of the bands of freely rotating molecules are probably better criteria for the assignment of vibrational frequencies than the frequently used depolarization factors.

## EXPERIMENTAL METHODS

Since the density of a gas at a pressure of a few atmospheres is lower than the liquid density by two or three orders of magnitude, the Raman scattering of the gas is very weak compared with that of an equal volume of liquid. This reduction

[1] *Manuscript received May 16, 1952.*
*Contribution from the McLennan Laboratory, University of Toronto, Toronto, Ontario.*
[2] *Holder of Scholarships under the National Research Council of Canada, 1946-49. Present address: Taymouth Industries, Toronto 16, Ontario.*
[3] *Holder of Scholarships under the National Research Council of Canada, 1946-48. Present address: Carleton College, Ottawa, Ontario.*

in scattered intensity must be counterbalanced by increasing the volume of the scattering medium and by increasing the radiation density of the exciting light. In addition, the intensity of the stray light entering the spectrograph must be kept low relative to the Raman intensity by careful design of the Raman tube, if satisfactory spectra are to be obtained.

The Raman tube shown in Fig. 1 is made of standard wall Pyrex tubing, 35 mm. in internal diameter, and can withstand gas pressures of at least 10 atmospheres. The illuminated portion, 60 cm. long, is separated from the window

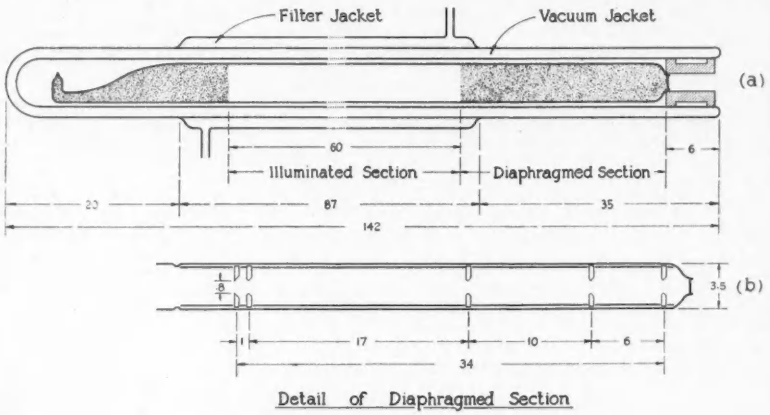


FIG. 1. Raman tube for low pressure gases.

by a diaphragmed section, and is terminated in a cone which serves as a light trap. The diaphragms, made of opaque black glass, have apertures 8 mm. in diameter with sharply beveled edges to minimize reflections. A condensing lens forms an image of the slit of the spectrograph at and within the aperture of the back diaphragm, and an image of the collimator lens at and within the diaphragm nearest the window.

The tube is placed inside a vacuum flask, 1.4 meters long, open at the window end. The temperature is controlled by a heating coil of chromel wire wound in an open coil on the tube, and is measured by thermocouples placed at five points along the tube. At an average temperature of 150°C. the greatest variation along the tube is about 8°C. A jacket, 1 cm. thick and completely covering the illuminated section of the Raman tube, is fused to the outer wall of the vacuum flask. Either water or a filter solution circulated through this jacket at a constant temperature eliminates the thermal exchange between the lamps and the Raman tube. A solution of sodium nitrite is used to isolate Hg4358A radiation from the higher frequencies in the mercury spectrum. A thickness of 1 cm. of this solution saturated at 25°C. transmits 90% of Hg4358A, but only 5% of Hg4078A and 1% of Hg4047A. For some spectra the faint mercury lines in the region of 5000A were removed by saturating the sodium nitrite solution with rhodamine-B.

It was found that cooling the electrodes of a low pressure mercury lamp permits the current, and hence the intensity, to be increased several-fold without a large increase in vapor density. Cooling is effected by circulating water through a finger which projects through the mercury pool into the vapor phase above (Fig. 2). The intensity of Hg4358A increases linearly with current up to at least 15 amperes, the normal operating current. In addition to the increased intensity this lamp has other desirable characteristics. There is no appreciable broadening of the spectral lines, since the hyperfine structures are resolvable. The ratio of line intensities to the intensity of the continuous background is higher than for uncooled lamps. The lamp is very stable in operation, and the intensity of Hg4358A is not noticeably reduced over a period of 1000 hr. The lamp is started by heating with a bunsen burner and applying a high voltage between two starting electrodes. Five lamps of the design shown in Fig. 2 were used with

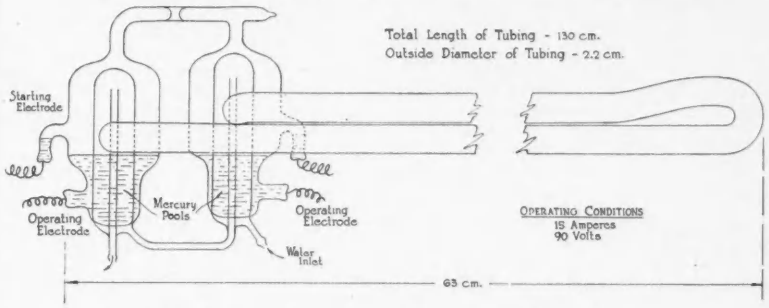


FIG. 2. High-current mercury arc with water-cooled electrodes.

the Raman tube for gases and gave a total length of discharge of about six meters. They were arranged symmetrically about the tube; thus, the transmission of the spectrograph was the same for both the isotropic and the anisotropic parts of the scattered light since both were unpolarized.

The Raman spectra were recorded photographically with a double prism glass spectrograph with two interchangeable cameras. The short camera with an F/4 lens of focal length 30 cm. gives a reciprocal linear dispersion of 225 cm.$^{-1}$ per mm. at Hg4358A. The long camera with an F/10 lens of focal length 75 cm. gives a dispersion of 90 cm.$^{-1}$ per mm. Antireflection coatings on the F/4 objective improved its transmission by about 30%, and reduced the stray light in the spectrograph.

The photographic plates were calibrated for intensities by replacing the slit of the spectrograph with a stepped slit and photographing the continuous spectrum of a Kipp and Zonen standard tungsten band lamp. Photographic densities were measured with a Leeds and Northrup recording microphotometer. From calibration curves determined at the wave length of each Raman band in the spectrum, the relative intensities of the bands on a given plate were evaluated from the known distribution of intensity in the spectrum of the standard lamp.

Calibration spectra were recorded on each plate with the same exposure times as the Raman spectra. Since the same optical arrangement was used for all calibration spectra, relative intensities of Raman bands on different plates and for different substances could be deduced from the known current-intensity characteristics of the standard lamp. The accuracy of such a comparison is dependent on the reproducibility of the intensity of irradiation from exposure to exposure. Relative intensities for different substances were also measured directly by mixing known amounts of the substances two at a time and photographing their superimposed Raman spectra. The relative intensities obtained by both methods were consistent, but since two photographic processes are involved in the former and only one in the latter, the relative intensities obtained by the mixture method were used to correlate the data in Tables I to VI.

The frequencies of the broad Raman bands were measured from the microphotometer trace because this method is more objective than visual measurements. To correct for nonuniformity in the pitch of the drive screw an auxiliary scanning unit was added to the microphotometer. A heavily aluminized glass plate with accurately spaced transparent rulings was attached to the plate carriage, and scanned by the image of a filament lamp. The light from this system was directed onto the phototube of the microphotometer, producing pips on the microphotometer trace spaced at intervals corresponding accurately to 0.25 mm. on the plate. Raman shifts were determined from the separations of the bands from the moderately exposed Rayleigh lines Hg4108A• Hg4916A, and Hg5026A, using the known dispersion curve of the spectrograph. An iron arc spectrum was photographed on each plate to check the constancy of the dispersion which varied slightly with temperature.

## EXPERIMENTAL RESULTS

The spectra of methane, its chlorine derivatives, and methyl bromide were investigated. With the exception of methane which was taken directly from the gas cylinder, the substances were introduced into the Raman tube by a two-stage distillation. The quantity introduced was sufficient to give a maximum saturated vapor pressure of about seven atmospheres. During an exposure the Raman tube was kept at a temperature high enough to vaporize the substance completely. Thirty-two of the thirty-five fundamental bands of the molecules were recorded on Eastman 103*a*-O and 103*a*-J plates, with exposure times ranging from 1 to 24 hr.

The experimental results are listed in Tables I to VI. The Raman shift given for each band is that of the main maximum. When it is certain that a Fermi resonance is present, the maxima of both bands are given, and the resonance is indicated by a bracket. For frequencies or intensities determined from two or more plates the mean deviation is given. The related integrated intensities, $i_\lambda$, listed in the tables are reduced values. For the fundamentals they are the measured relative integrated intensities divided by the molar density of the vapor and multiplied by the factor $\{1 - \exp(-h\nu_\lambda c/kT)\}(\nu - \nu_\lambda)^4$, where $\nu_\lambda$

is the Raman shift, $\nu$ the frequency of the exciting light, and the other symbols have their usual meanings. Thus these values are independent of the conditions of the experiment; they are the squares of the matrix elements of the polarizability for the $v = 0$ to $v = 1$ transitions in a common arbitrary unit chosen so that the value for $\nu_3$ of methane is 1000. For overtones and combination tones the listed values were obtained by applying the density and frequency reduction factors, but not the temperature factor.

## VIBRATIONAL ANALYSIS

Since rotation must be practically unhindered at the gas pressures used the rotational structure of the rotation vibrational bands should be fully developed. For methane, some of the rotational lines were resolved; for the other compounds only the intensity distribution in the envelope of the rotational structure was measured. However, the intensity contours of the unresolved bands are very useful in the assignment of the bands to the vibrational modes of the molecule. For a totally symmetric ($a_1$) vibration of a symmetric top molecule the band consists of a strong sharp $Q$ branch with rotational wings ($O$, $P$, $R$, and $S$ branches). The intensity of the wings relative to the $Q$ branch depends on the depolarization factor, and is zero for cubic symmetry. For a nontotally symmetric or a degenerate vibration all the branches have nearly equal intensities; hence the $Q$ branch is less pronounced than for totally symmetric vibrations and, with low resolution, appears merged with the wings. For a degenerate vibration Coriolis interaction between the vibration and the free rotation can lead to a broadening of the band and a decrease in the intensity of the central maximum. For asymmetric top molecules the contours of the bands can be more complicated, but are characteristic of the modes of vibration.

The vibrational assignments, given in Tables I to VI, are based on the band contours, reproduced in Figs. 3-8. These assignments confirm in all cases those listed by Herzberg (8). A detailed discussion of each spectrum follows.

*Methane* (Table I, Fig. 3)

In addition to the strong bands, $\nu_1(a_1)$ and $\nu_3(f_2)$, observed by Dickinson, Dillon, and Rasetti(6) and by MacWood and Urey (10), a band was found

TABLE I

THE RAMAN SPECTRUM OF GASEOUS METHANE

| Observed Raman shifts, cm.$^{-1}$ | Assignment | Reduced relative intensity, $i_A$ |
|---|---|---|
| 1300 (liquid) (5) | $\nu_4(f_2)$ | 8 |
| 1535.4 ± 0.6 | $\nu_2(e)$ | 160 ± 6 |
| 2582 ± 2 | $2\nu_4(A_1 + E + F_2)$ | — |
| 2915.0 ± 0.6 | $\nu_1(a_1)$ | 990 ± 20 |
| 3017.0 ± 0.6 | $\nu_3(f_2)$ | 1000 ± 20 |

at $\Delta\nu = 1535$ cm.$^{-1}$ from Hg4358A, when Hg4047A and its companion lines were removed from the exciting light by a filter. This band, which has a

sharp $Q$ branch with approximately one-fifth of the intensity of the band, must be assigned to the fundamental $\nu_2(e)$. Burgess (3) has recently shown that this vibration is weakly active in the infrared and that the frequency of the $Q$ branch

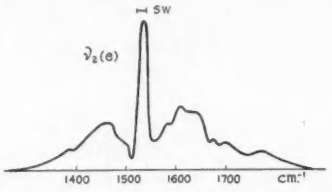


FIG. 3. The $\nu_2$ Raman band of methane.

is 1533.6 cm.$^{-1}$ The wings of the Raman band show features characteristic of discrete rotational structure but the resolution obtained does not warrant a detailed analysis, particularly as the structure is being reinvestigated at higher dispersion. The resolution of the individual rotation lines of $\nu_3(f_2)$ was somewhat better than that obtained by earlier workers, but the frequencies will not be given here since the band structure has recently been measured at much higher dispersion (17). The faint diffuse band with its center at 2670 cm.$^{-1}$ is probably the overtone of $2\nu_4$.

*Carbon Tetrachloride* (Table II, Fig. 4)

The doubly degenerate vibration $\nu_2$ gives rise to a Raman band with a maximum at 221 cm.$^{-1}$ corresponding to the $Q$ branch. The partially resolved

TABLE II

THE RAMAN SPECTRUM OF GASEOUS CARBON TETRACHLORIDE

| Observed Raman shifts, cm.$^{-1}$ | Assignment | Reduced integrated intensity, $i_\lambda$ |
|---|---|---|
| 221 ± 2 | $\nu_2(e)$ | 154 ± 10 |
| 310.0 ± 0.6 | $\nu_4(f_2)$ | 214 ± 10 |
| 434 ± 1 | $2\nu_2(A_1)$ | |
| 459.0 ± 0.6 | $\nu_1(a_1)$ | 291 ± 4 |
| 756 ± 2 | $\nu_1 + \nu_4(F_2)$ | 316 ± 6 |
| 794.3 ± 0.8 | $\nu_3(f_2)$ | |
| 1557.0 ± 0.6 | $\nu_1 + \nu_4 + \nu_3\ (A_1 + E + F_2)$ | 34 ± 6 |
| 1585 ± 2 | $2\nu_3\ (A_1 + E + F_2)$ | |

maxima at 211 and 230 cm.$^{-1}$ are at the calculated positions of the maxima in the $O$ and $S$ branches respectively. The maximum at 230 cm.$^{-1}$ is more intense than that at 211 cm.$^{-1}$, showing that an underlying component is present which can be classified as the $2\nu_2(E) - \nu_2$ transition if a negative anharmonicity is assumed. The frequency of the transition, $2\nu_2(A_1) - \nu_2$, calculated from the observed frequency of $2\nu_2(A_1)$ (see below), is 434 − 221 = 213 cm.$^{-1}$; thus, this component falls on the maximum in the $O$ branch and, as expected, is weaker than $2\nu_2(E) - \nu_2$.

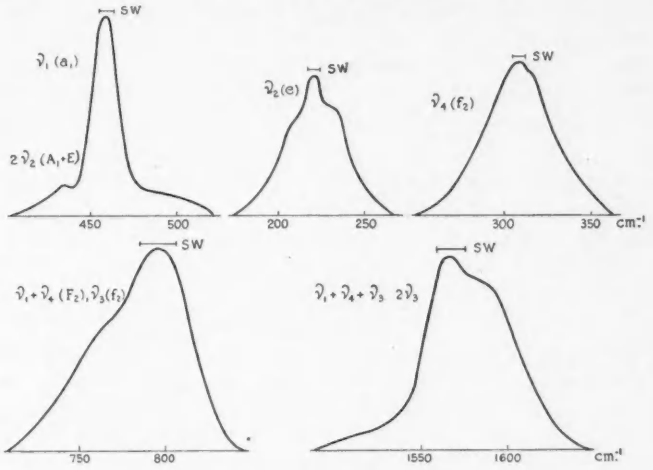


FIG. 4. Raman bands of carbon tetrachloride.*

The triply degenerate frequency $\nu_4$ shows only a central maximum. Since there is a Coriolis interaction between the mutually degenerate modes, the resultant splitting of the rotational branches leads to an almost symmetrical contour without maxima in the wings.

The triply degenerate fundamental $\nu_3$ has two components of unequal intensities, in agreement with the observations of Morino, Watanabe, and Mizushima (11). The positions and relative intensities of the components are qualitatively consistent with an inexact Fermi resonance between $\nu_3(f_2)$ and $\nu_1 + \nu_4(F_2)$. The small changes in frequency, chiefly in $\nu_3$ and $\nu_4$, in passing from the gas to the liquid are sufficient to make the resonance almost exact in the liquid where two components of equal intensity are observed (22). The difference in the relative intensities of the two components in the gas and the liquid confirms that a Fermi resonance is involved rather than a departure of the molecule from tetrahedral symmetry. The abnormally intense overtone of $\nu_3$ has two components which can be classified as $\nu_1 + \nu_3 + \nu_4$ and $2\nu_3$. A third component, which was observed in the liquid (22) at 1524 cm.$^{-1}$ and which can be assigned to $2\nu_1 + 2\nu_4$, is not prominent in the gas, because the resonance is less exact.

The totally symmetric frequency $\nu_1$ gives a band accompanied by wings which cannot be interpreted as due to rotation. The definite maximum at 434 cm.$^{-1}$ is undoubtedly caused by a Fermi resonance of the $A_1$ part of $2\nu_2$ with $\nu_1$. The broad wing on the high frequency side of $\nu_1$ must be due to the transition $\nu_3 - \nu_4$ with a calculated position $794 - 310 = 484$ cm.$^{-1}$. Such a component has been noted in the liquid by Rank and Van Horn (15) confirming the

*In these diagrams a common intensity scale has not been used since there is an intensity ratio of over 100 between the weakest and strongest bands.

theoretical prediction of Horiuti (9). The stronger component $(\nu_1 + \nu_4) - \nu_4$ should occur at $756 - 310 = 446$ cm.$^{-1}$, but is obscured by the isotopic broadening of the main component of $\nu_1$. The diffuseness of $\nu_3 - \nu_4$ arises from the rotational structure characteristic of this type of vibration; also, weaker components due to transitions between higher levels in Fermi resonance may be present.

*Methyl Chloride* (Table III, Fig. 5)

Symmetric top molecules such as methyl chloride, methyl bromide, and chloroform have three totally symmetric ($a_1$) and three doubly degenerate ($e$) vibrations.

TABLE III

THE RAMAN SPECTRUM OF GASEOUS METHYL CHLORIDE

| Observed Raman shifts, cm.$^{-1}$ | Assignment | Reduced integrated intensity, $i_\lambda$ |
|---|---|---|
| 725.3 ± 0.6 | $\nu_3(a_1)$ | 126 ± 4 |
| 1012 ± 2 | $\nu_6(e)$ | 11 ± 4 |
| 1370 (liquid) (20) | $\nu_2(a_1)$ | |
| 1473 ± 2 | $\nu_5(e)$ | 55 ± 4 |
| 2874 ± 2 | $2\nu_5(A_1)$ | 28 ± 3 |
| 2965.5 ± 0.6 | $\nu_1(a_1)$ | 221 ± 4 |
| 3043 ± 1 | $\nu_4(e)$ | 189 ± 6 |

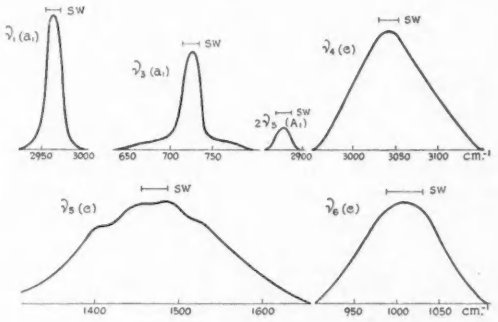


FIG. 5. Raman bands of methyl chloride.

Five fundamentals and one overtone ($2\nu_5$) were observed for methyl chloride. Two of the totally symmetric vibrations, $\nu_1$ and $\nu_3$, are immediately identified by the strong $Q$ branch and the weak rotational wings characteristic of such vibrations. The low intensity of the wings for $\nu_1$ indicates that the line is highly polarized. The frequency, 725.3 cm.$^{-1}$, of $\nu_3$ differs from the infrared value, 732 cm.$^{-1}$ (2), by more than experimental error, but agrees with the value given by Nielsen and Ward (12), who observed the $\nu_1$ and $\nu_3$ bands in the Raman

spectrum of the gas. The third totally symmetric vibration $\nu_2$, at 1355 cm.$^{-1}$ according to infrared data, must have a very low intensity since it was not observed.

The doubly degenerate bands $\nu_4$ and $\nu_6$ have contours resembling Gaussian error curves as predicted by Teller (18) from the theory of Coriolis interaction. The $\nu_6$ band is extremely weak and the contour given in Fig. 5 cannot be considered very accurate. The $\nu_5$ band is broader and shows four maxima; these features are probably due to the larger value of $\zeta$ for this vibration. The center of the band, taken midway between the two central maxima, is about 18 cm.$^{-1}$ higher than the origin of the infrared band. This illustrates the fact that, unless at least partial resolution of the band is achieved, the vibrational frequency corresponding to such broad bands cannot be found accurately.

*Methyl Bromide* (Table IV, Fig. 6)

All six fundamental frequencies and one overtone ($2\nu_5$) were observed. The doubly degenerate band, $\nu_6$, is broad and extremely weak. The totally symmetric

TABLE IV

THE RAMAN SPECTRUM OF GASEOUS METHYL BROMIDE

| Observed Raman shifts, cm.$^{-1}$ | Assignment | Reduced integrated intensity, $i_\lambda$ |
|---|---|---|
| 609 ± 1 | $\nu_3(a_1)$ | 188 ± 2 |
| 956 ± 5 | $\nu_6(e)$ | ~0.4 |
| 1309 ± 1 | $\nu_2(a_1)$ | 11 ± 2 |
| 1456 ± 4 | $\nu_5(e)$ | 57 ± 2 |
| 2862 ± 2 | $2\nu_5(A_1)$ | 27 ± 4 |
| 2972 ± 1 | $\nu_1(a_1)$ | 172 ± 4 |
| 3068 ± 4 | $\nu_4(e)$ | 133 ± 9 |

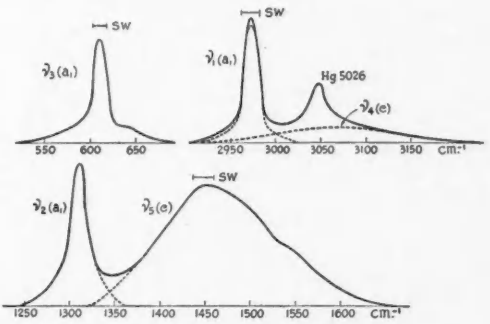


FIG. 6. Raman bands of methyl bromide.

and doubly degenerate bands can be distinguished immediately by their contours. The frequencies of the totally symmetric bands are in good agreement with

infrared values, but the frequencies of the central maxima of the degenerate bands are all somewhat higher than the infrared values.

*Chloroform* (Table V, Fig. 7)

All six fundamental bands and one overtone ($2\nu_5$) band were observed in chloroform. Except for $\nu_3$ and $\nu_6$ the frequencies agree well with those obtained

TABLE V

THE RAMAN SPECTRUM OF GASEOUS CHLOROFORM

| Observed Raman shifts, $cm.^{-1}$ | Assignment | Reduced integrated intensity, $i_\lambda$ |
|---|---|---|
| $255.5 \pm 0.5$ | $\nu_6(e)$ | $225 \pm 8$ |
| $364.8 \pm 0.5$ | $\nu_3(a_1)$ | $168 \pm 6$ |
| $671.1 \pm 0.6$ | $\nu_2(a_1)$ | $174 \pm 2$ |
| $767.7 \pm 0.6$ | $\nu_5(e)$ | $155 \pm 2$ |
| $1218 \pm 3$ | $\nu_4(e)$ | $46 \pm 2$ |
| $1527 \pm 2$ | $2\nu_5(A_1 + E)$ | $15 \pm 2$ |
| $3032.0 \pm 0.5$ | $\nu_1(a_1)$ | $157 \pm 6$ |

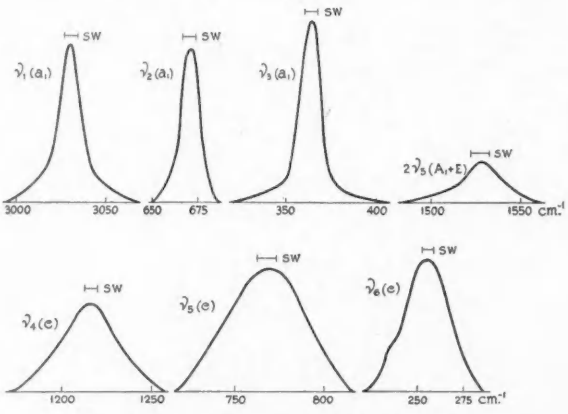


FIG. 7. Raman bands of chloroform.

by Nielsen and Ward (12), who measured all the fundamentals in the vapor. The assignment of the bands is immediately evident from the intensity contours and the frequencies. The low frequency bands, $\nu_2$ and $\nu_6$, are asymmetric; the low frequency component of $\nu_6$ is unquestionably real, and is possibly $3\nu_6 - 2\nu_6$ shifted to lower frequency as a consequence of resonance degeneracy with $\nu_5$.

*Methylene Chloride* (Table VI, Fig. 8)

If methylene chloride has a tetrahedral structure of point group $C_{2v}$ there should be nine fundamentals, of which four are $A_1$ species, one $A_2$, two $B_1$, and two $B_2$. The contours of the totally symmetric bands for the asymmetric top

TABLE VI

THE RAMAN SPECTRUM OF GASEOUS METHYLENE CHLORIDE

| Observed Raman shifts, cm.$^{-1}$ | Assignment | Reduced integrated intensity, $i_\lambda$ |
|---|---|---|
| 281.5 ± 0.6 | $\nu_4(a_1)$ | 69 ± 2 |
| 712.9 ± 0.6 | $\nu_3(a_1)$ | 137 ± 4 |
| 748 ± 2 | $\nu_9(b_2)$ | 38 ± 6 |
| ~ 893 | $\nu_7(b_1)$ | — |
| 1153 ± 2 | $\nu_5(a_2)$ | 7 ± 2 |
| 1255 (liquid) (21) | $\nu_8(b_2)$ | — |
| 1430.1 ± 0.8 | $\nu_2(a_1)$ | 22 ± 2 |
| 1493 ± 2 | $2\nu_9(A_1)$ | — |
| 2854 ± 2 | $2\nu_2(A_1)$ | 5 ± 2 |
| 2995.7 ± 0.4 | $\nu_1(a_1)$ | 108 ± 4 |
| 3040 ± 2 | $\nu_6(b_1)$ | 98 ± 6 |

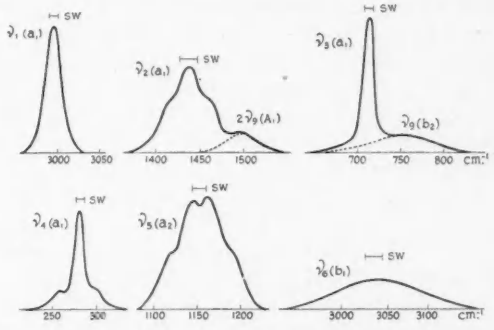


FIG. 8. Raman bands of methylene chloride.

should show a strong $Q$ branch with rotational wings, just as for the symmetric top. There is therefore no doubt that the Raman bands at 2996, 1430, 713, and 281 cm.$^{-1}$ correspond to the $A_1$ type vibrations. Of particular interest is the contour of $\nu_2(a_1)$ at 1430 cm.$^{-1}$. In the liquid this line has a depolarization factor of 6/7 (4), which has led to some doubt as to the assignment of the band. In the gas, however, the band has the characteristic appearance of an $a_1$ vibration; the comparatively high intensity in the wings shows that the depolarization factor is in fact large.

The contour of the band at 1153 cm.$^{-1}$ is remarkable in that there are four maxima with a central minimum; the intensity distribution resembles that of a type $B$ infrared band, the envelope of which has been calculated by Badger and Zumwalt (1); the $Q$ lines form two maxima on either side and fairly close to the band origin. A consideration of the structure of Raman bands for the asymmetric top shows that this distribution of intensity should occur for the torsional oscillation (type $A_2$) for the $C_{2v}$ point group. The band can therefore be unambiguously assigned to $\nu_5(a_2)$.

The bands at 3040 and 748 cm.$^{-1}$ are broad and flat with a single maximum. It is clear that they correspond to the antisymmetric species $B_1$ or $B_2$; they are assigned to the frequencies $\nu_6(b_1)$ and $\nu_9(b_2)$ respectively. A very weak band at 893 cm.$^{-1}$ is assigned to $\nu_7(b_1)$. The band found in the liquid at 1255 cm.$^{-1}$ (21) and interpreted as $\nu_8(b_2)$ was not observed in the vapor.

## DISCUSSION OF THE RELATIVE INTENSITIES

The polarizability theory of the Raman effect, as developed by Placzek (13), shows that the intensity of a fundamental Raman band can be expressed:

$$I_\lambda \propto N(\nu - \nu_\lambda)^4(45\alpha'^2 + 13\gamma'^2)(Q_\lambda)_0^2/\{1 - \exp(-h\nu_\lambda c/kT)\},$$

where $\alpha'$ and $\gamma'^2$ are, respectively, the average value and the anisotropy of the derivative of the polarizability with respect to the normal coordinate $Q$, $(Q)_0 = \sqrt{h/8\pi^2 c\nu_\lambda}$, and $N$ is the number of scattering molecules. It is assumed that the incident light is unpolarized and confined to directions perpendicular to the direction of observation. The frequency factor $(\nu - \nu_\lambda)^4$ and the temperature factor depend on the conditions of the experiment and can be eliminated from the experimental intensities. Furthermore, when intensities from different compounds are compared using the same experimental arrangement, they can be reduced to *relative intensities of scattering per molecule*, $i_\lambda$, by dividing the experimental intensities by a factor proportional to the number of molecules per unit volume. Then one can write

$$i_\lambda = C(45\alpha'^2 + 13\gamma'^2)$$

where $C$ is a constant for all bands. The relative intensities for the fundamental bands in Tables I to VI have been reduced in this way.

From considerations of symmetry it is possible to state whether the constants $\alpha'$ and $\gamma'^2$ have values different from zero for a vibration of a given symmetry species, and thus to make predictions concerning the activity of the vibration in Raman effect and the depolarization of the band. In general, however, it is not possible to evaluate $\alpha'$ or $\gamma'^2$ in terms of more fundamental quantities without the use of an oversimplified model. Therefore, the only expedient is a semi-empirical approach such as that of Wolkenstein (23), based on bond polarizabilities.

### *Experimental Test of the Bond Polarizability Theory of Raman Intensities*

In Wolkenstein's theory, it is assumed that (*a*) one of the principal axes of the polarizability of the bond coincides with the direction of the bond and the other two principal polarizabilities are equal for a bond of the single type, (*b*) the bond polarizabilities change when the bond length changes, and (*c*) the bond polarizabilities are independent of changes in the bond angles. The polarizability of a single bond XY can therefore be characterized by four constants—the principal polarizabilities $(\alpha_{XY})_1$ along the bond and $(\alpha_{XY})_2$ perpendicular to the bond, and the rates of change of these, $(\alpha'_{XY})_1$ and $(\alpha'_{XY})_2$, with respect to the bond length. When the geometrical and dynamic problem of calculating the intensities of the Raman bands of a given molecule is solved, it is

found that only certain combinations of the bond polarizabilities and their derivatives occur in the expressions for the intensities. These are:

$\gamma^2_{XY} \equiv (a_1 - a_2)^2_{XY}$, the anisotropy of the bond polarizability,

$a'_{XY} \equiv (1/3)(a'_1 + 2a'_2)_{XY}$, the mean rate of change of the bond polarizability, and

$\gamma'^2_{XY} \equiv (a'_1 - a'_2)^2_{XY}$, the anisotropy of the rate of change of the bond polarizability.

A fourth constant, $a_{XY} \equiv (1/3)(a_1 + 2a_2)$, the mean bond polarizability, is not involved in Raman intensities.

Wolkenstein, using this concept of bond polarizabilities and assuming valence force fields, derived formulae for the relative intensities and depolarizations of the Raman bands of the linear and the bent symmetrical molecule, $XY_2$, and the tetrahedral molecule, $XY_4$. However, the intensity data available were insufficient for an adequate test of the theory.

Since in methane and its chlorine derivatives only CH and CCl bonds occur, the relative intensities and depolarizations of the Raman bands depend on only six constants $\gamma^2_{CH}$, $a'_{CH}$, $\gamma'^2_{CH}$, $\gamma^2_{CCl}$, $a'_{CCl}$, and $\gamma'^2_{CCl}$. In principle, these constants can be evaluated (apart from ambiguities regarding sign) from six of the 28 measured intensities for this series of compounds, and the validity of the theory tested by calculating the remaining intensities and depolarization factors. In practice, however, the problem is not simple since force constants enter into the intensity formulae for those vibrations of the molecule for which there are other vibrations of the same symmetry species. It has been stressed recently by various authors (e.g. Glockler and Tung (7), Torkington (19)) that a unique set of force constants cannot be obtained from the observed vibrational frequencies of a molecule, because the most general force field, even when a high degree of symmetry is present, involves more constants than there are frequencies. Consequently, if the calculated intensities for such vibrations do not agree with the observed, one does not know whether the theory is invalid or the force field is inadequate. It is found, moreover, that the calculated intensities are very sensitive to the force constants. However, when a vibration is the only one of its symmetry species present in the molecule, the force constants do not appear explicitly in the expression for the intensity; they enter implicitly through the frequency, $\nu_\lambda$, which can be measured experimentally. Thus, these vibrations can be used to check the validity of the theory without a detailed knowledge of the force field.

A direct test of the theory can be carried out by considering $\nu_2(e)$ of $CH_4$ and $\nu_5(a_2)$ of $CH_2Cl_2$. The normal mode $\nu_2(e)$ of $CH_4$ is the superposition of two modes, $\nu_{2a}$ and $\nu_{2b}$, where $\nu_{2b}$ is the torsional oscillation of the two $CH_2$ groups relative to one another and $\nu_{2a}$ is the deformation vibration orthogonal to this. Since there appear to be errors in some of the formulae given by Wolkenstein for tetrahedral molecules, we have calculated the intensity of $\nu_2(e)$ from first principles. The calculation gives

$$i(\nu_{2a}, CH_4) = i(\nu_{2b}, CH_4) = 104\gamma^2_{CH}/m_1 l_1^2 \nu_2;$$

thus,

$$i(\nu_2, CH_4) = 208\gamma^2_{CH}/m_1 l_1^2 \nu_2,$$

in which $m_1$ is the mass of the H-atom and $l_1$ is the length of the CH bond.

The intensity of $\nu_5(a_2)$, the torsional vibration of $CH_2Cl_2$, can also be calculated easily. The result is

$$i(\nu_5, CH_2Cl_2) = 52(\gamma_{CH} + K\gamma_{Cl})^2/(m_1 l_1^2 + K^2 m_2 l_2^2)\nu_5,$$

in which $m_2$ is the mass of the Cl atom, $l_2$ the length of the CCl bond, and $K = m_1 l_1^2/m_2 l_2^2$. Since $K$ is very small ($\sim 0.01$), the expression reduces to

$$i(\nu_5, CH_2Cl_2) = 52\gamma^2_{CH}/m_1 l_1^2 \nu_5.$$

The calculated intensity ratio of these two bands is

$$I(\nu_2, CH_4)/I(\nu_5, CH_2Cl_2) = 4(\nu_5/\nu_2) = 3.0.$$

The measured ratio is 23 (from Tables I and VI). Although the measured ratio has a large percentage error arising mainly from the error in the intensity of the very faint $\nu_5$ band of $CH_2Cl_2$, there is no doubt that it is greater than the calculated value by a factor of 5 to 10. It is therefore concluded that the anisotropy of the bond polarizability is not a constant of the bond.

A second simple test of the bond polarizability theory can be carried out for both CH and CCl bonds by considering the relative intensities of the $a_1$ vibration of $XY_4$, the $b$ vibration of the $XY_2$ group in $Z_2XY_2$, and the XY stretching vibration in $Z_3XY$. For the CH bond the series used is $CH_4$, $CH_2Cl_2$, and $CHCl_3$; for the CCl bond, $CCl_4$, $CH_2Cl_2$, and $CH_3Cl$. The intensity formulae are (23):

$$i(\nu_{a_1}, XY_4) = (180/\nu_{a_1})(1/m_Y)\alpha'^2_{XY},$$

$$i(\nu_b, YX_2 \text{ in } Z_2XY_2) = (14/\nu_b)(1/m_Y + 4/3m_{XZ_2})\gamma'^2_{XY},$$

$$i(\nu_{a_1}, XY \text{ in } Z_3XY) = (1/\nu_{a_1})(1/m_Y + 1/m_{XZ_3})(45\alpha'^2_{XY} + 13\gamma'^2_{XY}).$$

The depolarization factor of $\nu_{a_1}$ (XY in $Z_3XY$) is given by:

$$\rho = \frac{6\gamma'^2_{XY}}{45\alpha'^2_{XY} + 7\gamma'^2_{XY}}.$$

For the CH bond, $\nu_1(a_1)$ of $CH_4$ and $\nu_6(b_1)$ of $CH_2Cl_2$ were used for the calculation of the constants $\alpha'^2_{CH}$ and $\gamma'^2_{CH}$, and $\nu_1(a_1)$ of $CHCl_3$ as the check. The results are given in Table VII. The agreement is seen to be poor, and the conclusion is reached that the rate of change of polarizability is strongly

TABLE VII

| | Calculated | Experimental |
|---|---|---|
| $i(\nu_1, CHCl_3)$ | 314 | 157 |
| $\rho(\nu_1, CHCl_3)$ | 0.12 | 0.24(4) |

dependent on the nature of the neighboring bonds. To reproduce the experimental values above $\alpha'^2_{CH}$, calculated from $\nu_1$ of $CH_4$, would have to be reduced by a factor of two.

A similar calculation for the CCl bond was made using $\nu_1(a_1)$ of $CCl_4$ and $\nu_9(b_2)$ of $CH_2Cl_2$ to determine $\alpha'^2_{CCl}$ and $\gamma'^2_{CCl}$, and using $\nu_3(a_1)$ of $CH_3Cl$ as a check (Table VIII). In this case the agreement for $i$ is better than for the CH bond,

TABLE VIII

| | Calculated | Experimental |
|---|---|---|
| $i(\nu_3, CH_3Cl)$ | 177 | 126 |
| $\rho(\nu_3, CH_3Cl)$ | 0.062 | 0.15(4) |

but is nevertheless not good. Agreement can be obtained by assuming that $\alpha'^2_{CCl}$ in $CH_3Cl$ is smaller than $\alpha'^2_{CCl}$ in $CCl_4$ by a factor of 0.72. This also gives a slight improvement in the agreement for $\rho$.

The inadequacy of the bond polarizability theory is also apparent from a comparison of the intensities of the bands characteristic of the $CH_3$ group in methyl chloride and methyl bromide. Although the intensities of the deformation frequency, $\nu_5(e)$, are almost the same in the two compounds, those of the stretching frequencies, $\nu_1(a_1)$ and $\nu_4(e)$, in $CH_3Cl$ are 28% and 42% higher, respectively, than in $CH_3Br$. The frequencies, on the other hand, show changes of less than 1%. Even more striking is the difference in the intensities of the symmetrical deformation vibration, $\nu_2(a_1)$, of the $CH_3$ group in these two molecules; in gaseous methyl chloride the band could not be detected, whereas in methyl bromide it was easily recorded. In these cases, the intensity of the band is therefore much more dependent on the types of the neighboring bonds than is the frequency. If a comprehensive theory of Raman intensities can be developed, experimental intensities can perhaps be used along with the frequencies in determining a unique set of force constants for molecules.

*Total Intensities of Vibrational Raman Scattering*

The total intensity of the vibrational Raman scattering, $\sum i_\lambda$, is plotted in Fig. 9 for each molecule of the series. The high value of the total intensity in methane is noteworthy; this intensity is concentrated in the $\nu_1$ and $\nu_3$ bands, which are more than three times as intense as any other band in this group of compounds. In proceeding along the series from methane to carbon tetrachloride, the total intensity falls to a minimum for methylene chloride and then rises

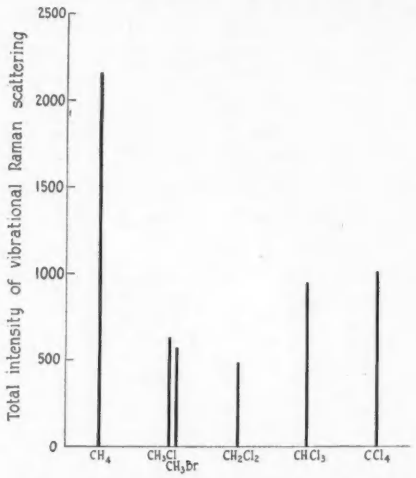


FIG. 9. Comparison of total intensities of vibrational Raman scattering.

again. There is therefore a correlation of the total intensity with the degree of symmetry of the molecule; with decreasing symmetry the total intensity decreases.

## INTENSITY DISTRIBUTION IN TOTALLY SYMMETRIC RAMAN BANDS OF SYMMETRICAL TOP MOLECULES

For totally symmetrical vibrations of freely rotating molecules the division of intensity between the five branches of the band is related to the value of $a'^2/\gamma'^2$ and hence to the value of $\rho$. The isotropic (polarized) scattering which depends on $a'^2$ is all contained in the $Q$ branch, whereas the anisotropic (depolarized) scattering which depends on $\gamma'^2$ is distributed throughout all five branches. For transverse observation the division of intensity is as follows:

$$i_Q \propto (45a'^2 + 13x\gamma'^2),$$

$$i_{OPRS} \propto 13(1 - x)\gamma'^2,$$

$$i_{\text{total}} \propto (45a'^2 + 13\gamma'^2),$$

where $x$ depends on the ratio of the moments of inertia and can be found from curves, valid for $B \ll kT$, given by Placzek and Teller (14). If $I_Q/I_{OPRS}$ has been obtained experimentally, $a'^2/\gamma'^2$ and $\rho$ can be evaluated.

The intensity distributions in the $\nu_3$ bands of $CH_3Cl$ and $CH_3Br$ were carefully measured and used to determine $a'^2/\gamma'^2$. The theoretical distribution in the wings was obtained from curves of Placzek and Teller, using the appropriate values of $B$ and $kT$. The theoretical distribution was then modified for the finite slit width and matched to the experiment contour by adjusting the intensity

scale factor. The extent and general shape of the wings agreed very well with the theoretical curve, as shown for $CH_3Br$ in Fig. 10. The contour of the $Q$ branch

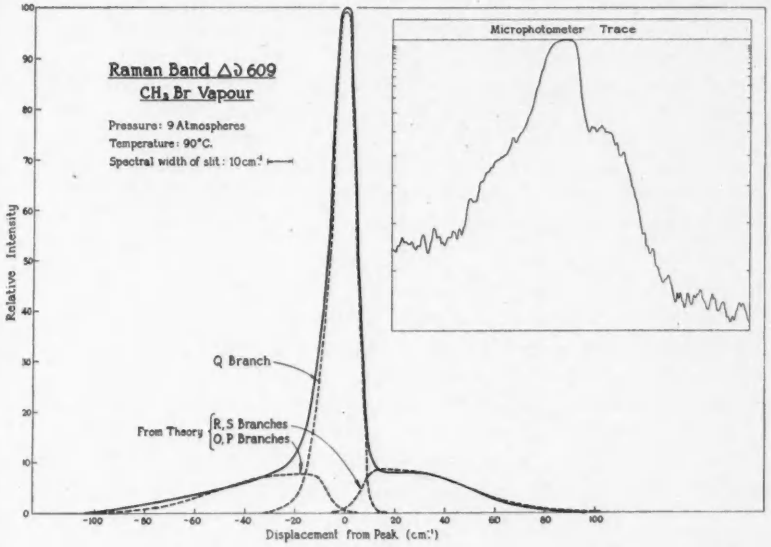


FIG. 10. Intensity distribution in a totally symmetric Raman band ($\nu_3$ band of methyl bromide).

was obtained by subtracting the theoretical curves for the wings from the experimental contour. The values of $\alpha'^2/\gamma'^2$ and $\rho$, calculated by the method outlined, are given in Table IX.

TABLE IX

DEPOLARIZATION FACTORS FOR TOTALLY SYMMETRICAL RAMAN BANDS

| Raman band | $I_Q/I_{OPRS}$, experimental | $\alpha'^2/\gamma'^2$ | $\rho$ (vapor), calculated from $I_Q/I_{OPRS}$ | $\rho$ (liquid), experimental (4) |
|---|---|---|---|---|
| $\nu_3$ of $CH_3Br$ | 1.6 | 0.33 | 0.28 | 0.20 |
| $\nu_3$ of $CH_3Cl$ | 2.2 | 0.48 | 0.21 | 0.15 |

The formulae used for the evaluation of $\rho$ are strictly valid only for transverse observation, but in our experiments no attempt was made to prevent oblique rays from entering the scattering medium. Oblique rays increase the observed isotropic intensity over the anisotropic, since the scattering in the forward or backward direction is proportional to $90\alpha'^2 + 14\gamma'^2$ compared with $45\alpha'^2 + 13\gamma'^2$ in the transverse direction. The $\rho$ values obtained by the above procedure are therefore lower than the actual values. It is noteworthy that the $\rho$ values measured by Cabannes and Rousset (4) for the liquid are still lower. The

probable explanation is that the $\rho$ values of Cabannes and Rousset refer essentially to the $Q$ branch. Even though molecular rotation in the liquid is hindered to a large extent, some of the anisotropic scattering falls in the wings of the line and is not included in the depolarization measurement unless a very wide slit is used.

The effect of oblique rays on the $\rho$ values cannot be large, since their intensity is greatly reduced by the inverse square law and reflection losses. This conclusion is substantiated by the fact that the $\rho$ values, representing lower limits of the actual values for the vapor, are nevertheless higher than the values for the liquid. Thus the use of the formulae for transverse observation in the calculations given in the discussion of relative intensities is justified.

## STRUCTURE OF THE $Q$ BRANCHES OF THE $\nu_3$ BANDS OF $CH_3Cl$ AND $CH_3Br$

Even with a comparatively wide slit the $Q$ branch of the $\nu_3$ bands in $CH_3Br$ and $CH_3Cl$ show distinct asymmetry. Accurate intensity contours for the $Q$ branches of these bands, obtained by using a narrow slit (3 cm.$^{-1}$) and the fine-grained Ilford Special Lantern plates, are reproduced in Figs. 11 and 12. The rotational wings are suppressed because of the small slit width.

The obvious causes of a marked asymmetry of the $Q$ branch are: (*a*) transitions from excited vibration levels giving rise to components shifted by anharmonicity,

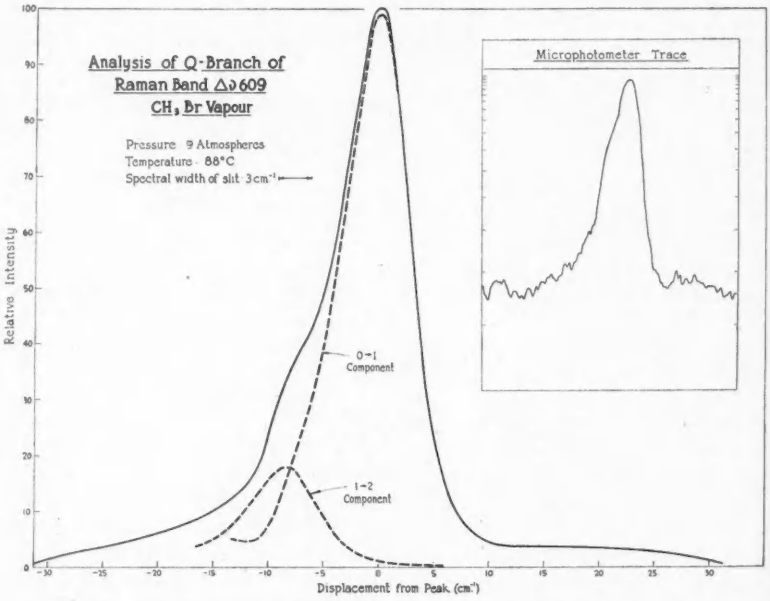


FIG 11. Intensity contour of the $Q$ branch of the $\nu_3$ band of methyl bromide.

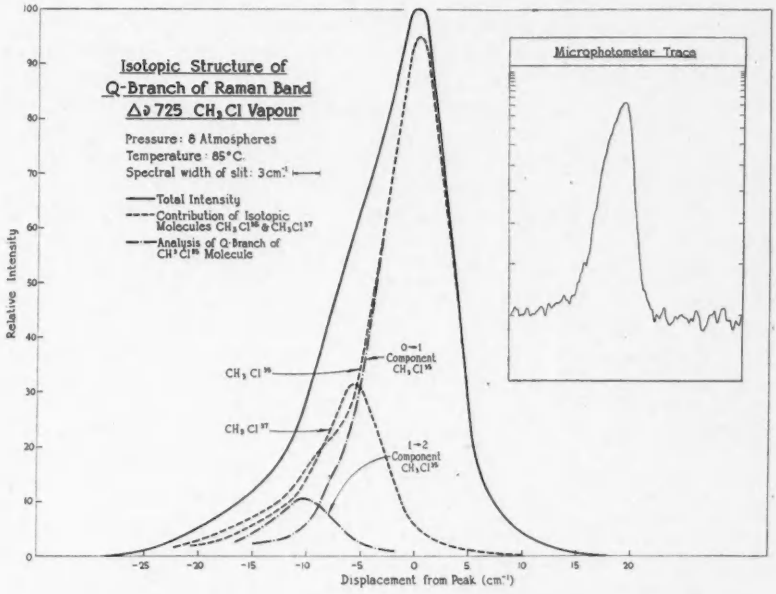


FIG. 12. Intensity contour of the $Q$ branch of the $\nu_3$ band of methyl chloride.

and ($b$) the presence of two or more isotopic forms of the molecule. Both effects can be calculated approximately for the $\nu_3$ vibration since it is the characteristic vibration of the substituted bond and can be treated in a diatomic approximation.

For $CH_3Br$ the effect of anharmonicity alone needs to be considered. The only transition from an excited vibrational state having an appreciable intensity is the $2 \leftarrow 1$ transition; it gives a component shifted towards lower frequencies by $2x_e\nu_3$ from the $1 \leftarrow 0$ component. The anharmonicity constant, $x_e$, can be calculated approximately from the dissociation energy, $D$, of the C Br bond by the formula $x_e = \nu_3/4D$. The ratio of the intensities of the two components is given by $I_{2\leftarrow 1}/I_{1\leftarrow 0} = 2 \exp(-hc\nu_3/kT)$. The shift calculated from $D = 2.63$ ev. (16) is 8.3 cm.$^{-1}$, and the intensity ratio for the temperature of the vapor in the experiment is 0.2.

The experimental contour was analyzed by a graphical method. The high frequency side of the band contains a negligible intensity contribution from the $2 \leftarrow 1$ transition. Therefore, by taking the ordinates of the $1 \leftarrow 0$ component beginning at the high frequency side, and plotting a corresponding ordinate reduced by the factor 0.18 and shifted 8.3 cm.$^{-1}$ towards lower frequencies, the intensity contour was separated into two parts. The components resulting from this analysis are approximately symmetrical, showing that the asymmetry of the $Q$ branch in this case is due mainly to anharmonicity.

For $CH_3Cl$ the chlorine isotope effect must also be considered. The line of the molecule containing the heavier isotope is shifted towards lower frequencies by the amount, $\nu_3(1 - \mu/\mu_i)$, where $\mu$ and $\mu_i$ are respectively the reduced masses in a diatomic approximation of $CH_3 - Cl^{35}$ and $CH_3 - Cl^{37}$. The calculated shift is 5.8 cm.$^{-1}$, and the intensity ratio of the components is 3.06:1, the relative abundance of the chlorine isotopes. The analyses of the experimental intensity curve gave two components, still quite asymmetric, as shown in Fig. 12. Calculations for the anharmonicity predict a shift of 10.5 cm.$^{-1}$ and an intensity of 0.11 for the $2 \leftarrow 1$ component relative to the $1 \leftarrow 0$ component. An analysis of the $CH_3Cl^{35}$ component with these data gave two symmetrical components. The asymmetry of the $\nu_3$ band in $CH_3Cl$ is thus explained.

For both molecules the contour of the $Q$ branch after correction for anharmonicity and isotope effect still shows a half width of 7 cm.$^{-1}$. Since the exciting line is very narrow and the spectral slit width was only 3 cm.$^{-1}$, the $Q$ branch must have an intrinsic half width of 5 to 6 cm.$^{-1}$. This half width is probably due to interaction between vibration and rotation, since it has been shown recently that isotropic Raman scattering is not broadened to any extent by collisions (5).

## REFERENCES


1. Badger, R. M. and Zumwalt, L. R. J. Chem. Phys. 6: 711. 1938.
2. Bennett, W. H. and Meyer, C. F. Phys. Rev. 32: 888. 1928.
3. Burgess, J. S. Phys. Rev. 76: 302. 1949.
4. Cabannes, J. and Rousset, A. Ann. phys. 19: 229. 1933.
5. Crawford, M. F., Welsh, H. L., and Harrold, J. H. Can. J. Phys. 30: 81. 1952.
6. Dickinson, R. G., Dillon, R. T., and Rasetti, F. Phys. Rev. 34: 582. 1929.
7. Glockler, G. and Tung, J. J. Chem. Phys. 13: 388. 1945.
8. Herzberg, G. Molecular spectra and molecular structure. II. Infrared and Raman spectra of polyatomic molecules. D. Van Nostrand Company, Inc., New York. 1945.
9. Horiuti, J. Z. Physik 84: 380. 1933.
10. MacWood, G. E. and Urey, H. C. J. Chem. Phys. 4: 402. 1936.
11. Morino, V., Watanabe, I., and Mizushima, S. Sci. Papers Inst. Phys. Chem. Research (Tokyo), 39: 348. 1942.
12. Nielsen, J. R. and Ward, N. E. J. Chem. Phys. 5: 201. 1937.
13. Placzek, G. Marx, Handb. d. Radiologie VI(2). (Akademische Verlagsgesellschaft m.b.H, Leipzig, 1934).
14. Placzek, G. and Teller, E. Z. Physik 81: 209. 1933.
15. Rank, D. H. and Van Horn, J. A. J. Optical Soc. Am. 36: 454. 1946.
16. Samuel, R. Revs. Modern Phys. 18: 103. 1946.
17. Stoicheff, B. P., Cumming, C., St. John, G. E., and Welsh, H. L. Phys. Rev. 84: 592. 1951.
18. Teller, E. Hand- und Jahrb. d. chem. phys. 9, II: 43. 1934.
19. Torkington, P. J. Chem. Phys. 17: 357. 1949.
20. Wagner, J. Z. physik. Chem., B, 40: 36. 1938.
21. Wagner, J. Z. physik. Chem., B, 45: 69. 1939.
22. Welsh, H. L., Crawford, M. F., and Scott, G. D. J. Chem. Phys. 16: 97. 1948.
23. Wolkenstein, M. W. J. Phys. (U.S.S.R.), 5: 185. 1941.

# THE THEORY OF NEUTRON DIFFRACTION BY GASES. I[1]

By N. K. Pope[2]

ABSTRACT

An expression for the total, elastic and inelastic, differential cross section for scattering of thermal neutrons by a rigid polyatomic molecule is derived. In summing over the final rotational states of the molecule the change in energy of the neutron is assumed negligibly small compared to the neutron's initial energy. The validity of this approximation is discussed. The rigidity of the molecule is then relaxed and the expression obtained for the cross section amended to take account of the vibrational motion of the nuclei. It is shown that the elastic scattering from a vibrating molecule is equivalent to that from a set of uncoupled anisotropic oscillators placed at the mean nuclear sites. Detailed results are given for spherical top molecules of the type $YX_4$. Good agreement is found with the experimental pattern of carbon tetrafluoride but not with that of methane.

## INTRODUCTION

Neutron diffraction by gases may be used to determine nuclear scattering cross sections, mean internuclear distances, and the amplitudes of nuclear vibrations. In order to do this it is necessary to derive expressions for the differential cross sections which can be compared with measured diffraction patterns. Unfortunately, while it is possible in principle to write down the differential cross section in the Born approximation, in general so many transitions are involved that detailed calculation is impossible. Only in isolated cases, e.g. deuterium (12), is a complete, quantum mechanical calculation possible.

Consider, however, another scattering process in which the incident particle can cause many transitions, the scattering of X rays by matter. The X-ray scattering by a rigid molecule was first treated classically by Debye (8), who used a model in which the momenta of the scattering atoms due to molecular rotation were neglected. The quantum mechanical treatment of X-ray scattering (22), (4) on the other hand is usually simplified by disregarding the change in momentum of the scattered photons. An analogous situation arises in the treatment of neutron scattering by gases. A semiclassical model for nonspin scattering (2) has been proposed which is identical (apart from a necessary transformation of the differential cross section to the laboratory coordinate system) with Debye's model for X-ray scattering. In this paper it is shown that the quantum mechanical formulation leads, if the momentum change of the scattered neutron is neglected, essentially to the same result as the semiclassical model. A special case has been discussed by Spiers (19).

There are, however, major differences between X-ray and neutron scattering. The energy of an X-ray quantum is always large compared to the spacing of the electronic energy levels and therefore the semiclassical treatment can be applied

[1] *Manuscript received May 5, 1952.*
*Contribution from Atomic Energy of Canada Limited, Chalk River Laboratory, Chalk River, Ont. Issued as A.E.C.L. No. 2.*

[2] *Most of the work reported in this paper was accomplished while the author was a Postdoctorate Fellow of the National Research Council of Canada.*
*The results were presented at the Montreal Meeting of the Royal Society of Canada, June 1951. (Trans. Roy. Soc. Can. 45: 186. 1951.)*

to the scattering as a whole. For neutron diffraction by gases the changes in neutron momentum due to transitions between rotational states can usually be neglected but momentum changes due to transitions between states of vibration cannot be neglected. It is thus necessary to treat vibrational transitions by quantum mechanics, while the semiclassical method may usually be applied to the rotational transitions.

However, thermal neutron energies are so small that they are not always large in comparison with the changes in rotational energy which may arise, with appreciable probability, in scattering from light molecules. For such molecules the semiclassical calculation of the scattering starts to break down for large angle scattering. It is possible, however, to improve the approximation by expanding all functions of the final neutron momentum in powers of the fractional momentum change. This procedure has been carried out successfully for neutron diffraction by spherical top molecules (15) and will be submitted for publication in the immediate future. Rigid diatomic molecules with like nuclei of spin one have been discussed by Alcock and Hurst (3). The above approximate methods of treating scattering can be successfully applied to any system for which inelastic scatterings involving energy changes of the order of the incident neutron energy can be neglected.*

The first part of the paper is devoted to the derivation of and discussion of the validity of the semiclassical differential cross section of a rigid polyatomic molecule. A general expression is then derived for the cross section of a vibrating molecule which involves an integration over all directions of the vector of momentum transfer. It is shown that there exists a good approximation to this cross section which, for elastic† scattering, can be interpreted as the coherent scattering cross section of a set of anisotropic oscillators placed at the mean nuclear sites. The effective amplitudes of vibrations, and hence the scattering powers of the oscillators, are functions of the eigenvectors of the normal modes of vibration of the molecule. The elastic scattering powers are calculated for spherical top molecules of the type $YX_4$. Explicit formulae are given for the elastic and the single phonon inelastic differential cross sections. The formulae are then compared with the measured patterns of carbon tetrafluoride (3) and methane (3) to obtain the bond length and coherent fluorine cross section for the former. Integrals over the directions of the momentum transfer vector are evaluated in an appendix.

## 1. THE BORN APPROXIMATION

Consider the scattering of a thermal neutron of mass $m$, and momentum $\mathbf{p}_0$ (in the center of mass coordinate system) by a system of $n$ nuclei situated at sites $\mathbf{r}_k (k = 1 \ldots n)$; $\mathbf{r}_k$ is measured from the center of mass of the system of nuclei. Fermi (9) and Breit (6) have justified the use of the Born approximation to derive the differential scattering cross section, provided that the following

*The author's attention has recently been drawn to a paper by G. Placzek (now in the press) in which methods similar to those outlined above have been used to investigate neutron scattering by systems of heavy nuclei.

†Unless it is obvious from the context that the contrary holds, the words "elastic" and "inelastic" will be applied only to changes in vibrational energy.

pseudo-potential $U_k$ is used for the interaction Hamiltonian of the neutron and each nucleus $k$.

$$U_k = -(2\pi\hbar^2/m)\{A_k + C_k[I_k(I_k+1)]^{-\frac{1}{2}}\mathbf{I}_k\cdot\mathbf{I}\}\delta(\mathbf{r}-\mathbf{R}_k). \tag{1.1}$$

$2\pi\hbar$ is Planck's constant, $\frac{1}{2}\mathbf{I}$ and $\mathbf{I}_k$ are the spin operators, and $\mathbf{r}$ and $\mathbf{R}_k$ are the position vectors in the laboratory coordinate system of the neutron and the nucleus $k$ respectively. Also

$$\begin{aligned} A_k &= (I_k+1)(2I_k+1)^{-1}f_k^{+} + I_k(2I_k+1)^{-1}f_k^{-}, \\ C_k &= [I_k(I_k+1)]^{\frac{1}{2}}(2I_k+1)^{-1}(f_k^{+}-f_k^{-}), \end{aligned} \tag{1.2}$$

with $f_k^{+}$ and $f_k^{-}$ the bound scattering lengths for the nucleus $k$. In terms of these quantities the bound cross section $\sigma_k$ for a single nucleus can be written either as a mean of the two types of spin-scattering

$$\sigma_k = 4\pi[(I_k+1)(2I_k+1)^{-1}(f_k^{+})^2 + I_k(2I_k+1)^{-1}(f_k^{-})^2] \tag{1.3}$$

or as the sum of the coherent and incoherent cross sections

$$\sigma_k = 4\pi(A_k^{\,2} + C_k^{\,2}). \tag{1.4}$$

If no coupling is assumed between the nuclear spins and between the spin forces and the motion of the nuclei, the state of the scatterer can be described by a set of quantum numbers $J$ associated with the nuclear motion and a set $M_k$ for the $z$ components of the spin angular momenta of the nuclei.* The group $M_k$ augmented by the corresponding quantity for the neutron is written $M$ for short. The energy of the scattering system depends only on the quantum numbers $J$ and is written $E_J$. In general the neutron will exchange energy with the scatterer during the collision according to the equation

$$(p_0^{\,2}/2\mu m) + E_J = (p^2/2\mu m) + E_{J'}, \tag{1.5}$$

$p^2$ being the momentum of the scattered neutron (in the center of mass system), $E_{J'}$ the final energy of the scatterer, and $\mu m$ the reduced mass of the neutron and the scatterer. After integration over the position coordinates of the neutron and center of mass of the scatterer, the partial differential cross section, $\sigma_{JJ'}(\theta)$, associated with the transition $J \rightarrow J'$ and scattering of the neutron through an angle $\theta$ into a solid angle $d\Omega$ is given by the Born approximation as

$$\begin{aligned} \sigma_{JJ'}(\theta) = \mu^2 \mathsf{S}_M \sum_{M'} (p/p_0)\Big|\sum_K \langle MJ|\{A_k + C_k[I_k(I_k+1)]^{-\frac{1}{2}}\mathbf{I}_k\cdot\mathbf{I}\} \\ \times \exp(i\mathbf{Q}\cdot\mathbf{r}_k)|M'J'\rangle\Big|^2. \end{aligned} \tag{1.6}$$

Here $\mathsf{S}_M$ represents the process of averaging the cross section over all the initial spin states and $\sum_{M'}$ summation over all the final spin states. Dirac's notation is used for matrix elements. Since $\hbar\mathbf{Q} = \mathbf{p}_0 - \mathbf{p}$, $\hbar\mathbf{Q}$ is the momentum transferred from the neutron to the scatterer during the collision.

*At very low temperatures it may be necessary to take account of the coupling between nuclear spins due to the presence of identical nuclei.*

The summation over $M'$ can be carried out by using the closure property of complete sets of states, giving, if $B_k$ is written for $A_k + C_k[I_k(I_k+1)]^{-\frac{1}{2}}\mathbf{I}_k\cdot\mathbf{I}$,

$$\sigma_{JJ'}(\theta) = \mu^2(p/p_0)\sum_{kk'}\langle J|\exp(i\mathbf{Q}\cdot\mathbf{r}_k)|J'\rangle \times\langle J'|\exp(-i\mathbf{Q}\cdot\mathbf{r}_{k'})|J\rangle\sum_M\langle M|B_kB_{k'}|M\rangle. \tag{1.7}$$

The last factor in (1.7) is the mean trace of the product of the operators $B_k$ and $B_{k'}$. The product can be written

$$B_kB_{k'} = A_kA_{k'} + A_kC_{k'}[I_{k'}(I_k+1)]^{-\frac{1}{2}}\mathbf{I}_k\cdot\mathbf{I} + A_{k'}C_k[I_k(I_k+1)]^{-\frac{1}{2}}\mathbf{I}_{k'}\cdot\mathbf{I} + C_kC_{k'}[I_kI_{k'}(I_k+1)(I_k+1)]^{-\frac{1}{2}}(\mathbf{I}_k\cdot\mathbf{I})(\mathbf{I}_{k'}\cdot\mathbf{I})$$

$$B_k^2 = A_k^2 + \{2A_kC_k[I_k(I_k+1)]^{-\frac{1}{2}} - C_k^2I_k(I_k+1)\}\mathbf{I}_k\cdot\mathbf{I} + C_k^2[I_k(I_k+1)]^{-1}I_k^2.$$

Since the trace of any spin operator is zero and the mean trace of $I_k^2$ is $I_k(I_k+1)$ one obtains

$$\sum_M\langle M|B_kB_{k'}|M\rangle = A_kA_{k'} + C_k^2\delta_{kk'}. \tag{1.8}$$

The differential cross section, $\sigma(\theta')$, for neutron scattering through an angle $\theta'$ in the laboratory system is obtained from the partial cross section $\sigma_{JJ'}(\theta)$ in the following way. First, the partial cross section is transformed to the laboratory coordinate system. It is then summed over all final states $J'$ (consistent with conservation of energy) and finally it is averaged over all initial states $J$. In this paper it is assumed that the center of mass of the scatterer is initially at rest in the laboratory system. If necessary a correction can be applied for the Maxwellian distribution of molecular velocities (19). However for the heavy molecules considered here the correction is small and has been ignored.

If (1.8) is substituted in (1.7), $\sigma(\theta')$ can be written in the following form:

$$\sigma(\theta') = \mu^2\sum_J\sum_{J'}(p/p_0)X(p_0/pA)\sum_{kk'}(A_kA_{k'} + C_k^2\delta_{kk'}) \times\langle J|\exp(i\mathbf{Q}\cdot\mathbf{r}_k)|J'\rangle\langle J'|\exp(-i\mathbf{Q}\cdot\mathbf{r}_{k'})|J\rangle. \tag{1.9}$$

Here $X(p_0/pA)$ is the function introduced to transform cross sections of molecules from the center of mass coordinate system to the laboratory one. This function is given in a report by Spiers (19). For molecules initially at rest in the laboratory system it is given to a sufficient approximation for the present purpose by

$$X(p_0/pA) = 1 + 2(p_0/pA)\cos\theta' + (p_0/pA)^2(\cos^2\theta' - \tfrac{1}{2}\sin^2\theta') + \ldots, \tag{1.10}$$

in which $A$ is the ratio of the mass of the molecule to the mass of the neutron. From the definition of $\hbar\mathbf{Q}$

(1.11) $$\hbar Q = (p_0^2 + p^2 - 2pp_0 \cos\theta)^{\frac{1}{2}}$$

and

(1.12) $$\theta = \theta' + \sin^{-1}[(p_0/pA)\sin\theta']$$

so that all the quantities appearing in $\sigma(\theta')$ can be expressed as functions of $\theta'$.

Equation (1.9) gives the differential cross section in the laboratory system for neutron scattering by any system of nuclei for which all types of spin coupling and motion of the center of mass can be neglected. The first restriction makes (1.9) inapplicable to very few systems; also (1.9) can be extended to take account of the motion of the center of mass. Further, if the incident neutron energy is small compared to the separation of the energy levels $E_J$, and if, also, $kT$ is small compared to the first excited level, then only a few terms of the summations over states need to be considered. In general these two conditions are not satisfied, and in this case, the evaluation of the cross section from (1.9) requires a prohibitive amount of labor.

When, however, all the probable energy changes of an independent part of the motion of the scatterer are small compared with the energy of the incident neutron, the cross section can be simplified by neglecting the corresponding changes in energy of the scattered neutron. This approximation has already been used to go from (1.6) to (1.7). In this case the cross section has been simplified by neglecting the changes in energy of the scattered neutron which should be associated with changes in directions of the nuclear spins. In the next section another example is discussed, viz. the cross section for a gas of rigid molecules. The cross section resulting from this approximation is called "semiclassical" because it is identical in form with that used by Alcock and Hurst.

## 2. THE SEMICLASSICAL CROSS SECTION FOR A RIGID MOLECULE

The conditions under which the change in energy of the scattered neutrons may be neglected will now be investigated. That the possible transitions of the molecule in the collision are limited may be suspected from considering the angular momentum about the center of mass of the molecule. If the maximum radius of the molecule is $r$, $\hbar Qr$ is the maximum change in angular momentum which neutrons of given incident energy and given scattering angle may suffer. On account of the relation between the energy and angular momentum of the molecule, the maximum change in energy of a molecule in a given initial state is thus determined by the maximum amount of angular momentum the neutron can transfer.

For spherical top and linear molecules the argument may be put more precisely as follows. For the moment let $k$ denote an outlying nucleus in the molecule. Now

(2.1) $$\exp(i\mathbf{Q}\cdot\mathbf{r}_k) = \sum_L (2L+1) i^L j_L(Qr_k) P_L(\cos\alpha)$$

where $P_L(x)$ is a Legendre polynomial and $\alpha$ is the angle between $\mathbf{Q}$ and $\mathbf{r}_k$. The functions $j_L(Qr_k)$ go to zero as $(Qr_k)^L$ and rise to a first maximum at ap-

proximately $Qr_k = L$ (17). This means that the series (2.1) for $\exp(i\mathbf{Q}\cdot\mathbf{r}_k)$ can be cut off at some value $L'$ slightly greater than $Qr_k$. Then it is easily shown, by inserting the wave functions, that the transition probabilities from states $J$ to $J \pm L$ vanish for all $L$ greater than $L'$. The energy levels are given by

$$E_J = (\hbar^2/2\pi I)J(J+1)$$

$$= (\hbar^2/2\pi A'm\kappa^2)J(J+1) \tag{2.2}$$

where $I$ is the moment of inertia about an axis perpendicular to the linear molecule or any axis in the spherical top. $\kappa$ is the "radius of gyration" and $A'm$ the mass of a molecule which differs from the actual one by having no mass at its center of mass. The maximum value of the ratio $E_{JJ'}/E_0$ occurs for $J' = J + L'$ where it is now assumed that $L'$ is $Qr_k \approx (4\pi r_k/\lambda)\sin(\theta/2)$. Here $E_0$ and $\lambda$ are the neutron energy and wave length respectively in the center of mass system. Then one can write

$$E_{J,J+L'}/E_0 = (4\mu/\pi A')[(r_k/\kappa)^2\sin^2(\theta/2) + (2J+1)(\lambda r_k/4\pi\kappa^2)\sin(\theta/2)]. \tag{2.3}$$

If, now, the average value of $J$ occurring at a temperature $T$ is estimated by equating $E_J$ to $kT$, (2.3) becomes

$$E_{J,J+L'}/E_0 = (4\mu/\pi A')[(r_k/\kappa)^2\sin^2(\theta/2) + (1 + 8\pi A'm\kappa^2 kT/\hbar^2)^{\frac{1}{2}}(\lambda r_k/4\pi\kappa^2)\sin(\theta/2)]. \tag{2.4}$$

The validity condition for the semiclassical approximation requires that $E_{J,J+L'}/E_0 \ll 1$. This will always hold for molecules with a sufficiently large moment of inertia, or for neutrons scattered through small enough angles. Increasing the temperature makes it more difficult to satisfy the condition, owing to increased level spacing with increased excitation. The condition is not necessarily satisfied for neutrons of infinite energy. For this case the first term on the right side of (2.4) does not vanish. On the other hand, if the approximation of infinite energy is made by neglecting the mass of the neutron, then $(\mu/A') \to 0$ and the approximation is valid.

An order of magnitude estimate of $E_{J,J+L'}/E_0$ may be obtained by replacing $\sin^2(\theta/2)$ by its maximum value and by putting (for the region in which neutron diffraction is important) $r_k = \lambda = \kappa$. Then (2.4) reduces to

$$E_{J,J+L'}/E_0 = (4\mu/\pi A')[1 + (1 + aA'T)^{\frac{1}{2}}/4\pi] \tag{2.5}$$

where $a$ is of the order of $\frac{1}{2}(\text{deg.K.})^{-1}$. Thus for low temperatures one must have $A'/\mu \approx A' \gg 1$ and for high temperatures

$$(\pi^2/\mu)(A'/T)^{\frac{1}{2}} \approx \pi^2(A'/T)^{\frac{1}{2}} \gg 1.$$

The differential cross section for a rigid molecule is given by (1.9), provided the energy levels and wave functions for the rigid molecule are used. It is assumed then that the energy of the incident neutron is so large that all energy changes which have a significant probability of occurring can be neglected. A negligible change, therefore, is made in the cross section by extending the sum-

mation $\sum_{J'}$ over all final states even though sufficient energy is not available for transitions to the added states. It follows that

$$p \rightarrow p_0, \tag{2.6}$$

$$Q \rightarrow Q_0 = (4\pi/\lambda)\sin(\theta/2), \tag{2.7}$$

$$X \rightarrow X_0 = 1+(2/A)\cos\theta'+(1/A)^2(\cos^2\theta'-\tfrac{1}{2}\sin^2\theta')+\ldots. \tag{2.8}$$

The summation over $J'$ can now be carried out by using the closure property and the cross section can be expressed in terms of the mean trace of $\exp(i\mathbf{Q}_0\cdot\mathbf{r}_{kk'})$, thus

$$\sigma(\theta') = \mu^2 X_0 \sum_{kk'} (A_k A_{k'} + C_k^2\delta_{kk'}) \sum_J \langle J|\exp(i\mathbf{Q}_0\cdot\mathbf{r}_{kk'})|J\rangle \tag{2.9}$$

where

$$\mathbf{r}_{kk'} = \mathbf{r}_k - \mathbf{r}_{k'}. \tag{2.10}$$

Now according to (2.9), $\sigma(\theta')$ involves $\mathbf{Q}_0$ only in the combination $\mathbf{Q}_0\cdot\mathbf{r}_{kk'}$. This product can always be written as $Q_0 r_{kk'}$ times a function of the angle variables specifying the orientation of the molecule. The matrix element depends, therefore, only on the magnitude of $\mathbf{Q}_0$ and not on its orientation. Thus the cross section is unchanged by averaging over the directions of $\mathbf{Q}_0$. Under this process $\exp(i\mathbf{Q}_0\cdot\mathbf{r}_{kk'})$ becomes $j_0(Q_0 r_{kk'})$ where $j_n(x)$ is a spherical Bessel function (17). The scattering no longer depends on the initial state and therefore the thermal average drops out and the cross section becomes

$$\sigma(\theta') = \mu^2 X_0 \sum_{kk'} (A_k A_{k'} + C_k^2\delta_{kk'})\, j_0(Q_0 r_{kk'}). \tag{2.11}$$

This is the semiclassical cross section for a rigid polyatomic molecule. It has been derived without using the properties of the rotational state wave functions. The properties of the latter are important only when changes in the neutron energy are taken into account.

Alcock and Hurst obtained their cross section by considering the neutron wave to be scattered from a rigid set of points, which are at rest but may have any orientation. Equation (2.11) is the intuitive generalization of the Alcock and Hurst formula for nuclei with spin. If the nuclei have spin the scattering length at each site $k$ may be $f_k^+$ or $f_k^-$. If the cross section is written down for a particular distribution of scattering lengths at the sites and then averaged over all possible distributions (2.11) is obtained apart from the factor $\mu^2$. Alternatively (2.11) can be written as a sum of a term which involves the coherent scattering lengths $A_k$ plus a term which involves the incoherent scattering lengths $C_k$. From the definitions of $A_k$ and $C_k$, it follows that the coherent part of the cross section is due to the scattering from the mean distribution of scattering lengths, and the incoherent part is proportional to the mean square fluctuation in scattering lengths.

The Born approximation for the cross section can be interpreted in the following way. For a transition $J \rightarrow J'$ the amplitude of the scattered wave is

averaged over all orientations of the rigid molecule with a probability density equal to the product of the initial and final state wave functions. The partial cross sections are proportional to the square of the averaged amplitudes. In effect, the neutrons are scattered by the orientation probability density with interference occurring between different molecular orientations. If, however, the conditions of the semiclassical approximation are satisfied the application of the closure property to the final states ensures that, when all the partial cross sections are added, only those wave amplitudes which are scattered from the same molecular orientation contribute to the cross section, i.e. there is no longer interference between different orientations of the same molecule.

## 3. THE CROSS SECTION FOR A VIBRATING MOLECULE

The nuclei in an actual molecule do not maintain a rigid structure, but are in fact vibrating about mean positions. Since the amplitude of vibration for a given harmonic field varies inversely as the square root of the mass the rigid molecule approximation should be best for molecules which do not contain light nuclei. The modification induced in the semiclassical cross section for a rigid molecule by allowing relative nuclear displacements is studied in this section.

If the interaction between the motions of rotation and vibration is neglected the states can be defined by a set of two or three rotational quantum numbers $J$ and a group of vibrational quantum numbers $\nu$. The partial differential cross section for a transition from an initial state $(\nu, J)$ to a final state $(\nu', J')$ is given by (1.9). Now if it is assumed that the change in energy of the scattered neutron associated with any change in rotational quantum number from $J$ to $J'$ can be neglected, then a semiclassical approximation to the cross section for each vibrational transition $\nu \rightarrow \nu'$ is easily obtained. In the usual approximation of small displacements the spacing of the vibrational energy levels is independent of excitation and hence the energy change of the scattered neutron is a function only of the difference between corresponding members of the groups of quantum numbers $\nu$, $\nu'$ defining the initial and final states. Let $\lambda$ represent the group of numbers so obtained. Symbolically, one has

$$\lambda = \nu' - \nu. \tag{3.1}$$

In the following it is convenient to calculate $\sigma^{\lambda}(\theta')$, the average over the initial states, $\nu$, of the partial cross section for a given value of $\lambda$. After a calculation which is similar to that carried out for a rigid molecule one obtains from (1.9)

$$\sigma^{\lambda}(\theta') = (\mu^2 X_\lambda p_\lambda / p_0) \sum_{kk'} (A_k A_{k'} + \delta_{kk'} C_k^2) [\mathsf{S}_\nu (f_k^{\nu,\nu+\lambda} f_{k'}^{\nu,\nu+\lambda}) \exp(i\mathbf{Q}_\lambda \cdot \mathbf{r}_{kk'})]^{\dagger}. \tag{3.2}$$

Here $p_\lambda$ is the momentum of the scattered neutron as given by the equation

$$p_0^2/2\mu m + E_\nu = p_\lambda^2/2\mu m + E_{\nu+\lambda}, \tag{3.3}$$

$E_\nu$, $E_{\nu+\lambda}$ are the initial and final vibrational energy levels, $X_\lambda$ is the same function of $p_\lambda$ as $X$ is of $p$ in (1.10), $\mathsf{S}_\nu$ denotes the thermal average over the initial states of vibration, and a dagger over a bracket denotes the average of the bracket over the directions of $\mathbf{Q}_\lambda$ where, of course,

$$\hbar\mathbf{Q}_\lambda = \mathbf{p}_0 - \mathbf{p}_\lambda. \tag{3.4}$$

The displacement of a vibrating nucleus is represented by $\mathbf{r}_k + \mathbf{u}_k$, where $\mathbf{r}_k$ is now the displacement of the equilibrium position from the center of mass and $\mathbf{u}_k$ the displacement from the equilibrium position. The vibrational matrix elements are

$$f_k^{\nu,\nu+\lambda} = \langle \nu | \exp(i\mathbf{Q}_\lambda \cdot \mathbf{u}_k) | \nu + \lambda \rangle. \tag{3.5}$$

Equation (3.2) contrasts the semiclassical and quantum mechanical calculation of the cross section. The quantum mechanical result is expressed in terms of scattering powers $f_k$, which are averages of wave amplitudes; the semiclassical result is expressed as an average of the square of the amplitude, i.e. intensity.

The remainder of this section is devoted to the evaluation of the thermal average $\mathsf{S}_\nu f_k^{\nu,\nu+\lambda} f_{k'}^{\nu,\nu+\lambda}$. To do this it is necessary to introduce the apparatus of normal coordinates.

For small displacements the potential energy $\mathscr{V}$ and the kinetic energy $\mathscr{T}$ for vibration are

$$\mathscr{V} = \tfrac{1}{2} \sum_{kk'} \sum_{\alpha\beta} D_{\alpha\beta}^{kk'} u^k{}_\alpha \, u^{k'}{}_\beta, \tag{3.6}$$

$$\mathscr{T} = \tfrac{1}{2} \sum_k m_k u_k{}^2$$

where $u^k{}_\alpha$ is the $\alpha$ component of $\mathbf{u}_k$ in a cartesian system of axes which has its origin at $\mathbf{r}_k$ and is fixed in the molecule. If normal coordinates $\xi_i$ are introduced by the orthogonal transformation (4)

$$u^k{}_\alpha = \sum_i m_k^{-\frac{1}{2}} e_\alpha(k|i) \xi_i \tag{3.7}$$

the potential and kinetic energies become

$$\mathscr{V} = \tfrac{1}{2} \sum_i \omega_i{}^2 \xi_i{}^2, \tag{3.8}$$

$$\mathscr{T} = \tfrac{1}{2} \sum_i \dot{\xi}_i{}^2.$$

The $\mathbf{e}(k|i)$ are known as the reduced eigenvectors and $\omega_i$ is the angular frequency of the $i^{\text{th}}$ normal mode of oscillation. The energy $E_i$ of the $i^{\text{th}}$ mode is

$$E_i = \hbar\omega_i(\nu_i + \tfrac{1}{2}) \tag{3.9}$$

and its wave function $\psi_{\nu_i}(\xi_i)$ is

$$\psi_{\nu_i}(\xi_i) = [2^{\nu_i} \nu_i! (\pi/\alpha_i)^{\frac{1}{2}}]^{-\frac{1}{2}} \exp(-\tfrac{1}{2}\alpha_i \xi_i{}^2) H_{\nu_i}(\alpha_i^{\frac{1}{2}} \xi_i) \tag{3.10}$$

where

$$\alpha_i = \omega_i/\hbar \tag{3.11}$$

and $H_\nu(x)$ is a Hermite polynomial. The wave function for the whole molecule is $\prod_i \psi_{\nu_i}$ corresponding to an energy $\sum_i E_i$.

If one introduces the abbreviation

$$b\binom{k}{i} = m_k^{-\frac{1}{2}} \mathbf{Q}_\lambda \cdot \mathbf{e}(k|i) \tag{3.12}$$

the scattering power for the $k^{\text{th}}$nucleus can be written in terms of normal coordinates thus

$$f_k^{\nu,\nu+\lambda} = \prod_i \langle \nu_i | \exp[ib\binom{k}{i}\xi_i] | \nu_i + \lambda_i \rangle$$

$$= \prod_i [(\pi/a_i) 2^{2\nu_i+\lambda_i} \nu_i!(\nu_i+\lambda_i)!]^{-\frac{1}{2}} \int_{-\infty}^{\infty} \exp[ib\binom{k}{i}\xi_i - a_i\xi_i^2]$$

$$\times H_{\nu_i}(a_i^{\frac{1}{2}}\xi_i) H_{\nu_i+\lambda_i}(a_i^{\frac{1}{2}}\xi_i)\, d\xi_i$$

$$(3.13) \qquad = \prod_i [\nu_i!/(\nu_i+\lambda_i)!]^{\frac{1}{2}} \left[ -b\binom{k}{i}^2 \Big/ 2a_i \right]^{\lambda_i/2} \exp\left[ -b\binom{k}{i}^2 \Big/ 4a_i \right]$$

$$\times L_{\nu_i}^{\lambda_i}\left[ b\binom{k}{i}^2 \Big/ 2a_i \right].$$

The last equation is obtained from the preceding one by using the Fourier transform of the product of the wave functions (14). $L_\nu^\lambda$ is a generalized Laguerre Polynomial.* If

$$(3.14) \qquad z_i = \exp(-\tfrac{1}{2}\hbar\omega_i/kT) = \exp(-\beta_i)$$

the explicit form of the thermal average is

$$\mathsf{S}_\nu f_k^{\nu,\nu+\lambda} f_{k'}^{\nu,\nu+\lambda} = \prod_i (1-z_i) \sum_{\nu_i} z_i^{\nu_i} \langle \nu_i | \exp\left\{ \left[ ib\binom{k}{i} \right] \xi_i \right\} | \nu_i + \lambda_i \rangle$$

$$(3.15) \qquad \times \langle \nu_i | \exp\left[ ib\binom{k}{i} \right] \xi_i | \nu_i + \lambda_i \rangle^*$$

$$= \prod_i \left[ b\binom{k'}{i} \Big/ 2a_i \right]^{\lambda_i} \exp\left\{ -\left[ b\binom{k}{i}^2 + b\binom{k'}{i}^2 \right] \Big/ 4a_i \right\} (1-z_i)$$

$$(3.16) \qquad \times \sum_{\nu_i} [\nu_i! z_i^{\nu_i}/(\nu_i+\lambda_i)!] L_{\nu_i}^{\lambda_i}\left[ b\binom{k}{i}^2 \Big/ 2a_i \right] L_{\nu_i}^{\lambda_i}\left[ b\binom{k'}{i}^2 \Big/ 2a_i \right]$$

$$(3.17) \qquad = \prod_i z_i^{-\lambda_i/2} \exp\left\{ -\left[ \frac{b\binom{k}{i}^2 + b\binom{k'}{i}^2}{4a_i} \right] \left( \frac{1+z_i}{1-z_i} \right) \right\} I_{\lambda_i}\left[ \frac{b\binom{k}{i} b\binom{k'}{i} z_i^{\frac{1}{2}}}{a_i(1-z_i)} \right].$$

The summation in (3.16) over $\nu_i$ has been evaluated by using a formula due to Hardy (7). $I_\lambda$ is a modified Bessel function (7). These equations are valid for both positive and negative values of $\lambda_i$ corresponding to a gain or loss of energy by the oscillators. If the generating function of the modified Bessel functions is used (3.17) can be summed over all positive and negative values of $\lambda_i$ to give

$$\prod_i \exp\left\{ -\left[ b\binom{k}{i} - b\binom{k'}{i} \right]^2 (\hbar/4\omega_i) \coth(\beta_i/2) \right\}.$$

This expression represents the thermal average of all matrix elements from an initial state. Its value is well known from the treatment of X-ray scattering by

*See Reference 14, p. 84.

crystal lattices (5). For most gases at room temperature the argument of the modified Bessel function,

$$b\binom{k}{i}b\binom{k'}{i}\frac{z_i^{\frac{1}{2}}}{a_i(1-z_i)},$$

is so small that the Bessel function may be replaced by the first term of its series expansion. The thermal average then becomes

$$\sum_\nu f_k^{\nu,\nu+\lambda} f_{k'}^{\nu,\nu+\lambda}$$

$$= \prod_i \frac{z_i^{(|\lambda_i|-\lambda_i)/2}}{|\lambda_i|!}\left[\frac{b\binom{k}{i}b\binom{k'}{i}}{2a_i(1-z_i)}\right]^{|\lambda_i|} \exp\left\{-\left[\frac{b\binom{k}{i}^2 + b\binom{k'}{i}^2}{4a_i}\right]\left(\frac{1+z_i}{1-z_i}\right)\right\}. \tag{3.18}$$

It is convenient to introduce the following abbreviations

$$a'_i = a_i(1+z_i)/(1-z_i), \tag{3.19}$$

$$T^\lambda_k = (4m_k)^{-1}\sum_i (a'_i)^{-1}[\mathbf{Q}_\lambda \cdot \mathbf{e}(k|i)]^2 \tag{3.20}$$

and then, substituting the expressions for the thermal averages in (3.2), one obtains for the cross section

$$\sigma^\lambda(\theta') = \mu^2 X_\lambda \frac{p_\lambda}{p_0}\sum_{kk'} (A_kA_{k'} + C_k^2\delta_{kk'})\{\exp(i\mathbf{Q}_\lambda \cdot \mathbf{r}_{kk'} - T^\lambda_k - T^\lambda_{k'})$$

$$\times \prod_i z_i^{-\lambda_i/2} I_{\lambda_i}\left[\frac{b\binom{k}{i}b\binom{k'}{i}z_i^{\frac{1}{2}}}{a_i(1-z_i)}\right]\Big\}^\dagger \tag{3.21}$$

$$\approx \mu^2 X_\lambda \frac{p_\lambda}{p_0}\sum_{kk'} (A_kA_{k'} + C_k^2\delta_{kk'})\{\exp(i\mathbf{Q}_\lambda \cdot \mathbf{r}_{kk'} - T^\lambda_k - T^\lambda_{k'})$$

$$\times \prod_i z_i^{(|\lambda_i|-\lambda_i)/2}\left[\frac{b\binom{k}{i}b\binom{k'}{i}}{2a_i(1-z_i)}\right]^{|\lambda_i|}\Big\}^\dagger. \tag{3.22}$$

From the last equation it can be seen that the differential cross section for the neutron to gain a given amount of energy, say $\Delta E$, is $\exp(-\Delta E/kT)$ times the cross section for the neutron to lose this amount of energy. If the contribution of any pair of nuclei $k$ and $k'$ to the cross section is written $\sigma_{kk'}{}^\lambda(\theta')$ then the ratio of the contributions corresponding to the energy changes $\lambda$ and $\lambda'$ can be shown to be given approximately by

$$\frac{\sigma_{kk'}{}^\lambda(\theta')}{\sigma_{kk'}{}^{\lambda'}(\theta')} \approx \prod_i \frac{z_i^{|\lambda_i|-\lambda_i}[m(m_km_{k'})^{-\frac{1}{2}}E_0/\hbar\omega_i]^{|\lambda_i|}}{z_i^{|\lambda_i'|-\lambda_i}[m(m_km_{k'})^{-\frac{1}{2}}E_0/\hbar\omega_i]^{|\lambda_i'|}}. \tag{3.23}$$

If $E_0/h$ is comparable with the frequencies of vibration, inelastic scatterings (especially multiple transitions) are improbable except from pairs of light nuclei. If only one oscillator gains one quantum of energy $\sigma_{kk'}{}^\lambda(\theta')$ is smaller than the corresponding quantity for elastic scattering by the factor $m(m_km_{k'})^{-\frac{1}{2}}$. If the oscillator loses a quantum of energy $\sigma_{kk'}{}^\lambda(\theta')$ is further reduced by the Boltzmann

factor $\exp(-\hbar\omega_i/kT)$. Similar results have been obtained by Weinstock (21) for the scattering of neutrons by crystals.

In order to interpret the scattering from $CF_4$, Alcock and Hurst (3) suggested that the vibration of each nucleus could be represented by the ground state of a three-dimensional isotropic harmonic oscillator. A generalization of this model is suggested by (3.22). The elastic scattering from a set of uncoupled anisotropic oscillators (not necessarily in their ground states) is given, in the approximation of (3.22), by

$$\sigma(\theta') = \mu^2 X_0 \sum_{kk'} (A_k A_{k'} + C_k^2 \delta_{kk'})[f_k f_{k'} \exp(i\mathbf{Q}_0 \cdot \mathbf{r}_{kk'})]^\dagger \tag{3.24}$$

$$f_k = \exp[-\tfrac{1}{2}(Q_x^2 a_x^2 + Q_y^2 a_y^2 + Q_z^2 a_z^2)], \tag{3.25}$$

where $a_x$, $a_y$, and $a_z$ are the mean amplitudes of vibration in the $x$, $y$, and $z$ directions respectively. Their values are given by the following equation:

$$a_\alpha^2 = \frac{\hbar}{2\omega_\alpha m_k} \frac{1 + z_\alpha}{1 - z_\alpha}, \quad \alpha = x, y, z. \tag{3.26}$$

Now $T_k^0$ is given by (3.20) as a quadratic form in the components of $\mathbf{Q}_0$. By a proper choice of axes this form can be diagonalized and written

$$T_k^0 = \tfrac{1}{2} \sum_\alpha Q_\alpha^2 \sum_i a_i^2 [e_\alpha(k|i)], \quad \alpha = x, y, z. \tag{3.27}$$

Thus the elastic cross section given by (3.22) is the same as that for a set of uncoupled oscillators provided their mean amplitudes, $a_\alpha^k$, along the axes of the form $T_k^0$ are defined by

$$(a_\alpha^k)^2 = \sum_i a_i^2 [e_\alpha(k|i)]^2. \tag{3.28}$$

The effective square amplitude along any axis is the sum of the squares of the mean displacements along that axis for all the modes of vibration.

The representation of the elastic scattering as that due to a set of uncoupled anisotropic oscillators is only possible when the approximate form of the cross section is used. If all the nuclei have spin zero it is easily shown that (3.22) for elastic scattering represents the scattering from the mean nuclear density, i.e.

$$\sigma^0(\theta') = \mu^2 X_0 \left[ \left| \sum_k A_k \mathsf{S}_\nu f_k^{\nu,\nu} \exp(i\mathbf{Q}_0 \cdot \mathbf{r}_k) \right|^2 \right]^\dagger$$

$$= \mu^2 X_0 \left[ \left| \sum_k A_k \exp(i\mathbf{Q}_0 \cdot \mathbf{r}_k - T_k^0) \right|^2 \right]^\dagger.$$

In analogy with Zachariasen's terminology for X-ray scattering from crystals (23) this may be called the order or coherent scattering and the difference between this and the total cross section, (3.21), the disorder scattering. While it is possible to choose a set of uncoupled oscillators to give the same coherent scattering as that from a set of coupled oscillators the disorder scattering from the two sets will not be the same. The quantity $F_k^0 = e^{-T_k^0}$ may be defined as the elastic nuclear scattering power.

The approximate cross section will now be worked out in detail for spherical top molecules of the type $YX_4$ for elastic scattering and for the simplest case of inelastic scattering. The calculation is divided into two parts: (1) the calculation of the elastic nuclear scattering powers, (2) the average over the directions of **Q**.

## 4. THE NUCLEAR SCATTERING POWER FOR THE $YX_4$ MOLECULE

To evaluate $T_k^{\lambda}(k = Y, X_1, \ldots, X_4)$ it is necessary to find the eigenvectors for the molecule $YX_4$. The eigenvalue problem has been formulated by Johnston and Dennison (13) in the following coordinate system. The positions of the four nuclei $X_s(s = 1, \ldots, 4)$* are fixed relative to their center of gravity $G$ by means of the mutual displacements $q_1, q_2, \ldots, q_6$ of the particles along the edges of the tetrahedron defined by the equilibrium configuration of the $X_s$, $q_1$ and $q_2$, $q_3$ and $q_4$, $q_5$ and $q_6$ relating to opposite edges of the tetrahedron. The displacement of Y relative to $G$ is given by the three cartesian components $x$, $y$, and $z$ where the $x$, $y$, and $z$ axes are the joins of the midpoints of the opposite edges associated with $q_1$, $q_2$,; $q_3$, $q_4$; and $q_5$, $q_6$ of the equilibrium tetrahedron. If $\lambda$ is written for $\omega_i^2$ the eigenvectors and eigenfrequencies are the solutions of the following matrix equation.*

(4.1)

$$\begin{vmatrix}
a-\mu'\lambda & . & . & e & -e & . & . & . & . \\
. & a-\mu'\lambda & . & . & . & e & -e & . & . \\
. & . & a-\mu'\lambda & . & . & . & . & e & -e \\
e & . & . & b-\frac{5}{8}m_X\lambda & d-\frac{1}{8}m_X\lambda & c+\frac{1}{8}m_X\lambda & c+\frac{1}{8}m_X\lambda & c+\frac{1}{8}m_X\lambda & c+\frac{1}{8}m_X\lambda \\
-e & . & . & d-\frac{1}{8}m_X\lambda & b-\frac{5}{8}m_X\lambda & c+\frac{1}{8}m_X\lambda & c+\frac{1}{8}m_X\lambda & c+\frac{1}{8}m_X\lambda & c+\frac{1}{8}m_X\lambda \\
. & e & . & c+\frac{1}{8}m_X\lambda & c+\frac{1}{8}m_X\lambda & b-\frac{5}{8}m_X\lambda & d-\frac{1}{8}m_X\lambda & c+\frac{1}{8}m_X\lambda & c+\frac{1}{8}m_X\lambda \\
. & -e & . & c+\frac{1}{8}m_X\lambda & c+\frac{1}{8}m_X\lambda & d-\frac{1}{8}m_X\lambda & b-\frac{5}{8}m_X\lambda & c+\frac{1}{8}m_X\lambda & c+\frac{1}{8}m_X\lambda \\
. & . & e & c+\frac{1}{8}m_X\lambda & c+\frac{1}{8}m_X\lambda & c+\frac{1}{8}m_X\lambda & c+\frac{1}{8}m_X\lambda & b-\frac{5}{8}m_X\lambda & d-\frac{1}{8}m_X\lambda \\
. & . & -e & c+\frac{1}{8}m_X\lambda & c+\frac{1}{8}m_X\lambda & c+\frac{1}{8}m_X\lambda & c+\frac{1}{8}m_X\lambda & d-\frac{1}{8}m_X\lambda & b-\frac{5}{8}m_X\lambda
\end{vmatrix}
\begin{vmatrix} x \\ y \\ z \\ q_1 \\ q_2 \\ q_3 \\ q_4 \\ q_5 \\ q_6 \end{vmatrix} = 0$$

The masses of the X and Y particles are $m_X$ and $m_Y$ respectively and

$$\mu' = 4m_X m_Y (4m_X + m_Y)^{-1}. \tag{4.2}$$

On account of its symmetry the potential energy can be expressed as a quadratic form involving only five independent constants, $a$, $b$, $c$, $d$, and $e$.

The molecule has four fundamental angular frequencies $\omega_I$, $\omega_{II}$, $\omega_{III}$, $\omega_{IV}$ which are singly, double, triply, and triply degenerate respectively. Johnston and Dennison quote the following equations for the frequencies,

$$\begin{aligned}
m_X\lambda_I &= 4b + 4d + 16c, \\
m_X\lambda_{II} &= b + d - 2c, \\
m_X(\lambda_{III} + \lambda_{IV}) &= m_X a(\mu' + 2b - 2d)^{-1}, \\
m_X^2\lambda_{III}\lambda_{IV} &= (2m_X/\mu')(ab - ad - 2e^2).
\end{aligned} \tag{4.3}$$

**Although $X\lambda$ has been used for the transformation factor from the center of mass system, the notation should not lead to confusion. $\lambda$ is also used in this section for $\omega_i^2$.*

Knowing the values of the frequencies one can then solve for the eigenvectors. It is easily verified by direct substitution in (4.1) that the orthonormal* set of vectors shown in Table I is a suitable set of eigenvectors provided that the numbers $S_{III}$ and $S_{IV}$ are solutions of the equations

$$a - \mu'\lambda_\rho + 4\sqrt{2}\,eS_\rho = 0, \quad \rho = \text{III, IV},$$
$$e + (b - d - \tfrac{1}{2}m_X\lambda_\rho)2\sqrt{2}S_\rho = 0. \tag{4.4}$$

TABLE I

EIGENVECTORS IN SYMMETRY COORDINATES

| $(i)$ | Frequency | $n_i^2$ | $x$ | $y$ | $z$ | $q_1$ | $q_2$ | $q_3$ | $q_4$ | $q_5$ | $q_6$ |
|---|---|---|---|---|---|---|---|---|---|---|---|
| 1 | $\omega_I$ | $3m_X/2$ | 0 | 0 | 0 | 1 | 1 | 1 | 1 | 1 | 1 |
| 2 | $\omega_{II}$ | $4m_X$ | 0 | 0 | 0 | −1 | −1 | 1 | 1 | 0 | 0 |
| 3 | $\omega_{II}$ | $12m_X$ | 0 | 0 | 0 | −1 | −1 | −1 | −1 | 2 | 2 |
| 4 | $\omega_{III}$ | $\frac{1}{8}\mu' + m_X S_{III}^2$ | 1 | 0 | 0 | $S_{III}$ | $-S_{III}$ | 0 | 0 | 0 | 0 |
| 5 | $\omega_{III}$ | $\frac{1}{8}\mu' + m_X S_{III}^2$ | 0 | 1 | 0 | 0 | 0 | $S_{III}$ | $-S_{III}$ | 0 | 0 |
| 6 | $\omega_{III}$ | $\frac{1}{8}\mu' + m_X S_{III}^2$ | 0 | 0 | 1 | 0 | 0 | 0 | 0 | $S_{III}$ | $-S_{III}$ |
| 7 | $\omega_{IV}$ | $\frac{1}{8}\mu' + m_X S_{IV}^2$ | 1 | 0 | 0 | $S_{IV}$ | $-S_{IV}$ | 0 | 0 | 0 | 0 |
| 8 | $\omega_{IV}$ | $\frac{1}{8}\mu' + m_X S_{IV}^2$ | 0 | 1 | 0 | 0 | 0 | $S_{IV}$ | $-S_{IV}$ | 0 | 0 |
| 9 | $\omega_{IV}$ | $\frac{1}{8}\mu' + m_X S_{IV}^2$ | 0 | 0 | 1 | 0 | 0 | 0 | 0 | $S_{IV}$ | $-S_{IV}$ |

*The modes of vibration $(i)$ are numbered consecutively from 1 to 9, their angular frequencies are shown in the second column, the components of the eigenvector belonging to the $i^{th}$ mode are written in the line labeled by the appropriate value of $i$. $1/n_i$ is the normalizing factor for the $i^{th}$ eigenvector, and $S_{III}$ and $S_{IV}$ are solutions of (4.4).*

If $\lambda_\rho$ is eliminated from these equations one obtains a quadratic equation in $S_\rho$ whose roots are $S_{III}$ and $S_{IV}$. On the other hand the elimination of $S_\rho$ leads to the equations for $\lambda_{III}$ and $\lambda_{IV}$.

The relations between the symmetry coordinates of Johnston and Dennison and the cartesian $u_a^k$ defined in Section 3 are given in Table II which shows the

TABLE II

RELATION BETWEEN SYMMETRY AND CARTESIAN COORDINATES $u_a^k$

| Symmetry coordinate | Y | $X_1$ | | | $X_2$ | | | $X_3$ | | | $X_4$ | | |
|---|---|---|---|---|---|---|---|---|---|---|---|---|---|
| $x = 1$ | $K\,0\,0$ | $L$ | 0 | 0 | $L$ | 0 | 0 | $L$ | 0 | 0 | $L$ | 0 | 0 |
| $y = 1$ | $0\,K\,0$ | 0 | $L$ | 0 | 0 | $L$ | 0 | 0 | $L$ | 0 | 0 | $L$ | 0 |
| $z = 1$ | $0\,0\,K$ | 0 | 0 | $L$ | 0 | 0 | $L$ | 0 | 0 | $L$ | 0 | 0 | $L$ |
| $q_1 = 2\sqrt{2}$ | 0 0 0 | $-\frac{1}{2}$ | 1 | 1 | $\frac{1}{2}$ | 0 | 0 | $\frac{1}{2}$ | 0 | 0 | $-\frac{1}{2}$ | $-1$ | $-1$ |
| $q_2 = 2\sqrt{2}$ | 0 0 0 | $-\frac{1}{2}$ | 0 | 0 | $\frac{1}{2}$ | $-1$ | 1 | $\frac{1}{2}$ | 1 | $-1$ | $-\frac{1}{2}$ | 0 | 0 |
| $q_3 = 2\sqrt{2}$ | 0 0 0 | 1 | $-\frac{1}{2}$ | 1 | 0 | $\frac{1}{2}$ | 0 | $-1$ | $-\frac{1}{2}$ | $-1$ | 0 | $\frac{1}{2}$ | 1 |
| $q_4 = 2\sqrt{2}$ | 0 0 0 | 0 | $-\frac{1}{2}$ | 0 | $-1$ | $\frac{1}{2}$ | 1 | 0 | $-\frac{1}{2}$ | 0 | 1 | $\frac{1}{2}$ | $-1$ |
| $q_5 = 2\sqrt{2}$ | 0 0 0 | 1 | 1 | $-\frac{1}{2}$ | $-1$ | $-1$ | $-\frac{1}{2}$ | 0 | 0 | $\frac{1}{2}$ | 0 | 0 | $\frac{1}{2}$ |
| $q_6 = 2\sqrt{2}$ | 0 0 0 | 0 | 0 | $-\frac{1}{2}$ | 0 | 0 | $-\frac{1}{2}$ | $-1$ | 1 | $\frac{1}{2}$ | 1 | $-1$ | $\frac{1}{2}$ |

*The magnitudes of the cartesian components of the nuclear displacements $u_a^k$ produced, for the values of the symmetry coordinate shown in the first column, are given in the column underneath the corresponding nuclei. The equilibrium positions $X_1$, $X_2$, $X_3$, $X_4$ lie in the directions (1, 1, 1), (−1, −1, 1), (−1, 1, −1), (1, −1, −1) respectively. All cartesian systems are parallel to the one at G. $K = \mu'/m_Y$ and $L = -\mu'/4m_X$. Terms involving powers of $q_i/2r_{XY}$ higher than the first have been neglected.*

*N.B. The metric tensor of the space is given by the kinetic energy tensor.

TABLE III

REDUCED EIGENVECTORS ($\mathbf{e}(k|i)$)

| Mode ($i$) | $N_i^2$ | $\mathbf{e}(Y\|i)$ | $\mathbf{e}(X_1\|i)$ | $\mathbf{e}(X_2\|i)$ | $\mathbf{e}(X_3\|i)$ | $\mathbf{e}(X_4\|i)$ |
|---|---|---|---|---|---|---|
| 1 | 12 | $O\ O\ O$ | $1\quad 1\quad 1$ | $-1\quad -1\quad 1$ | $-1\quad 1\quad -1$ | $1\quad -1\quad -1$ |
| 2 | 8 | $O\ O\ O$ | $1\quad -1\quad 0$ | $-1\quad 1\quad 0$ | $-1\quad -1\quad 0$ | $1\quad 1\quad 0$ |
| 3 | 24 | $O\ O\ O$ | $1\quad 1\quad -2$ | $-1\quad -1\quad -2$ | $-1\quad 1\quad 2$ | $1\quad -1\quad 2$ |
| 4 | $N_{III}^2$ | $M\ O\ O$ | $L\quad S_{III}\quad S_{III}$ | $L\quad S_{III}\quad -S_{III}$ | $L\quad -S_{III}\quad S_{III}$ | $L\quad -S_{III}\quad -S_{III}$ |
| 5 | $N_{III}^2$ | $O\ M\ O$ | $S_{III}\quad L\quad S_{III}$ | $S_{III}\quad L\quad -S_{III}$ | $-S_{III}\quad L\quad -S_{III}$ | $-S_{III}\quad L\quad S_{III}$ |
| 6 | $N_{III}^2$ | $O\ O\ M$ | $S_{III}\quad S_{III}\quad L$ | $-S_{III}\quad -S_{III}\quad L$ | $S_{III}\quad -S_{III}\quad L$ | $-S_{III}\quad S_{III}\quad L$ |
| 7 | $N_{IV}^2$ | $M\ O\ O$ | $L\quad S_{IV}\quad S_{IV}$ | $L\quad S_{IV}\quad -S_{IV}$ | $L\quad -S_{IV}\quad S_{IV}$ | $L\quad -S_{IV}\quad -S_{IV}$ |
| 8 | $N_{IV}^2$ | $O\ M\ O$ | $S_{IV}\quad L\quad S_{IV}$ | $S_{IV}\quad L\quad -S_{IV}$ | $-S_{IV}\quad L\quad -S_{IV}$ | $-S_{IV}\quad L\quad S_{IV}$ |
| 9 | $N_{IV}^2$ | $O\ O\ M$ | $S_{IV}\quad S_{IV}\quad L$ | $-S_{IV}\quad -S_{IV}\quad L$ | $S_{IV}\quad -S_{IV}\quad L$ | $-S_{IV}\quad S_{IV}\quad L$ |

$N_{III}^2 = (\mu'/m_X) + 8\,S_{III}^2$, $N_{IV}^2 = (\mu'/m_X) + 8\,S_{IV}^2$, $L = -\mu'/4m_X$, $M = \mu'\,(m_X m_Y)^{-\frac{1}{2}}$.

*$1/N_i$ is a normalizing factor. The cartesian components of the vectors $\mathbf{e}(k|i)$ for different modes of vibration are given in columns for different values of $k$.*

displacements of the nuclei for specific values of the symmetry coordinates. The reduced eigenvectors $\mathbf{e}(k|i)$ are obtained from the set given in Table I by using the transformation defined in Table II and are shown in Table III. If the values of $\mathbf{e}(k|i)$ are substituted in (3.20) one obtains $T^{\lambda}{}_{k}$ which can be written in the following form

$$T^{\lambda}{}_{k} = \gamma_k Q_\lambda{}^2 + \delta_k Q\begin{pmatrix}\lambda\\ k\end{pmatrix}^2. \tag{4.5}$$

Equation (4.5) for $T^{\lambda}{}_{k}$ has symmetry characteristic of the $YX_4$ molecule. For $k = X_s$, $Q\begin{pmatrix}\lambda\\ k\end{pmatrix}$ will be written $Q\begin{pmatrix}\lambda\\ s\end{pmatrix}$ and is defined by the equation

$$Q\begin{pmatrix}\lambda\\ s\end{pmatrix} = \sqrt{3}(\mathbf{Q}_\lambda \cdot \mathbf{r}_k)/r_k; \tag{4.6}$$

it is undefined for $k = Y$. The other constants are given by

$$\gamma_Y = \left(\frac{\mu'}{2m_Y}\right)^2\left[\frac{1}{a'_{III}(\mu' + 8m_X S_{III}{}^2)} + \frac{1}{a'_{IV}(\mu' + 8m_X S_{IV}{}^2)}\right] \quad \text{for } k = Y,$$

$$\gamma_X = \frac{1}{16m^2}\left[\frac{m}{a'_{II}} + \frac{(\mu' + 4m_X S_{III})^2}{4a'_{III}(\mu' + 8m_X S_{III}{}^2)} + \frac{(\mu' + 4m_X S_{IV})^2}{4a'_{IV}(\mu' + 8m_X S_{IV}{}^2)}\right]$$

$$\text{for } k = X_s,\ s = 1, 2, 3, 4. \tag{4.7}$$

$$\delta_Y = 0 \text{ for } k = Y,$$

$$\delta_X = \frac{1}{8m_X}\left[\frac{1}{6a'_I} - \frac{1}{6a'_{II}} - \frac{S_{III}(\mu' - 2m_X S_{III})}{a'_{III}(\mu' + 8m_X S_{III}{}^2)} - \frac{S_{IV}(\mu' - 2m_X S_{IV})}{a'_{IV}(\mu' + 8m_X S_{IV}{}^2)}\right]$$

$$\text{for } k = X_s.$$

The elastic nuclear scattering powers are

$$F_Y{}^0 = \exp(-\gamma_Y Q_0{}^2) \tag{4.8}$$

$$\begin{aligned} F_X{}^0 &= \exp\left\{-\left[\gamma_X Q_0{}^2 + \delta_X Q\begin{pmatrix}0\\ s\end{pmatrix}^2\right]\right\} \\ &= \exp\{-[\gamma_X Q_x{}^2 + \gamma_X Q_y{}^2 + (\gamma_X + \delta_X)Q_z{}^2]\} \end{aligned} \tag{4.9}$$

if $Q_x$, $Q_y$, $Q_z$ are the components of $\mathbf{Q}_0$ in a cartesian system which has the $z$ axis along $\mathbf{r}_{X_s}$. Equations (4.8) and (4.9) show that the scattering power of the Y nucleus has spherical symmetry, while that of an X nucleus (because of the factor $\delta_X$) has symmetry only about the line $\mathbf{r}_{X_s}$. From (3.25) it follows that the scattering from the Y atom is equivalent to that from an isotropic oscillator of mean amplitude $(2\gamma_Y)^{\frac{1}{2}}$, while the scattering from an X atom is equivalent to that from an anisotropic oscillator with mean amplitudes $(2\gamma_X)^{\frac{1}{2}}$, $(2\gamma_X)^{\frac{1}{2}}$, $[2(\gamma_X + \delta_X)]^{\frac{1}{2}}$ along the directions of $Q_x$, $Q_y$, and $Q_z$ respectively. $\sqrt{\delta_X}$ is a measure of the difference in amplitudes of vibration along and perpendicular to the bond direction.

## 5. THE DIFFERENTIAL CROSS SECTIONS FOR THE $YX_4$ MOLECULE

### *A. Elastic Scattering*

If the explicit values of the nuclear scattering powers are inserted in the equation for the elastic differential cross section it becomes

$$\sigma^0(\theta') = \mu^2 X_0 \sum_{kk'} (A_k A_{k'} + C_k^2 \delta_{kk'}) L^0_{kk'}, \tag{5.1}$$

where

$$L^0_{kk'} = \exp\left[-(\gamma_k + \gamma_{k'})Q_0^2\right]\left\{\exp\left[i\mathbf{Q}_0 \cdot \mathbf{r}_{kk'} - \delta_k Q\binom{0}{k}^2 - \delta_{k'} Q\binom{0}{k}^2\right]\right\}_{\dagger}. \tag{5.2}$$

For neutron diffraction by a fixed system of rigid nuclei $L^0_{kk'}$ is $\exp(i\mathbf{Q}_0 \cdot \mathbf{r}_{kk'})$: $L_{kk'}$ defined by (5.2) shows how the effects of rotation and vibration modify the simple exponential factor.

The evaluation of the averages over the directions of $\mathbf{Q}_0$ is carried out in the Appendix. $L^0_{kk'}$ depends on the anisotropy parameter, $\delta_X$, in an intricate way. For $k \neq k'$ the average can be expressed as a series in spherical Bessel functions whose arguments are $Q_0 r_{kk'}$ and whose coefficients are increasing powers of $\delta_X Q_0 / r_{kk'} = (4\pi\delta_X/\lambda r_{kk'}) \sin(\theta/2)$. If $\sqrt{\delta_X}$ is small enough, when compared with the wave length and internuclear distances, only the first terms in the series need to be considered. In this case the cross section reduces to

$$\begin{aligned}\sigma^0(\theta') = \mu^2 X_0 \{ & (A_Y^2 + C_Y^2)\exp(-2\gamma_Y Q_0^2) \\ & + 4(A_X^2 + C_X^2)\exp[-2(\gamma_X + \delta_X)Q_0^2] \\ & + 8A_X A_Y \exp[-(\gamma_Y + \gamma_X + 3\delta_X)Q_0^2] j_0(Q_0 r_{XY}) \\ & + 12A_X^2 \exp[-2(\gamma_X + 2\delta_X)Q_0^2] j_0(Q_0 r_{XX'})\}.\end{aligned} \tag{5.3}$$

If $\delta_X$ were zero one would expect the scattering to be the same as that from five spherical balls of appropriate density placed on a rigid rotating framework. This conclusion is confirmed by putting $\delta_X = 0$ in (5.3), whereupon the cross section becomes identical with that for a rigid molecule ( (2.11) ) except that each term is modified by the product of two scattering powers to take account of interference within the balls.

Before this equation can be compared with experiment $X_0$ and $Q_0$ have to be expressed in terms of $\theta'$. If the following abbreviations are introduced

$$\begin{aligned} Q_{00} &= (4\pi/\lambda) \sin(\theta'/2) \\ Q_{01} &= Q_{00} \cos^2(\theta'/2) \end{aligned} \tag{5.4}$$

then to the first power in $1/A$ one can write

$$\begin{aligned} \exp(-aQ_0^2) &= [1 - (2a/A)Q_{00}Q_{01}] \exp(-aQ_{00}^2), \\ j_0(Q_0 r) &= j_0(Q_{00} r) - (1/A)Q_{01} r\, j_1(Q_{00} r). \end{aligned} \tag{5.5}$$

The cross section can then be written

$$\sigma^0(\theta') = \mu^2[\sigma_0^0(\theta') + (1/A)\sigma_1^0(\theta')] \tag{5.6}$$

with

$$\sigma_0{}^0(\theta') = (A_Y{}^2 + C_Y{}^2)\exp(-2\gamma_Y Q_{00}{}^2) + 4(A_X{}^2 + C_X{}^2)\exp[-2(\gamma_X + \delta_X)Q_{00}{}^2] + 8A_X A_Y \exp[-(\gamma_Y + \gamma_X + 3\delta_X)Q_{00}{}^2] j_0(Q_{00} r_{XY}) + 12A_X{}^2 \exp[-2(\gamma_X + 2\delta_X)Q_{00}{}^2] j_0(Q_{00} r_{XX'}) \tag{5.7}$$

and

$$\sigma_1{}^0(\theta') = (A_Y{}^2 + C_Y{}^2)(2\cos\theta' - 4\gamma_Y Q_{00}Q_{01})\exp(-2\gamma_Y Q_{00}{}^2) + 4(A_X{}^2 + C_X{}^2)[2\cos\theta' - 4(\gamma_X + \delta_X)Q_{00}Q_{01}]\exp[-2(\gamma_X + \delta_X)Q_{00}{}^2] + 8A_X A_Y \exp[-(\gamma_Y + \gamma_X + 3\delta_X)Q_{00}{}^2] \times \{[2\cos\theta' - 2(\gamma_X + \gamma_Y + 3\delta_X)Q_{00}Q_{01}]j_0(Q_{00} r_{XY}) - Q_{01} r_{XY} j_1(Q_{00} r_{XY})\} + 12A_X{}^2 \exp[-2(\gamma_X + 2\delta_X)Q_{00}{}^2] \times \{[2\cos\theta' - 4(\gamma_X + 2\delta_X)Q_{00}Q_{01}]j_0(Q_{00} r_{XX'}) - Q_{01} r_{XX'} j_1(Q_{00} r_{XX'})\}. \tag{5.8}$$

$\sigma_1{}^0(\theta')$ arises in two ways owing to the relationship between (i) elements of solid angle and (ii) scattering angles in the center of mass and laboratory systems. For most spherical top molecules the first term in $1/A$ is sufficient for 1% accuracy. Methane is an exception.

*B. Inelastic Scattering*

The only inelastic processes which have an appreciable probability for neutrons whose wave lengths lie in the 1Å region are those in which one oscillator emits or absorbs one quantum of energy. The cross section for this process is given by (3.22) if all $\lambda_i$ are put equal to zero except one, say $\lambda_j$, which is put equal to $\pm 1$. The corresponding cross sections $\sigma^{\lambda_i=1}(\theta')$, $\sigma^{\lambda_i=-1}(\theta')$ are given by

$$\begin{matrix}\sigma^{\lambda_i=1}(\theta') = 1 \\ \sigma^{\lambda_i=-1}(\theta') = z_j\end{matrix}\Bigg\} \frac{\mu^2 X_j}{2a_j(1-z_j)} \frac{p_j}{p_0} \sum_{kk'} [A_k A_{k'} + \delta_{kk'} C_k{}^2] \times \left[b\binom{k}{j} b\binom{k'}{j} \exp(i\mathbf{Q}_j \cdot \mathbf{r}_{kk'} - T^{\lambda}{}_k - T^{\lambda}{}_{k'})\right]^{\dagger}. \tag{5.9}$$

The upper line corresponds to the neutron losing a quantum of energy $\hbar\omega_j$; the lower to the neutron gaining a quantum $\hbar\omega_j$. The meaning of quantities with a suffix $J$ is obvious. Now quantities $L_{kk'}^{\omega J}$, analogous to $L_{kk'}^{0}$ are introduced by the equation

$$L_{kk'}^{\omega J} = \frac{m}{(m_k m_{k'})^{\frac{1}{2}}} \exp[-(\gamma_k + \gamma_{k'})Q_J{}^2] \times \left\{\sum_j \left[\frac{\mathbf{Q}_J \cdot \mathbf{e}(k|j)}{Q_j}\right]\left[\frac{\mathbf{Q}_J \cdot \mathbf{e}(k'|j)}{Q_j}\right] \exp\left[i\mathbf{Q}_J \cdot \mathbf{r}_{kk'} - \delta_k Q\binom{J}{k}^2 - \delta_{k'} Q\binom{J}{k'}^2\right]\right\}^{\dagger}. \tag{5.10}$$

In this equation $\hbar\omega_J$ is equal to the change in neutron energy which may be positive or negative. The expression is summed over all degenerate modes $j$ for which

$\omega_J = |\omega_J|$. All quantities with a suffix $J$ are defined for positive and negative values of $\omega_J$. The quantities $L^{\omega_J}_{kk'}$ are calculated in the appendix and are listed in Table IV. Since

$$Q_J^2 = \tfrac{1}{4}(4\pi/\lambda)^2[1 + (p_J/p_0)^2 - 2(p_J/p_0)\cos\theta] \tag{5.11}$$

it is easily seen that

$$Q_J^2/2a_J m = (E_0/E_J)(\lambda Q_J/2\pi)^2. \tag{5.12}$$

TABLE IV $L^{\omega_J}_{kk'}$

$$L^{\omega_I}_{YY} = L^{\omega_I}_{YX_s} = L^{\omega_{II}}_{YY} = L^{\omega_{II}}_{YX_s} = 0$$

$$L^{\omega_I}_{X_sX_s} = (m/8m_X)\exp(-2\gamma_X Q^2)[\tfrac{1}{2}\sqrt{\pi}D^{-3}\mathrm{erf}D - D^{-1}\exp(-D^2)]$$

$$L^{\omega_I}_{X_sX_{s'}} = (m/12m_X)\exp[-2(\gamma_X + 2\delta_X)Q^2][-2j_0(QR) + (5 - 2D^2)(QR)^{-1}j_1(QR)]$$

$$L^{\omega_{II}}_{X_sX_s} = (m/8m_X)\exp(-2\gamma_Y Q^2)[\tfrac{1}{2}\sqrt{\pi}(2D^{-1} - D^{-3})\mathrm{erf}D + D^{-2}\exp(-D^2)]$$

$$L^{\omega_{II}}_{X_sX_{s'}} = (m/12m_X)\exp[-2(\gamma_X + 2\delta_X)Q^2][-j_0(QR) + (1 - D^2)(QR)^{-1}j_1(QR)]$$

$$L^{\omega_{III}}_{YY} = (m/m_Y)(M/N_{III})^2\exp(-2\gamma_Y Q^2)$$

$$L^{\omega_{III}}_{X_sX_s} = (m/2m_X N_{III}^2)\exp(-2\gamma_X Q^2)\{(\tfrac{1}{2}\sqrt{\pi})[2(S_{III} - L)^2 D^{-1} + 3(S_{III}^2 + 2LS_{III})D^{-3}]\mathrm{erf}D - 3(S_{III}^2 + 2LS_{III})D^{-2}\exp(-D^2)\}$$

$$L^{\omega_{III}}_{YX_s} = (m\mu'/m_X m_Y N_{III}^2)\exp[-(\gamma_X + \gamma_Y)Q^2]\{(2S_{III} + L)j_0(QR_{XY}) - [6S_{III} - (2S_{III} + L)D^2](QR_{XY})^{-1}j_1(QR_{XY})\}$$

$$L^{\omega_{III}}_{X_sX_{s'}} = (m/m_X N_{III}^2)\exp[-2(\gamma_X + 2\delta_X)Q^2]\{[(S_{III} + L)^2 - 2S_{III}^2]j_0(QR) + (S_{III}^2 - 6L + D^2[(S_{III} + L)^2 - 2S_{III}^2](QR)^{-1})j_1(QR)\}$$

The quantites $L^{\omega_{I,V}}_{kk'}$ are obtained from $L^{\omega_{III}}_{kk'}$ by replacing III by IV. In order to simplify the writing suffixes have been omitted from $Q$. $D^2$ has been written for $6\delta_X Q^2$, and $R$ has been used for the distance between two X nuclei.

If (5.10), (5.11), and (5.12) are put in (5.9) the cross section becomes

$$\sigma^{\omega_J}(\theta') = \begin{matrix}1\\ z_J\end{matrix}\Big\{\frac{\mu^2 X_J}{1 - z_J}\frac{E_0}{E_J}\left(\frac{\lambda Q_J}{2\pi}\right)^2\frac{p_J}{p_0}[(A_Y^2 + C_Y^2)L^{\omega_J}_{YY} + 4(A_X^2 + C_X^2)L^{\omega_J}_{XX} + 8A_X A_Y L^{\omega_J}_{XY} + 12A_X^2 L^{\omega_J}_{XX'}]. \tag{5.13}$$

The upper line is to be used for positive $\omega_J$, the lower for negative $\omega_J$. The inelastic cross section for neutrons whose wave length is of the order of 1Å is so small compared to the elastic cross section that it is not necessary to consider

the small correction introduced by transforming the cross section to the laboratory system. $X_J$ can be put equal to unity and $\theta$ equal to $\theta'$.

The cross sections are functions of the nuclear scattering cross sections, the internuclear distances, and the mean amplitudes of nuclear vibrations. The latter quantities depend on the force constants of the molecule and these cannot always be determined uniquely.

## 6. APPLICATIONS

### *A. Carbon Tetrafluoride*

For this molecule there are only four relations between the five force constants and the frequencies (Equation (4.3) ). It is not possible, therefore, to express the force constants in terms of the frequencies without either making some assumption about the field or obtaining another relation. For $CF_4$ the Urey-Bradley field (20), which assumes central forces plus forces perpendicular to the bond line, has been used. The relation between this field, which has four independent constants in the potential energy, and the general field has been discussed by Rosenthal (16). Rosenthal gives the following series of equations for a set of force constants in terms of the frequencies.

$$A = \frac{1}{2}\mu'\left\{\lambda_{III} + \lambda_{IV} + [(\lambda_{III} - \lambda_{IV})^2 - 32D/\mu' m_X]^{\frac{1}{2}}\right\},$$

$$B = \frac{1}{16}m_X\left\{\lambda_{III} + \lambda_{IV} - [(\lambda_{III} - \lambda_{IV})^2 - 32D/\mu' m_X]^{\frac{1}{2}}\right\},$$

$$C = \frac{1}{4}m_X\lambda_{II},$$

$$D = \frac{5}{8}m_X(1 + 25m_X/2\mu')^{-1}\left\{\lambda_{III} + \lambda_{IV} - \frac{4}{5}(\lambda_I + \lambda_{II})\right.$$
$$\left. \mp [(1 + 25m_X/2\mu')(\lambda_{III} - \lambda_{IV})^2 - 128(m_X/\mu')(5\lambda_{III} + 5\lambda_{IV} - 4\lambda_I - 4\lambda_{II})^2]^{\frac{1}{2}}\right\},$$

$$E = \frac{1}{16}m_X\lambda_I. \tag{6.1}$$

The relation between the force constants is

$$10B - 2C - D - 8E = 0. \tag{6.2}$$

There are two sets of solutions corresponding to the two values of $D$. The set of solutions for which $12B + 4C - 16E > 0$ has been selected because the set for which $12B + 4C - 16E < 0$ is not usually regarded as being physically acceptable (16).

Johnston and Dennison (13) give the following relations between their force constants and those of Rosenthal's:

$$a = A, \quad c = \frac{2}{3}(E - C), \quad e = \sqrt{2}D,$$
$$b = 2B + \frac{2}{3}(2C + E), \quad d = -2B + \frac{2}{3}(2C + E). \tag{6.3}$$

The observed wave numbers, $\eta_i = \omega_i/2\pi C$ ($C$ is the velocity of light) in units of cm.$^{-1}$, are (10)

$$\eta_{\mathrm{I}} = 904, \eta_{\mathrm{II}} = 437, \eta_{\mathrm{III}} = 1265, \eta_{\mathrm{IV}} = 630.$$

These lead to the following values of the force constants which are expressed in units of $10^5$ dynes per cm.

$$a = 9.405, b = 2.381, c = 0.025, d = -0.190, e = 1.100.$$

The values of $S_{\mathrm{III}}$ and $S_{\mathrm{IV}}$ follow immediately from (4.4)

$$S_{\mathrm{III}} = 0.0608, \quad S_{\mathrm{IV}} = -1.1213.$$

For neutrons of wave length 1.063Å in the laboratory system (energy 0.0723 ev.), the dimensionless quantities $(4\pi/\lambda)^2\gamma_{\mathrm{Y}}$, $(4\pi/\lambda)^2\gamma_{\mathrm{X}}$, and $(4\pi/\lambda)^2\delta_{\mathrm{X}}$ are given from (4.7) as $6.934 \times 10^{-2}$, $5.660 \times 10^{-2}$, and $0.548 \times 10^{-2}$ respectively.

The only mode in $CF_4$ which can be excited by the incident neutrons is the doubly degenerate one of frequency $\omega_{\mathrm{II}}$ which is associated with a transition energy of 0.0542 ev. Since the superelastic scattering is so small only the most important term, which again is the one associated with the doubly degenerate mode, is considered. The cross section $\sigma(\theta')$ has therefore been calculated from

$$\sigma(\theta') = \mu^2[\sigma_{00}^0(\theta') + (1/A)\sigma_{01}^0(\theta')] + \sigma^{\omega_{\mathrm{II}}}(\theta') + \sigma^{-\omega_{\mathrm{II}}}(\theta'). \tag{6.4}$$

Anisotropy of the nuclear motion is so small in $CF_4$ that $(4\pi/\lambda)^2\delta_{\mathrm{X}}$ has been neglected in calculating the inelastic scattering.

The theoretical cross section has been compared with the experimental results* of Alcock and Hurst (3) by multiplying it by a normalizing factor. This and the coherent fluorine cross section were adapted by the method of least squares for a best fit. The results are shown graphically in Fig. 1. The full line

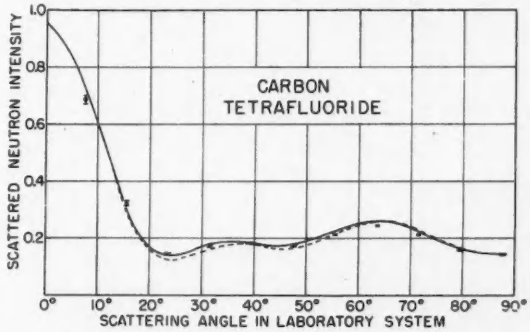


FIG. 1. The scattering of neutrons of wave length 1.063Å by carbon tetrafluoride. The points with standard deviations are taken from the experimental work of Alcock and Hurst (3). An outer effect correction has been applied to the first point. The experimental points have been fitted by the continuous curve which has been computed for a carbon fluorine bond length of 1.33Å and a coherent fluorine cross section of 3.46 barns. The dotted curve is drawn for a rigid molecule with a fixed center of mass.

**An "outer effect" correction has been applied to the first point. See Reference 3.*

curve has been drawn for a carbon–fluorine bond length of 1.33Å (3), a bound carbon cross section of 5.52 barns (1), and a bound total cross section for fluorine of 3.99 barns (1).

The value of the coherent fluorine cross section for a best fit is 3.46 barns. The only other measurement of the coherent fluorine cross section is one of 3.8 barns obtained by Shull and Wollan (18) from crystal diffraction measurements. Shull and Wollan, however, quote 5.2 barns for the bound carbon cross section. Use of this value for the bound carbon cross section leads to a value of 3.65 barns for the coherent fluorine cross section.

The dotted curve is drawn for a rigid molecule with a fixed center of mass. The agreement between the experimental points and the theoretical curve is good. The corrections for nuclear vibration and transformation to the laboratory system are small for carbon tetrafluoride.

Using the numerical values of $\gamma_Y$, $\gamma_X$, and $\delta_X$, one finds that the mean nuclear density of the carbon nucleus is equivalent to that of an isotropic oscillator with a mean amplitude of 0.032Å, while that of a fluorine nucleus is equivalent to that of an anisotropic oscillator with mean amplitudes of 0.028Å perpendicular to the bond direction and 0.030Å along the bond direction. These calculated amplitudes are in general agreement with the value of 0.032Å obtained by Alcock and Hurst (3) from fitting the diffraction pattern by the scattering from a set of identical isotropic oscillators in their ground states.

*B. Methane*

By calculating the internal angular momenta associated with the frequencies $\omega_{III}$ and $\omega_{IV}$ Johnston and Dennison obtained another relation between the frequencies and the force constants. Using this relation and, in addition, data from the spectrum of methyl deuteride they calculated the following values for the force constants: (the units are $10^5$ dynes per cm.)

$$a = 7.670, b = 1.616, c = -0.018, d = -0.289, e = 1.807.$$

They used the following values for the wave numbers in units of cm.$^{-1}$:

$$\eta_I = 2914, \eta_{II} = 1520, \eta_{III} = 3014, \eta_{IV} = 1304.$$

Following the same procedure as was adopted for $CF_4$ gives

$$S_{III} = 0.8187, \quad S_{IV} = -0.4553$$

and

$$(4\pi/\lambda)^2\gamma_Y = 1.323 \times 10^{-2}, \quad (4\pi/\lambda)^2\gamma_X = 28.63 \times 10^{-2},$$

$$(4\pi/\lambda)^2\delta_X = 10.17 \times 10^{-2}.$$

The equivalent system of oscillators consists of one isotropic oscillator with a mean amplitude of 0.014Å for carbon and one anisotropic oscillator, with mean amplitudes of 0.064Å perpendicular to the bond and 0.075Å along the bond for each proton.

Since neither the neutron energy nor the temperature is high enough to excite to any appreciable extent vibrational modes only the cross section for elastic scattering is needed. The elastic cross section has been computed for a carbon hydrogen bond length of 1.093Å (10), a bound total hydrogen cross section of 80.4 barns (1), and a coherent hydrogen cross section of 1.77 barns (11).

The computed cross section is compared in Fig. 2 with the pattern measured by Alcock and Hurst (3). A dotted line is again drawn for a rigid molecule with

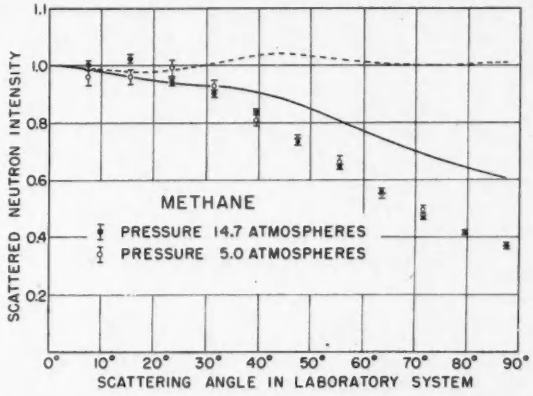


FIG. 2. The scattering of neutrons of wave length 1.063Å by methane. The points with standard deviations are taken from the experimental work of Alcock and Hurst (3). The experimental points have been fitted at small angles by the continuous curve. The poor fit at large angles shows the breakdown of the semiclassical approximation at large angles for molecules with a small moment of inertia. The dotted curve is drawn for a rigid molecule with a fixed center of mass.

a fixed center of mass. It is seen that the effects of vibration and the transformation to the laboratory system, while much greater for $CH_4$ than for $CF_4$, account for only half of the fall off of the experimental points from the dotted line. This is to be expected, since it follows from (2.4) that for 90° scattering at room temperature the greatest change in the energy of the neutron which can occur with a not too small probability is almost equal to its incident energy. The corresponding energy change for scattering from $CF_4$ is only one-sixth of the incident energy. The semiclassical approximation is thus unable to give an adequate description of large angle scattering by $CH_4$.

## 7. CONCLUSION

It has been shown that the diffraction by gases whose molecules do not contain light nuclei can be adequately described by a theory which treats the rotational motion in the semiclassical approximation and assumes all vibrations to be of small amplitude. The theory can therefore be used to analyze experimental results and hence to obtain information about nuclear scattering cross sections, internuclear distances, and the amplitudes of nuclear vibrations. If light nuclei are present corrections have to be made to the semiclassical theory. These will be submitted for publication in a separate paper.

The author wishes to express his thanks to Dr. Hurst for many stimulating discussions and to Miss Mary MacGregor who has done most of the numerical work.

## APPENDIX:
## AVERAGES OVER THE DIRECTIONS OF THE MOMENTUM TRANSFER VECTOR

### *A. Elastic Scattering*

In this appendix, use is made of the following integral:

$$\frac{1}{2}\int_{-1}^{1}(A+Bx^2+Cx^4)\exp(iax)\,dx = (A+B+C)\,j_0(a)-(B+2C)(2/a)\,j_1(a) + 2C(2/a)^2 j_2(a).$$

The required average is given in (5.2) and has the form

$$L^0_{kk'} = \exp[-(\gamma_k+\gamma_{k'})Q_0^2]\left\{\exp\left[i\mathbf{Q}\cdot\mathbf{r}_{kk'} - \delta_k Q\binom{0}{k}^2 - \delta_{k'}Q\binom{0}{k'}^2\right]\right\}^{\dagger}.$$

There are four cases to be considered.

(1) $L^0_{\mathrm{Y\,Y}} = \exp(-2\gamma_{\mathrm{Y}}Q_0^2)$

(2) $L^0_{\mathrm{X}_s\mathrm{X}_s} = (1/4\pi)\exp(-2\gamma_{\mathrm{X}}Q_0^2)\int_0^{\pi}\int_0^{2\pi}\exp(-6\delta_{\mathrm{X}}Q_0^2\cos^2\alpha)\sin\alpha\,d\alpha\,d\beta,$

where $\alpha$, $\beta$ are spherical polar coordinates of $\mathbf{Q}_0$ in a system with $\mathbf{X}_s$ for pole. It follows easily that

$$L^0_{\mathrm{X}_s\mathrm{X}_s} = (\pi^{\frac{1}{2}}/2)(6\delta_{\mathrm{X}}Q_0^2)^{-\frac{1}{2}}\exp[-2(\gamma_{\mathrm{X}}+\delta_{\mathrm{X}})Q_0^2]\,\mathrm{erf}^*(6\delta_{\mathrm{X}}Q_0^2)^{\frac{1}{2}}$$

$$\approx \exp[-2(\gamma_{\mathrm{X}}+\delta_{\mathrm{X}})Q_0^2].$$

(3) $L^0_{\mathrm{Y\,X}} = \frac{1}{4\pi}\exp[-(\gamma_{\mathrm{X}}+\gamma_{\mathrm{Y}})Q_0^2]\int_0^{\pi}\int_0^{2\pi}\exp\left[i\mathbf{Q}_0\cdot\mathbf{r}_{\mathrm{X\,Y}} - \delta_{\mathrm{X}}Q\binom{0}{\mathrm{X}}^2\right]\sin\alpha\,d\alpha\,d\beta.$

If $x$ is substituted for $\cos\alpha$ and $\exp(-3\delta_{\mathrm{X}}Q_0^2x^2)$ is expanded the average becomes

$$L^0_{\mathrm{Y\,X}} = \frac{1}{2}\exp[-(\gamma_{\mathrm{X}}+\gamma_{\mathrm{Y}})Q_0^2]\int_{-1}^{1}(1-3\delta_{\mathrm{X}}Q_0^2x^2+4\tfrac{1}{2}\delta_{\mathrm{X}}{}^2Q_0^4x^4\ldots) \times\exp(iQ_0r_{\mathrm{X\,Y}}x)\,dx$$

$$= \exp[-(\gamma_{\mathrm{X}}+\gamma_{\mathrm{Y}}+3\delta_{\mathrm{X}})Q_0^2][j_0(Q_0r_{\mathrm{X\,Y}}) + (6\delta_{\mathrm{X}}Q_0/r_{\mathrm{X\,Y}})j_1(Q_0r_{\mathrm{X\,Y}}) + (6\delta_{\mathrm{X}}Q_0/r_{\mathrm{X\,Y}})^2 j_2(Q_0r_{\mathrm{X\,Y}})\ldots].$$

(4) $L^0_{\mathrm{X}_1\mathrm{X}_2} = \left(\frac{1}{4\pi}\right)\exp(-2\gamma_{\mathrm{X}}Q_0^2)\int_0^{\pi}\int_0^{2\pi}\exp\left\{i\mathbf{Q}_0\cdot\mathbf{r}_{12} - \delta_{\mathrm{X}}\left[Q\binom{0}{1}^2 + Q\binom{0}{2}^2\right]\right\}\sin\alpha\,d\alpha\,d\beta.$

* $\mathrm{erf}\,x = (2/\sqrt{\pi})\int_0^x \exp(-t^2)\,dt.$

For brevity $X_1$, $X_2$ have been written 1, 2, respectively. Now if the polar axis is taken along $\mathbf{r}_1 - \mathbf{r}_2$ and the azimuth is measured from $\mathbf{r}_1 + \mathbf{r}_2$, the integral can be written

$$L^0_{X,X} = \frac{1}{4\pi}\exp\left[-(2\gamma_X + 4\delta_X)Q_0^2\right] \times \int_{-1}^{1}\int_{0}^{2\pi} \exp\left[iQ_0 r_{12}x + 2\delta_X Q_0^2(1-x^2)(1+\sin^2\beta)\right]dx\,d\beta.$$

The integral can be evaluated by expanding in powers of $\delta_X$ with the result,

$$L^0_{X,X} = \exp\left[-(2\gamma_X + 4\delta_X)Q_0^2\right]\left[j_0(Q_0 r_{12}) + 3(2\delta_X Q_0/r_{12})j_1(Q_0 r_{12}) + 9\tfrac{1}{2}(2\delta_X Q_0/r_{12})^2 j_2(Q_0 r_{12}) + \ldots\right].$$

*B. Inelastic Scattering*

According to (5.10) integrals of the following type are required:

$$L_{kk'} = Q_j^{-2}\exp\left[-(\gamma_k + \gamma_{k'})Q_j^2\right]\int(\mathbf{f}\cdot\mathbf{Q}_j)(\mathbf{g}\cdot\mathbf{Q}_j)\exp\left\{i\mathbf{Q}_j\cdot\mathbf{r}_{kk'} - \delta_X\left[Q\left(\frac{j}{k}\right)^2 + Q\left(\frac{j}{k'}\right)^2\right]\right\}d\omega/4\pi,$$

where

$$\mathbf{f} = (m/m_k)^{\frac{1}{2}}\mathbf{e}(k|j), \quad \mathbf{g} = (m/m_{k'})^{\frac{1}{2}}\mathbf{e}(k'|j)$$

and $d\omega$ is the element of solid angle in which the vector $\mathbf{Q}_j$ lies.

Just as for elastic scattering, four cases have to be considered.

(1) $$L_{YY} = Q_j^{-2}\exp\left(-2\gamma_Y Q_j^2\right)\int(\mathbf{f}\cdot\mathbf{Q}_j)^2 d\omega/4\pi = \tfrac{1}{3}f^2\exp\left(-2\gamma_Y Q_j^2\right)$$

(2) $$L_{X,X} = Q_j^{-2}\exp\left(-2\gamma_X Q_j^2\right)\int(\mathbf{f}\cdot\mathbf{Q}_j)^2\exp\left[-2\delta_X Q\left(\frac{j}{1}\right)^2\right]d\omega/4\pi.$$

The components of $\mathbf{f}$, $\mathbf{g}$ have been computed in cartesian systems which are parallel to the one at $G$. However, in order to evaluate the integral, it is convenient to introduce a new set of axes with the new $z$ axis along $\mathbf{X}_1$. If the unit vectors

$$\mathbf{i} = (1/\sqrt{6})(1, 1, -2), \quad \mathbf{j} = (1/\sqrt{2})(-1, 1, 0), \quad \mathbf{k} = (1/\sqrt{3})(1, 1, 1)$$

are used to define the directions of the new $x$, $y$, and $z$ axes the new $z$ axis can be taken as pole and then the average over the azimuth $\beta$ applies only to the factor $(\mathbf{f}\cdot\mathbf{Q}_j)^2$. If the components of $\mathbf{f}$ in the new system are $(F_x, F_y, F_z)$ the average reduces to

$$L_{X,X} = \tfrac{1}{2}\exp\left(-2\gamma_X Q_j^2\right)\int_{-1}^{1}\left[\tfrac{1}{2}(F_x^2 + F_y^2)(1-x^2) + F_z^2 x^2\right] \times \exp\left(-6\delta_X Q_j^2 x^2\right)dx$$

$$= \exp\left(-2\gamma_X Q_j^2\right)\left\{(F_x^2 + F_y^2 - 2F_z^2)(24\delta_X Q_j^2)^{-1}\exp\left(-6\delta_X Q_j^2\right) + \tfrac{1}{4}\left[F_x^2 + F_y^2 - (F_x^2 + F_y^2 - 2F_z^2)(12\delta_X Q_j^2)^{-1}\right](\pi/6\delta_X Q_j^2)^{\frac{1}{2}}\operatorname{erf}(6\delta_X Q_j^2)^{\frac{1}{2}}\right\}.$$

If the components of $\mathbf{f}$ in the original cartesian system are $(f_x, f_y, f_z)$ the last equation becomes

$$(3)\quad L_{X_1X_1} = \tfrac{1}{2}\exp(-2\gamma_X Q_j^2)\{[\tfrac{2}{3}(f_x^2 + f_y^2 + f_z^2 - f_xf_y - f_yf_z - f_zf_x) + (f_xf_y + f_yf_z + f_zf_x)(6\delta_X Q_j^2)^{-1}](\pi/24\delta_X Q_j^2)^{\frac{1}{2}}\operatorname{erf}(6\delta_X Q_j^2)^{\frac{1}{2}} - (f_xf_y + f_yf_z + f_zf_x)(6\delta_X Q_j^2)\exp(-6\delta_X Q_j^2)\}.$$

$$L_{YX_1} = Q_j^{-2}\exp[-(\gamma_X + \gamma_Y)Q_j^2](\mathbf{f}\cdot\mathbf{Q}_j)(\mathbf{g}\cdot\mathbf{Q}_j) \times \exp\left[i\mathbf{Q}_j\cdot\mathbf{r}_{1Y} - \delta_X Q\begin{pmatrix} j \\ 1 \end{pmatrix}^2\right]d\omega/4\pi.$$

If, now, the same set of axes is introduced as in the last integral the average over the azimuth $\beta$ can be performed in the same way. The integral becomes

$$L_{YX_1} = \tfrac{1}{2}\exp[-(\gamma_X + \gamma_Y + 3\delta_X)Q_j^2]\int_{-1}^{1}[\tfrac{1}{2}(F_xG_x + F_yG_y)(1-x^2) + F_zG_zx^2] \times \exp[iQ_jr_{XY} - 3\delta_X Q_j^2(x^2-1)]dx$$

$$= \exp[-(\gamma_X + \gamma_Y + 3\delta_X)Q_j^2][F_zG_zj_0(Q_jr_{XY}) + (F_xG_x + F_yG_y - 2F_zG_z + 6\delta_X Q_j^2F_zG_z)(Q_jr_{XY})^{-1}j_1(Q_jr_{XY})].$$

The last line has been obtained by expanding the exponential in $\delta_X Q_j^2$ and keeping only terms up to the first order in $\delta_X Q_j^2$. When the components of $\mathbf{f}$, $\mathbf{g}$ are expressed in the original coordinate system the value of the average is

$$L_{YX_1} = \exp[-(\gamma_X + \gamma_Y + 3\delta_X)Q_j^2\{\tfrac{1}{3}(f_x + f_y + f_z)(g_x + g_y + g_z)j_0(Q_jr_{XY}) - [f_xg_y + f_yg_x + f_xg_z + f_zg_x + f_yg_z + f_zg_y - 2(f_x + f_y + f_z)(g_x + g_y + g_z)\delta_X Q_j^2] \times (Q_jr_{XY})^{-1}j_1(Q_jr_{XY})\}.$$

$$(4)\quad L_{X_1X_2} = Q_j^{-2}\exp(-2\gamma_X Q_j^2)\int(\mathbf{f}\cdot\mathbf{Q}_j)(\mathbf{g}\cdot\mathbf{Q}_j)\exp\left\{i\mathbf{Q}_j\cdot\mathbf{r}_{12} - \delta_X\left[Q\begin{pmatrix} j \\ 1 \end{pmatrix}^2 + Q\begin{pmatrix} j \\ 2 \end{pmatrix}^2\right]\right\}d\omega/4\pi.$$

After introducing a new set of axes parallel to the unit vectors

$$\mathbf{i} = (0, 0, 1),\quad \mathbf{j} = (1/\sqrt{2})(1, -1, 0),\quad \mathbf{k} = (1/\sqrt{2})(1, 1, 0)$$

and expanding the exponential up to the first power of $\delta_X Q_j^2$ one can write this as

$$L_{X_1X_2} = \left(\frac{1}{4\pi}\right)Q_j^{-2}\exp[-2(\gamma_X + 2\delta_X)Q_j^2]\int_{-1}^{1}\int_0^{2\pi}(\mathbf{f}\cdot\mathbf{Q}_j)(\mathbf{g}\cdot\mathbf{Q}_j) [1 + 2\delta_X Q_j^2(1-x^2)(1+\sin^2\beta)]\exp(iQr_{12}x)\,dx\,d\beta$$

$$= \exp[-2(\gamma_X + 2\delta_X)Q_j^2][F_zG_zj_0(\mathbf{Q}_j\cdot\mathbf{r}_{12}) + (4\delta_X Q_j^2F_zG_z + F_xG_x + F_yG_y - 2F_zG_z + 2\delta_X Q_j^2F_zG_z)(Q_jr_{12})^{-1}j_1(Q_jr_{12})]$$

$$= \exp[-2(\gamma_X + 2\delta_X)Q_j^2]\{\tfrac{1}{2}(f_x + f_y)(g_x + g_y)j_0(Q_j r_{12})$$

$$- \tfrac{1}{2}[f_x g_x + f_y g_y + 3f_x g_y + 3f_y g_x - 2f_z g_z + 6\delta_X Q_j^2 (f_x + f_y)(g_x + g_y)]$$

$$\times (Q_j r_{12})^{-1} j_1(Q_j r_{12})\}.$$

Now the quantities $L^{\omega J}_{kk'}$ defined in (5.10) can be calculated by putting in appropriate values for $\mathbf{f}$ and $\mathbf{g}$ and summing over the degenerate modes. The results are given in Table IV.

## REFERENCES


1. ADAIR, R. K. Revs. Modern Phys. 22: 249. 1950.
2. ALCOCK, N. Z. and HURST, D. G. Phys. Rev. 75: 1609. 1949. See also FERMI, E. and MARSHALL, L. Phys. Rev. 71: 666. 1947.
3. ALCOCK, N. Z. and HURST, D. G. Phys. Rev. 83: 1100. 1951.
4. BORN, M. Repts. Progress. Phys. Phys. Soc. 9: 294. 1942-3.
5. BORN, M. and SARGINSON, K. Proc. Roy. Soc. (London), A, 179: 69. 1941.
6. BREIT, G. Phys. Rev. 71: 215. 1947.
7. See COPSON, E. T. An introduction to the theory of functions of a complex variable. The Clarendon Press, Oxford. 1935. p. 270, example 30.
8. DEBYE, P. Ann. Physik, 46: 809. 1915.
9. FERMI, E. Ricerca sci. 7: 13. 1936.
10. HERZBERG, GERHARD. Infrared and raman spectra of polyatomic molecules. D. Van Nostrand Company, Inc., New York, 1949.
11. HUGHES, D. J., BURGY, M. T., and RINGO, G. R. Phys. Rev. 77: 291. 1950.
12. HURST, D. G. and ALCOCK, N. Z. Can. J. Phys. 29: 36. 1951.
13. JOHNSTON, M. and DENNISON, D. M. Phys. Rev. 48: 868. 1935.
14. MAGNUS, W. and OBERHETTINGER, F. Special functions of mathematical physics. Chelsea Publishing Company, New York, 1949. p. 120.
15. POPE, N. K. and FELDMAN, G. Phys. Rev. 85: 703. 1952.
16. ROSENTHAL, JENNY. Phys. Rev. 46: 739. 1934.
17. Cf. SCHIFF, L. I. Quantum mechanics. McGraw-Hill Book Company, Inc. New York. 1949.
18. SHULL, C. G. and WOLLAN, E. O. Phys. Rev. 81: 527. 1951.
19. SPIERS, J. A. National Research Council (Canada) Report CRT-417, April, 1949; N.R.C. No. 1940, unpublished; and SPIERS, J. A. Phys. Rev. 75: 1765. 1949.
20. UREY, H. C. and BRADLEY, JR., C. A. Phys. Rev. 38: 1969. 1931.
21. WEINSTOCK, R. Phys. Rev. 65: 1. 1944.
22. WENTZEL, G. Z. Physik, 43: 1. 1927.
23. ZACHARIASEN, W. H. Theory of X-ray diffraction in crystals. John Wiley and Sons, Inc., New York, 1946.

## NOTE

### NUCLEAR CONSTANTS FOR REACTOR STUDIES*

The following data on nuclear constants of importance in connection with general reactor studies have been released by the United States, United Kingdom, and Canada, effective April 7, 1952.

The following information is declassified concerning the nuclear properties of uranium, plutonium, and xenon which are of importance in connection with general reactor studies:

1. *Thermal Neutron Cross Sections for Uranium* (These are currently accepted values in barns for 2200 meters per second neutrons.)

| Thermal neutron cross sections for: | $U^{235}$ | $U^{238}$ | Natural U |
|---|---|---|---|
| Fission | 549 | 0 | 3.92 |
| Capture | 101 | 2.80 | 3.5 |
| Scattering | 8.2 | 8.2 | 8.2 |

2. *Neutrons per Thermal Neutron Fission*

$$\nu = 2.5 \pm 0.1 \text{ for } U^{235}$$

3. *Fast Fission Effect*

3.1 The following are typical values of the fast fission contribution to the reactivity of research reactors:

3.1.1 In a reactor of the "CP-2" or "GLEEP" type: 2.9%

3.1.2 In a reactor of the "CP-3" or "ZEEP" type: 3.1%

3.2 The following are values of nuclear constants for natural uranium bombarded by *neutrons above the $U^{238}$ fission threshold* in a heterogeneous uranium reactor, which may be used for illustrative purposes:

3.2.1 Average fission cross section = 0.29 barns

3.2.2 Average radiative capture cross section = 0.04 barns

3.2.3 Average number of neutrons emitted per fission = 2.55

3.2.4 Average total cross section = 4.3 barns

3.2.5 Average inelastic scattering cross section = 2.47 barns

3.2.6 Average elastic scattering cross section = 1.5 barns

4. *Resonance Absorption Integral*

4.1 An approximate empirical formula for the effective value of the resonance absorption integral in a uranium lump at room temperature is given by:

*Issued as A.E.C.L. No. 4.

$$\int \sigma_c(E)\, dE/E = A[1 + \mu(S/M)]$$

where the integral is taken over the resonance energy band given in 4.3 below, $S$ is the lump surface area in cm.$^2$, and $M$ is the mass of the lump in grams.

The constants $A$ and $\mu$ depend on the total scattering cross sections associated with each uranium atom. They are, therefore, different for uranium metal or oxide lumps. In fact, $A$ is proportional to the 0.415 power of the scattering cross section associated with each uranium atom up to the scattering cross section of 1000 barns. For uranium metal, $A = 9.25$ barns and $\mu = 2.67$ gm./cm.$^2$ For $U_3O_8$, $\mu = 1.67$ gm./cm.$^2$ The limiting value of the integral at great dilution is 240 barns.

4.2 The approximate temperature dependence of the integral given under 4.1 is given by

$$\int \sigma_c(E)\, dE/E = A[1 + \alpha T + \mu(S/M)]$$

where $\alpha \simeq 10^{-4}$ per centigrade degree, the temperature $T$ is in degrees centigrade, and $A$ and $\mu$ are as in 4.1.

4.3 The logarithmic width of the resonance energy band $\log_e (E_0/E_1)$ is about 5.6 for uranium metal and 7.3 for $U_3O_8$ or $UO_2$.

4.4 The inverse diffusion length $\kappa_0$ for resonance neutrons in uranium metal of density $\rho$ gm. per cm.$^3$ is $\kappa_0 = 0.022\ \rho$ cm.$^{-1}$

5. *Plutonium Cross Sections*

5.1 Average values for the fission and capture cross sections of plutonium 239 for an approximately Maxwellian neutron spectrum with a most probable neutron velocity of 2200 meters per second are 664 barns and 361 barns, respectively.

5.2 Neutrons per thermal neutron fission of $Pu^{239} = 3.0 \pm 0.1$.

6. Thermal neutron absorption cross section of $Xe^{135} = 3.5 \times 10^6$ barns.

## LETTERS TO THE EDITOR

*Under this heading brief reports of important discoveries in physics may be published. These reports should not exceed 600 words and, for any issue, should be submitted not later than six weeks previous to the first day of the month of issue. No proof will be sent to the authors.*

### The Superconductive Transition in Lead*

Measurements of the magnetic and resistive properties of the "hard" superconductors niobium (1) and tantalum (4) have shown that these metals are not "ideal" homogeneous superconductors, but have a behavior which may be explained on the basis of extensions of Mendelssohn's "sponge" model (3). Previously observed discrepancies between the magnetic and resistive critical fields for lead (2), normally regarded as a "soft" superconductor, suggested that it might exhibit similar anomalous behavior.

Measurements were therefore made on spectrographically pure lead supplied by Messrs. Johnson Matthey, laboratory number 4138. The samples were in the form of wire cold-extruded to a diameter of 0.043 cm. with a length of 60 cm., "concertina-ed" at every 6 cm. Coils, each 5 cm. long (5), were slipped over four of the 10 sections and connected in series with a galvanometer. When a longitudinal magnetic field is discontinuously destroyed, the deflection of this galvanometer determines the change of magnetic flux through the specimen. Current and potential leads were soldered with Wood's metal to the ends of the lead specimen.

Figs. 1 and 2 show some of the results obtained. The magnetic transition is approximately discontinuous, i.e. from this point of view alone the lead behaves as an ideal superconductor; the resistance transition, however, covers a range of magnetic field the extent of which varies

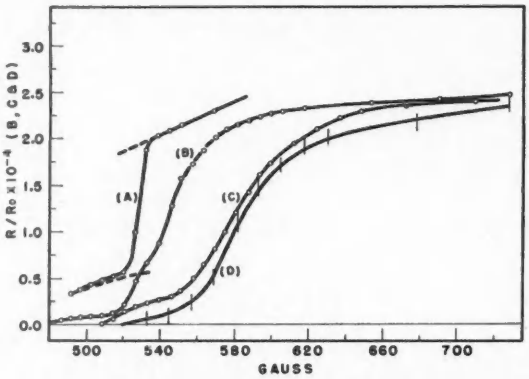


Fig. 1. Transitions in lead at 4.21°K. (*A*) ballistic galvanometer deflection (in arbitrary units); (*B*), (*C*), and (*D*) resistive transitions at 94, 10, and 2 ma.

both with the temperature and the measuring current. In the latter connection it may be remarked that the highest current used—94 ma., chosen to give a current density equal to the lower current density used by MacDonald (2)—would provide a surface field of 6.7 gauss.

As in the case of tantalum, the postulate of a disconnected "filament" structure in the lead may be used to explain these results.

The absence of any measurable frozen-in-flux shows both that the filaments are small in total volume and that they do not form a connected "mesh" capable of freezing a measurable field in the bulk material, which contrasts with the results found for niobium specimens (1). Secondly, the resistance curves are displaced to the left as the measuring current increases showing the effect of the field generated by the current in the filaments. This field progressively destroys the superconductivity of the filaments, and a sufficiently high current density will thus give the illusion of an ideal superconducting specimen since there will then be approximate

**Issued as N.R.C. No. 2816.*

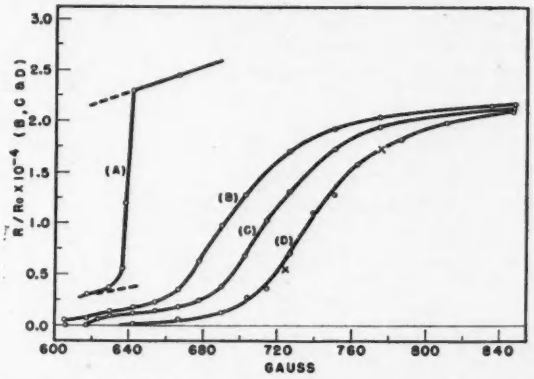


Fig. 2. Transitions in lead at 3.28°K. (*A*) ballistic galvanometer deflection (in arbitrary units); (*B*), (*C*), and (*D*) resistive transitions at 94, 30, and 10 ma. *X* gives the approximate position for 2 ma.

agreement between the magnetic and resistive transitions. In fact, however, a more satisfactory fundamental approach involves using a current so small that the state of the filaments is unaffected by it. Such a current in the present case is almost at the limit of sensitivity of the measuring system, but it appears to be of the order of 2 ma. at 4.2°K. and slightly higher at 3.3°K. This is a current density of 3 amp. cm.$^{-2}$, the current density being the appropriate function in this case, contrasting with the product of current density and the radius which is appropriate when considering the Silsbee effect in an "ideal" superconductor.

It is apparent that the resistance of the specimen continues to increase with increasing magnetic field, at least up to 1300 gauss, the highest field used. This phenomenon, existing only below the normal transition temperature, has been observed previously by van den Berg(6), who deduced a "corrected" resistance of his specimen by extrapolating the observed resistance to zero field. At low current densities this becomes a somewhat arbitrary procedure, however, owing to the nonlinear resistance–field relationship and to the difficulty of assigning a terminal field for the superconducting normal transition.

The writer is indebted to Dr. D. K. C. MacDonald for suggesting these measurements.

1. Jackson, L. C. and Preston-Thomas, H. Phil. Mag. 41: 1284. 1950.
2. MacDonald, D. K. C. and Mendelssohn, K. Proc. Roy. Soc. (London), A, 200: 66. 1949.
3. Mendelssohn, K. Proc. Roy. Soc. (London), A, 152: 34. 1935.
4. Preston-Thomas, H. Phys. Rev. In press. 1952.
5. Preston-Thomas, H. Rev. Sci. Instruments. In press. 1952.
6. van den Berg, G. J. Physica, 14: 111. 1948.

Received July 14, 1952.

H. Preston-Thomas†
Division of Physics,
National Research Council,
Ottawa, Canada.
†*National Research Laboratories Postdoctorate Fellow.*

## Some Atomic Masses for Tellurium

We have recently measured the following atomic mass differences with a double-focusing mass spectrograph (3): $\frac{1}{2}Te^{122} - Ni^{61}$, $\frac{1}{2}Te^{124} - Ni^{62}$, $\frac{1}{2}Te^{128} - Ni^{64}$, and $\frac{1}{2}Te^{130} - Cu^{65}$. These data have been combined with existing information concerning the masses of $Ni^{61}$, $Ni^{62}$, $Ni^{64}$, and $Cu^{65}$ to obtain the masses of $Te^{122}$, $Te^{124}$, $Te^{128}$, and $Te^{130}$. Relative masses for all the stable isotopes of tellurium, except $Te^{120}$, have been obtained (11) by Silvey, Hardy, and Townes. Using these relative masses together with our absolute ones, we have computed the most probable masses for $Te^{122}$, $Te^{124}$, $Te^{128}$, and $Te^{130}$.

The experimental mass differences, which have been determined by the doublet method, are as follows: $\frac{1}{2}Te^{122} - Ni^{61} = 0.0209 \pm 3$ AMU, $\frac{1}{2}Te^{124} - Ni^{62} = 0.0230 \pm 2$ AMU (7), $\frac{1}{2}Te^{128} - Ni^{64} = 0.0244 \pm 3$ AMU, and $\frac{1}{2}Te^{130} - Cu^{65} = 0.0257 \pm 2$ AMU. In view of the uncertainty in the mass of $C^{12}$, calculations of the tellurium masses have been carried out using both the Minnesota mass spectroscopic value of $12.003842 \pm 4$ AMU (1), and the transmutation value of $12.003804 \pm 17$ AMU (9). The mass of $Te^{122}$ has been calculated using figures for the mass of $Ni^{61}$ of $60.94910 \pm 10$ AMU (based on $C^{12} = 12.003842$) and $60.94905 \pm 4$ AMU (based on $C^{12} = 12.003804$). These are weighted means of the Minnesota value (2), and our value for $Ni^{60} = 59.94931 \pm 14$ AMU plus the Chalk River measurement $Ni^{61} - Ni^{60} = 0.99980 \pm 3$ AMU (8). The mass of $Te^{124}$ has been computed from the Minnesota figure for $Ni^{62}$(2). The mass of $Te^{128}$ has been computed using $Ni^{64} = 93.94751 \pm 7$ AMU. This is the weighted mean of the Minnesota (2) and our values (5). Finally, the mass of $Te^{130}$ has been calculated using the Minnesota figure for $Cu^{65}$ (2).

The experimental masses for $Te^{122}$, $Te^{124}$, $Te^{128}$, and $Te^{130}$ are shown in Table I. Also shown are the adjusted values obtained by combining the Columbia mass difference ratios (11) with the experimental masses. The ratios used in this "adjustment of conditioned measurements" were $(Te^{130} - Te^{128})/(Te^{128} - Te^{124}) = 0.50019 \pm 12$, and $(Te^{124} - Te^{122})/(Te^{128} - Te^{124}) = 0.49956 \pm 12$.

Using the Columbia results we have also calculated the masses of $Te^{123}$, $Te^{125}$, and $Te^{126}$. These are shown at the bottom of Table I.

TABLE I

| Te isotope | Minnesota carbon C = 12.003842 ± 4 | | Transmutation carbon C = 12.003804 ± 17 | |
|---|---|---|---|---|
| | Experimental value, AMU | Adjusted value, AMU | Experimental value, AMU | Adjusted value, AMU |
| 122 | 121.9400 ± 6 | 121.9395 ± 4 | 121.9399 ± 6 | 121.9393 ± 4 |
| 124 | 123.9396 ± 4 | 123.9397 ± 4 | 123.9392 ± 4 | 123.9394 ± 4 |
| 128 | 127.9438 ± 6 | 127.9443 ± 4 | 127.9438 ± 6 | 127.9440 ± 4 |
| 130 | 129.9482 ± 4 | 129.9479 ± 4 | 129.9477 ± 4 | 129.9475 ± 4 |
| 123 | | 122.9426 ± 10 | | 122.9423 ± 10 |
| 125 | | 124.9431 ± 4 | | 124.9428 ± 4 |
| 126 | | 125.9424 ± 4 | | 125.9420 ± 4 |

Earlier measurements with our instrument gave the values (5): $Te^{126} = 125.9427 \pm 10$ AMU, $Te^{128} = 127.9471 \pm 10$ AMU, and $Te^{130} = 129.9467 \pm 9$ AMU (all based on $C^{12} = 12.003804$). The first and last of these are in satisfactory agreement with the present values, but the second is too large, a fact which has already been noted (4).

Sher, Halpern, and Mann (10) have found the lowest $(\gamma,n)$ threshold for tellurium to be $6.5 \pm 0.2$ Mev. This can be fairly certainly assigned to the $Te^{125}$ $(\gamma,n)$ reaction, in poor agreement with the value of $5.2 \pm 0.6$ Mev. deduced from Table I. The $Te^{123}$ $(\gamma,n)$ threshold of $5.3 + 1.1$ Mev., deduced from Table I, is likewise much too small. It appears, therefore, as if the microwave absorption work involving $Te^{123}$ and $Te^{125}$ is in error. The reasonableness of the measured $Te^{125}$ $(\gamma,n)$ threshold is borne out by values for two nearby even–odd nuclides, $Cd^{113}$ and $Sn^{119}$, which are $6.44 \pm 0.15$ Mev. and $6.51 \pm 0.15$ Mev., respectively (6).

The authors wish to acknowledge gratefully the support in this work of the National Research Council of Canada and the Research Council of Ontario.

1. COLLINS, T. L., NIER, A. O., and JOHNSON, W. H., JR. Phys. Rev. 84: 717. 1951.
2. COLLINS, T. L., NIER, A. O., and JOHNSON, W. H., JR. Phys. Rev. 86: 408. 1952.
3. DUCKWORTH, H. E. Rev. Sci. Instruments, 21: 54. 1950.
4. DUCKWORTH, H. E. Symposium on mass spectroscopy in physics research. Washington, D.C. Sept. 6, 1951.
5. DUCKWORTH, H. E., KEGLEY, C. L., OLSON, J. M., and STANFORD, G. S. Phys. Rev. 83: 1114. 1951.
6. HANSON, A. O., DUFFIELD, R. B., KNIGHT, J. D., DIVEN, B. C., and PALEVSKY, H. Phys. Rev. 76: 578. 1949.
7. HOGG, B. G. and DUCKWORTH, H. E. Phys. Rev. 86: 567. 1952.
8. KINSEY, B. B., BARTHOLOMEW, G. A., and WALKER, W. H. Phys. Rev. 78: 481. 1950.
9. LI, C. W., WHALING, W., FOWLER, W. A., and LAURITSEN, C. C. Phys. Rev. 83: 512. 1951.
10. SHER, R., HALPERN, J., and MANN, A. K. Phys. Rev. 84: 387. 1951.
11. SILVEY, G., HARDY, W. A., and TOWNES, C. H. Bull. Am. Phys. Soc. 27 (No. 3): 60. 1952.

RECEIVED JULY 7, 1952.
DEPARTMENT OF PHYSICS,
MCMASTER UNIVERSITY,
HAMILTON, ONT.

BENJAMIN G. HOGG†
HENRY E. DUCKWORTH

†*Holder of a National Research Council of Canada Fellowship.*

# CANADIAN JOURNAL OF PHYSICS

## Notice to Contributors

GENERAL: Manuscripts should be typewritten, double spaced, and the **original and one extra copy** submitted. Style, arrangement, spelling, and abbreviations should conform to the usage of this Journal. Names of all simple compounds, rather than their formulas, should be used in the text. Greek letters or unusual signs should be written plainly or explained by marginal notes. Superscripts and subscripts must be legible and carefully placed. Manuscripts should be carefully checked before being submitted, to reduce the need for changes after the type has been set. If authors require changes to be made after the type is set, they will be charged for changes that are considered to be excessive. **All pages, whether text, figures, or tables, should be numbered.**

ABSTRACT: **An abstract of not more than about 200 words, indicating the scope of the work and the principal findings, is required.**

ILLUSTRATIONS:

(i) *Line Drawings:* All lines should be of sufficient thickness to reproduce well Drawings should be carefully made with India ink on white drawing paper, blue tracing linen, or co-ordinate paper **ruled in blue only**; any co-ordinate lines that are to appear in the reproduction should be ruled in black ink. Paper ruled in **green, yellow, or red should not be used** unless it is desired to have all the co-ordinate lines show. Lettering and numerals should be neatly done in India ink preferably with a stencil (**do not use typewriting**) and be of such size that they will be legible and not less than one millimeter in height when reproduced in a cut three inches wide. All experimental points should be carefully drawn with instruments. Illustrations need not be more than two or three times the size of the desired reproduction, but the ratio of height to width should conform with that of the type page. **The original drawings and one set of small but clear photographic copies are to be submitted.**

(ii) *Photographs:* Prints should be made on glossy paper, with strong contrasts; they should be trimmed to remove all extraneous material so that essential features only are shown. Photographs should be submitted **in duplicate**; if they are to be reproduced in groups, one set should be so arranged and mounted on cardboard with rubber cement; the duplicate set should be unmounted.

(iii) *General:* **The author's name, title of paper, and figure number should be written in the lower left hand corner (outside the illustration proper) of the sheets on which the illustrations appear.** Captions should not be written on the illustrations, but typed together at the end of the manuscript. All figures (including each figure of the plates) should be numbered consecutively from 1 up (arabic numerals). **Each figure should be referred to in the text.** If authors desire to alter a cut, they will be charged for the new cut.

TABLES: Each table should be typed on a separate sheet. Titles should be given for all tables, which should be numbered in Roman numerals. Column heads should be brief and textual matter in tables confined to a minimum. **Each table should be referred to in the text.**

REFERENCES: **These should be listed alphabetically by authors' names, numbered in that order, and placed at the end of the paper.** The form of literature citation should be that used in this Journal. **Titles of papers should not be given.** The first page only of the references cited should be given. **All citations should be checked with the original articles.** Each citation should be referred to in the text by means of the key number.

REPRINTS: A total of 50 reprints of each paper, without covers, are supplied free to the authors. Additional reprints will be supplied according to a prescribed schedule of charges. On request, covers can be supplied at cost.

Approximate charges for reprints may be calculated from the number of printed pages, obtained by multiplying by 0.6 the number of manuscript pages (double-spaced typewritten sheets, 8½ in. by 11 in.) and making allowance for space occupied by line drawings and half-tones (not inserts). The cost per page is tabulated at the back of the reprint request form sent with the galley.

## *Contents*


Page

Alpha Particles from the Photodisintegration of Silver and Bromine—*R. N. H. Haslam, A. G. W. Cameron, J. A. Cooke, and E. H. Crosby* - - - - - - - - - - - - - - - - - - - - - - 349

Electron Microscope Studies of Evaporated Cadmium and Zinc—*R. S. Sennett, T. A. McLauchlan, and G. D. Scott* - - - - 370

The Low Energy Spectrum of Cosmic-ray Mesons at Sea Level at High Geomagnetic Latitudes—*D. C. Rose and A. G. Voisin* - 373

Further Observations on the Macromosaic Structure of Tin Single Crystals—*E. Teghtsoonian and Bruce Chalmers* - - - - - - 388

Efficiency of the Long Boron Counter for Fast Neutrons—*S. A. Kushneriuk* - - - - - - - - - - - - - - - - - - - - 402

Superlattice Studies in the Systems Silver–Magnesium–Tin and Silver–Magnesium–Zinc—*W. G. Henry and G. V. Raynor* - - 412

Self-diffusion at Silver Surfaces—*W. C. Winegard and B. Chalmers* - 422

Slow $\pi$-Mesons in Cosmic-ray Stars and the Negative–Positive $\pi$-Meson Ratio—*J. Y. Mei and E. Pickup* - - - - - - - - - 430

Search for Anomalous Absorption of Ra(B + C) $\gamma$ Rays—*W. R. Dixon and G. N. Whyte* - - - - - - - - - - - - - - - 438

On the $\gamma$-Ray Spectrum of Ra(B + C)—*G. N. Whyte* - - - - - - 442

Mutual Inductance of Circuits on a Two Layer Earth—*James R. Wait* - - - - - - - - - - - - - - - - - - - - - - - - 450

Size Distribution of Cosmic Ray Stars in Photographic Emulsions—*J. Y. Mei* - - - - - - - - - - - - - - - - - - - - 453

The Disintegration of $Tm^{170}$—*R. L. Graham, J. L. Wolfson, and R. E. Bell* - - - - - - - - - - - - - - - - - - - - 459

The Photoneutron Cross Sections for the Reactions $Br^{81}(\gamma,n)Br^{80}$ and $Br^{81}(\gamma,n)Br^{80*}$ and an Analysis of the Ratio Between These Cross Sections—*L. Katz, L. Pease, and H. Moody* - - - - - - 476

Further Observations on Dendritic Growth in Metals—*F. Weinberg and Bruce Chalmers* - - - - - - - - - - - - - - - - 488

Note on the Resolving Power of Mass Spectrometers—*Larkin Kerwin* 503

Electromagnetic Fields of Current-carrying Wires in a Conducting Medium—*James R. Wait* - - - - - - - - - - - - - - - 512

Design and Performance of a Fused Silica Microbalance—*Hugh Carmichael* - - - - - - - - - - - - - - - - - - - - - 524

Initial Distribution of Compton Electrons—*H. E. Johns, D. V. Cormack, S. A. Denesuk, and G. F. Whitmore* - - - - - - 556

High Frequency Gas Discharge Breakdown in Neon—*A. D. MacDonald and D. D. Betts* - - - - - - - - - - - - - - - - 565

Raman Spectroscopy of Low Pressure Gases and Vapors—*H. L. Welsh, M. F. Crawford, T. R. Thomas, and G. R. Love* - - - 577

The Theory of Neutron Diffraction by Gases. 1—*N. K. Pope* - - - 597

Nuclear Constants for Reactor Studies—*Atomic Energy of Canada Ltd.* - - - - - - - - - - - - - - - - - - - - - - - - 624

Letters to the Editor:

The Superconductive Transition in Lead—*H. Preston-Thomas* 626

Some Atomic Masses for Tellurium—*B. G. Hogg and H. E. Duckworth* - - - - - - - - - - - - - - - - - - - - - - 628


*Printed* in Canada *by* University of Toronto Press